

WASM: Minerals, Energy and Chemical Engineering

**High-Pressure Microfluidic Crystallization of Active
Pharmaceutical Ingredients Using a Gas Antisolvent Process**

Deepali Arora

0000-0002-2400-3076

**This thesis is presented for the Degree of
Doctor of Philosophy
of
Curtin University**

May 2021

Declaration

To the best of my knowledge and belief this thesis contains no material previously published by any other person except where due acknowledgment has been made. This thesis contains no material which has been accepted for the award of any other degree or diploma in any university.

12 May 2021

To,
My Parents,
Brother and Uncle

Statement of Attribution

“Arora, D.; Sedev, R.; Beh, C. C.; Priest, C.; Foster, N. R., Precipitation of Drug Particles Using a Gas Antisolvent Process on a High-Pressure Microfluidic Platform. Industrial & Engineering Chemistry Research 2020, 59 (25), 11905-11913.”

	Con-ception and de-sign	Acquisi-tion of data & method	Data condi-tioning & manipula-tion	Analy-sis & statisti-cal method	Interpre-tation & dis-cussion	Final ap-proval
Emeritus Prof Neil R. Foster	<input checked="" type="checkbox"/>	<input type="checkbox"/>	<input type="checkbox"/>	<input type="checkbox"/>	<input type="checkbox"/>	<input checked="" type="checkbox"/>
I acknowledge that these represent my contribution to the above research output Signature: See appendices section 8.4 Date:						
Dr Rossen Sedev	<input checked="" type="checkbox"/>	<input checked="" type="checkbox"/>	<input checked="" type="checkbox"/>	<input checked="" type="checkbox"/>	<input checked="" type="checkbox"/>	<input checked="" type="checkbox"/>
I acknowledge that these represent my contribution to the above research output Signature: Date: 20 April 2021						
Dr Chau Chun Beh (Jane)	<input type="checkbox"/>	<input type="checkbox"/>	<input type="checkbox"/>	<input type="checkbox"/>	<input checked="" type="checkbox"/>	<input checked="" type="checkbox"/>
I acknowledge that these represent my contribution to the above research output Signature: Date: 22/4/2021						
Prof Craig Priest	<input checked="" type="checkbox"/>	<input type="checkbox"/>	<input type="checkbox"/>	<input type="checkbox"/>	<input checked="" type="checkbox"/>	<input checked="" type="checkbox"/>
I acknowledge that these represent my contribution to the above research output Signature: Date: 26/4/2021						

Every reasonable effort has been made to acknowledge the owners of copyright material. I would be pleased to hear from any copyright owner who has been omitted or incorrectly acknowledged.

Deepali Arora

Abstract

This thesis presents one of the first demonstrations of the use of dense gas processes on a microfluidic platform for continuous crystallization of active pharmaceutical ingredients (APIs). The efficiency of pharmaceutical compounds is determined by their physicochemical properties which are strongly influenced by the size and morphology of the particles produced. These particle characteristics are determined during crystallization which makes it a crucial manufacturing step in the production of APIs. However, conventional crystallization techniques are batch-based and have issues associated with process and economic efficiencies. Thus, in this thesis we have focussed on developing a reliable and efficient platform for continuous API crystallization to overcome the limitations of the current methods.

The micromixer platform developed here uses dense phase CO₂ as the antisolvent to trigger API crystallization from an organic solution under dynamic flow conditions. This allows the integration of the advantages of greener processing and residue (organic)-free product offered by dense gas processes with the excellent process control and superior process homogeneity offered by microfluidic technology. Micromixers fabricated in Borofloat 33 (BF33) glass are used to study the gas-liquid mixing and are sandwiched within a stainless-steel holder that enables the use of standard connectors and off-the-shelf components. Light microscopy is used for monitoring the gas-liquid mixing. The main focus has been on the manipulation of the rate of supersaturation to trigger precipitation by on-chip solvent expansion. The influence of factors such as micromixer design (gas-to-liquid ratio, fluidic resistance), choice of API-solvent pair, solution concentration and mixing conditions (antisolvent properties, fluid speeds, residence time) is studied.

The influence of crystallization kinetics on particle size and morphology has been investigated. By changing the mixing conditions, particle size can be reliably varied between 0.1 μm and 500 μm . It was also shown that faster mixing forms smaller and highly crystalline particles. The formation of purely organic nanoflowers was demonstrated by tuning the API-solvent pair and mixing conditions without the use of any additives. The adaptability of the proposed set up towards different APIs (anticancer, antifungal, antileprotic, corticosteroid) was also confirmed. Furthermore, investigation of the influence of micromixer's fluidic resistance on gas-liquid mixing

and consequently on particle size and shape was investigated. Finally, the cocrystallization of two APIs from a binary solvent was attempted. The molar ratio of the APIs was varied to study the influence on crystal size and structure. We have produced coprecipitates containing a physical mixture of the APIs. The failure to produce cocrystals is attributed to the large difference in solubilities of the selected API pair and may be resolved by substantially varying API ratios and solution concentration to achieve the desired supersaturation state.

The microfluidic precipitation developed in this thesis offers an adaptable and continuous processing strategy for a range of pharmaceutical compounds. The platform may find application in both research and manufacturing. In a research context, it could be implemented to study and optimize crystallization outcomes for various drug compounds and their combinations. In a manufacturing context, it could be adapted for small-batch manufacturing of speciality drugs.

Acknowledgement of Country

We acknowledge that Curtin University works across hundreds of traditional lands and custodial groups in Australia, and with First Nations people around the globe. We wish to pay our deepest respects to their ancestors and members of their communities, past, present, and to their emerging leaders. Our passion and commitment to work with all Australians and peoples from across the world, including our First Nations peoples are at the core of the work we do, reflective of our institutions' values and commitment to our role as leaders in the Reconciliation space in Australia.

Acknowledgements

I thank God for His love, kindness and protection towards me and my loved ones. Particular thanks to Prof Vishnu Pareek for his ongoing support and encouragement that helped me navigate through my PhD. I am grateful to Prof Neil Foster for the provision of my PhD candidature, laboratory facilities at Curtin University and generous opportunities to present this work at conferences.

My sincere appreciation and special thanks to Dr Rossen Sedev and Prof Craig Priest for their immense support, ample guidance, resourceful criticism, and constructive suggestions that helped build this work. With a deep sense of gratitude, I would like to acknowledge the efforts of Dr Rossen Sedev that have helped me through my PhD and turn it into the success that it is.

To Dr Chau Chun Beh, thanks for helping me obtain chemicals and online research sources in the final year of my PhD. A special thanks to Dr Dimple Quyn for her wisdom, support and guidance that have been instrumental in overcoming various challenges during this time.

To the MMF facility at Curtin University (Dr Elaine, Dr Matthew, Dr Veronica and Dr Aaron), thanks for your guidance and patience through my learning period. A warm appreciation to the team at the ANFF facility in South Australia for helping me fabricate the micromixers and the holder that were at the heart of my project.

A heartfelt thanks to my best friends, Deepanshu Verma and Arpit Baral, for always being there for me regardless of what time of day it was. Deepanshu, it is through your support that I was able to embark this journey.

Most importantly, I would like to thank my family - my mother, father, brother, and uncle. Your constant and unbiased support and encouraging love has helped me realise every dream of mine. Your value in my life only grows with time.

Copyright statement

I have obtained permission from the copyright owners to use any third-party copyright material reproduced in the thesis (e.g. questionnaires, artwork, unpublished letters), or to use any of my own published work (e.g. journal articles) in which the copyright is held by another party (e.g. publisher, co-author).

Contents

Introduction.....	1
Chapter 1.....	4
Critical Review	4
1.1 Crystallization of APIs.....	4
1.2 Dense Gas Processes	27
1.3 Microfluidics for Crystallization of APIs.....	36
Previous Attempts to Combine High-Pressure Processes Relevant to Pharmaceutics and Microfluidics	40
Motivation, Scope and Objective: Incorporation of a Dense Gas Process on a Microfluidic Platform for the Continuous Crystallization of Pharmaceutical Compounds.....	44
Chapter 2.....	46
Materials and Methods	46
2.1. Materials.....	46
2.2 Micromixer Fabrication.....	53
2.3 High-Pressure Tests	57
2.4 Metal Holder.....	60
2.5 Connections to the Micromixer	61
2.6 Micromixer Cleaning	62
2.7 Experimental Rig	62
2.8 Micronization.....	63
2.9 Characterization	64
Chapter 3.....	70
Precipitation of Drug Particles Using a Gas Antisolvent Process on a High-Pressure Microfluidic Platform.....	70
3.1 Introduction	70
3.2 Gas-Liquid Mixing in Microreactors	71

3.3 Results and Discussion.....	74
3.4 Conclusions	87
Chapter 4.....	88
Influence of API-Solvent Pair Interactions on the Micro-precipitation Process	88
4.1 Introduction	88
4.2 Results and Discussion.....	88
4.3 Conclusions	108
Chapter 5.....	109
Influence of the Micromixer’s Fluidic Resistance on the Microcrystallization of APIs.....	109
5.1 Introduction	109
5.2 Results and Discussion.....	110
5.3 Conclusions	119
Chapter 6.....	120
Formation of Pharmaceutical Cocrystals Using CO ₂ -Antisolvent Microprecipitation	120
6.1 Introduction	120
6.2 Results and Discussion.....	125
6.3 Conclusions	135
7 Conclusions.....	136
8 Appendices.....	139
8.1 Holders for High-Pressure Experiments	139
8.2 Connectors for the Interface	140
8.3 Metal Holder.....	140
8.4 Attribution Statement.....	141
8.5 Copyright Permissions	142
References.....	180

List of Figures

Figure 1. Pictorial presentation of (a) amorphous form (b) crystalline form (c) hydrates & solvates, and (d) clathrates.(37)	5
Figure 2. Solubility of polymorphic forms of chloramphenicol palmitate in water over a range of temperature.(43)	6
Figure 3. Comparison of dissolution profile of milled drug (nano range) versus coarse drug (micronized and non-micronized) each containing Vitamin E TPGS.(6).....	8
Figure 4. The solute-supersolubility diagram.(63)	11
Figure 5. Induction time of carbamazepine polymorphs with respect to supersaturation ratios in different solvents at 25 °C.(68)	12
Figure 6. Schematic representation showing the dependence of nucleation barrier ΔG^* on radius r according to classical nucleation theory.(69).....	14
Figure 7. Effect of supersaturation on nucleation rate.(71)	15
Figure 8. Solubilities of α - and γ -IMC in ethanol at different temperatures.(74)	16
Figure 9. Phase diagram of H ₂ O–NaCl system.(75).....	17
Figure 10. Effect of antisolvent feeding rate on particle size distribution of product at 500 rpm.(76).....	18
Figure 11. The effect of solution pH on crystal number per well at 4 °C.(77)	18
Figure 12. Solubility of CaSO ₄ ·2H ₂ O in NaCl solution as a function of temperature.(78).....	19
Figure 13. Solubility of benzocaine in different solvents.(88).....	20
Figure 14. Process flow diagram for batch manufacturing route.(92).....	22
Figure 15. A continuous pharmaceutical process for ibuprofen.(100)	25
Figure 16. Pressure-temperature diagram for a pure substance.	29
Figure 17. Several processes for the preparation of particles.(132)	31
Figure 18. Expansion of an organic solution using dense phase CO ₂ and particle precipitation.....	33
Figure 19. Relative expansion of the liquid phase for the systems carbon dioxide–solvent at 298, 303 and 313 K.(143).....	34

Figure 20. Comparison between the conventional process and the GAS process for the synthesis of Cu-Indo.(114).....	34
Figure 21. SEM images of the particles produced from the GAS and the conventional process: (a) conventional process; (b) slow expansion; (c and d) fast expansion.(114)	36
Figure 22. Schematic diagram depicting the components of a microfluidic platform.(146).....	37
Figure 23. CO ₂ -expanded ethanol on a borosilicate glass micromixer. Change of flow ratio, corresponding to an ethanol mole fraction of (a) 0.5 and (b) 0.8.(187).....	42
Figure 24. Illustration of the high-pressure micromixer made of silicon-BF33, and experimental & numerical profiles for fluid flow.(189)	42
Figure 25. TEM image of TPE NPs synthesized by μ SAS at 40 °C and 100 bar. Inset: corresponding size distribution.(192)	43
Figure 26. Structure of griseofulvin.(195)	47
Figure 27. Chemical structure of Luteolin.(197).....	47
Figure 28. Chemical structure of Budesonide.(202).....	48
Figure 29. Chemical structure of Dapsone.(206)	49
Figure 30. The three micromixer devices employed in the micronization experiments.	53
Figure 31. The Spin Coating System used for micromixer fabrication.	55
Figure 32. Kloe Dilase650 Direct Laser Write system.	56
Figure 33. (a) Substrate with microfluidic channel design, (b) lid showing eight predrilled inlet/outlet ports, and (c) Hot Embosser EVG 520HE.....	57
Figure 34. The rig used to perform the high-pressure tests.....	58
Figure 35. Micromixer assembly employed for high-P tests.	59
Figure 36. Gas leaks observed during pressure test at 40 bar and 25 °C.	60
Figure 37. Schematic for the stainless-steel holder used for making high-pressure connections to the glass micromixer.....	61

Figure 38. (a) The top and bottom part of the metal holder and (b) schematic showing the connections to the glass micromixer sandwiched between the holder.....	61
Figure 39. Rig used in the micronization experiments.	62
Figure 40. Basic setup of a DLS measurement system.(221)	64
Figure 41. Schematic showing the basic principle for a scanning electron microscope.	66
Figure 42. Different signals generated by a sample when a beam of electrons excites it.(223).....	67
Figure 43. Operational principle of X-ray interaction with sample.....	68
Figure 44. Geometry of micromixers: (a) T-junction: narrow channel width 32 μm , wider channel width 121 μm , depth 26 μm ; (b) X-junction: narrow channel width 32 μm , wider channel width 125 μm , depth 20 μm ; (c) Stainless-steel holder.	71
Figure 45. Epifluorescence image of the flow-focusing microfabricated device.(225)	72
Figure 46. Representative flow patterns of air-water flow in a circular tube of 1 mm diameter as observed by Triplett et al. (1999a).(228).....	73
Figure 47. Diagrammatic representation and total resistance for the wider channels in: (a) T-junction micromixer and (b) X-junction micromixer.	76
Figure 48. Flow characteristics in the micromixers: (a) mass flow rate, F , as a function of driving pressure, ΔP ; (b) equilibrium mole fraction (mean and standard deviation) of carbon dioxide, x_2 , as a function of driving pressure, ΔP ; (c) residence time within the X-micromixer, τ_1 , (\square), and within the outlet tubing, τ_2 , (\triangle), as a function of driving pressure, ΔP	77
Figure 49. Particle size, d , as a function of driving pressure, ΔP , when using a: (a) T-junction microfluidic mixer, (b) X-junction micromixer. Concentration of Griseofulvin in DMF: (\circ) 0.1%, (∇) 0.5%, and (\square) 1.0%. The horizontal baseline (\blacklozenge) and the benchtop precipitation (\blacklozenge) shows the particle size obtained under the same conditions without using any CO_2	80
Figure 50. Mixing of DMF and CO_2 ($P_{\text{CO}_2} = 40$ bar, $P_{\text{DMF}} = 40$ bar, $\Delta P = 15$ bar, $c_{\text{GF}} = 0.1\%$) to form a gas-expanded DMF (GXL) when contacting in a (a) T-junction micromixer, and (b) X-junction micromixer.....	82

Figure 51. Mixing length, L_{mix} , inside a T-junction micromixer for DMF and CO_2 (supplied at 40, 50 and 60 bar) as a function of driving pressure, ΔP	83
Figure 52. (a) Rate of decrease of particle size with respect to driving pressure, $b (= -d \ln d / d \Delta P)$, as a function of the concentration of Griseofulvin in DMF, c_{GF} : (\square) X-junction micromixer, and (\circ) T-junction micromixer. (b) Size of particles produced at $\Delta P = 10$ bar, d_{10} , as a function of the concentration of Griseofulvin in DMF, c_{GF} : (\square) X-junction mixer, and (\circ) T-junction mixer.	84
Figure 53. SEM micrographs of griseofulvin particles precipitated without any additive: (a–c) without ultrasound, (d–f) with ultrasound.(253)	85
Figure 54. SEM images of Griseofulvin particles. (a) Obtained by precipitation from subcritical water (170 °C, 20 bar)(252). Obtained by precipitation from DMF using microfluidic gas antisolvent precipitation ($P_{CO_2} = 40$ bar, $P_{soln} = 40$ bar, $\Delta P = 20$ bar, $c_{GF} = 0.5\%$) using: (b) a T-junction micromixer and $\Delta P = 20$ bar, (c) a T-junction micromixer and $\Delta P = 10$ bar, and (d) an X-junction micromixer and $\Delta P = 20$ bar. ..	86
Figure 55. Schematic for the micro-GAS process.	89
Figure 56. Volumetric flow rate, Q vs ΔP trends for acetone, ethyl acetate and DMF at 25 °C. The error bars are within the symbol size.	90
Figure 57. Slope as a function of inverse of solvent viscosity (μ). The slope error is within the symbol size.....	91
Figure 58. Mixing length for CO_2 -acetone flow in the X-junction micromixer.	92
Figure 59. Mixing length (distance between the junction and the point of optical uniformity along the mixing channel), L_{mix} , as a function of solvent viscosity, μ (25 °C, fluid supply pressure is 40 bar). The total length of the mixing channel is 45 mm.	92
Figure 60. Mean particle size, d , of Griseofulvin particles precipitated from three different solvents at varying driving pressure, ΔP (25 °C, fluid supply pressure is 40 bar).	93
Figure 61. Volumetric expansion, ε , vs. equilibrium pressure, P (25 °C). EA and DMF data are from reference. (232) Acetone data are from reference.(233)	95
Figure 62. Relative volumetric expansion at 40 bar, ε_{40} (25 °C), as a function of the Hansen distance, R_a	97

Figure 63. Mean particle size, d , of Luteolin, Griseofulvin and Budesonide particles precipitated from DMF at varying driving pressure, ΔP (25 °C).	98
Figure 64. Molecular volume, V_M , solid-liquid free energy, γ_{SL} , and $\log P$ as functions of the API's molecular mass, M . The error bars are within the symbol size.	100
Figure 65. SEM images of Griseofulvin particles microprecipitated from (a) DMF, (b) Acetone and (c) Ethyl acetate (25 °C, $\Delta P = 25$ bar).	101
Figure 66. SEM images of Luteolin particles microprecipitated DMF (25 °C) at: (a) $\Delta P = 15$ bar, (b) $\Delta P = 20$ bar, and (c) $\Delta P = 25$ bar.	103
Figure 67. Schematic for trapezoidal window at the junction of the micromixer. ...	104
Figure 68. Left: Cumulative drug release (%) of DOX from DOX-loaded hybrid microflowers, and Right: SEM images of SeNPs shapes stabilized by FA-CP with variable FA-CP concentrations (a to e).(272)	105
Figure 69. SEM images for the growing shapes of the porous structure of aragonite.(280).....	106
Figure 70. Synthesis, crystallization and nano-assembly of 1, 2-bis(tritylthio)ethane. (a) Scheme illustrating the reaction conditions for the synthesis and crystallization of 1, 2-bis(tritylthio)ethane. (b) ORTEP diagram of 1,2-bis(tritylthio)ethane. (c) The schematic unit cell of 1, 2-bis(tritylthio)ethane, showing the type of interactions in phenyl embraces (The green dashed line indicates T shaped edge to face interaction, and the red dotted line indicates parallel displaced orientation). (d) False-coloured FE-SEM image showing flower like assembly.(273).....	107
Figure 71. (a) X1 micromixer (post-junction length = 52.5 mm); (b) X2 micromixer (post-junction length = 161.5 mm); (c) & (d) show the electrical circuit modelling the micromixer resistance ($R_2 > R_1$).	111
Figure 72. Liquid volumetric flow rates, under gas-liquid co-flow, obtained for X1 and X2 micromixers at fixed fluid input pressure (= 40 bar) and different driving pressure, ΔP . Error bars are within the symbol size.	112
Figure 73. Gas-liquid flow profiles observed in micromixers (a) X1 and (b) X2....	113
Figure 74. The particle size obtained from X1 and X2 micromixers at fixed fluid input pressure of 40 bar and variable fluid driving pressure ($c_{GF} = 0.1\%$).	114

Figure 75. Particle size obtained from the X2 micromixer at different fluid input and driving pressures ($c_{GF} = 0.1\%$).	115
Figure 76. The particle size obtained from the X1 micromixer at different fluid input and driving pressures ($c_{GF} = 0.5\%$).	116
Figure 77. SEM images of GF particles precipitated from the X2 micromixer at fixed gas input pressure, $P_{in} = 70$ bar, with variable fluid driving pressure of: (a) 20 bar, (b) 25 bar, and (c) 30 bar.	117
Figure 78. SEM images of the GF particles precipitated from the X2 micromixer at fixed fluid driving pressure, $\Delta P = 20$ bar, with variable input pressure of: (a) 40 bar, (b) 60 bar, and (c) 70 bar.	118
Figure 79. Cocrystal solubility advantage ($S_{cocrystal}/S_{drug}$) in aqueous media is related to the cofomer and drug solubility ratio ($S_{coformer}/S_{drug}$). It is observed that $S_{coformer}/S_{drug} > 10$ leads to $S_{cocrystal}/S_{drug} > 1$. The solubility values refer to a specific pH value shown by the numbers above the data points, at 25 °C.(312)	121
Figure 80. Common supramolecular synthons formed from carboxylic acids, amides, pyridines, and other aromatic nitrogens.(312).....	122
Figure 81. SEM images of itraconazole/l-malic acid cocrystals: (a1 and a2) obtained from n-heptane, and (b1 and b2) produced by GAS.(319)	123
Figure 82. Polarized light microscopy photographs of DAP-LT co-crystals.(317) .	124
Figure 83. PXRD patterns for untreated LT as received from the company: the green lines represent pattern obtained for the old stock whereas the red lines represent pattern obtained for the fresh stock.	125
Figure 84. PXRD patterns for untreated luteolin as reported in literature.(317, 320, 321) (Note: patterns have been vertically offset for clarity).	126
Figure 85. PXRD pattern for LT: untreated (as received) and treated (at $P_{in} = 40$ bar and $\Delta P = 25$ bar). Red lines represent treated LT and black lines represent untreated LT. (Note: patterns have been vertically offset for clarity).....	127
Figure 86. SEM images for Luteolin: (a) untreated and (b) treated material at $P_{in} = 40$ bar and $\Delta P = 25$ bar.	128
Figure 87. PXRD pattern for DAP: untreated (as received) and treated (at $P_{in} = 40$ bar and $\Delta P = 25$ bar). (Note: patterns have been vertically offset for clarity).	128

Figure 88. SEM images for DAP: (a) untreated and (b) treated material at $P_{in} = 40$ bar and $\Delta P = 25$ bar.	129
Figure 89. PXRD pattern for LT, DAP and DAP-LT (equimolar) samples processed at $P_{in} = 40$ bar and $\Delta P = 25$ bar. (Note: patterns have been vertically offset for clarity).	130
Figure 90. PXRD pattern for DAP-LT samples processed at $P_{in} = 40$ bar: blue lines ($\Delta P = 10$ bar, 5:1), pink lines ($\Delta P = 10$ bar, 1:1) and purple lines ($\Delta P = 25$ bar, 1:1). (Note: patterns have been vertically offset for clarity).	131
Figure 91. Comparison of the XRD peaks for the individual APIs and their mixtures. (Note: patterns have been vertically offset for clarity).	132
Figure 92. PXRD pattern of dapson (a), caffeine (b), physical mixture CAF/DAP (1:1) PM (c), cocrystal CAF/DAP (1:1) and simulated (d).(322)	133
Figure 93. SEM images for DAP-LT particles at $P_{in} = 40$ bar: (a) API ratio of 1:1 produced at $\Delta P = 25$ bar, (b) API ratio of 1:1 produced at $\Delta P = 10$ bar, and (c) API ratio of 5:1 produced at $\Delta P = 10$ bar.	134
Figure 94. (a) Two different holders (on left – polymer & on right – metal) used for testing the durability for commonly used components under high-pressures. (b) Widening of the port cavities in the polymer holder due to overtightening of flangeless fittings.	139
Figure 95. FEP tubing glued at the end that goes into the flangeless fitting.	140
Figure 96. Schematic showing the holder-micromixer assembly used for the high-pressure experiments.	140

List of Tables

Table 1. Batch vs. continuous flow synthesis of spirooxazine photochromic dyes. (This table is reproduced from work conducted and published by CSIRO (13, 101))	25
Table 2. Major pharmaceutical-related companies pursuing continuous production.(102)	26
Table 3. Conventional Methods of Micronization.(113)	28
Table 4. Comparison between GAS and Conventional Process for the Synthesis of Cu-Indo at 25 °C.(114)	35
Table 5. Ethanol concentrations, recommended dose, intake, and blood concentration from some common prescription drugs for infants and children. RD : recommended dose. BEC : Blood ethanol concentration.(212).....	50
Table 6. Common properties for solvents used in this study.(215-218).....	52
Table 7. Dimensions for the 3 micromixer designs.	54
Table 8. Scan parameters used in the XRD analysis.	69
Table 9. Hansen solubility parameters (256) and octanol-water partition coefficients (257) of the solvents used in this study. EA = ethyl acetate; DMF = dimethylformamide; δ = (total) solubility parameter (δ_D – dispersion component, δ_P – polar component, δ_H – hydrogen bonding component), logP = log(octanol-water partition coefficient).....	96
Table 10. Thermophysical parameters of the APIs used in this study. LT = Luteolin; GF = Griseofulvin; BD = Budesonide; M = molecular mass; ρ = density; VM = molecular volume (calculated as M/ρ); γ_{SL} = interfacial free energy (obtained from contact angle measurements); δ = solubility parameter.(261, 264-266).....	99
Table 11. Density and viscosity values for CO ₂ as a function of pressure (at T = 25 °C). The values for CO ₂ density and viscosity at different conditions were obtained using Peace Software.(306).....	115
Table 12. Experimental scheme for the cocrystallization of DAP & LT.....	125
Table 13. Peak positions for DAP, LT, and DAP-LT samples microprecipitated at P_{in} = 40 bar and ΔP = 25 bar.....	130
Table 14. Solubility values for DAP and LT in individual solvents at 25 °C.....	134

Introduction

Pharmaceutical crystallization is a crucial step in the manufacturing of medicinal products. It can be used for the separation or purification of intermediates or as the final step in the production of APIs.(1, 2) The size and morphology of the APIs is determined during the crystallization step and significantly influences their physicochemical properties such as solubility, dissolution rate, and chemical stability.(3, 4) This further effects the bio-efficacy of the final product.(5-7) Traditionally, pharmaceuticals are crystallized using batch-based processes, however, this has limitations such as longer processing times, higher waste-to-product ratios, product variability (due to process inhomogeneity), larger space requirements, higher maintenance requirements and increased environmental footprint.(8-11) Thus, it is important to develop methods that allow for controlled pharmaceutical crystallization in an efficient manner.

Continuous crystallization holds the potential to overcome the limitations of batch-based processes by optimization of process parameters to control the crystallization outcome and produce consistent high-quality product. Thus, there have been significant efforts in the pharmaceutical engineering and crystallization techniques to transition to continuous processing methods.(12-15)

Dense gas processes are gaining a lot of momentum in pharmaceutical processing. The use of high-pressure CO₂ as antisolvent allows for greener processing and easier elimination of organic residues. A significant amount of work has been done using supercritical CO₂ to extract, dissolve or precipitate pharmaceutical compounds including APIs, nutraceuticals, and biopolymers.(16-19) However, we propose the use of subcritical CO₂ as the antisolvent for pharmaceutical crystallization. Gas-expanded liquid formation is easily achieved with many organic solvents and can be used to trigger precipitation by decreasing the solubility of the solute. Thus, it can be applied to a wide range of pharmaceutical compounds. Microfluidics is another tool that offers unique capabilities as a processing technology owing to the excellent control over process parameters, superior process homogeneity, enhanced reproducibility, potential for adaptability, miniaturization of process chemistry (lab-on-a-chip) and optical access for in situ characterization.(20-24) The enhanced process control enables tight control over crystal size and morphology. Thus, this thesis reports a gas antisolvent

process on a microfluidic platform for continuous crystallization of APIs. The approach combines the advantages of greener processing and solvent-free product offered by dense gas technology with the excellent process control and reproducibility offered by microfluidics.

Chapter 1 discusses the different factors influencing pharmaceutical properties and techniques that are used to improve their in-situ bioavailability. A detailed discussion of the crystallization process and different crystallization techniques is provided. Finally, the limitation of batch crystallizers and the need to transition to continuous processing is argued. The integration of dense gas processes and microfluidics is proposed as a potential solution to resolve the issues associated with traditional crystallization methods. **Chapter 2** describes the high-pressure rig developed in this thesis. This includes the fabrication of glass microfluidic mixers and the bespoke stainless-steel holder. The APIs and chemicals used are presented. Detailed information on the micronization experiments is provided, including cleaning procedures. **Chapter 3** demonstrates the formation of a gas-expanded liquid (GXL) on the high-pressure microfluidic platform under dynamic flow conditions. Griseofulvin (GF), an antifungal drug, is used as the model API to demonstrate its continuous crystallization. The influence of residence time, micromixer design and solution concentration on the expansion process and crystallization are studied. **Chapter 4** focuses on the crystallization of various solute-solvent pairs and the formation of organic nanoflowers. The influence of solvent was investigated by precipitating GF from three different solvents (DMF, acetone and ethyl acetate). Whereas the influence of API was investigated by precipitating three different APIs (Luteolin, Griseofulvin and Budesonide) from DMF. **Chapter 5** explores the influence of the micromixer's fluidic resistance and antisolvent properties on the crystallization of GF from DMF. Two different micromixers consisting of the same junction geometry but different post-junction mixing lengths were used for this purpose. The antisolvent properties (density, viscosity) were varied by changing the fluid input pressures (40, 60 and 70 bar) at a fixed temperature (25 °C) for a given micromixer to study its influence on the microprecipitation process. In **Chapter 6**, the cocrystallization of two model APIs (Luteolin and Dapsone) is attempted to explore the potential of the high-pressure microfluidic platform for producing combination therapeutics. A binary mixture of acetone and ethanol was used as the solvent. The

drug-to-drug ratio was varied to investigate its influence on crystal structure of the microprecipitate.

Overall, this thesis presents the design and development of a high-pressure microfluidic platform for continuous pharmaceutical crystallization. A gas antisolvent method, using pressurized CO₂ as the antisolvent and traditional organic solvents, was used for the on-chip formation of gas-expanded liquid to trigger precipitation. Key parameters related to crystallization chemistry and kinetics were investigated to elucidate their influence on particle size and morphology. The formation of highly crystalline, purely organic crystals with unique morphologies was successfully demonstrated. This research could be used to develop a microfluidic crystallizer suitable for a wide range of APIs and their combinations. This platform would be advantageous in the small-batch manufacturing of pharmaceutical products with tightly controlled properties.

Chapter 1

Critical Review

1.1 Crystallization of APIs

A pharmaceutical product is made of two main components: the active pharmaceutical ingredient (API) and the excipient. The World Health Organization defines an active pharmaceutical ingredient as “a substance used in a finished pharmaceutical product, intended to furnish pharmacological activity or to otherwise have direct effect in the diagnosis, cure, mitigation, treatment or prevention of disease, or to have direct effect in restoring, correcting or modifying physiological functions in human beings”.(25) Other than APIs, the pharmaceutical products consist of excipients. These excipients exhibit little or no pharmacological activity as compared to the API but perform a variety of functional roles in the final dosage form including pH adjustment, stability, and binding.(26)

The API is the component in a pharmaceutical formulation that carries the therapeutic benefits. Crystallization is a crucial step in production of APIs as this is the step where the API properties are determined. This is because the characteristics of the API crystals such as size, shape and polymorph are determined at this stage and have a strong influence on the API properties. During crystallization, the atoms or molecules of the API arrange themselves into well-defined, three-dimensional crystal lattices to minimize the overall energy of the system. These atoms or molecules bind at fixed angles and distances which leads to crystal growth in a specific plane. Thus, control over the crystallization process enables control over the API properties.

Most APIs have multiple polymorphs, where the molecules in the crystal lattice can have different arrangements or conformations.(27, 28) These polymorphs may include amorphous solids, crystalline form, hydrates and solvates, and clathrates - Figure 1. Even though the polymorphs have similar chemical formula, they can have significantly different crystal structures which influences the API properties such as solubility, rate of dissolution, chemical stability, hygroscopicity and mechanical properties (density, hardness and melting point).(29-35) The ability to produce specific

polymorphs with desired properties is closely related to the efficiency of the drug development and manufacturing process, and also to the quality and stability of the final pharmaceutical product. Polymorphism in pharmaceuticals poses a major challenge to pharmaceutical scientists and process engineers as it directly influences the stability and properties of the final dosage form. One such example is the capsule form of Ritonavir (Norvir). It is an antiretroviral drug belonging to protease inhibitor class and is used to treat HIV-1 infection. Ritonavir was marketed in 1996, but had to be withdrawn from the market in 1998 due to spontaneous appearance of the stable and less soluble form II in Norvir semi-solid capsules.(36)

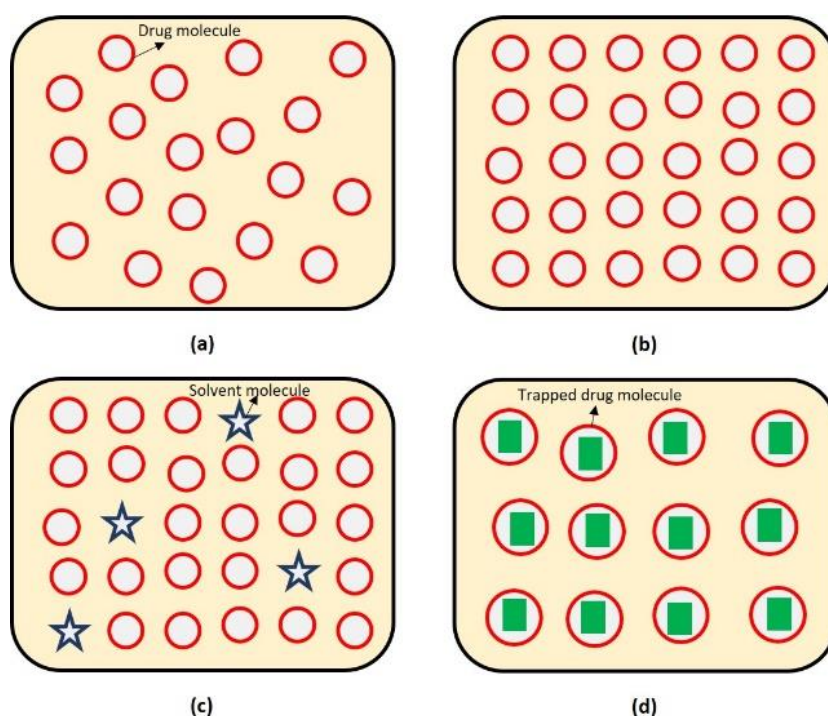


Figure 1. Pictorial presentation of (a) amorphous form (b) crystalline form (c) hydrates & solvates, and (d) clathrates.(37)

Alternatively, polymorphism is an opportunity to produce pharmaceuticals with tailor-made properties.(33, 34, 38) Thus, it is integral to reliably produce specific polymorphs with desired properties in the API development process. Long-term stability, enhanced solubility and dissolution rate, resistance to moisture absorbance, and ease of processing are some of the important features for a desirable polymorphic form.(39) Owing to the differences in the API properties, there have been continuous

efforts in pharmaceutical engineering and crystallization techniques to generate the desired API polymorphs in a robust and efficient manner. (33, 34, 38, 40, 41) This can be achieved by precise control of the crystallization process through controlled supersaturation, solvent selection, rate of crystallization, or temperature. These polymorphs are interesting to pharmaceutical companies since they may offer advantages over the original forms, e.g. improved bioavailability (solubility and dissolution rates) and different physicochemical properties (improved melting point and stability). For instance, the metastable polymorphs offer higher solubilities in comparison with the more stable forms and hence lead to improved bioavailability. Muramatsu et al.(42) have shown that the α form of crystalline chloramphenicol palmitate is less stable than its β form. Figure 2 shows the measured solubility of the α and β polymorphic forms in water as a function of temperature.(43) Clearly, the less stable α form exhibits higher solubility than the more stable β form at any temperature. Thus, production of metastable polymorphs can help in overcoming the existing limitation of drug bioavailabilities.(44-46)

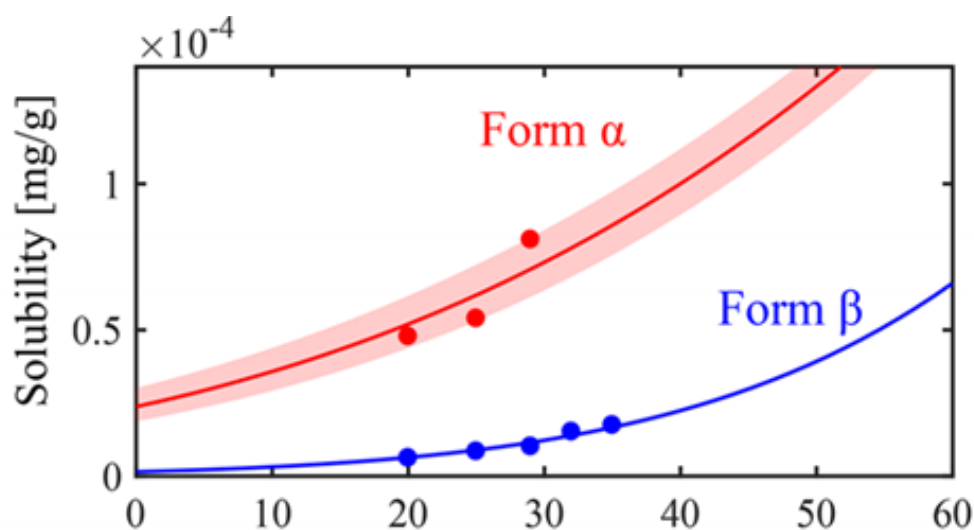


Figure 2. Solubility of polymorphic forms of chloramphenicol palmitate in water over a range of temperature.(43)

In addition to polymorphism, crystal size and shape are other crucial parameters that influence the bioavailability of pharmaceutical drugs. Pharmaceutical bioavailability is correlated with the API concentration in an aqueous environment. For poorly water-

soluble drugs, the rate of dissolution, dm/dt (mass dissolved per unit time, $\text{kg}\cdot\text{s}^{-1}$), is a limiting factor and is given by the Noyes-Whitney Equation(47):

$$\frac{dm}{dt} = DA \frac{c_E - c}{L} \quad 1$$

Here, D is the diffusion coefficient of the API ($\text{m}^2\cdot\text{s}^{-1}$), A is the area of solid-liquid contact (m^2), c_E is the equilibrium solubility of the API (kg or $\text{moles}\cdot\text{L}^{-1}$), c is its instantaneous value in the solution (kg or $\text{moles}\cdot\text{L}^{-1}$) and L is the thickness of the concentration medium (m). For a given solubility (c_E), the rate of dissolution is directly proportional to the area of the solid particles. Whereas the time for complete dissolution, τ , for spherical particles is proportional to the square of the initial particle size, d_0 (ρ is the density of the API)(48):

$$\tau = \frac{\rho d_0^2}{8Dc_E} \quad 2$$

Therefore, smaller particles or particles with increased surface area provide faster dissolution. Commonly, micron-sized particles are produced in the pharmaceutical industry, however, the bioavailability of poorly soluble compounds can be improved by further reduction of particle size down to the nanometre range. This is because smaller size of the nanoparticles results in larger total surface area which increases the amount available to permeate. The Ostwald–Freundlich equation is applicable to sub-micron sized spherical particles ($<1 \mu\text{m}$) and expresses the dependence of equilibrium solubility (also known as saturation solubility) on particle size as follows(49, 50):

$$\rho v \frac{RT}{M} \ln \frac{S_r}{S_\infty} = \frac{2\gamma_{sl}}{r} \quad 3$$

Here ρ is the solid density, v represents the molar volume, R is the gas constant, T is absolute temperature, M is the molar mass, S_r is the solubility of particles of radius r , S_∞ is the solubility of the solid with a plane surface (or consisting of large particles) and γ_{sl} is the solid-liquid interfacial tension. The combined effect of particle size reduction, enhanced surface area and saturation solubility, and a thinner diffusion layer could result in a paramount increase in the dissolution rate which improves the API bioavailability.(51)

The effect of particle size on solubility, dissolution, and bioavailability has been documented by many researchers.(6, 7, 52-54) Ghosh et al.(6) used a wet-media

nanomilling process to produce a nanosuspension of Vitamin E TPGS-based formulation. It was shown that the dissolution rate improved with reduction in particle size - Figure 3. The drop in dissolution occurred due to the switch of dissolution media from pH 2 to pH 6.8 with higher solubilities expected at pH 2 (compound is a free base). Moreover, some amount of precipitation would be expected at pH 6.8 which results in a lower dissolution value. When comparing the dissolution profile for the micronized (nm range) and non-micronized (μm range) drug formulations, significantly faster drug release was observed for the nanosuspension formulation.

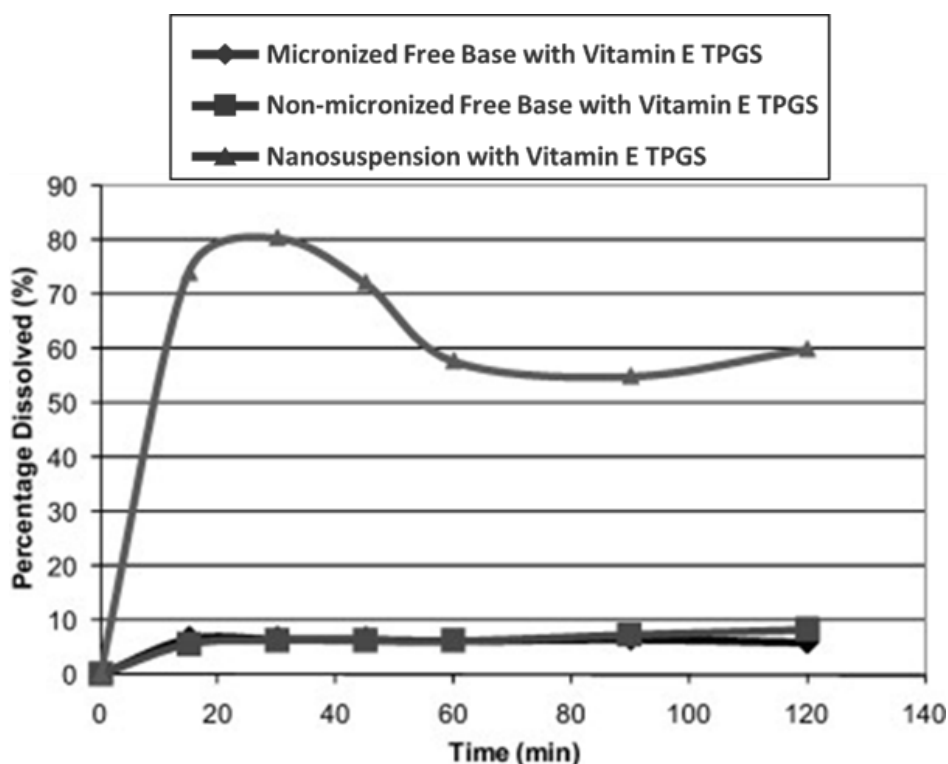


Figure 3. Comparison of dissolution profile of milled drug (nano range) versus coarse drug (micronized and non-micronized) each containing Vitamin E TPGS.(6)

Particle size and shape also influence the efficiency of the production process as they affect downstream operations such as formulation, filtration and drying.(5) Thus, particle shape and size are important to not only pharmaceutical scientists but also to process engineers in the design of manufacturing processes. Therefore, technologists are aiming to develop crystallization processes that offer tight control over the particle characteristics to improve the bioavailability of existing pharmaceutical products.

There are two main techniques for particle size reduction:

- Top-down approach: The top-down approach involves the process of breaking larger particles into smaller ones. This can be achieved via various milling techniques such as: media milling, microfluidization and high-pressure homogenization. The technique does not involve any harsh solvents; however, a high energy input is required. These processes can also be very inefficient. Often a lot of heat is generated which makes this technique unsuitable for processing heat-sensitive materials such as APIs.(36)
- Bottom-up approach: The bottom-up approach involves building up the particles from its molecules. With this technique, the drug is precipitated from a solution. Often an antisolvent is used to trigger precipitation. Various adaptations of this approach include: (i) solvent–antisolvent method; (ii) supercritical fluid processes; (iii) spray drying; and (iv) emulsion–solvent evaporation.(55, 56)

In the top-down approach, mechanical activation of pharmaceutical particles may occur during milling.(57) The overall surface energetics of particles may increase due to generation of localized amorphous regions and crystal defects.(58) This can cause instability issues during storage due to recrystallization of amorphous regions and/or reordering of crystal defects. For instance, an increase in the specific surface area of budesonide (~22% at 25 °C) was observed during storage after micronization. Temperature-dependent stress relaxation by intra-particle crack formation, crack propagation with time and particle fracture were proposed as a likely mechanism for the increase in surface area.(59) Another example is the re-crystallization of disordered regions in micronized revatropate hydrobromide during storage (~7 h for 1% sample).(60)

Bottom-up approaches have always been attractive to the pharmaceutical industry as these provide spatial control over process parameters, ease of scaling-up and platform stability. Thus, crystallization using an antisolvent (discussed in section 1.1.3) is widely used as a separation and filtration technique to obtain high-purity product.

1.1.1 Supersaturation

Supersaturation(61) is the thermodynamic driving force behind crystallization and is a prerequisite before a solid phase will appear in a saturated solution. It is usually defined as the logarithm of the saturation ratio, S (the ratio of actual concentration, c , to equilibrium concentration, c_E , under the same conditions) as follows:

$$S = \frac{c}{c_E} \quad 4$$

True thermodynamic supersaturation is the difference between the chemical potential of a substance in a given state and the equilibrium state, e.g., in solution (state 1) and in the crystal (state 2). Hence for an unsolvated solute crystallizing from a binary solution, this can be expressed as

$$\Delta\mu = \mu - \mu_E \quad 5$$

This chemical potential, μ , is defined in terms of the standard potential, μ_0 , and the activity, a , as

$$\mu = \mu_0 + RT \ln a \quad 6$$

Here R is the gas constant and T is the absolute temperature.

Hence the fundamental supersaturation can be re-written as:

$$S = \exp\left(\frac{\Delta\mu}{RT}\right) \quad 7$$

The state of supersaturation is an essential requirement for all crystallization operations. Figure 4 shows the different zones on a solubility-supersolubility diagram. The lower continuous curve in this diagram can be located with precision and is called the solubility curve. Whereas the upper, discontinuous curve is known as the supersolubility curve and represents the region where spontaneous crystallization occurs. This region is sensitive to the rate of supersaturation, presence of impurities and the solution's thermal history. The region between the supersaturated zone and the solubility line is the metastable zone. These three zones are characterized as follows:(62)

- The zone below the solubility line or stable zone where crystallization cannot occur;

- The zone between solubility and supersolubility curve (metastable zone width or MSZW) where spontaneous crystallization is improbable; and
- The supersaturated zone where spontaneous crystallization is probable but not inevitable.

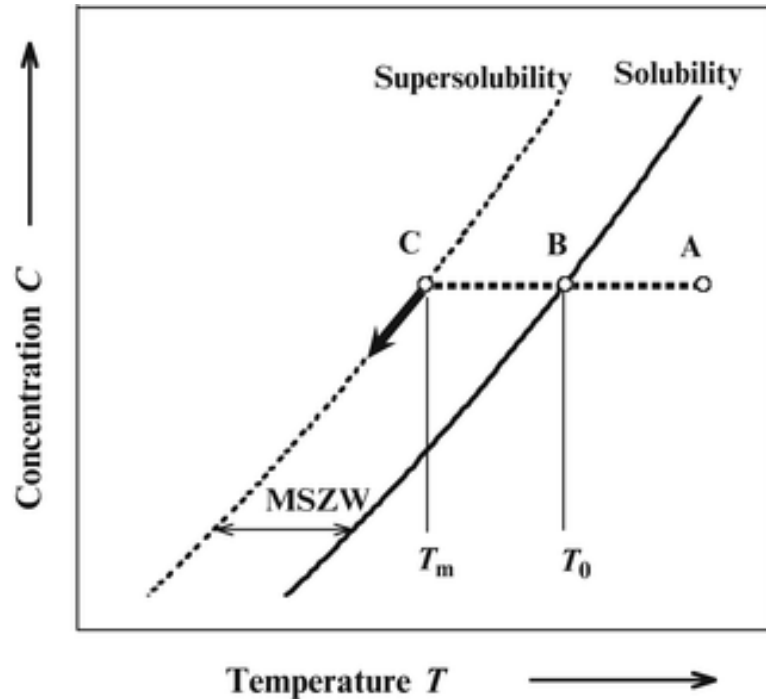


Figure 4. The solute-supersolubility diagram.(63)

By manipulating the supersaturation achieved, we can control the particle size, size distribution and shape.(64-67) Ouyang et al.(68) investigated the influence of supersaturation on the polymorphic nucleation behaviour of carbamazepine (CBZ). Figure 5 shows the variation in induction time of the different CBZ polymorphs crystallized from a solution at different supersaturation ratios. Here induction time is the time interval between the instance when the required amount of CBZ is introduced in the solvent mixture and the appearance of first crystals in the solution. Form II is dominant at higher supersaturation ratios when crystallizing from the solvents used except for acetone where form III is produced. This implies that for ethanol, toluene, 2-propanol, acetonitrile and nitromethane, a high supersaturation state is achieved which favours the formation of the metastable form II. Whereas for the same solvents, at intermediate supersaturation ratios (2.4 to 3.6), the stable polymorph III is formed

along with the metastable form II. The proportion of form II decreases with the decreasing supersaturation ratio. Thus, higher supersaturation rates favour the generation of metastable polymorphs (form II in this case), whereas for lower supersaturation rates, more stable polymorphs are formed.(38)

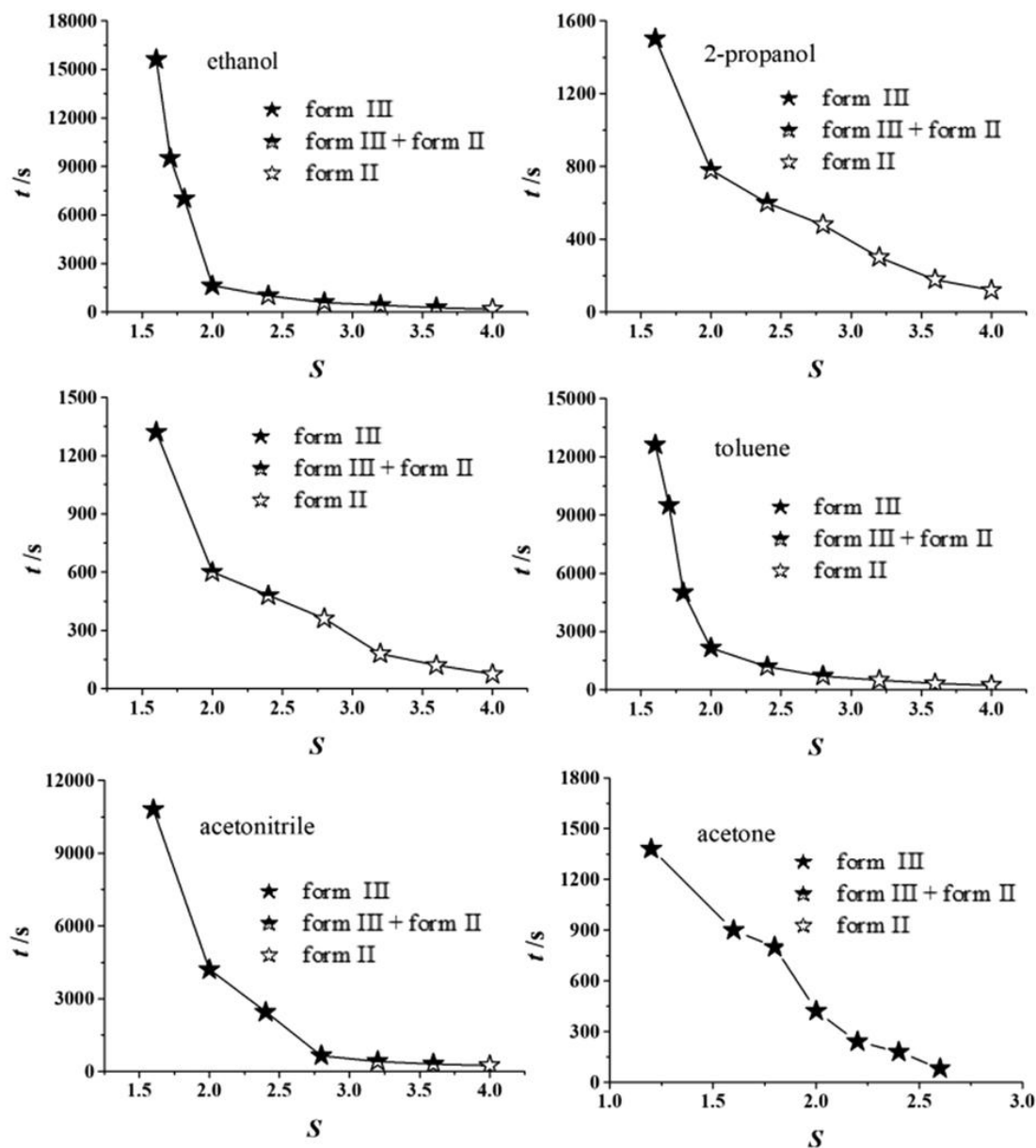


Figure 5. Induction time of carbamazepine polymorphs with respect to supersaturation ratios in different solvents at 25 °C.(68)

1.1.2 Crystallization Process

Two major events happen during the crystallization process namely, nucleation and crystal growth.

Nucleation is the initial process of random assembly where the ions/atoms/molecules of a material (referred to as constituents here) assemble in a nucleus. The gathering of constituents always occurs randomly, however only when a critical size is reached, the cluster will not redissolve and starts growing spontaneously. Nucleation can be categorised as homogenous or heterogenous. In homogenous nucleation, the constituents that are randomly moving through the bulk medium come in close vicinity and align together through chemical interactions where they start to grow by attracting more constituents. This type of nucleation requires high supersaturation. In heterogenous nucleation, an impurity or interface acts as a precursor on which the constituents attach to form a cluster and grow. This type of nucleation is more common because it is energetically more favourable. Also the bulk medium often contains foreign molecules, microscopic particles, bubbles, or other phases whose presence lowers the energy barrier for nuclei formation. It can happen in conjunction with homogenous nucleation. According to classical nucleation theory, the change in free energy of the system during homogeneous nucleation of a spherical nucleus is given by(69)

$$\Delta G = -\frac{4\pi r^3}{3v} k_B T \ln S + 4\pi r^2 \gamma \quad 8$$

Where ΔG is the change in system's free energy, $4\pi r^3/3v$ represents the cluster density, r is the cluster radius, v is the volume of a single molecule, T is the temperature, S is the supersaturation ratio, γ is the interfacial energy and k_B is the Boltzmann's constant. The first term in this equation reflects decrease in energy due to transition from dissolved to crystal state. The second term reflects the energy increase due to formation of a solid-liquid interface. The two terms and their sum are shown on Figure 6. The two terms in Equation 8 depend differently on r , and so the free energy, ΔG , of formation passes through a maximum r^* , where r^* is the radius of critical nucleus at which the probability of formation of a nucleus goes through a minimum. For small r , where $r < r^*$, the second term dominates and any cluster of that size will dissolve. At $r > r^*$, the opposite is true and any cluster larger than r^* will grow spontaneously.

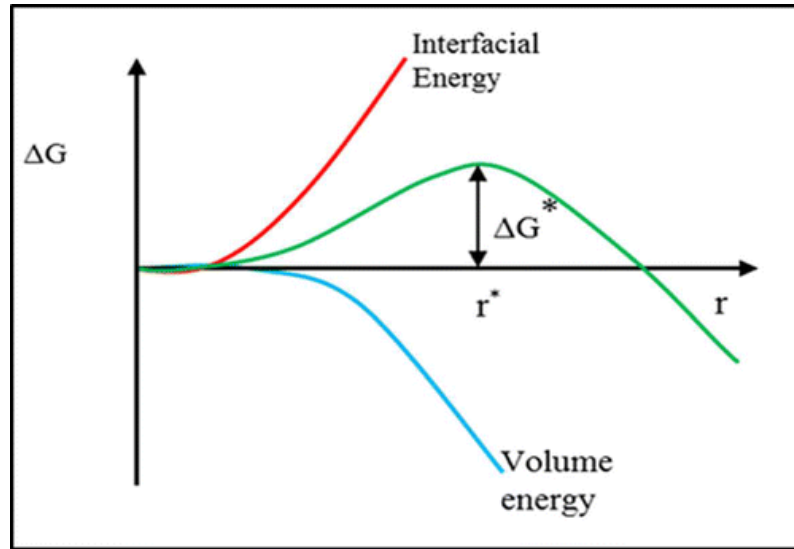


Figure 6. Schematic representation showing the dependence of nucleation barrier ΔG^* on radius r according to classical nucleation theory.(69)

The nucleation rate J , defined as the nuclei formed per unit volume in unit time ($\text{m}^{-3}\cdot\text{s}^{-1}$), is given by(69)

$$J = A \exp \left[-\frac{16\pi\gamma^3 v^2}{3k_B^3 T^3 (\ln S)^2} \right] \quad 9$$

Here A is a pre-factor which is determined from kinetic considerations. This equation indicates that three main variables govern the rate of nucleation namely- the temperature, T ; the degree of supersaturation, S ; and the interfacial tension, γ . Figure 7 gives a plot for Equation 9 showing that beyond a certain point where a critical supersaturation is reached, there is a rapid increase in the nucleation rate.

Crystal growth occurs after the nuclei have appeared. It is a dynamic process driven by supersaturation where particles further align with the critical nuclei. If the main mechanism of mass transport to nuclei is bulk diffusion, the linear growth rate, G , (length per unit time; $\text{m}\cdot\text{s}^{-1}$) is given by(70)

$$G = \frac{2D}{\rho_C \delta} (c - c_{\text{int}}) \quad 10$$

In this equation, D is the diffusion coefficient, ρ_C is the crystal density, c is the bulk solute concentration, and c_{int} is the solute concentration at the solid–liquid interface. Both nucleation and crystal growth play a crucial role in determining the crystal

structure, shape and size which defines the product quality. Hence, development and successful implementation of a crystallization process involves careful control of the process parameters to precisely manipulate the nucleation rate as well as the crystal growth rate to produce particles with desired characteristics.

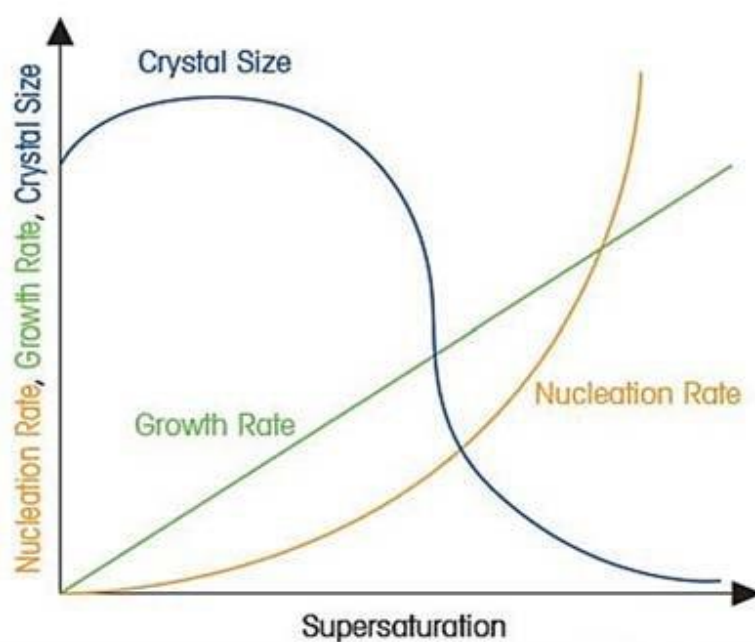


Figure 7. Effect of supersaturation on nucleation rate.(71)

1.1.3 Methods of Crystallization

The choice of crystallization method is determined by the thermodynamic and physical properties of the solute and solvent, as well as the required product purity.(61) Several methods can be used to trigger crystallization such as by cooling, antisolvent addition, pH adjustment, chemical reaction, or a combination of these. These methods have been discussed in detail as follows:

- a. **Cooling:** Solute solubility in each system is a function of temperature. With decreasing temperature, the solubility drops and can be used to trigger precipitation. This type of temperature-dependent solubility data is often used in industry to determine the cooling profile in a crystallizer.(72, 73) For example, indomethacin (IMC) was crystallized from ethanol using seeded cooling crystallization. The γ -IMC polymorph of IMC was used as the seed in this process

to induce crystallization of IMC. The measured solubility of metastable α -IMC and thermodynamically stable γ -IMC are shown in Figure 8. Upon rapid cooling of solutions from 45 °C to 5 °C, supersaturation was generated which triggered nucleation when the solution was maintained at 5 °C. The operating temperature played an important role in the crystallization process effecting both crystal size and shape. The metastable α -IMC polymorph was generated at 5 °C having fine needle-shaped crystals whereas γ -IMC was generated with a rhombic plate-like structure at higher temperatures.(74)

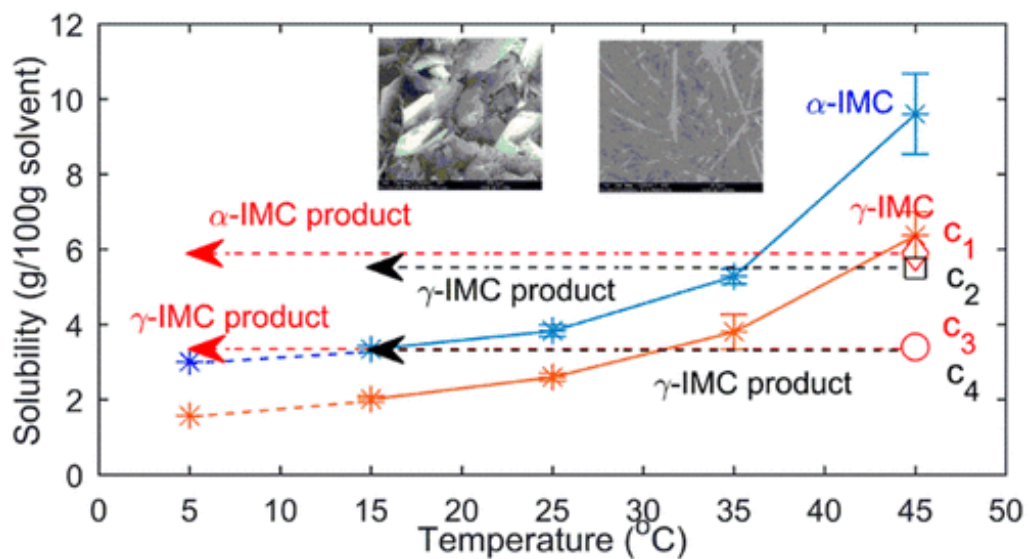


Figure 8. Solubilities of α - and γ -IMC in ethanol at different temperatures.(74)

- b. **Evaporation:** Solvent evaporation is another method of generating supersaturation in the system. Solvent removal from the system, by increasing temperature or through spray drying, increases the overall solute concentration which generates supersaturation and triggers solute precipitation. Evaporative crystallization is chosen if solubility does not show a strong positive dependence on temperature. It can be applied on a large scale in continuous bulk chemical production of, for instance, table salt - Figure 9. There is one hydrate in this system, $\text{NaCl}\cdot 2\text{H}_2\text{O}$, which crystallizes as monoclinic, thin platelets. Further, it decomposes at 0.15 °C to form solid NaCl and saturated brine. However, this crystallization is so slow that, upon rapid cooling, the broken curve in the phase

diagram is followed. The property of depressing the freezing point of water enables sodium chloride to be used in freezing mixtures and as a de-icing salt.(75)

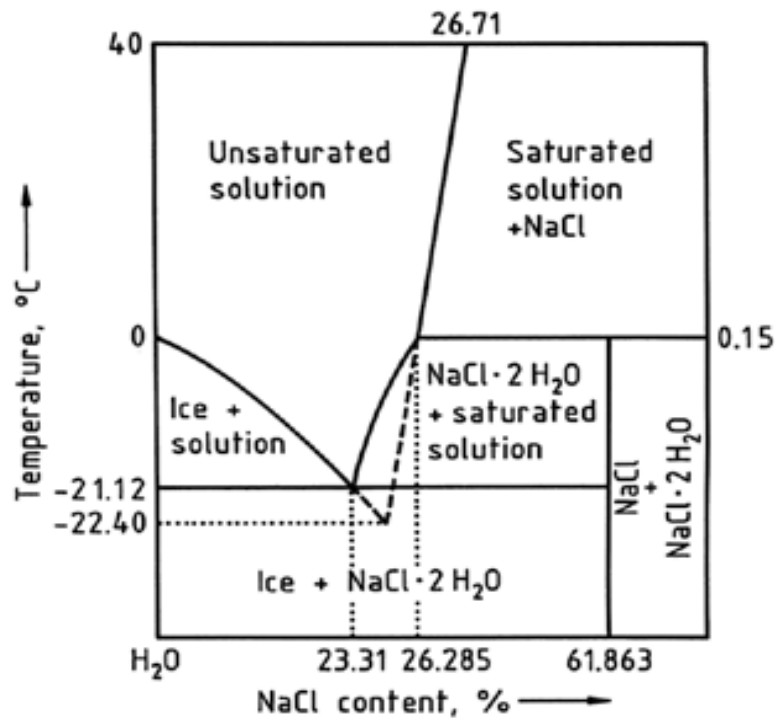


Figure 9. Phase diagram of H₂O-NaCl system.(75)

- c. **Addition of antisolvent:** Antisolvent addition for crystallization is based on careful selection of a solute-solvent-antisolvent system. The principle is based on selecting an antisolvent which is miscible with the solvent and for which the solute solubility is significantly lower. When the antisolvent is added to the system, solute solubility in the final mixture decreases leading to supersaturation. The degree of supersaturation achieved can be controlled based on the difference in solute solubility in the solvent and antisolvent, and rate of antisolvent addition. Crystallization of paracetamol from acetone-water mixture was performed by Yu et al(76) using water as the antisolvent. At fixed agitation speed, the influence of antisolvent feed rate on cumulative weight of the final product was investigated - Figure 10. The smallest mean size for the product was obtained at the largest addition rate i.e. 20 g/min. It was observed that the agglomeration degree of products deteriorates with increasing feeding rate ranging from 1 to 20 g/min due to enhanced nucleation.

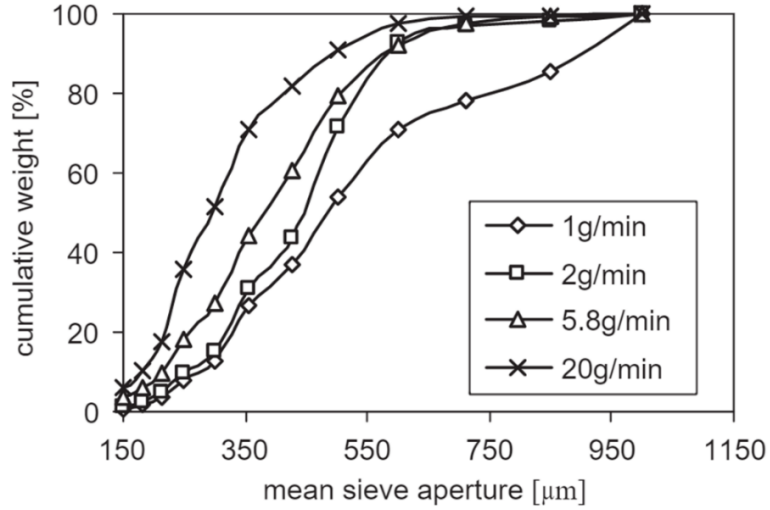


Figure 10. Effect of antisolvent feeding rate on particle size distribution of product at 500 rpm.(76)

- d. **Changing pH:** Solute solubility may be a function of pH, which can be used to decrease the solubility and generate supersaturation to trigger crystallization. Judge et al.(77) investigated the effects of pH on the nucleation rate of tetragonal lysozyme crystals. Figure 11 represents the crystal density (number of crystals produced in a fixed volume) as a function of pH at 4°C.

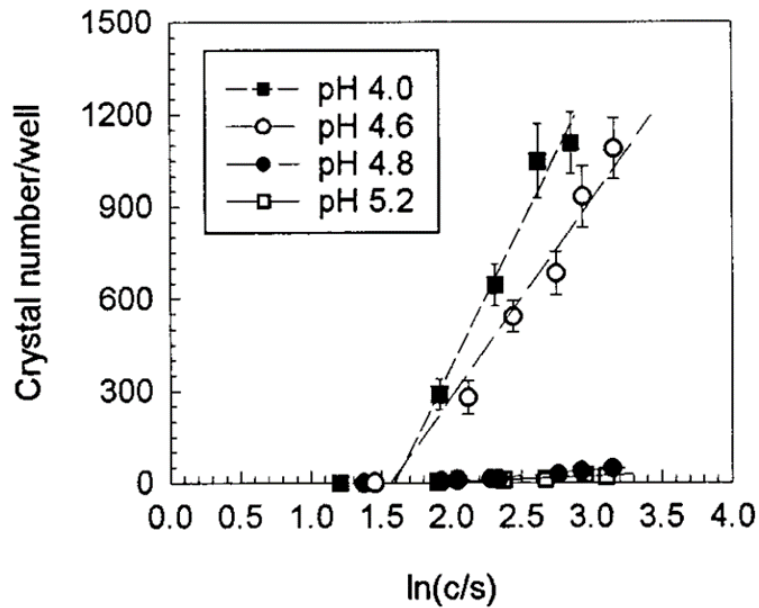


Figure 11. The effect of solution pH on crystal number per well at 4 °C.(77)

For fixed value of supersaturation, the crystal density changes by two orders of magnitude over the pH range 4.0–5.2 with the highest density obtained at pH of 4. Thus, in this work, crystal density decreases with an increase in solution pH.

- e. **Chemical reaction:** In this method, reactive species such as ions that participate in the precipitation process can be used to generate supersaturation. Thus, a decrease in solute solubility can be achieved by addition of reactive species. In a complex mixture system, selective crystallization of compounds to obtain the desired product becomes challenging. Synowiec et al.(78) investigated the crystallization kinetics using a chemical reaction for selective crystallization of calcium sulfate and calcium carbonate from brine. Brine contains Na^+ , Cl^- , SO_4^{2-} , Mg^{2+} , Ca^{2+} and K^- . The solubility of calcium sulfate in solution increases with the increase of NaCl concentration - Figure 12.

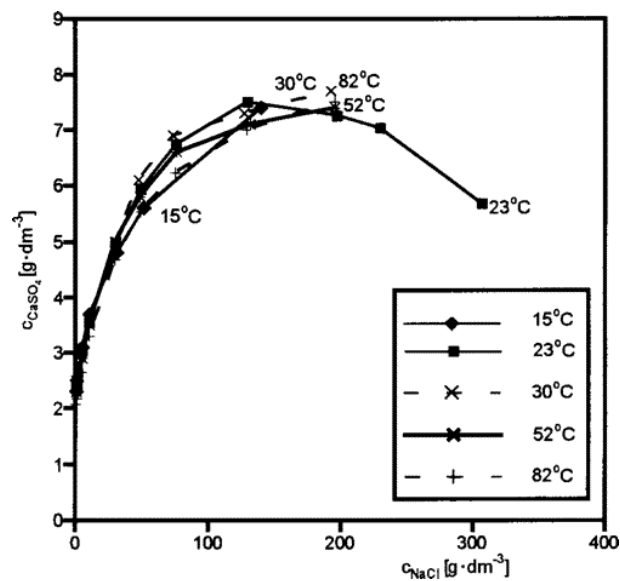
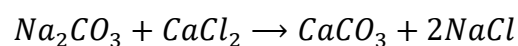
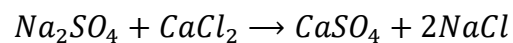
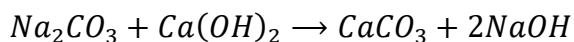
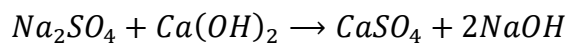


Figure 12. Solubility of $\text{CaSO}_4 \cdot 2\text{H}_2\text{O}$ in NaCl solution as a function of temperature.(78)

This process is based on mixing of two waste brines from (i) evaporative crystallization sodium chloride plant and (ii) ammonia soda production. As a result of this process, calcium sulfate and calcium carbonate are precipitated, according to the following chemical equations:





Thus selective precipitation of calcium sulfate dihydrate can be achieved by manipulation of sodium chloride concentrations which in turn influences the sodium sulfate concentrations in brine.(78)

1.1.4 Role of Solvent

Influence on the crystallization process further extends to solvent properties such as solubility parameters and polarizability, and the solute solubility in a selected solvent as it directly influences the supersaturation state. The type and choice of solvent plays a major role in polymorph selectivity and crystal morphology of the product. This is because the solvent can facilitate favourable interactions with solute clusters or nuclei on specific growing faces, which causes reduction in interfacial tension, thus improving the pace of crystal growth. This is the principle implemented in polymorph screening experiments where a range of solvents are used for the generation of all possible crystal forms.(79-85) Significant research has been conducted to study the direct influence of solvent selection on the outcomes of the crystallization process.(84-87) Cheuk et al.(88) investigated the solubility of benzocaine in different organic solvents - Figure 13.

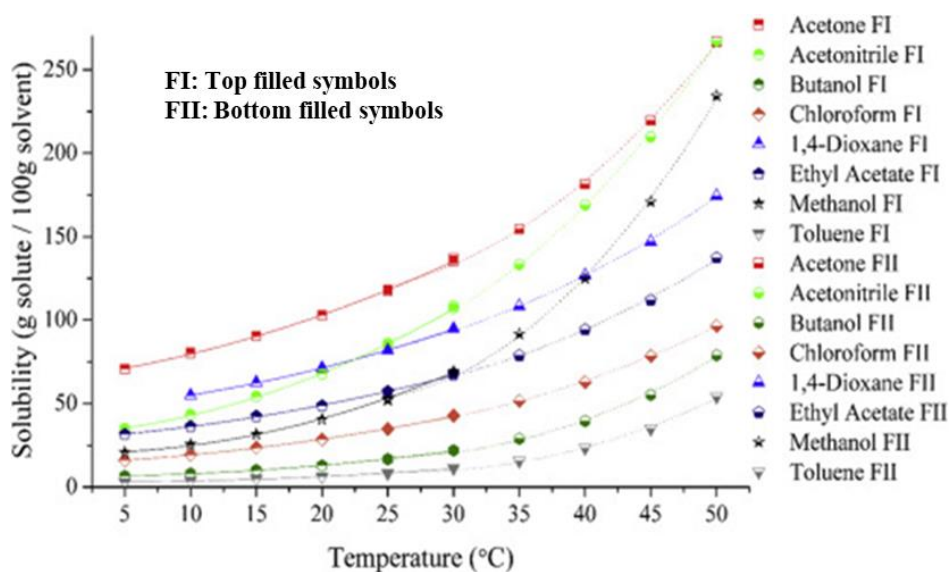


Figure 13. Solubility of benzocaine in different solvents.(88)

This solubility information can be used to determine the solvent or antisolvent based on the process parameters and requirements. For instance, at 5 °C, solubility is highest in acetone and lowest in toluene. Hence, acetone will be a good solvent for processes at this temperature whereas toluene will be a good antisolvent.

Solubility parameter is a very useful tool to predict molecular affinities, solubility, and solubility-related phenomena.(89) It is used in the selection criteria for determining a solvent for the crystallization process. The solubility parameter, δ (also known as total solubility parameter or Hildebrand solubility parameter) is defined as the square root of cohesive energy density of the solvent, u_c :

$$\delta = \sqrt{u_c} = \sqrt{\frac{\Delta H - RT}{V_M}} \quad 11$$

Here R is the gas constant, T is the temperature and V_M is the molar volume. Most often u_c is calculated from the molar enthalpy of vaporization, ΔH . The units of δ are $\text{MPa}^{1/2}$.(90)

Hansen Solubility Parameters (HSP)(91) are an extension of the Hildebrand parameter. Here, the total solubility parameter is split into three components: δ_D , δ_P , and δ_H . The parameter δ_D accounts for dispersion interaction, δ_P accounts for polar (dipole-dipole) interactions, and δ_H reflects hydrogen bonding between molecules. Thus, the total solubility parameter, δ , is composed of three components reflecting various physical contributions to the solvent's cohesive energy:

$$\delta^2 = \delta_D^2 + \delta_P^2 + \delta_H^2 \quad 12$$

The solubility of two materials is only possible when their intermolecular forces are similar because these forces need to be overcome for the molecules of one material to be separated by the molecules of the other material. Thus, the well-known idea that “like dissolves like” can be quantified using HSP. The compatibility between two components (1 and 2) is measured by the distance, R_a , defined as:

$$R_a^2 = 4(\delta_{D2} - \delta_{D1})^2 + (\delta_{P2} - \delta_{P1})^2 + (\delta_{H2} - \delta_{H1})^2 \quad 13$$

For a given compound, there is a solubility sphere of radius R_0 . Solvents within this sphere are similar enough to dissolve the compound. An RED number has been defined as

$$RED = \frac{R_a}{R_0}$$

Accordingly, a shorter Hansen distance (i.e. $RED < 1$) implies compatibility and $RED > 1$ implies incompatibility.

1.1.5 Current Trends in Pharmaceutical Crystallization

Presently, majority of pharmaceutical production is batch-based in nature which involves several steps or stages such as reaction, distillation, crystallization, and filtration - Figure 14. These batch-based processes have two major stages: the primary or upstream stage and the secondary or downstream stage. The primary stage involves the production and formulation of APIs, while the secondary stage involves addition of excipients, crystallization, filtration, and other purification steps. The final dosage form is produced in the secondary stage, ready for marketing.(8)

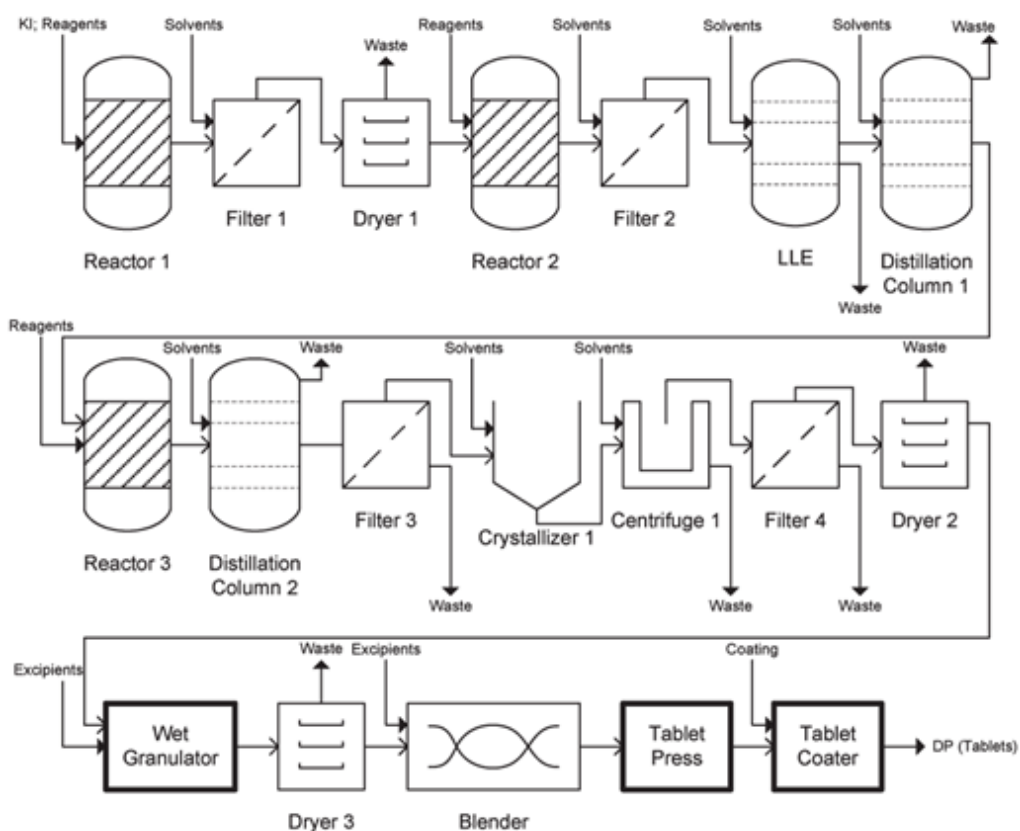


Figure 14. Process flow diagram for batch manufacturing route.(92)

The main advantage of batch-based manufacturing is that it is a well-established technique that is being employed in many sectors such as petroleum, pharmaceutical, fine chemicals, and food industry for a few centuries now. However, there are several limitations associated with the batch-based technique, some of which are summarized below:

- Larger space requirements for expensive and bulky equipment associated with each manufacturing stage.
- Larger hold times between the steps which can be as long as several months to produce a specific product which risks material degradation.
- Higher waste-to-product ratios (E-factor) especially in the case of APIs (25-100); this implies that 25-100 kg of waste is generated for every kilogram of API produced. This is very high in comparison with other well-established processes, for instance, the petrochemical industries have $E \ll 1$.(8)
- Cost-inefficiency due to higher maintenance requirements associated with the extensive equipment; a separation or purification step is often needed after each manufacturing step which makes this type of production very strenuous in nature.(9)
- Variability in product properties due to inhomogeneity of process parameters across large batches which affects reproducibility of solid-state properties of the product (stability, kinetics); a single process fault can render the whole batch unusable/unfit for further processing.(10)
- Difficulties in obtaining fundamental knowledge of the crystallization process to obtain accurate kinetics data for scaling up.
- Low drug efficiencies owing to large particle sizes and size distribution produced in tank reactors.
- Reproducibility issues due to polymorph transition and high degree of disorder in the form of crystal defects and amorphous regions due to downstream processing operations.(11)

The limitations of batch crystallizers affect the production process and product quality. This necessitates the need to develop alternative techniques that can provide improved process control, enhanced reproducibility and greener processing while lowering the overall manufacturing cost.(92, 93) This is driving researchers to explore continuous

crystallization as a potential candidate to overcome some of the limitations that are prevalent in batch-based crystallization.(94-96)

Continuous crystallizers are based on the principles of flow chemistry where a reaction is conducted in a continuous stream rather than in a flask.(97) These can offer faster reactions and superior control over the process parameters such as spatial homogeneity of concentration and temperature.(98) This technique is a way to simplify the complexity and decrease the cost associated with batch-based equipment whilst offering continuous processing. It has potential for uniform nucleation and crystal growth conditions across the reactor, thus enabling precise manipulation of the solid-state properties of final product.(10) Moreover, continuous processing allows for the use of automated monitoring systems for continuous quality checks and hence tight control over the product quality. Such processes can have predictive maintenance requirements which can help reduce the overall process cost which is often caused due to failed reactions or impurities in the system. It is also relatively easier to scale-up such processes. For instance, in batch crystallizers, scale-up might imply using reactors of significantly larger volumes which will require further process optimization, whereas for continuous crystallizers it might simply imply running an optimized process for a longer duration (or running n reactors in parallel).(99) It has been demonstrated that higher yields can be attained when using a continuous flow reactor.(13) Moreover, it is possible to lower the E-factor associated with pharmaceutical production as the process duration can be reduced (or stopped) when defects are detected in a batch which implies less waste.

A series of 3 plug flow reactors (PFRs) producing ibuprofen is shown in Figure 15. A continuous feed of reactants is fed to their respective reactors, each of which are maintained at the required temperature. Specific reactions involving the formation of a ketone (2) in PFR1 are followed by the formation of an ester (3) in PFR2. The outlet stream from the second reactor is mixed with a methanol-water KOH solution and fed into the third reactor, where the salt form of the API, K-ibuprofen is formed. This whole process takes place in a simplified, single run where the output of each step becomes the in-feed for its successive step. This process resulted in an excellent product purity (99%).(8)

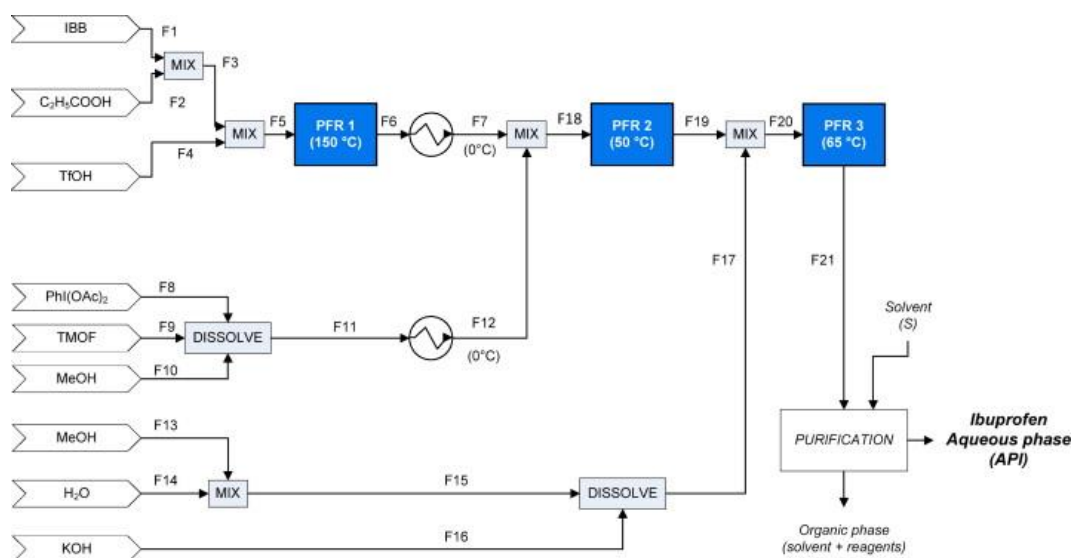


Figure 15. A continuous pharmaceutical process for ibuprofen.(100)

In a different work by FloWorks (CSIRO), a six-step linear sequence was transferred from a batch to a continuous flow process - Table 1. The work involved the synthesis of spirooxazine photochromic dyes. The reason to invest in flow synthesis of these dyes was the reduced yields obtained using batch-based processes (<50% for 18h reaction times). A two stage, continuous-flow process for the same showed significantly improved yields whilst reducing the waste produced by order(s) of magnitude at each reaction step.

Table 1. Batch vs. continuous flow synthesis of spirooxazine photochromic dyes. (This table is reproduced from work conducted and published by CSIRO (13, 101))

Reaction Step	Batch		Flow		Waste	Batch (L)	Flow (L)
	Yield %	PMI	Yield %	PMI			
1	85	119.4	98	6.6	Chlorinated waste	218	0
2					Non-chlorinated waste	612	74
3	70	173.2	85	18.5	Contaminated aqueous waste	418	33

4	85	119.4	98	5.2			
5	76	54.9	81	31.4	Liquid waste total (in litres)	1248	106
6	75	63.9	71	11.3	Energy total (in kWh)	18.5	1.6

Thus, owing to the advantages associated with continuous processing, more companies are opting for it especially when introducing a new product in the market. Table 2 shows companies across the globe that are investing into continuous manufacturing processes to transition away from batch-based processes.

Table 2. Major pharmaceutical-related companies pursuing continuous production.(102)

Country	Company	Initiatives
US	Eli Lilly and Company	Breast cancer medication (Verzenio™) approved by FDA in 2017.(103)
	Pfizer Inc.	Acute myeloid leukemia treatment agent approved by FDA in 2018.(104)
Switzerland	Novartis International AG	Initiated collaboration with MIT (Novartis-MIT Center for Continuous Manufacturing) in 2007. Established <i>CONTINUUS Pharmaceuticals(105)</i> to promote the development and introduction of continuous manufacturing systems.
South Korea	SK biotek Co. Ltd.	Owens one of the world's leading continuous manufacturing facilities.
Japan	Shionogi Pharma	Achieved the most of continuous manufacturing achievements and expertise accumulated by Shionogi & Co.(106)

	Takasago International Corp.(14, 15) Takasago Chemical Corp.	Successful adoption of continuous manufacturing for intermediates using LAH reducing agent. Actively promoted the switch to continuous manufacturing by partnering with Eli Lilly.(107)
--	---	--

However continuous manufacturing, compared to batch manufacturing, often involves a higher level of process design to ensure adequate process control and product quality.(108, 109) Thus owing to the significant economic and time scale investments, continuous processing has only found partial incorporation into the manufacturing business. Based on these initiatives, six pharmaceutical drugs have been produced:(110)

1. Vertex's ORKAMBI® (lumacaftor/ivacaftor)
2. Vertex's SYMKEVI® (tezacaftor/ivacaftor)
3. Johnson & Johnson's PREZISTA® (darunavir)
4. Eli Lilly's VERZENIO™ (abemaciclib)
5. Pfizer's DAURISMO™ (glasdegib)
6. Johnson & Johnson's TRAMACET

Even though there have been significant efforts in science and engineering to support the implementation of continuous pharmaceutical manufacturing, the transition has been slow.(111) However, in the coming decades, this transition may take over most industries especially the pharmaceutical industry owing to its potential to overcome the limitations of process inhomogeneity and higher E-factors associated with batch-based processing.(12, 112)

1.2 Dense Gas Processes

Particle size and shape play a crucial role in determining the bio-efficacy of drug formulations (see section 1.1), thus a range of micronization techniques are implemented to control these particle characteristics. These techniques allow for production of particles on the μm scale. The commonly employed micronization

techniques and their disadvantages are presented in Table 3. Fluid energy milling, spray drying and ball milling suffer from high temperature and electrostatic charging whereas the liquid antisolvent method suffers from the issue of residues in the final product.

Table 3. Conventional Methods of Micronization.(113)

Method	Size (μm)	Disadvantages
Fluid Energy Milling	1-5	high energy input, temperature increase, electrostatic charging, operation above ambient temperature
Spray Drying	~5	poor control over size distribution, energy-intensive
Lyophilization	<1	poor control over size distribution, solvent recovery
Solution Preparation Freeze-drying	<1	applicable to only a few substances
Liquid Antisolvent	0.1-100	organic residues in the final product(114)

Dense Gas Processes (DGPs) can be implemented for production of pharmaceutical compounds with the ability to tune particle crystallinity and produce (organic) residue-free products.(115) Dense gases (DGs) are gases under conditions near their critical point, but not necessarily in a supercritical state. Figure 16 shows the solid, liquid and gas phase boundaries for a pure substance. The technical flexibility of DGPs, including the fact that the gas can act as a solvent, co-solvent or an antisolvent, has led to the development of a large number of techniques for drug particle micronization.(16) The key technical advantage of DGs is that rather small variations in temperature and/or pressure allows for fine adjustment of fluid properties (ρ , μ) and therefore control over operational parameters.(116) Because of compression, the density is relatively high (“liquid-like”) and that increases the solvent power of the gas. At the same time, diffusivity is more “gas-like” and mass transfer is faster than it is in liquids.(117-119)

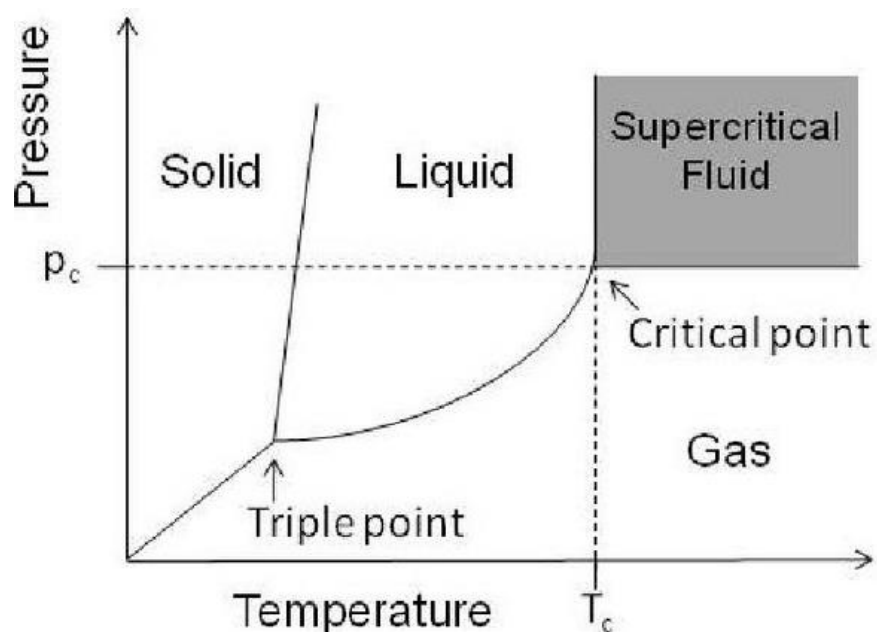


Figure 16. Pressure-temperature diagram for a pure substance.

Carbon dioxide is the commonly used DG because it is non-toxic, easily available, cheap, has fire suppression capabilities and is miscible with majority of organic liquids. The low critical temperature of CO₂ (304.21 K)(120) makes it suitable for processing heat-sensitive compounds such as APIs. Often the organic liquids used in the processing of pharmaceutical compounds are toxic in nature, such as dimethyl sulfoxide (DMSO) or carbon tetrachloride, and must be removed from the final product to meet the quality criteria.(121) CO₂ acts as a non-toxic, benign alternative to these and helps in the elimination of organic residues from the product. This is achieved by using pressurized CO₂ as the antisolvent in place of traditional organic liquids and/or washing the final product with excess CO₂ to remove any organic residues.(115, 122-126) Dense CO₂ can partially or completely replace the use of harmful organic liquids. It can play two major roles in processing pharmaceutical compounds: one is as a solvent and the second as an antisolvent.

In the case of using CO₂ as a solvent, the solid substance to be micronized is dissolved in compressed CO₂ and then rapidly depressurized which triggers precipitation due to decrease in the solvent power of CO₂. In the case of CO₂ as an antisolvent, the substance of interest is dissolved in a classical solvent (mostly organic liquid) which is miscible with CO₂. This miscibility reduces the solvent power for the solute and

triggers precipitation. Based on its role in the process, several methods have been devised and are briefly summarized in the following section.(123)

1.2.1 Types of Dense Gas Processes

a. Particles from Gas-Saturated Solution (PGSS)

This process involves melting (10–15 MPa, 373–393 K)(127) a solid through CO₂ expansion which is then sprayed through a nozzle resulting in rapid depressurization and cooling of the melt. This causes the melt to precipitate thus producing a fine powder (Figure 17a). Hence the technique is called Particles from Gas-Saturated Solution or PGSS. This technique only works for process temperatures close to the melting point of the solid. Sencar-Bozic et al.(17) showed that processing Nifedipine ($T_M=172-174$ °C) by PGSS at 185 °C can result in the micronization of particles (from 50 to 15 μm) with enhanced dissolution rate (~9 times in 1h) in water as compared to the unprocessed material. However, the temperatures employed in this technique are very high for processing pharmaceuticals and may lead to polymorph transition or degradation which affects the properties of the final product.

b. Precipitation with Compressed Antisolvent (PCA) and Aerosol Solvent Extraction System (ASES)

Another dense gas process employed for micronization is Precipitation with Compressed Antisolvent or PCA process. In this technique, an organic solution of an API is sprayed into a chamber filled with pressurized CO₂ - Figure 17b. The miscibility of CO₂ with the organic liquid droplets results in expansion of the droplets which triggers solute precipitation. Organic residues can be removed from the final product by washing with CO₂.(128) This technique can also be implemented in the production of solute crystals that have molecules of the dense gas incorporated within the crystal structure.(129, 130) The Aerosol Solvent Extraction System (ASES) is a variation of PCA which specifically uses supercritical CO₂. In this technique, the organic solvent used in the process is completely dissolved in the SCF which triggers solute precipitation due to reduction in solvent power.(131)

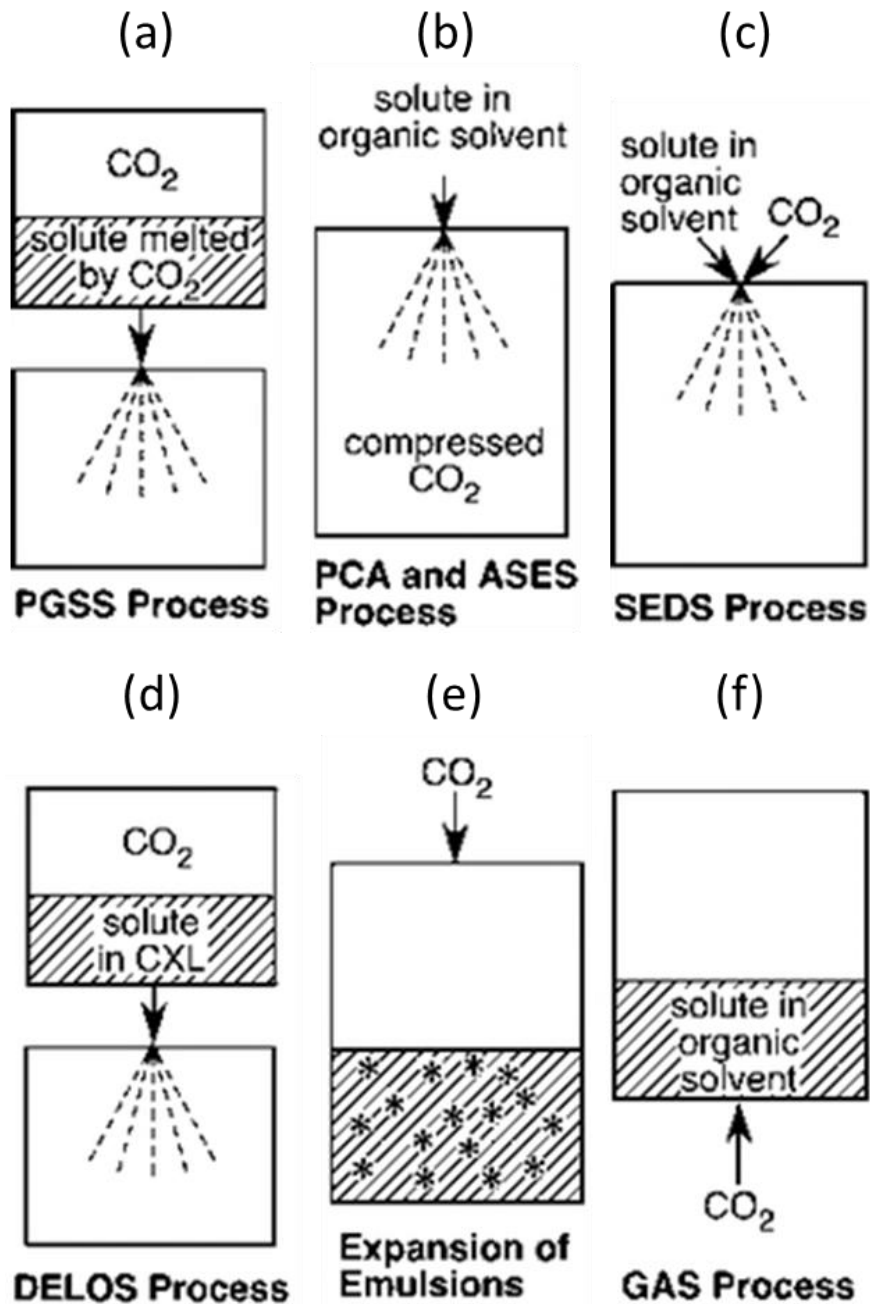


Figure 17. Several processes for the preparation of particles.(132)

c. Solution-Enhanced Dispersion by Supercritical Fluids (SEDS)

In the Solution-Enhanced Dispersion by Supercritical Fluids technique (SEDS), $scCO_2$ and organic solution are simultaneously fed through a coaxial nozzle - Figure 17c. This technique produces much finer particles in comparison with PCA or ASES. Subramaniam et al.(18, 19, 133) used an ultrasonic nozzle to extract the organic

solvent out of droplets to trigger solute precipitation. Submicron particles (0.5-10 μm) of hydrocortisone, ibuprofen, insulin, and paclitaxel were formed using this technique.

d. Depressurization of An Expanded Liquid Organic Solution (DELOS)

In the DELOS (Depressurization of an Expanded Liquid Organic Solution) technique, dense phase CO_2 is used as the antisolvent for expansion of an organic solution. However, in this technique, the solute concentration is kept significantly lower such that expansion with CO_2 does not trigger any solute precipitation. Upon sudden depressurization, CO_2 is released from the system which causes rapid cooling. This sudden lowering of temperature triggers precipitation - Figure 17d. The DELOS method was used to produce micron- and submicron-sized crystalline particles from a solution in acetone using CO_2 as the compressed fluid. Particle sizes less than 5 μm were produced which is 2 orders of magnitude smaller than the median particle diameter of the particles produced through conventional cooling crystallization technique from methanol solutions.(134, 135)

e. Precipitation of Particles from Reverse Emulsions

In this technique, CO_2 is used for the expansion of reverse emulsions of compounds dissolved in the aqueous core of a microemulsion - Figure 17e. This technique has been demonstrated for a protein(136) and an enzyme.(137) Chen et al.(138) have produced nanoparticles (7-38 nm) of trypsin protein by expansion of a reverse emulsion of sodium bis(2-ethylhexyl)sulfosuccinate (AOT)/ H_2O /isooctane reverse micelles with CO_2 (50 bar, 20 $^\circ\text{C}$). A variation of this technique can also be implemented for precipitating inorganic materials.(139, 140) Zhang et al.(139) produced ZnS particles using this technique by implementing a combined emulsion of ZnSO_4 dissolved in the aqueous cores and Na_2S (both in AOT-stabilized water in isooctane emulsions).

f. Gas Antisolvent (GAS) Process

This thesis focuses on the use of the Gas AntiSolvent (GAS) process for pharmaceutical crystallization. This technique relies on the miscibility of CO_2 with

organic solvents which causes volumetric expansion of the solvent, thus reducing its solvent power for solute which triggers precipitation - Figure 17f. Thus, CO₂ acts as the antisolvent in this process. The method was proposed in 1989 by Gallagher et al.(141) Modifications of the GAS process include supercritical antisolvent (SAS), particles by compressed antisolvent (PCA), and an aerosol solvent extraction system (ASES).(16, 142) The resulting mixture in GAS process is called a Gas-expanded liquid or GXL - Figure 18. These GXLs can exhibit solvent power and improved transport properties similar to CO₂.(132) In GAS process, parameters such as rate of antisolvent addition, temperature, and solution concentration influence particle properties such as size and crystal morphology. The equation(143) below can be used to measure the liquid expansion in a GAS process:

$$\varepsilon = \frac{\Delta V}{V} = \frac{V(T, P) - V_0(T, P_0)}{V_0(T, P_0)} \quad 15$$

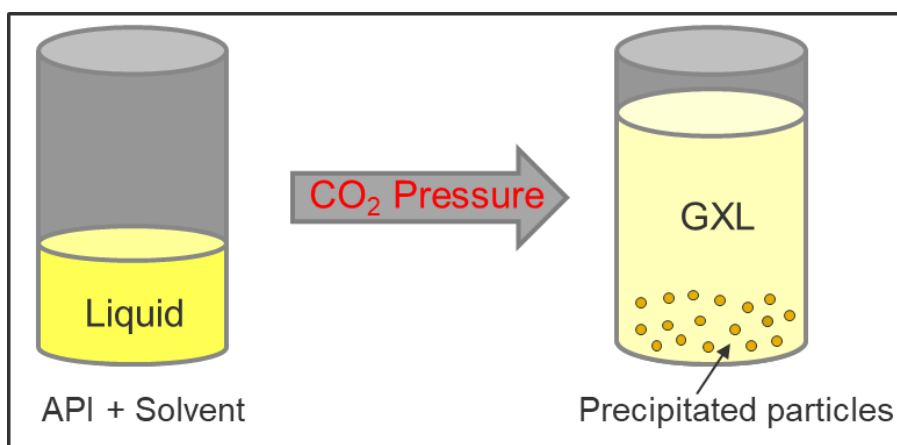


Figure 18. Expansion of an organic solution using dense phase CO₂ and particle precipitation.

Kordikowski et al.(143) measured the relative volumetric expansion of different solvents when pressurized with CO₂ at different process temperatures. Thus, for a given antisolvent, different solvents show a similar relative volume expansion behaviour - Figure 19, i.e. the ‘classical’ definition of volume expansion of the liquid phase. \tilde{V}_L is the molar volume of the liquid mixture and V_2 is the total volume of pure solvent at the same temperature and a reference pressure (normally atmospheric pressure).

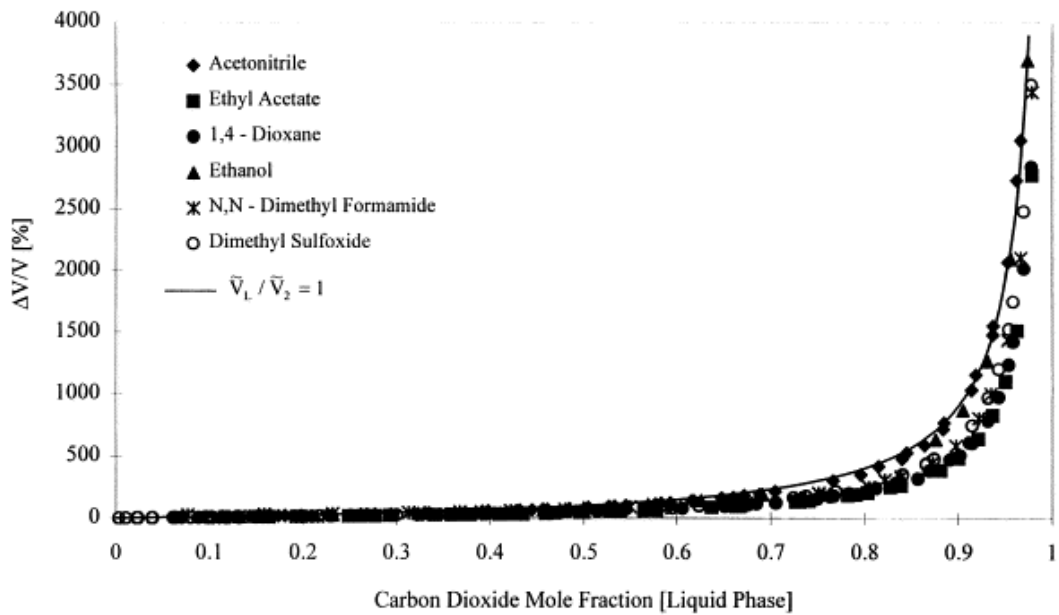


Figure 19. Relative expansion of the liquid phase for the systems carbon dioxide–solvent at 298, 303 and 313 K.(143)

Warwick et al.(114) used the GAS method to micronize particles of Copper Indomethacin (Cu-Indo) using subcritical CO₂ as antisolvent. The implementation of this technique simplified the API crystallization process - Figure 20.

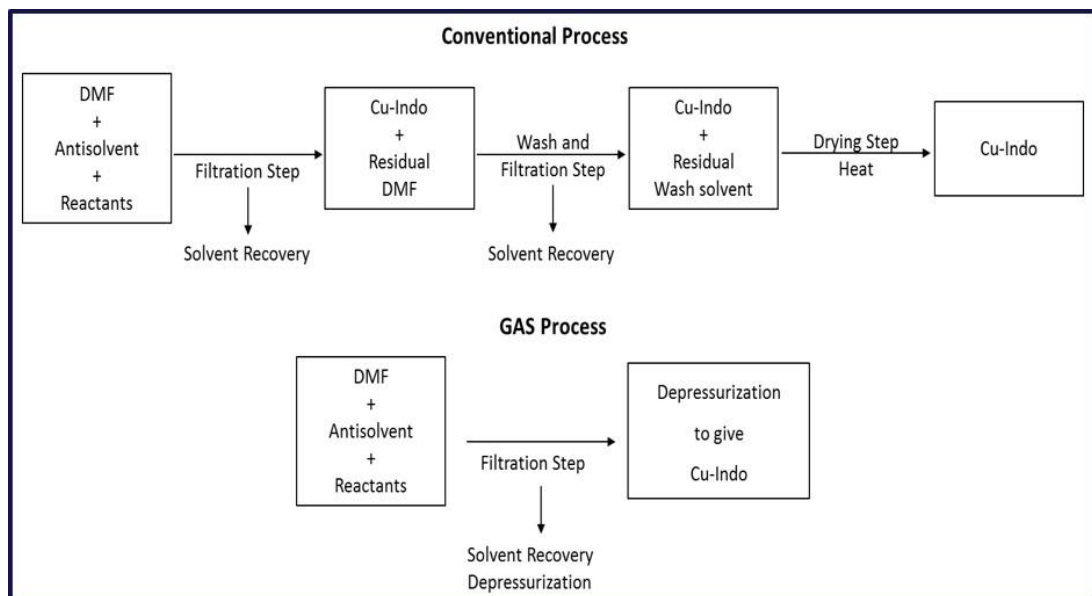


Figure 20. Comparison between the conventional process and the GAS process for the synthesis of Cu-Indo.(114)

He showed that the GAS process is a major improvement over the conventional technique and enabled single-step synthesis, faster crystallization rate, reduced solvent requirement, and control over particle size. Copper indomethacin was successfully synthesised and purified in a single vessel through selective crystallization of components under different process conditions (P, T) by using CO₂ as the antisolvent. It was shown that CO₂ can be an excellent alternative to the conventional organic antisolvent i.e. ethanol in this case. The product Cu-Indo, with greater than 95% purity, was produced in a single step at 25 °C. Table 4 shows the comparison of product yields achieved using the conventional organic liquid antisolvent i.e. ethanol and the gas antisolvent i.e. CO₂.

Table 4. Comparison between GAS and Conventional Process for the Synthesis of Cu-Indo at 25 °C.(114)

Antisolvent	P (MPa)	Cu-Indo (mg/g)	% yield
Ethanol	0.1	5	40
CO ₂	5.8	5	85
Ethanol	0.1	50	75
CO ₂	5.8	50	98
Ethanol	0.1	200	91
CO ₂	5.8	200	96

The rate of liquid expansion could be manipulated by changing process parameters such as pressure, temperature, or rate of antisolvent addition which substantially varied the size and morphology of the particles produced - Figure 21. Rapid expansion produced microparticles with sizes below 10 µm and a bipyramidal shape (Figure 21 c and d) whereas rhombic crystals (Figure 21b) with sizes between 10 and 20 µm were produced in case of slow expansion.

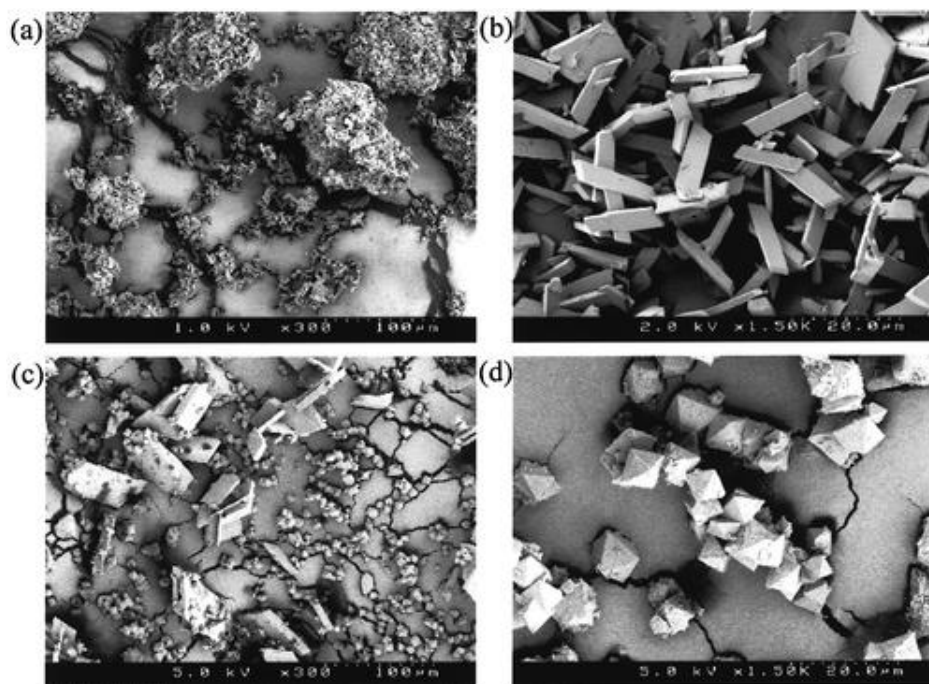


Figure 21. SEM images of the particles produced from the GAS and the conventional process: (a) conventional process; (b) slow expansion; (c and d) fast expansion.(114)

1.3 Microfluidics for Crystallization of APIs

For pharmaceutical manufacturing, it is desirable to produce formulations with tight control over the product properties in a highly reproducible and efficient way to avoid issues arising due to product variability (discussed in previous sections). Moreover, the need for considerable process engineering to change batch volumes, represents a barrier when moving from small prototype particle formulations to large-scale volumes for clinical studies. Integrated microfluidic technology can be a solution to overcome the challenges and limitations associated with pharmaceutical processing.(144) Microfluidic technologies exploit fluid handling and manipulation at a very small (sub-millimetre) scale. It is a multidisciplinary field that includes physics, chemistry, engineering, and nanotechnology. Microfluidic devices have at least one characteristic dimension below 100 μm . The fluid elements on that scale are small but large enough to obey the law of continuous media, e.g. the continuity equation.(145) Thus, fluid properties such as density and pressure or the fluid velocity are well defined at any point and are continuous functions of space and time.

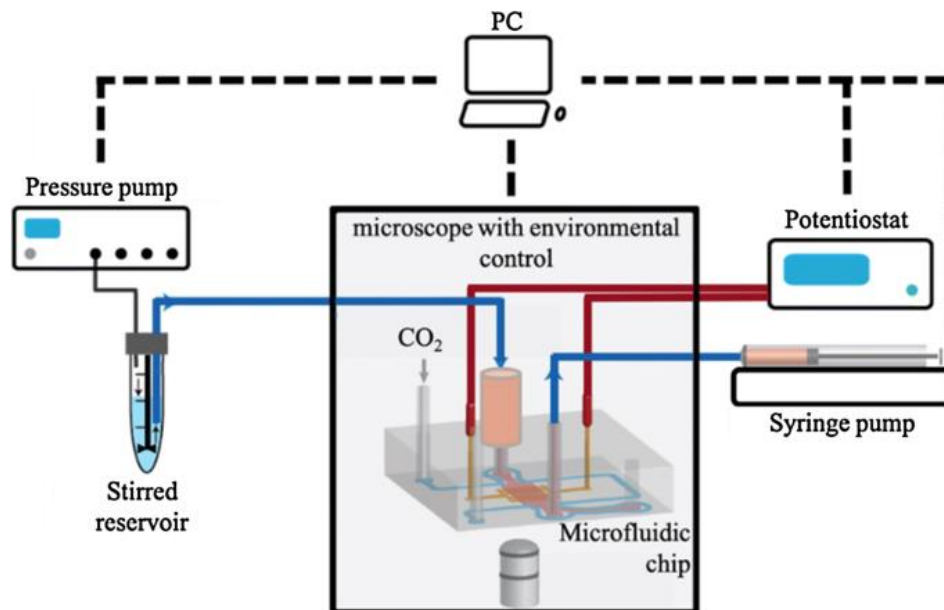


Figure 22. Schematic diagram depicting the components of a microfluidic platform.(146)

Microfluidic devices can be made of different materials, however, material characteristics such as mechanical performance (ability to withstand high P and T), fluid mechanism (mass diffusion and thermal diffusion), and physicochemical properties (optical, chemical resistance) need to be assessed for the desired application. Based on this, microfluidic devices can be made in metal (stainless-steel)(147), semiconductor (silicon)(148), ceramic(149), glass(150) ((BF33)(151), Quartz(152)), polymer ((PDMS)(153), PMMA(154)) and paper(155) (Whatman filter paper). It serves as a miniaturized analytical technology for biomedical and chemical applications.(156-160) However, it has recently been implemented as a processing and production technology as well.(147, 148, 161-169)

The following discussion of basic physics in microfluidics is based on Chapter 2 from the book - Microfluidics: Fundamental, Devices and Applications.(24)

The fluid mechanics equations governing a bulk fluid in motion are also applicable in microfluidics. These are briefly presented below.

Mass Conservation Principle (Continuity Equation)

According to this principle, the fluid mass can pass through any of the tube's cross-sectional area without loss. The mass of fluid crossing each section of the pipe per unit

time is the mass flow rate ($\text{kg}\cdot\text{s}^{-1}$). It remains constant as formulated in Equation 16 where 1 and 2 are the two tube positions of cross-sectional areas A_1 and A_2 .

$$A_1\rho_1u_1 = A_2\rho_2u_2 \quad 16$$

Here, ρ_1 and ρ_2 are fluid densities through A_1 and A_2 , and u_1 and u_2 are effective velocities of the fluid flowing through A_1 and A_2 .

Poiseuille's Law

The pressure-driven, steady-state flow in channels is known as Poiseuille flow. It is the final class of analytical solutions to the Navier–Stokes equation. In a Poiseuille-type flow, pressure difference between the two ends of a straight, rigid channel drives the fluid flow. Equation 17 is the simplest form for this law. Here ΔP is fluid driving pressure and Q is volumetric fluid flow rate. The fluidic resistance, R , is the resistance to fluid flow in a given channel and is related to channel cross-section, length, and fluid properties.

$$\Delta P = RQ \quad 17$$

Poiseuille law was initially formulated for circular channels, however, analytical solutions have been obtained for a variety of other cross-sections. In rectangular channels, the ratio of channel width (w) and height (h) controls flow parameters such as the hydraulic resistance and flow profile. The fluidic pressure difference, ΔP , of a rectangular channel of length L with a high aspect ratio (i.e., $w \gg h$) can be calculated using Equation 18 assuming laminar flow conditions:

$$\Delta P = \frac{12\mu LQ}{wh^3} \quad 18$$

This equation shows that ΔP is directly proportional to the fluid viscosity (μ).

Flow in Microchannels

The flow profile for fluids can be predicted using the Reynolds number. The Reynolds number (Re) is a dimensionless quantity estimated using the ratio of the inertial forces to the viscous forces:

$$Re = \frac{\rho ud}{\mu} \quad 19$$

Here ρ and μ are the fluid density and viscosity, respectively, d is the hydrodynamic channel diameter and u is the average fluid speed. Thus, based on the magnitude of Re , fluid flow can be classified into three main regimes:(170)

- Laminar flow - $Re < 2300$
- Transient flow - $Re > 2300$ and $Re < 4000$
- Turbulent flow - $Re > 4000$

In microfluidic devices, owing to the reduced dimensions, the viscous force effect dominates flow behaviour as compared to the macroscale wherein inertial force effect may be dominant. Hence, at such small scales, flow is usually laminar in nature (low Reynolds number) and thus allows for precise control of contact and reaction times. Because of that the dominant mass transport type changes from convection to diffusion.(171) The large area-to-volume ratio enhances both mass and heat transfer.(20-22, 172) Thus, process optimization can be achieved for small volumes of fluids with excellent control over process parameters.(23) There are also the benefits of reduced sample/reagent consumption, reduction of contamination risk, lower cost per analysis, enhancement of sensitivity and specificity, and overall increase in reliability.(173)

Mixing in Microchannels

In laminar flow, the liquid streamlines do not cross each other and therefore any mixing must be achieved via diffusion. When mixing occurs via diffusion, its efficiency can be estimated by F_{mix} :

$$F_{mix} = \frac{Dt}{l^2} \quad 20$$

Here D is the diffusion coefficient, t is the stream contact time available for mixing, and l is a system dimension perpendicular to the direction of the flow. In general, the mixing process ranges from substantial up to almost complete for F_{mix} values in the range of 0.1–1.0. Mixing in microchannels can be facilitated through change of flow profile (laminar/turbulent) and mixer geometry (channel length, cross-sectional area).

The above is valid for liquids which are effectively incompressible, however, it can be more complex for gases.

It is easier to control the microenvironment for particle formation in a microfluidic micromixer as compared to conventional crystallizers where heterogeneous mixing creates local particle environments that favour particle formation in some instances and particle growth in others, leading to product inhomogeneity.(174-176) Another major advantage is the continuous nature of microfluidics technology which allows for continuous monitoring through on-chip analytical probes. This allows to keep the product quality under strict check and reduce wastage. Moreover, this technology offers greater flexibility over device design i.e. channel cross-section which can be tuned as per the process requirements. This is similar to manipulating liquid expansion in the GAS process by altering the process conditions to achieve controlled crystallization. Furthermore, it is easier to scale-up this technology through process parallelization and simple numbering up of the devices which allows for direct implementation of this technology for industrial use. This makes microfluidics technology an excellent tool to realise process intensification of small-batch manufacturing.(177) This path to scale-up contrasts with batch-based manufacturing methods which often require complex and time-consuming process optimization as the batch size scales. The adaptability of microfluidic platforms is much more universal in comparison with other techniques which makes it an attractive candidate for processing of a range of pharmaceutical compounds.

Previous Attempts to Combine High-Pressure Processes Relevant to Pharmaceuticals and Microfluidics

The integration of a dense gas process with microfluidics is a viable approach to efficient and continuous production of high-quality APIs with enhanced control over the crystallization process. This integrated technique would combine the advantages offered by the individual techniques. For instance, the benefits of faster crystallization, elimination of organic residues and greener processing, offered by dense gas processes, will add to the high reproducibility, process homogeneity, adaptability, design flexibility and ease of scale-up, offered by microfluidics. The use of compressed carbon dioxide as a benign and green antisolvent is common in dense gas processes. The use of higher driving pressure in the microfluidic circuit will considerably increase fluid flow rates and mixing efficiency thus leading to higher

throughputs. Dense gas processes implemented on a microfluidic platform would be highly valuable for producing pharmaceutical or nutraceutical formulations.

One of the major challenges to implementing this idea is to realise high-pressure microfluidics (HPMF). This is technically challenging because of the increased pressure needed to work with CO₂ as an antisolvent. Material selection for device fabrication is crucial for the realization of such a platform. Microfluidic devices made in polymer (PDMS or PMMA) cannot withstand the process conditions (pressure, temperature, resistance to chemicals) associated with dense gas-based pharmaceutical processing. It is possible to make microfluidic devices made of metal such as stainless-steel by using conventional machining, electroforming, electrodischarge machining, or laser ablation. These metal microreactors are capable of withstanding high pressure and heat loads and show resistance towards toxic/reactive chemicals. These have been used for chemical synthesis,(178) fluorination reactions,(179, 180) and material synthesis.(181) For instance, supercritical water (650 °C and 250 bar) was used for the gasification of organic molecules in microreactors made in stainless-steel.(182, 183) Ceramic microreactors can also withstand very high temperature and pressure.(184, 185) However, these microreactors are costly to manufacture,(184) and in situ optical characterization is severely restricted in metal and ceramic microreactors.

Microfluidic devices made of glass provide optical access, mechanical strength and high chemical resistance. The standard procedure for fabricating these devices will be discussed in section 2.2 of Chapter 2. They are capable of withstanding moderately high temperatures (100 °C) and pressures (up to 400 bar).(186) Andersson et al.(187) used a borosilicate glass micromixer to study the flow profile and mixing of CO₂ with ethanol at high pressure and room temperature, 82 bar and 21 °C - Figure 23. The device design consisted of a simple T-junction with ethanol flowing through the main channel (300 µm × 120 µm) and CO₂ through the side channel (76 µm × 8 µm), followed by a 54 mm long meander. Silica capillaries were used to introduce fluids into the micromixer. Capillaries were inserted into the sides and glued to the micromixers using a two-component epoxy glue (Araldite Rapid, Huntsman Advanced Materials). The fluids meet at the junction and gradually mix along length of the main channel. The relative permittivity of the gas-expanded liquid was measured using integrated platinum electrodes.

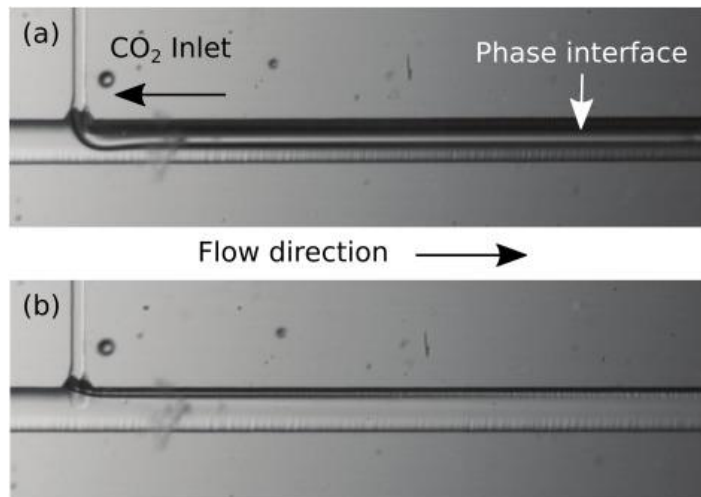


Figure 23. CO₂-expanded ethanol on a borosilicate glass micromixer. Change of flow ratio, corresponding to an ethanol mole fraction of (a) 0.5 and (b) 0.8.(187)

Marre et al.(188) fabricated a silicon-on-glass micromixer where the microchannels were etched in silicon with a top BF33 substrate. The micromixer can withstand pressure and temperature up to 300 bar and 400 °C - Figure 24.

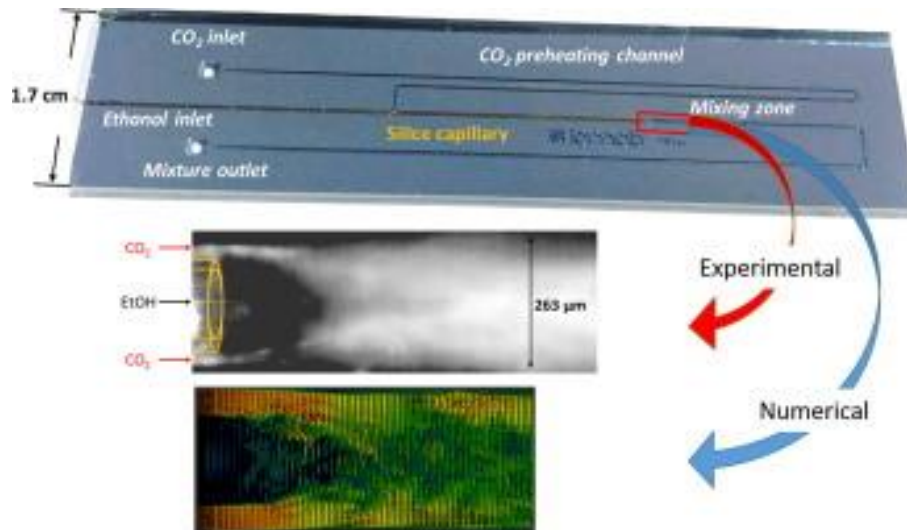


Figure 24. Illustration of the high-pressure micromixer made of silicon-BF33, and experimental & numerical profiles for fluid flow.(189)

The system was used to study high-pressure fluid flow under laminar(190) and turbulent(191) conditions. Ethanol and CO₂ were selected as model solvents at

supercritical conditions, in which the two fluids are completely miscible. Influence of process temperature, microchannel cross-section, Reynolds number and CO₂/ethanol ratio on the final mixing efficiency was investigated. A general behaviour for fluid mixing was noticed and was divided into different zones based on the relationship between a time dimensionless number (the ratio of mixing time to diffusion time) and an energy dimensionless number (the ratio of CO₂ kinetic energy to ethanol's).

A similar set up was used to produce tetraphenylethylene (TPE) nanoparticles from the solvent, Tetrahydrofuran (THF) using supercritical carbon dioxide (sc-CO₂) as antisolvent in a microfluidic, supercritical antisolvent process (μ SAS). Successful production of NPs with an average size of (9 ± 3) nm was realised - Figure 25.(192)

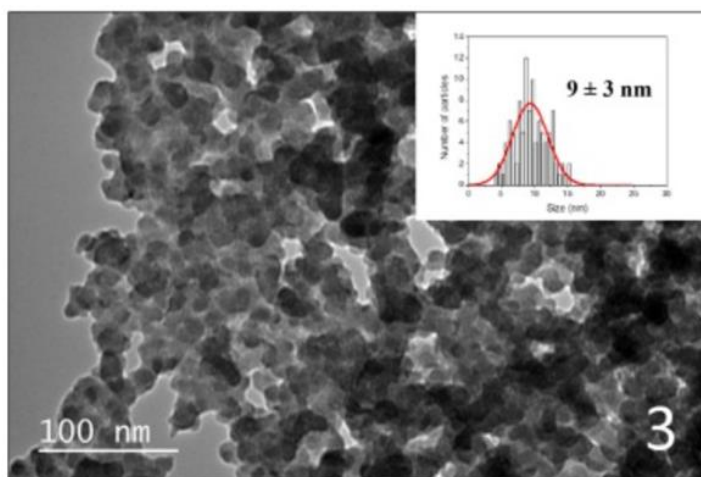


Figure 25. TEM image of TPE NPs synthesized by μ SAS at 40 °C and 100 bar. Inset: corresponding size distribution.(192)

In a different work, a silicon-on-glass micromixer was used where the microchannels were etched in the silicon substrate which was anodically bonded to a 500 μ m thick Pyrex plate. This was fixed in a frame which counteracts the pressure inside the microchannel thus, enabling high-pressure stability (pressure drops of up to 500 bar) and a leak proof and reversible connection between the microsystem and the high-pressure equipment. The frame consisted of a 5 mm-thick quartz glass plate pressed on the Pyrex side and a flat polished steel surface on the silicon side of the microsystem. A small gap in the metal frame was made to allow for optical

measurements. The whole construction was a compromise between mechanical stability and quality of the optical access.(193)

Motivation, Scope and Objective: Incorporation of a Dense Gas Process on a Microfluidic Platform for the Continuous Crystallization of Pharmaceutical Compounds

These set-ups can sustain high pressure however, the specialized pumps add to the overall cost, the silicon-on-glass microchips are relatively complex to fabricate, and the silica tubing glued at the microchip ports increases the chances of process failure. Thus, the work was restricted to a few highly specialized groups. We conclude that there has been significant interest in the development of high-pressure microfluidic systems. It holds the potential to serve as a future processing technology for pharmaceuticals, however, the research is still in its early stages. Significant work needs to be done to study the influence of processing conditions on the crystallization outcomes and performance of these devices.

This calls for the development of a platform that is simpler, enables the use of standard fluid-delivery connectors, and milder process conditions. There is the added opportunity to explore the influence of key process parameters on the crystallization kinetics and chemistry. The use of a microGAS process using subcritical CO₂ as the antisolvent has not been studied extensively for the processing of pharmaceutical compounds and their combinations. Such platform can be used to study the crystallization outcomes for a range of APIs and their combinations by simple manipulation of the process parameters.

This thesis focuses on the development of such a platform that will enable the use of on-chip liquid expansion for API precipitation using subcritical CO₂ as the antisolvent. A bespoke metal holder is fabricated to sandwich the micromixer that enables the use of standard connectors and tubing while allowing simpler change of micromixer design. The micromixer can be sandwiched between the two parts of the metal holder and connections can be made using standard Swagelok and HPLC connectors, reversibly and without the use of superglue. The proposed technique holds direct relevance to the pharmaceutical industry as it allows for continuous pharmaceutical

crystallization in a controlled fashion. The focus will be on investigating the influence of process chemistry and kinetics on API crystallization to control particle size and morphology. This work can serve as a basis to further develop and optimize this technology for implementation as a small-batch manufacturing system to produce high-quality pharmaceutical compounds.

Our set-up is simple, uses glass-on-glass micromixers (made by standard microfabrication techniques), allows for the connection of fluid delivery pumps commonly used with dense gas processes (ISCO pumps), the use of off-the-shelf components and an easier exchange of microfluidic chips. The setup is reliable, shows potential for fluid handling at up to 100 bar and is accessible to any operator after a short training.

Chapter 2

Materials and Methods

This chapter provides a description of the materials, micromixer fabrication process, experimental methods and instrumentation used throughout the thesis. Specific experimental details and techniques are further described in the relevant experimental chapters.

2.1. Materials

2.1.1 Active Pharmaceutical Ingredients

There are four APIs used in this project namely Griseofulvin (GF), Luteolin (LT), Budesonide (BD), and Dapsone (DAP). The pharmaceutical significance, supplier, and chemical structure of each of these APIs is discussed below.

Griseofulvin

Griseofulvin or GF (>97.0%) was supplied by TCI. It is an antifungal polyketide with the chemical formula (2S,6'R)-7-chloro-4,6-dimethoxybenzofuran-3-one-2-spiro-1'-(2'-methoxy-6'-methylcyclohex-2'-en-4'-one). The API was received as a dry powder and is white or yellowish in colour. The chemical structure of GF is shown in Figure 26.

The oral bioavailability of the drug is limited by its poor water solubility (8.64 mg.L⁻¹).⁽⁴⁾ Dandagi et al.⁽¹⁹⁴⁾ showed that nanoparticles of GF prepared by an emulsion solvent diffusion method (600-900 nm) showed marked improvement in dissolution profile (> 95% at 120 minutes) when compared to the pure drug (3-4 μm, ~70% at 120 minutes) and thus offer greater bioavailability.

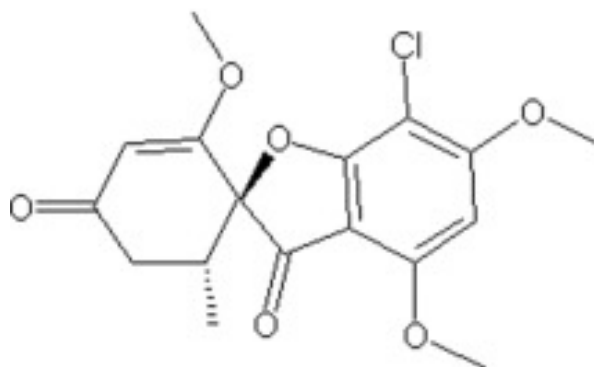


Figure 26. Structure of griseofulvin.(195)

Luteolin

Luteolin or LT (98.4% purity) was supplied by Cayman Chemical. It is a naturally occurring flavonoid biophenol found in common dietary sources such as fruits and vegetables.(196) The chemical structure of LT is 2-(3,4-dihydroxyphenyl)-5,7-dihydroxychromen-4-one - Figure 27.

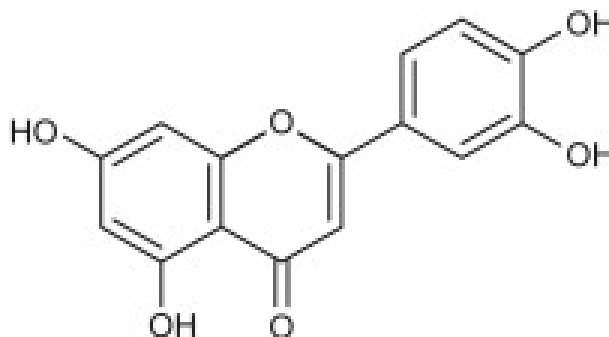


Figure 27. Chemical structure of Luteolin.(197)

It consists of two benzene rings connected by a three-carbon ring containing oxygen and a C-C double bond, and has 4 —OH groups at positions 3', 4' 5 and 7. The bioactivity of LT is linked to the hydroxyl moieties and the C-C double bond. LT shows anticancer, antioxidant and antiinflammatory properties. Upon administration, LT scavenges free radicals, protects cells from reactive oxygen species (ROS)-induced damage and induces direct cell cycle arrest and apoptosis in tumour cells. This inhibits tumour cell proliferation and suppresses metastasis. Another important characteristic

of this API is that it can be used in the therapy of central nerve system diseases, including brain cancer as it can permeate the blood-brain barrier.(198)

Budesonide

Budesonide or BD ($\geq 99\%$ purity) was purchased from Sigma-Aldrich. The chemical formula for BD is ([RS]-1 β , 16 α 17, 21-tetrahydroxypregna-1, 4-diene-3, 20-dione cyclic 16, 17-acetal with butyraldehyde). It is a non-halogenated corticosteroid with the chemical structure shown in Figure 28.(199) It is the active antiinflammatory ingredient in some nasal inhalers.(200) This API is used to treat asthma, however, it can also be used in the treatment and prevention of nasal polyps which are often associated with asthma or recurring infections. Hence, it can be used as a bronchodilator agent, an anti-inflammatory drug, or a drug allergen.(201)

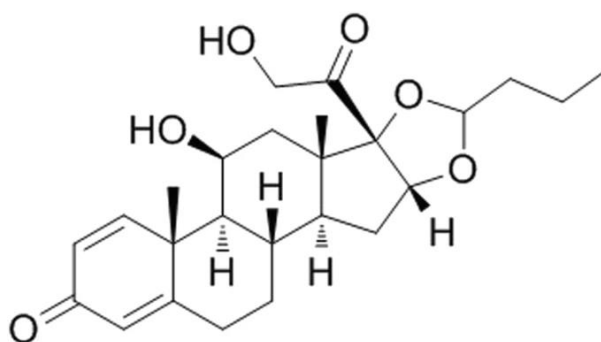


Figure 28. Chemical structure of Budesonide.(202)

Anti-inflammatory agents are crucial in the treatment of asthma. Due to the high ratio of topical anti-inflammatory to systemic activity in BD, it is one of the most extensively used inhaled glucocorticoid.(199)

Dapsone

Dapsone or DAP (Pharmaceutical Secondary Standard; Certified Reference Material) was purchased from Sigma-Aldrich. It is a sulfone consisting of phenyl groups where the hydrogen at the 4th position is substituted by an amino group - Figure 29. It is

primarily an antileprotic drug due to its actions against *Mycobacterium leprae*. However, it also possesses antimalarial(203), anti-infective(204), and antiinflammatory(205) properties.

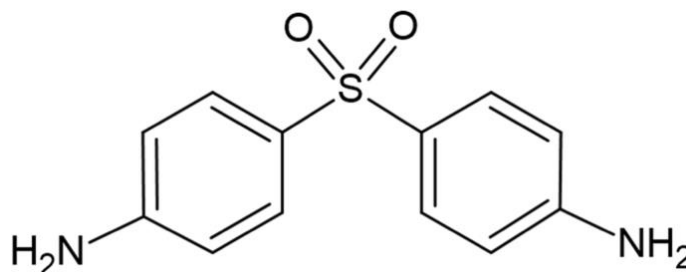


Figure 29. Chemical structure of Dapsone.(206)

DAP is used in the treatment of herpetiform dermatitis. It acts by blocking the synthesis of folic acid in microorganisms by inhibiting the dihydroprotease synthetase enzyme.(207)

2.1.2 Solvents

Dimethylformamide (99.8%), ethanol ($\geq 99.5\%$), acetone ($\geq 99.9\%$) and ethyl acetate (99.8%) were supplied by Sigma-Aldrich. DI water was obtained from a Hydro-Check 414R System. All reagents were used as supplied.

N, N-Dimethyl formamide

N, N-Dimethyl formamide or DMF belongs to the class of formamides where methyl groups replace the amino hydrogen. It is a colourless, hygroscopic liquid.

It holds a lot of significance as a universal solvent in the pharmaceutical industry owing to its aprotic nature, low volatility, and high dielectric constant.(208) This makes DMF significantly useful in the pharmaceutical industry where it is used as a reaction and crystallization solvent.(209)

Ethanol

Ethanol or ethyl alcohol belongs to the family of alcohols and has the chemical formula $\text{CH}_3\text{CH}_2\text{OH}$. It is one of the most widely implemented organic liquid in the pharmaceutical industry.(210)

Ethanol is present in prescription (Table 5) and non-prescription drug products as an active ingredient be it oral, parenteral, and topical (including inhalation). Ethanol also possesses pharmacological actions as an antipyretic, sedative, antiseptic, and cooling agent.(211)

Table 5. Ethanol concentrations, recommended dose, intake, and blood concentration from some common prescription drugs for infants and children. RD : recommended dose. BEC : Blood ethanol concentration.(212)

Prescription drug	Ethanol conc. (mL/dL)	Drug RD (mg/kg/dose)	EtOH intake from RD (mg/kg)	BEC from RD (mg/dL)
ALGINOR	15.1	2.5	30.3	5.0
AMINOMAL ELIXIR	20.0	25.0	128.0	21.3
FERRO-COMPLEX	14.0	10.0*	93.0	13.2
FROBEN	16.0	1.3	34.1	5.7
RAPITUX	31.3	1.0	41.7	6.9
PUERNOL	11.5	16.7	66.7	11.1
ZADITEN	2.5	0.1	8.3	1.4

Acetone

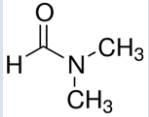
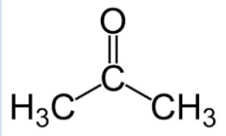
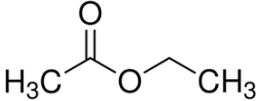
Acetone or propanone belongs to the family of ketones with the chemical formula CH_3COCH_3 . It is used as an excipient in pharmaceutical ingredients and fillers to deliver the appropriate amount of dose as it regulates the proper density of pills and liquid medicines. However, the concentrations of this solvent in the drug product needs to be strictly regulated as at high concentrations, it becomes a depressant of the central nervous system.

Ethyl Acetate

Ethyl acetate is a colourless liquid with the formula $\text{C}_4\text{H}_8\text{O}_2$. It is the ester of ethanol and acetic acid. Any inhalation, oral or dermal exposure results in rapid absorption of this chemical. In oral administration or inhalation exposure, it undergoes hydrolyzation to form ethanol before it gets absorbed in the gastrointestinal or upper respiratory tract. It is regarded as safe for use as a synthetic flavouring agent by the US Food and Drug Administration.(213)

These organic liquids (DMF, ethanol, acetone, and ethyl acetate) are either used as solvents, antisolvents or excipients in the manufacturing of pharmaceutical products and hence can be found as residual components in the final product. Table 6 lists the important properties for each of these solvents. Since there is no therapeutic benefit from residual solvents, the final products should contain no higher levels of residual solvents than can be supported by safety data. Based on the extent of toxicity associated with these organics, these are classified into different classes which have different recommended doses. Ethanol, ethyl acetate and acetone belong to class 3 solvents and are regarded as less toxic and of lower risk to human health. The recommended dose for these solvents is 50 mg per day or less (corresponding to 5000 ppm or 0.5%). Whereas DMF belongs to class 2 of solvents and the recommended dose for it is 8.8 mg per day and the concentration limit is 880 ppm.(214)

Table 6. Common properties for solvents used in this study.(215-218)

Solvent	Density (g.cm ⁻³)	Viscosity (mPa.s)	Solubility Parameter (MPa ^{1/2})	Dielectric Constant	Molecular Structure
DMF	0.945	0.928	24.8	36.7	
Ethanol	0.789	1.07	26.5	24.6	H ₃ C – CH ₂ – OH
Acetone	0.785	0.301	20.0	20.7	
Ethyl Acetate	0.903	0.426	18.1	6.0	

2.1.3 Gases

High-purity carbon dioxide (food grade) and nitrogen (99.99%) were supplied by Coregas (Perth, Australia).

Carbon dioxide

Carbon dioxide (CO₂) is a linear, non-polar molecule. CO₂ is present in the atmosphere and possesses fire suppression capabilities. Given its non-toxic and non-polar nature, it can be used for processing a range of organic compounds.

It holds significance in the pharmaceutical industry as an environmentally benign alternative to conventional processing fluids (mostly organics). Particle formation using dense phase CO₂ is one of the most popular implementations of CO₂ in the pharmaceutical industry. It can be used as a solvent, antisolvent or cosolvent based on

the reaction chemistry and physical state of gas. Dense Gas processing ensures residue-free, safe processing of compounds (discussed in detail in section 1.2).(219, 220)

2.2 Micromixer Fabrication

The microfluidic devices and the bespoke metal holder were fabricated at the South Australian node of the Australian National Fabrication Facility, University of South Australia (<https://www.anff-sa.com/>).

2.2.1 Microchannel Design

We performed our experiments using three different micromixer designs in this project - Figure 30. These are the T-junction (T1), the X-junction (X1) and the X-junction with a long channel post-junction (X2). In T1 micromixer, we have a wider straight channel which comes and meets with a narrower channel coming from the side. The fluids flowing from the two channels meet at a junction followed by a straight channel of the same width as that of the wide channel. The wider channel is used for flowing the liquid, whereas carbon dioxide is supplied through the narrow channel in all the experiments.

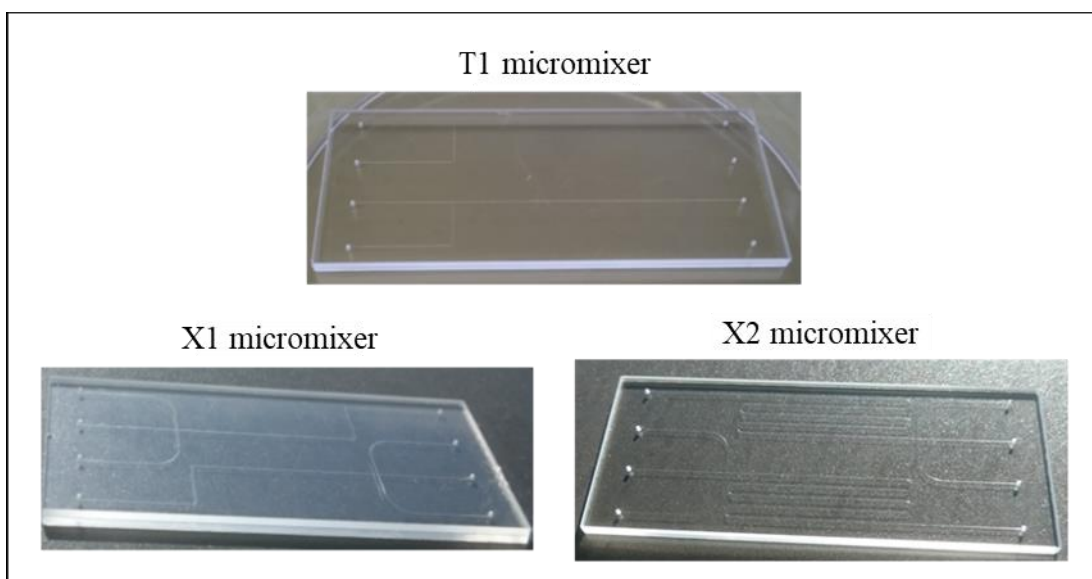


Figure 30. The three micromixer devices employed in the micronization experiments.

The second micromixer consists of three inlets joining at an X-junction (X1). The two side channels are used to feed the liquid (solvent or solution), and carbon dioxide enters the system through the narrower, centre channel. A channel with width equivalent to that of the side channels follows post-junction to the outlet.

The third micromixer design, X2, is the same as X1, however, a long serpentine channel follows post junction. The post-junction channel length for X2 micromixer is approximately 3 times more than the post-junction channel length in X1. The dimensions for each of these micromixers are listed in Table 7.

Table 7. Dimensions for the 3 micromixer designs.

Micromixer Design	Wide Channel		Narrow Channel		Channel length (post-junction), mm	Channel depth (μm)
	w (μm)	l(mm)	w (μm)	l (mm)		
T1	120.7	15	32.2	23	45	26
X1	124.6	21.3	32.3	15	52.5	19.7
X2	105.2	21.3	17	15	161.5	19.4

2.2.2 Device Design and Lithography

The micromixer designs were prepared using DraftSight software which is a 2D and 3D CAD solution that can create, edit, view and mark-up any DWG file. These files (in .lwo format) are used with the laser writing equipment (Kloe Dilase 650 Direct Laser Write system) implemented in the fabrication process.

The next step is to transfer these designs onto the BF33 substrate. The fabrication involves standard lithography techniques and wet etching. The BF33 substrates are rinsed with acetone followed by IPA. Piranha (3-parts of sulphuric acid and 1-part of hydrogen peroxide) clean is performed to remove organic impurities.

After cleaning, the substrate is coated with a thin layer of Cr (12.5 nm) followed by a thick layer of Au (150 nm) using a sputter depositor (HHV/Edwards TF500). This is

followed by coating the substrate with AZ1518 photoresist using a spin coater, Karl Suss Delta 80 - Figure 31.

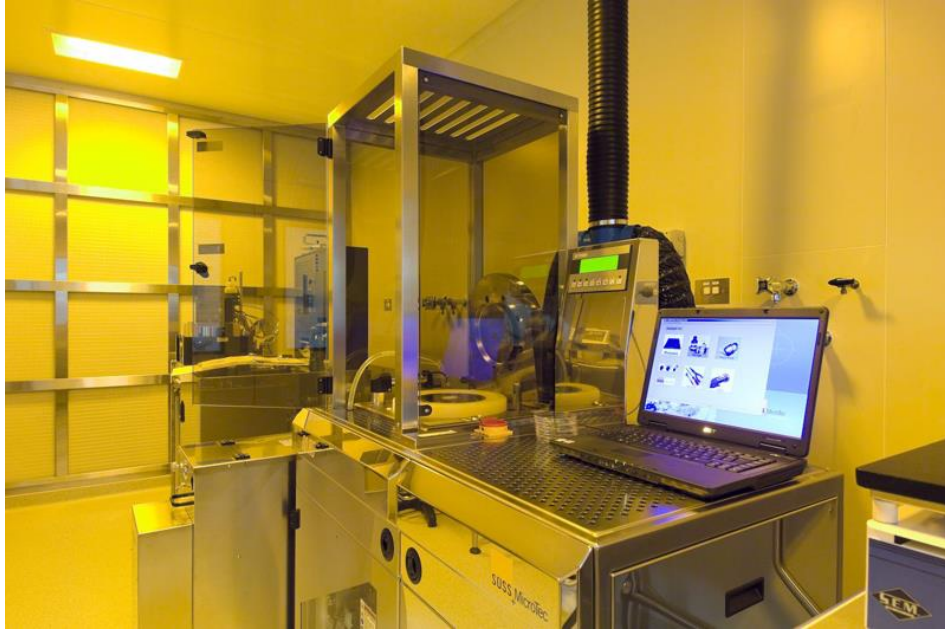


Figure 31. The Spin Coating System used for micromixer fabrication.

A pre-bake step is performed to stabilize the photoresist at 105 °C for 1 minute. The substrate is mounted onto the Kloe Dilase 650 Direct Laser Write system - Figure 32 and the desired design is transferred onto the substrate. The exposed resist is then developed in AZ 726 MIF developer followed by rinsing with water. This is followed by design inspection using light microscopy.

The process steps are shown below:

- Substrate cleaning (acetone, IPA)
- Au/Cr coating (sputter deposition)
- PR coating (spin coater)
- Soft bake (hot plate)
- PR exposure (laser writer)
- PR development
- Design inspection (light microscope)



Figure 32. Kloe Dilase650 Direct Laser Write system.

Following design transfer onto the glass substrate, microchannels are etched into the substrate in the following order:

- Au etching
- Cr etching
- BF33 etching

After development, this PR layer is used as a mask to selectively etch away the Au and Cr metal layers from regions where the channels will be formed. For etching the gold layer, an aqueous solution of KI/I_2 is used whereas an aqueous solution of ammonium cerium nitrate is used for etching the chromium layer. The substrates are then etched in HF to obtain the desired microchannel dimensions. Etching using HF is a wet chemical etching method and results in isotropic etch profiles, i.e. the etch rate is the same in all directions.

After etching BF33 substrate, the PR, Au and Cr layers are removed from the remainder of the substrate using acetone, KI/I_2 solution, and aqueous solution of ammonium cerium nitrate, respectively in the stated order.

2.2.3 Substrate Bonding

The substrate and lid are cleaned using piranha solution, performed with extreme caution, followed by rinsing with water. The substrate and lid (Figure 33 a and b) are activated with concentrated KOH (3M) followed by rinsing with water and drying with nitrogen. The substrate is then pre-bonded to a lid of the same material with eight predrilled inlet/outlet ports. Pre-bonded substrate and lid are checked under a light microscope to inspect the channel alignment with ports. The pre-bonded substrates are annealed at 630 °C and 1800 N for 30 minutes using an EVG 520HE Hot Embosser to achieve permanent bonding - Figure 33c.

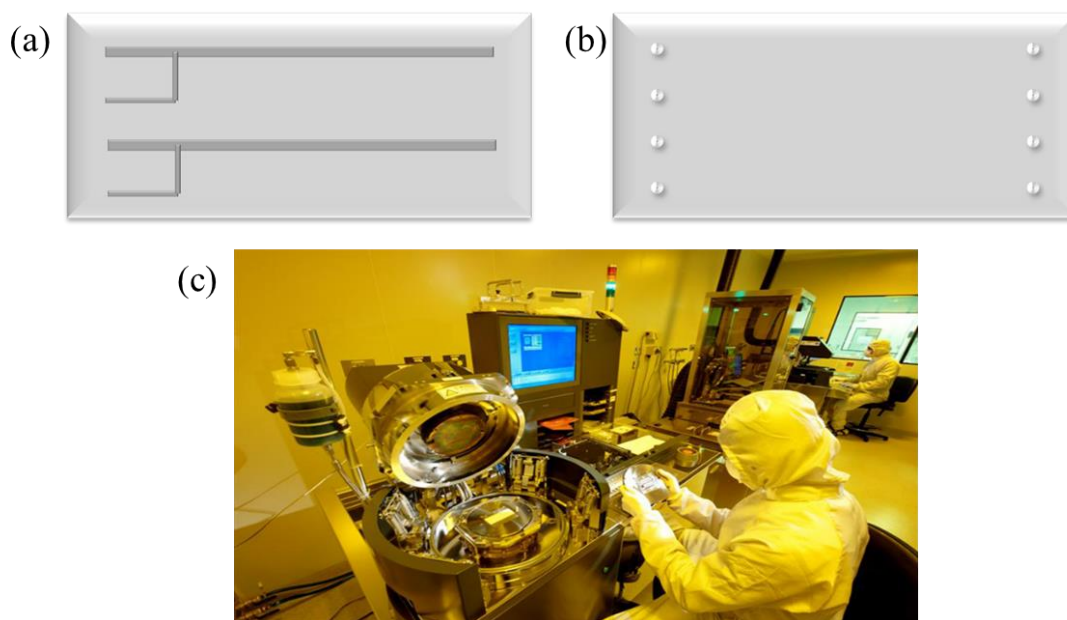


Figure 33. (a) Substrate with microfluidic channel design, (b) lid showing eight predrilled inlet/outlet ports, and (c) Hot Embosser EVG 520HE.

2.3 High-Pressure Tests

A series of pressure tests were performed on the glass micromixers, connectors, and micromixer holder to test the pressure limit for individual components.

2.3.1 Experimental Rig

A simple micromixer-holder-connector assembly was employed to test the durability of individual components under high pressures (up to 100 bar, 25 °C) - Figure 34.

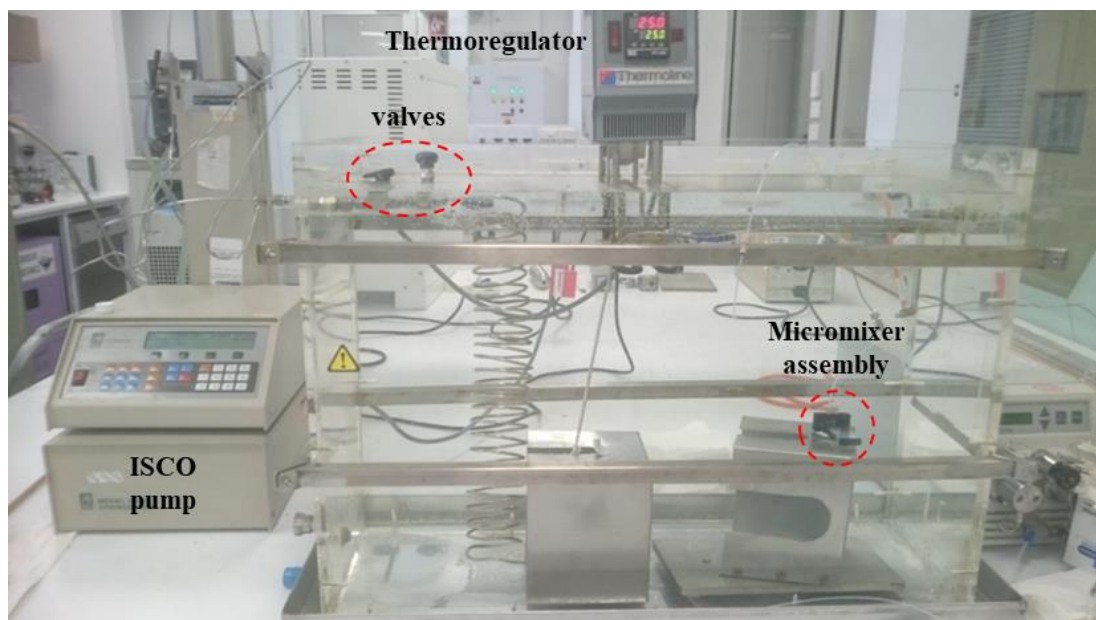


Figure 34. The rig used to perform the high-pressure tests.

The micromixer was made in BF33 using standard lithography procedures (section 2.2). The performance of two different holders was tested where the holder design was the same but the materials for the holder were different. One holder was made in Poly(methyl methacrylate) or PMMA using 3D printing at the University of South Australia (Mawson Lakes, Adelaide). The micromixer assembly consisted of a microfluidic device placed on top of a spacer (a stack of BF33 substrates) to fit the PMMA holder with the micromixer ports facing up - Figure 35. Flangeless fittings (Upchurch-Idex-Flngls Sys Hdls PEEK 1/16) consisting of ferrules (Peek, natural, 1/4-28 flat-bottom, 1/16" OD) were used for interfacing the micromixer with the connectors. A series of 1/16" stainless-steel (ss) tubing and FEP 1/16" tubing was used to interface the micromixer assembly with Teledyne ISCO 260D syringe pumps. The other holder was of equivalent design, made in stainless-steel using microdrilling procedures, and did not require a spacer assembly.

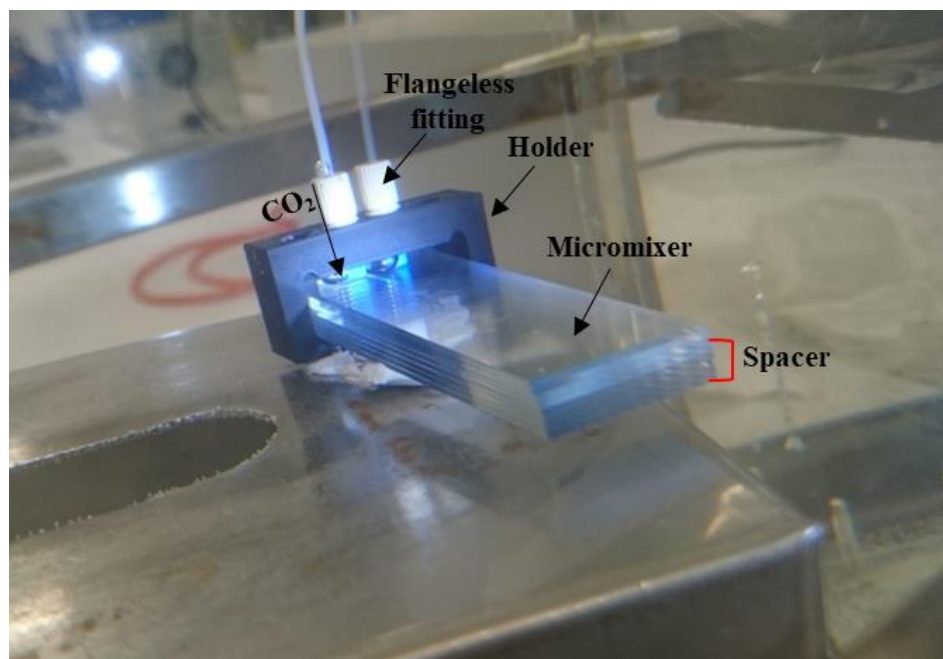


Figure 35. Micromixer assembly employed for high-P tests.

The ss tubing was connected to the fluid reservoir and polymer tubing was connected to the micromixer. The syringe pump was maintained at (3.0 ± 0.1) °C with the help of a chiller (Julabo Corio CD200-F). A reservoir, made in stainless-steel, was used for pressure and temperature stabilization for CO₂. The desired CO₂ pressure was built in the reservoir (stainless-steel vessel, 75 ml) at a constant flow rate ($5 \text{ ml}\cdot\text{min}^{-1}$) and then allowed to stabilize. A needle valve was used to slowly introduce pressurized CO₂ into the micromixer. The outlet of the micromixer was initially kept open to the water bath to allow for the pressurized CO₂ to flow. Different values of pressure were tested, starting at 40 bar, and building up to 100 bar (in steps of 10 bar), at a constant temperature of 25 °C.

2.3.2 Observations and Conclusions

We compare the two holders used in the high-pressure experiments for interfacing the micromixer. For the polymer holder, gas leaks were observed at the interface between the ferrules and the micromixer which can be seen as a series of bubbles - Figure 36, even at the lowest pressure employed (40 bar). Tightening the flangeless fittings further destroyed the threads in the holder (see Appendices section 8.1). Therefore, the PMMA holder was not used for the remainder of the thesis.

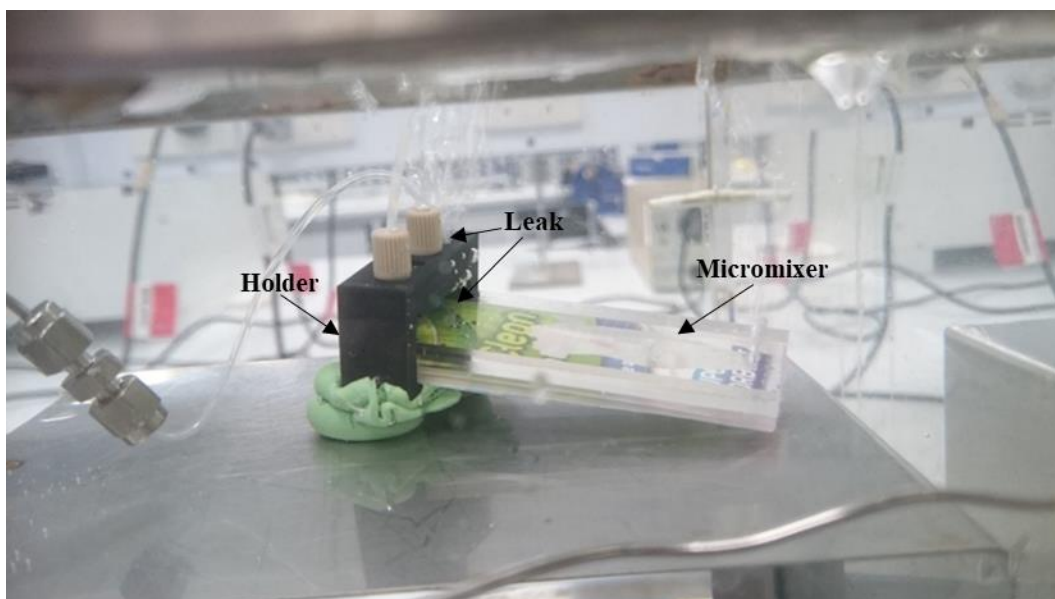


Figure 36. Gas leaks observed during pressure test at 40 bar and 25 °C.

The analogous metal holder also failed for similar reasons. The micromixer cracked at the edge where it connects with the holder. Most likely this happens due to the uneven pressure from the metal holder across the micromixer's edges (see Appendices section 8.1).

This necessitated the development of a customized holder assembly that allows us to use high-pressure fittings (see Appendices section 8.2) to interface the glass micromixer with the fluid delivery system whilst maintaining homogenous pressure across the entire assembly. Hence, we design and fabricate a holder in stainless-steel that sandwiches the micromixer between two metal platforms with ports for the HPLC fittings (to replace the polymer fittings). Careful considerations were made for sandwiching and interfacing the micromixer to avoid any of the failures stated above (see Appendices section 8.3).

The details and schematic for the holder design and connections to the micromixer are discussed in detail in the following sections (sections 2.4 and 2.5).

2.4 Metal Holder

The metal holder developed for this project is shown in Figure 37.

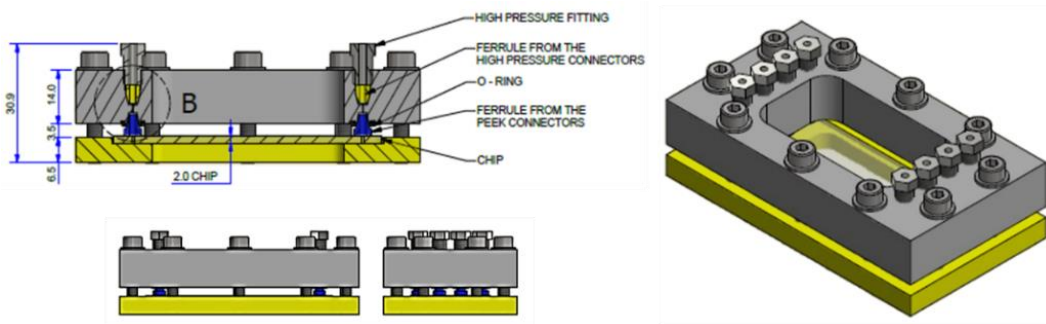


Figure 37. Schematic for the stainless-steel holder used for making high-pressure connections to the glass micromixer.

The holder is made of stainless-steel 316 by microdrilling the metal substrate. Microdrilling is the process of drilling of holes less than 0.5 mm (0.020 in) in size. The part is made on a Kira CNC 3 axis milling machine. The CNC programs are written using the CAD model that was created using Autodesk Inventor and a CAM software called SolidCAM.

2.5 Connections to the Micromixer

The bespoke metal holder is used for interfacing a glass micromixer with the high-pressure fluid delivery system - Figure 38.

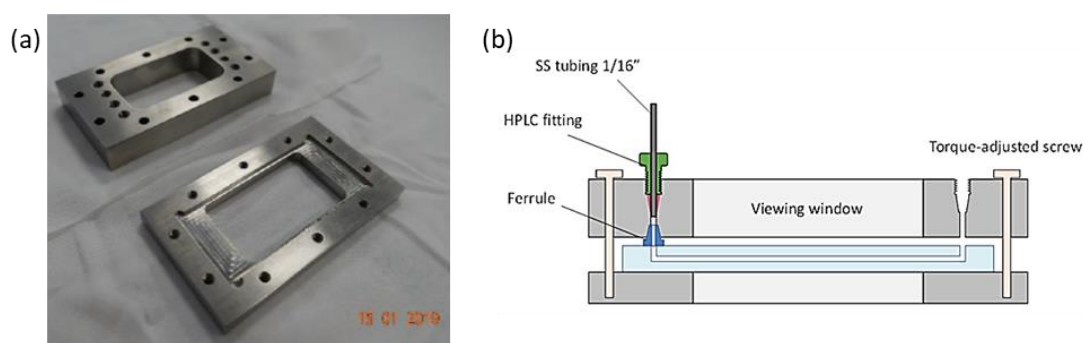


Figure 38. (a) The top and bottom part of the metal holder and (b) schematic showing the connections to the glass micromixer sandwiched between the holder.

The micromixer is placed on a groove on the bottom part of the metal holder. Eight ferrules (PeeK, natural, 1/4-28 flat-bottom, 1/16" OD) are inserted in the top part of the

holder lid. The two parts are held together using 10 stainless-steel bolts. HPLC fittings (Valco ZBU1XC) on the top of the holder are connected to the inlet and outlet lines using 1/16" tubing (FEP or stainless-steel).

2.6 Micromixer Cleaning

The micromixers are cleaned using a suitable solvent and DI water for several minutes before and after each experiment using Mitos P-pumps (Dolomite) followed by drying with nitrogen.

2.7 Experimental Rig

The schematic for the high-pressure microfluidic rig built and commissioned in this work is shown - Figure 39. Connections to the micromixer have been discussed in section 2.5.

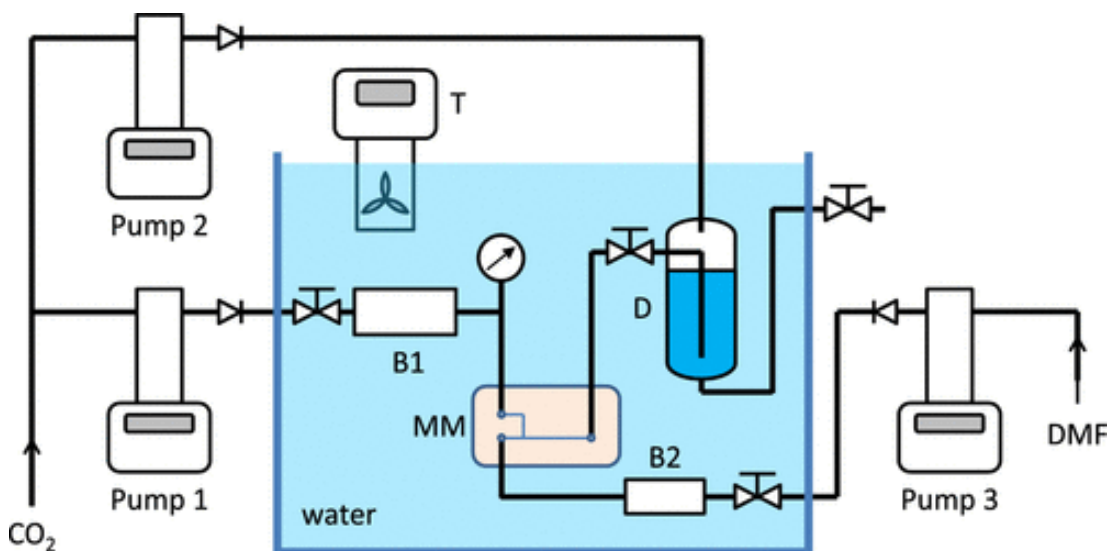


Figure 39. Rig used in the micronization experiments.

The microfluidic platform MM is inserted vertically in the water tank to allow for visualization using a light microscope (OMAX 2X - 270X 14MP Simal-focal Zoom Stereo). Three syringe pumps (Teledyne ISCO 260D) are used in this set-up. Pumps 1 & 2 are used for supplying pressurized CO₂ for input gas and back pressures,

respectively, and syringe pump 3 is used for supplying pressurized liquid (solvent, API solution) via standard stainless-steel Swagelok connectors and tubing (1/16" OD). B1 (stainless-steel vessel, 75 ml) and B2 (stainless-steel vessel, 12 ml) are buffer vessels used for temperature and pressure stabilization for the gas and liquid, respectively. The pressurized fluids stabilize in the buffer vessels for at least an hour to allow for smooth fluid delivery. A pressure transducer (Druck DPI 104) is used for monitoring the process pressure. The operating temperature is maintained at (25.0 ± 0.1) °C by submerging all components in a water bath equipped with a heater circulator T (Thermoline Unistat 130). Syringe pumps 1 & 2 are maintained at a constant temperature of (3.0 ± 0.1) °C with the help of a chiller (Julabo Corio CD200-F). The two pumps are filled with liquid CO₂ for reliable pumping. Pump 2 controls the back pressure in discharge vessel D by filling it with CO₂ at a fixed value (kept lower than the fluid input pressure and helps to decide and maintain fixed fluid driving pressure, ΔP , in the system).

2.8 Micronization

Micronization is performed by flowing a fixed solution concentration, fluid input pressures and back pressure for each experimental run. The pressurized CO₂ (pump 1) and API solution (pump 3) are introduced in the relevant channels of the micromixer.

For a given set of experiments, the fluid input pressure is kept equal and fixed whereas the fluid driving pressure is varied by changing the back pressure (pump 2). After fluid stabilization in the reservoir vessels, fluids are introduced into the micromixer by gradually opening the needle valves. The mixture flows through the micromixer MM, the connecting tubing, and then reaches the discharge vessel D, which is 75% filled with DI water. The residual solvent is removed from the product by continuously flowing depressurized CO₂ out of the discharge vessel D. For each experimental run, the driving pressure is kept fixed and collection is done for 15 minutes. The aqueous suspension is then depressurized and collected for particle analysis. Throughout the experiment, all the rig components including the buffer vessels, connectors and the microfluidic platform are maintained at a constant temperature (25 °C) in the thermal bath.

2.9 Characterization

2.9.1 Dynamic Light Scattering

Dynamic Light Scattering (DLS) is a valuable characterization method used for the determination of particle size (nm- μm) in a suspension. The schematic demonstrating a simple DLS instrument is shown in Figure 40. In principle, DLS makes use of a laser source and a detector. A single frequency laser is directed to the sample suspension in a transparent cuvette where laser hits the sample on one side and gets scattered by the particles in the suspension. The detector on the other side captures the scattered light and evaluates modulation of the scattered light intensity as a function of time.

The relation between the speed of particles and particle size is given by the Stokes-Einstein equation as follows:

$$D = \frac{k_B T}{6\pi\eta R_H} \quad 21$$

Here D is the translational diffusion coefficient ($\text{m}^2 \cdot \text{s}^{-1}$), k_B is the Boltzmann constant ($\text{m}^2 \cdot \text{kg} \cdot \text{K}^{-1} \cdot \text{s}^{-2}$), T is the temperature measured in kelvin, η is the fluid viscosity ($\text{Pa} \cdot \text{s}$) and R_H is the hydrodynamic radius (m).

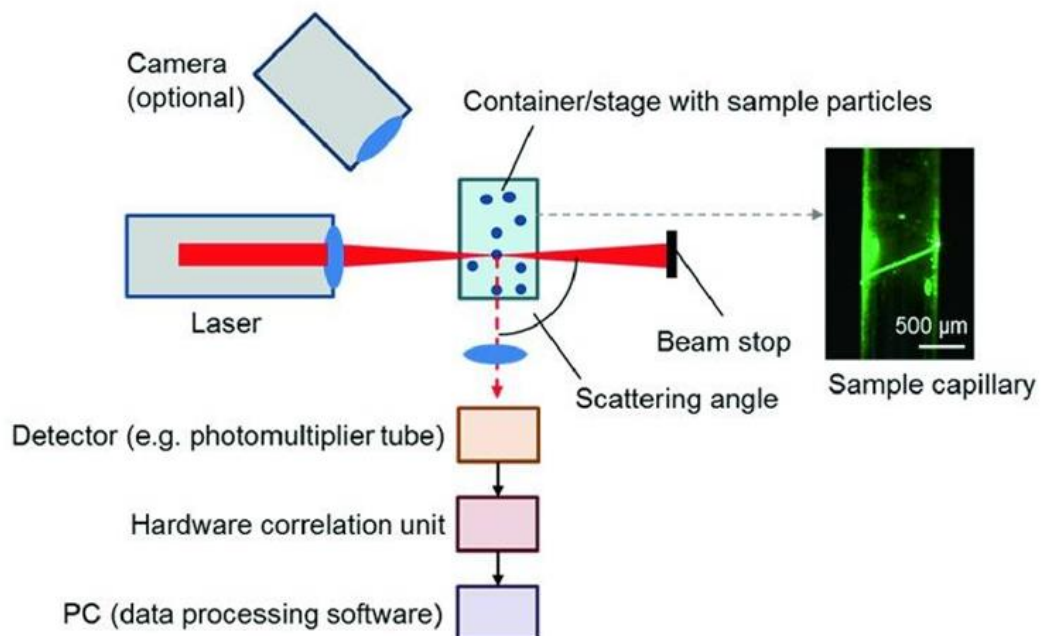


Figure 40. Basic setup of a DLS measurement system.(221)

DLS measurements were performed on Zetasizer Nano ZS (Malvern) to assess the particle size. A small volume of the sample (~3 ml) was taken in a transparent cuvette which is sonicated for 5 minutes just before performing DLS measurements to minimize the effect of aggregation.

The software generates a set of data for each sample. There are two main parameters: Z-average value and polydispersity index (PDI). The Z-average value refers to the mean value of the particle's hydrodynamic diameter. Whereas the polydispersity index is a measure of the width of the particle size distribution ($PDI = \text{square of the ratio of standard deviation to mean diameter}$).⁽²²²⁾

DLS characterization was used to determine the average size of the API crystals generated using the proposed microGAS platform as well as monitor the PDIs for each sample collected. The size distribution obtained for the samples is dependent on the mixing conditions. The broad tendency is that slow gas-liquid mixing results in bigger particles and larger size distributions, whereas smaller PDIs were obtained in case of faster mixing. The reason for the wide size distribution in some samples is the collection method used. Collection for the microcrystallized particles was performed for 15 minutes in water under pressure. During this, the start and stop periods for fluid flow and stabilization can take up to 1 minute which is at least an order of magnitude larger than the fluid residence times in the micromixer (Figure 48c, Chapter 3). This results in variability in the precipitation conditions which are different to the conditions experienced on-chip during well-established continuous flow. Moreover, the sample collection involves depressurization of the suspension carrying the API crystals (section 2.8) which is done manually by gradually opening a shut-off valve. A collective effect of this results in variation in process conditions which results in wider size distribution for the crystals produced. This variation is reduced in the case of intense gas-liquid mixing which results in faster fluid flow and stabilization.

The limitation of larger size distribution can be overcome by gaining enhanced control over the start and stop periods of the experiment along with automation of the sample collection method. However, since our main aim is developing and implementing high-pressure microfluidics for continuous API crystallization, rig automation was not included within the scope of this work. We focused on the development of a rig to

realise the proposed microGAS process and map the role of key parameters that influence API microcrystallization.

2.9.2 Scanning Electron Microscopy

A scanning electron microscope (SEM) makes use of an electron source, an array of electromagnetic lenses (condenser and objective lens) and detectors along with a sample holder at the bottom of the chamber - Figure 41. SEM is used to gather information about surface topography/geometry or surface composition. A beam of electrons produced at the chamber top using an electron source is made incident on the sample. The electrons are accelerated through a column comprising of a combination of various lenses and apertures which focuses the e-beam on the sample surface. The e-beam penetrates the sample surface, up to a few micrometers usually. This depth is a function of the accelerating voltage and density of the sample.

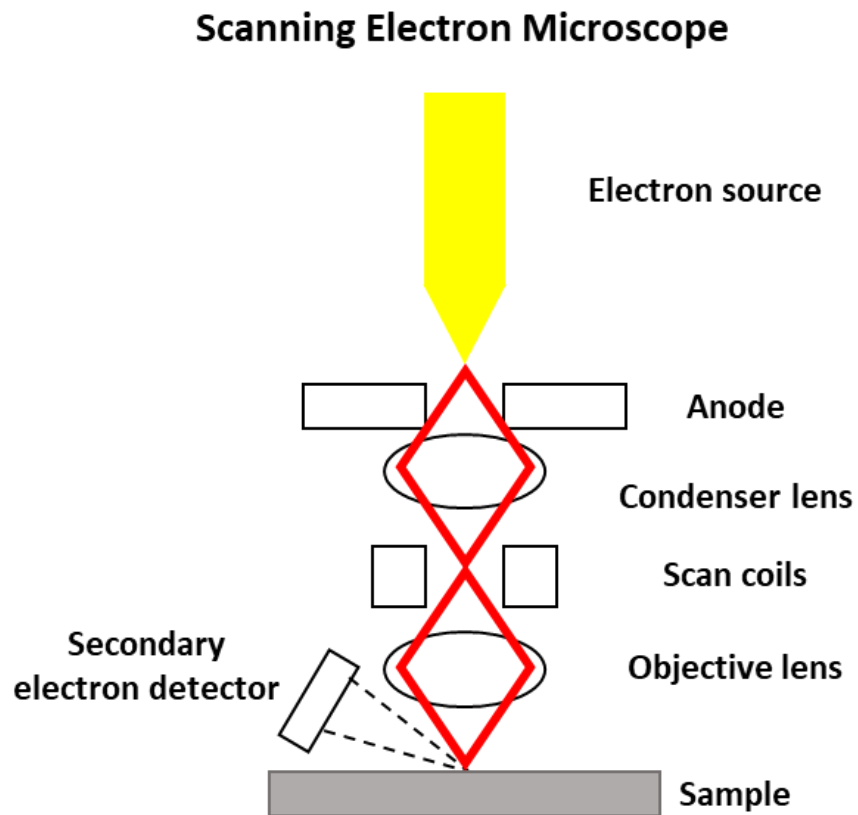


Figure 41. Schematic showing the basic principle for a scanning electron microscope.

The high energy e^- -beam interacts with the sample and responds by producing secondary electrons, backscattered electrons and X-rays that are characteristic of the sample - Figure 42. These are gathered by the detectors which form an image that is displayed on a computer screen. A combination of pumps evacuates both the column through which the electron beam is manoeuvred and directed towards the sample and the chamber where the sample is mounted over a stage. Scan coils present above the objective lens control beam position on the sample.

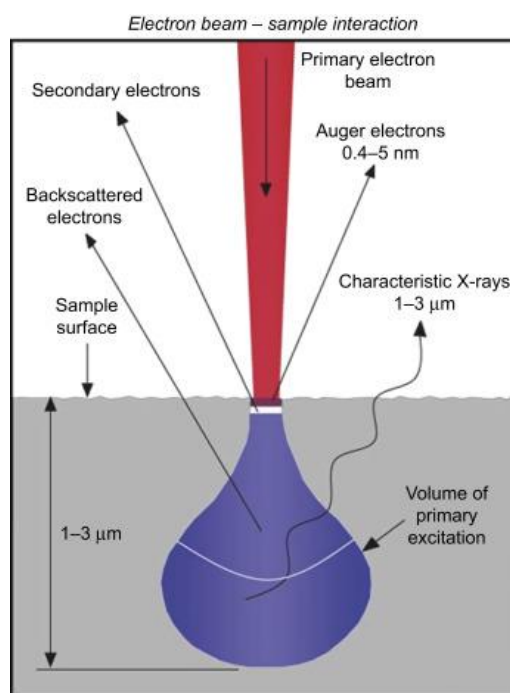


Figure 42. Different signals generated by a sample when a beam of electrons excites it. (223)

NEON FIB-SEM, CLARA FESEM and MIRA VP-FESEM microscope were used for imaging the samples. Sample preparation involved the use of aluminium stubs which were cleaned with ethanol and acetone prior to use to avoid any impurities. The micronized API particles were collected as a suspension in water. Each sample was sonicated for 5 minutes before sample preparation to minimize the effect of aggregation. A droplet of the sample was placed on a clean stub and allowed to dry overnight in a fumehood. This was followed by coating the samples with a thin platinum layer (Sputter coater, Cressington 208HR) at 40 mA for 2.5 minutes under vacuum (0.2 mbar), then stored in a vacuum desiccator until electron imaging.

2.9.3 Powder X-Ray Diffraction

Powder X-Ray Diffraction (PXRD) is used in identifying and determining the crystallographic structure of a material or an unknown sample. It provides important information about the unit cell dimensions and phase identification by comparing the gathered data with standard reference patterns. We can identify the material as each material has a unique d-spacing (distance between the planes of atoms that give rise to diffraction peaks). The operational principle of X-ray interaction with a sample is shown in Figure 43. The sample for powder-XRD analysis needs to be finely ground and homogenised. A cathode ray tube (CRT) is employed to generate monochromatic X-rays which are filtered, collimated, and concentrated towards the sample. The crystalline sample act as 3D diffraction gratings for incident X-rays with wavelengths matching to the spacing between plains of a crystal lattice.

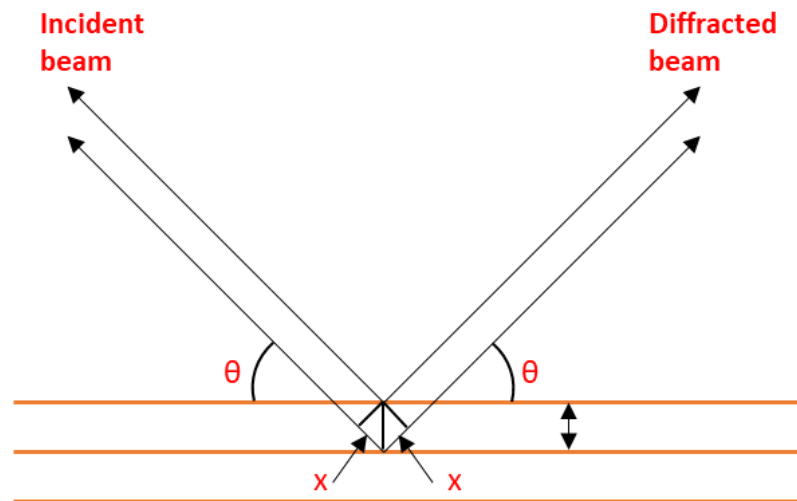


Figure 43. Operational principle of X-ray interaction with sample.

Monochromatic X-Ray interaction with the crystalline lattice generates constructive interference when conditions satisfy the Bragg's law given by:(224)

$$n\lambda = 2d \cdot \sin\theta \quad 22$$

Here n is an integer, λ is the X-ray wavelength, d is the spacing of crystal layers and θ is the incident angle. These electromagnetic waves are diffracted and detected by scanning the material through a range of 2θ angles. The diffraction peaks are converted

into d-spacing, which by relating to the standard reference patterns, allows identification of the material because each material has a set of unique d-spacing.

XRD was used to compare crystalline structure of the samples produced. PXRD was measured on a powder diffractometer D8 Advance (Bruker AXS, Germany), with a copper $K\alpha$ radiation source (40 kV & 40 mA) with a LynxEye detector. The parameters used in the recipe for XRD are listed in Table 8.

Table 8. Scan parameters used in the XRD analysis.

Scan parameter	Value
2θ scan range	4.5-90°
Step size	0.014°
Time/step	0.5 s
Total scan time	60 minutes

The differences in the XRD patterns for the APIs and their combination were used as a guide to validate the formation of cocrystals.

Chapter 3

Precipitation of Drug Particles Using a Gas Antisolvent Process on a High-Pressure Microfluidic Platform¹

3.1 Introduction

In this chapter, we implement the developed high-pressure microfluidic rig for continuous and controlled crystallization of a model API using the gas antisolvent process. The GAS process involves pressurising an organic solution with CO₂ (section 1.2.1). The miscibility between pressurized CO₂ and organic solvent leads to volumetric expansion which reduces the solvent power and results in a state of supersaturation thereby causing solute precipitation. Thus, gas-liquid mixing and volumetric expansion of the solvent in particular has a significant influence on the outcome of the precipitation process. Mixing conditions affect the precipitate properties such as particle size, morphology, and crystal structure. To achieve controlled crystallization, it is necessary to have homogenous gas-liquid mixing and avoid variation in product quality. This is difficult to achieve in a large-scale reactor. The excellent control over process parameters offered by microfluidics along with the continuous nature of the technology allows for homogenous gas-liquid mixing and continuous precipitation under well-determined conditions.(143)

Volume expansion of the organic liquid phase using subcritical CO₂ on a microfluidic platform is the primary focus of this chapter. Thus, the first step is to form a gas-expanded liquid in a micromixer under dynamic flow and use it for precipitation of a model pharmaceutical compound. DMF is used as the organic solvent and subcritical CO₂ is used as the antisolvent in this study. The model API used in this work is Griseofulvin (GF) which is an antifungal drug (section 2.1.1). Two simple micromixer designs: a T-junction (T1) and an X-junction (X1) are employed to study the influence of gas-liquid ratios on mixing and liquid expansion - Figure 44.

¹ The results presented in this chapter were published in *Ind. Eng. Chem. Res.* 2020, 59, 25, 11905–11913.

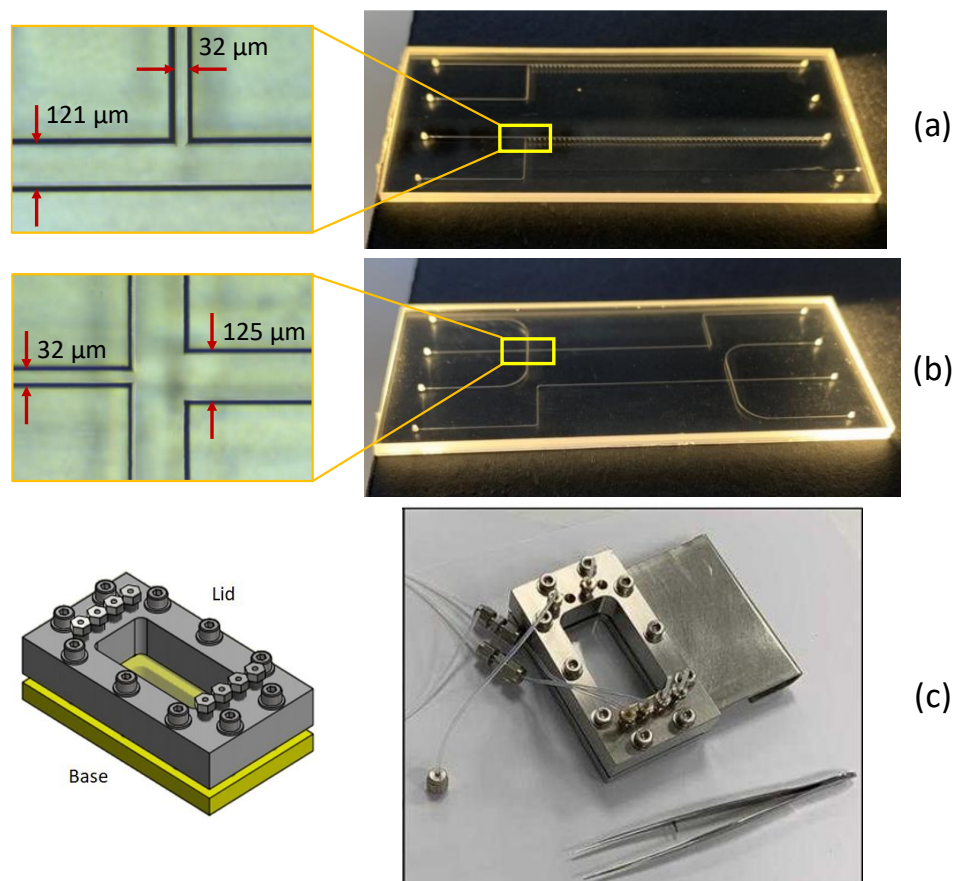


Figure 44. Geometry of micromixers: (a) T-junction: narrow channel width 32 μm , wider channel width 121 μm , depth 26 μm ; (b) X-junction: narrow channel width 32 μm , wider channel width 125 μm , depth 20 μm ; (c) Stainless-steel holder.

The influence of several parameters such as fluid driving pressure, antisolvent properties (ρ , μ), and solution concentration on gas-liquid mixing and consequently the precipitate properties was investigated. The precipitate was characterized using DLS and SEM.

3.2 Gas-Liquid Mixing in Microreactors

Classically in microfluidics, researchers have focused on liquid-liquid flow and reactions happening at the interface. Knight et al.(225) demonstrated the formation and control of nanoscale, submerged fluid jets of fluorescent dye, 5-carboxyfluorescein, (through the centre channel) and non-fluorescent buffer, tris-HCl (pH=8.5), (from the

side channels) using a flow focussing microfluidic device - Figure 45. Mix times of less than $10\ \mu\text{s}$ and sample consumption rates of nanoliters per second were achieved.

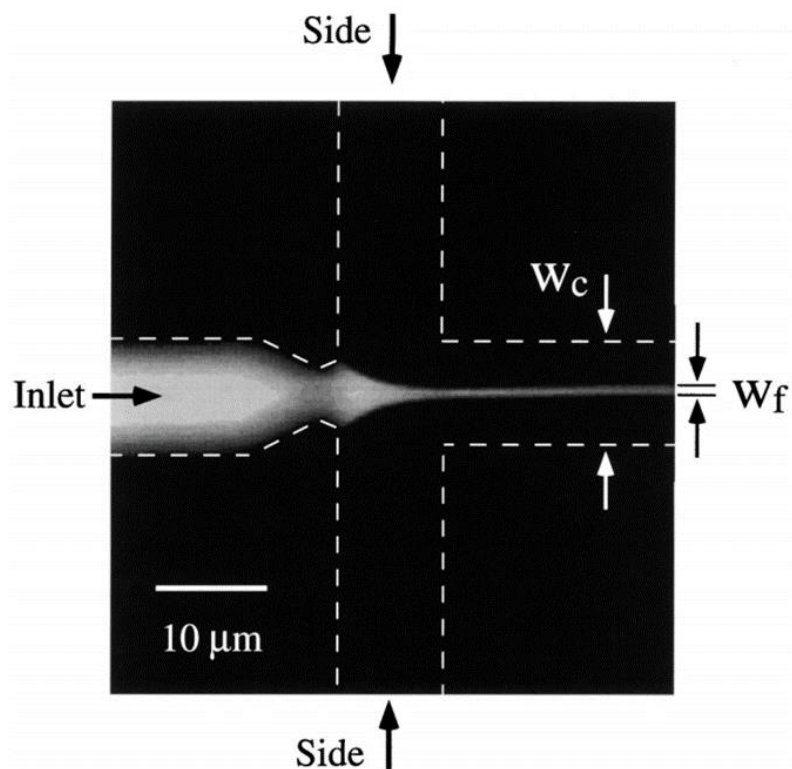


Figure 45. Epifluorescence image of the flow-focusing microfabricated device.(225)

The large and well-defined interfacial area and precise control of reaction conditions in microfluidics offer unique and exciting opportunities in the study of gas-liquid co-flow and mixing owing to a significant reduction in mass-transfer limitations. Yet, microfluidic studies of the kinetics of fast gas-liquid reactions remain a challenge due to poorly defined interface between the gas and liquid phases which results in uncertainty in determining mass-transfer parameters.(220, 226, 227) A range of microreactor geometries based on different contacting principles have been developed to study two-phase flow such as the T-mixer or flow focussing microreactor. These are based on two basic approaches to bring the gas-liquid phase in contact: continuous phase microreactors and dispersed phase microreactors.

Continuous phase microreactors: In this type of microreactors, both the phases are continuous with large interfaces. Both gas and liquid have individual streams and are

fed individually (Figure 46 – slug-annular or annular flow). The crucial design issue of these reactors is the way the interface, liquid film, or both are stabilized.

Dispersed phase microreactors: In these microreactors, one phase is dispersed into the other using adequate micromixer design or a micromixer upstream of the reactor section (Figure 46 – bubbly or slug flow). Such micromixers may also consist of a single channel of micro or large dimension. A gas-liquid dispersion is created by an inlet which induces merging of the gas and liquid streams. Among these are microstructured falling film, overlapping channel, and mesh reactors.

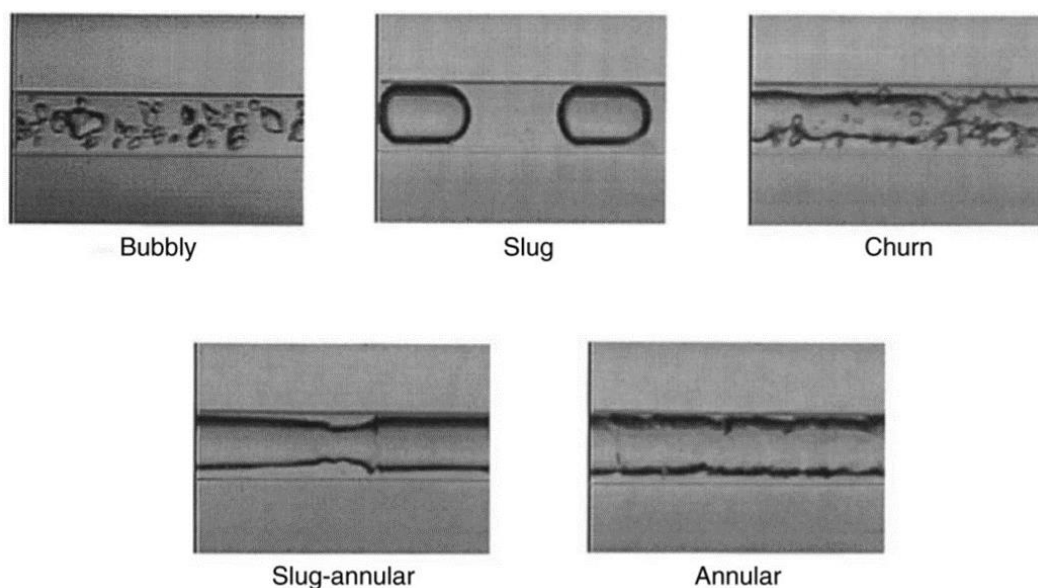


Figure 46. Representative flow patterns of air-water flow in a circular tube of 1 mm diameter as observed by Triplett et al. (1999a).(228)

Different types of gas-liquid flow profiles can be observed based on the hydrodynamic conditions - Figure 46. However, the gas-to-liquid flow rate ratio is one of the most critical parameters. The flow profiles can range from bubble flow where the bubble diameter is smaller than channel's, to slug flow where the equivalent bubble diameter is larger than the channel's as the ratio goes up - Figure 46. At very high ratios for the gas-to-liquid flow rates (ideally > 1), annular flow is observed where gas flows at the channel core with a thin liquid annulus film on either side - Figure 46. In this case the reactor goes from dispersed-phase to continuous-flow reactor. Under these conditions, flow disturbances such as waves can occur and entrainment of the liquid film into the

gas core may take place. The channel geometry (shape, cross-section) also plays a significant role in determining the flow profile as it can be used to control gas-to-liquid ratios for a given ratio of the flow rates.

Although in dispersed-phase reactors transport limitations between the two phases are significantly reduced due to increased gas-liquid interface, there is generally a degree of uncertainty concerning the actual fluid geometries and available interfacial areas.(226)

We have focussed on continuous gas-liquid flow in a microchannel of different mixer designs (T1 and X1, Figure 44 a and b) by applying the same fluid input pressures for the gas and the liquid. The different mixer designs allow us to vary the gas-to-liquid flow ratios (the volume of liquid to gas is twice in case of X1 micromixer as compared to the T1 micromixer) to study the influence on mixing. It is easier to map the gas-liquid phase boundary in our transparent micromixers which allow for visual estimation of mixing lengths and thus avoid the uncertainty issues associated with dispersed flow in standard stainless-steel reactors.

In this work we have used a high-pressure microfluidic rig (Figure 39) explained in detail in section 2.7. The supply pressures for the gas and liquid were kept the same in each experiment (40, 50 and 60 bar) and the back pressure was varied to tune the driving pressure, ΔP (10, 15 and 20 bar). Following the gas-liquid mixing in the micromixer, sample suspension carrying the precipitated API particles was collected in the discharge vessel (D) for 15 minutes. GF concentration in DMF was varied from 0.1 to 1% (w/w) to study the influence of concentration on the microprecipitate size.

3.3 Results and Discussion

The pressure-driven, steady-state laminar flow in channels is known as Poiseuille flow (section 1.3). In a Poiseuille flow, pressure difference between the two ends of a straight, rigid channel drives the fluid flow. This law was initially formulated for circular channels; however, it can be modified for application to other cross-sections such as the commonly produced rectangular channels (channel profile for the micromixers used in this study). In rectangular channels, the ratio of channel width (w) and height (h) controls flow parameters such as the hydraulic resistance and flow

profile. The average fluid velocity and properties determine its flow profile in the microchannel and can be estimated using Reynold's number (Re) as follows:

$$Re = \frac{\rho u d}{\mu} \quad 23$$

Here ρ is fluid density, u is average fluid speed, d is channel's hydraulic diameter and μ is fluid viscosity. The Reynolds numbers for the fluids, under individual fluid flow or co-flow conditions, are estimated by using the fluid's density and viscosity under the given pressure and temperature, the average fluid speeds estimated using volumetric flow rates and the channel cross-section.

First take the simplest case of DMF flow through the micromixer under a set of conditions (P_{in} , ΔP , T). The flow of pure solvent through the micromixers (without any addition of CO_2) was a Poiseuille type flow, i.e. laminar ($Re = 30-150$) and the flow rate, Q , vs driving pressure, ΔP , dependence could be described with a single hydraulic resistivity, R :

$$\Delta P = RQ \quad 24$$

Whereas Ohm's law for electrical circuits helps to relate the electrical current, I , with the resistance, R , and potential drop, ΔV , across the circuit as follows:

$$\Delta V = IR \quad 25$$

Thus, the Poiseuille law for hydraulic resistivity can be treated in complete analogy to electric resistivity in DC circuits.(225, 229)

The hydraulic resistivity for a rectangular channel (width w , height h , length L) is proportional to the fluid viscosity, μ , and is given by:(229)

$$R = \frac{12\mu L}{wh^3 \left(1 - 0.630 \frac{h}{w}\right)} \quad 26$$

Total resistivity for the T-micromixer when flowing solvent through the wider channel is the sum of the resistivities encountered before and after the junction - Figure 47a. In the X-micromixer the resistivity before the junction is half of the resistivity of a single side channel (the two are connected in parallel) and must be added to the resistivity of the outflow channel - Figure 47b.

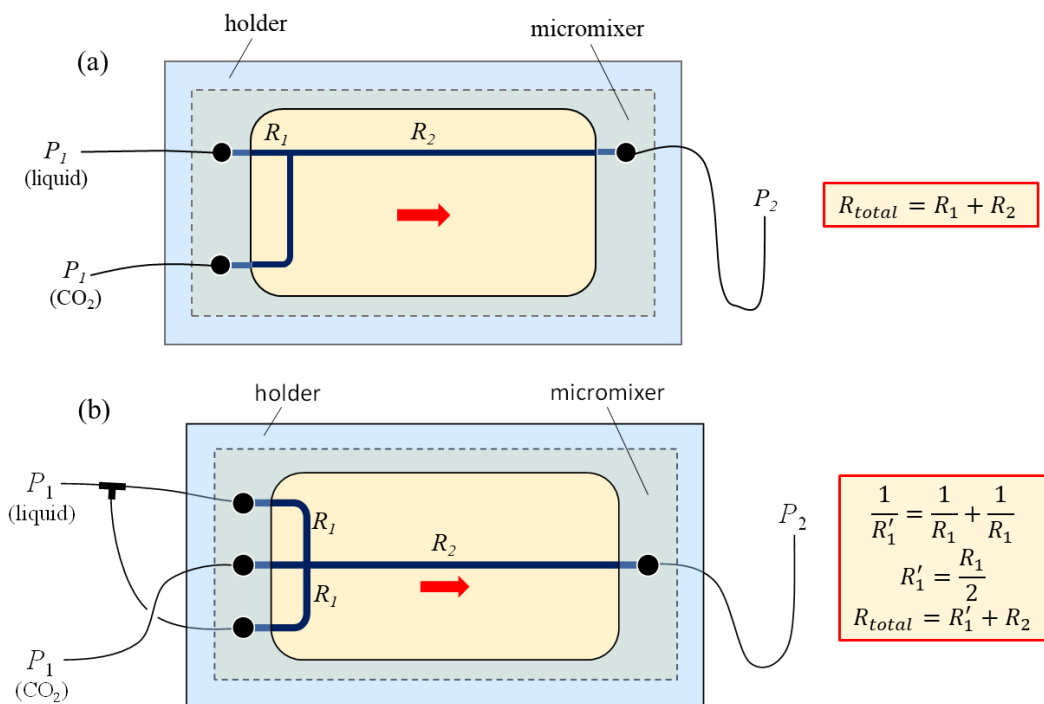


Figure 47. Diagrammatic representation and total resistance for the wider channels in: (a) T-junction micromixer and (b) X-junction micromixer.

Next, we co-flow the gas and liquid through the micromixers at fixed and equal input pressures, and different fluid driving pressures. This was done to investigate the gas-liquid mixing at different ΔP and influence on precipitate properties. The gas-liquid co-flow results in mixing of the two fluids in the micromixer is shown in Figure 48. This resultant mixture is effectively a GXL. It was noted that when DMF and carbon dioxide co-flow, the total mass flow rate is larger, and the Reynolds number increases ($Re = 100-300$). The mass flow rates measured in an X-junction micromixer are plotted in Figure 48a. The mass flow rates, $F (= \rho Q)$, were obtained by using the densities $\rho_{DMF} = 944 \text{ kg/m}^3$ for DMF(230), $\rho_{CO_2} = 93.6 \text{ kg/m}^3$ for $CO_{2(231)}$, and $\rho_{GXL} = 978 \text{ kg/m}^3$ for the CO_2 -expanded solvent.(232) The CO_2 flow rates (under gas-liquid co-flow) are more scattered than the ones for the solvent. These fluctuations can be attributed to the higher Reynolds numbers reached in the side channel ($Re = 6000-8000$). After the junction, the two fluids mix rapidly and the solvent co-flow rates do not fluctuate much.

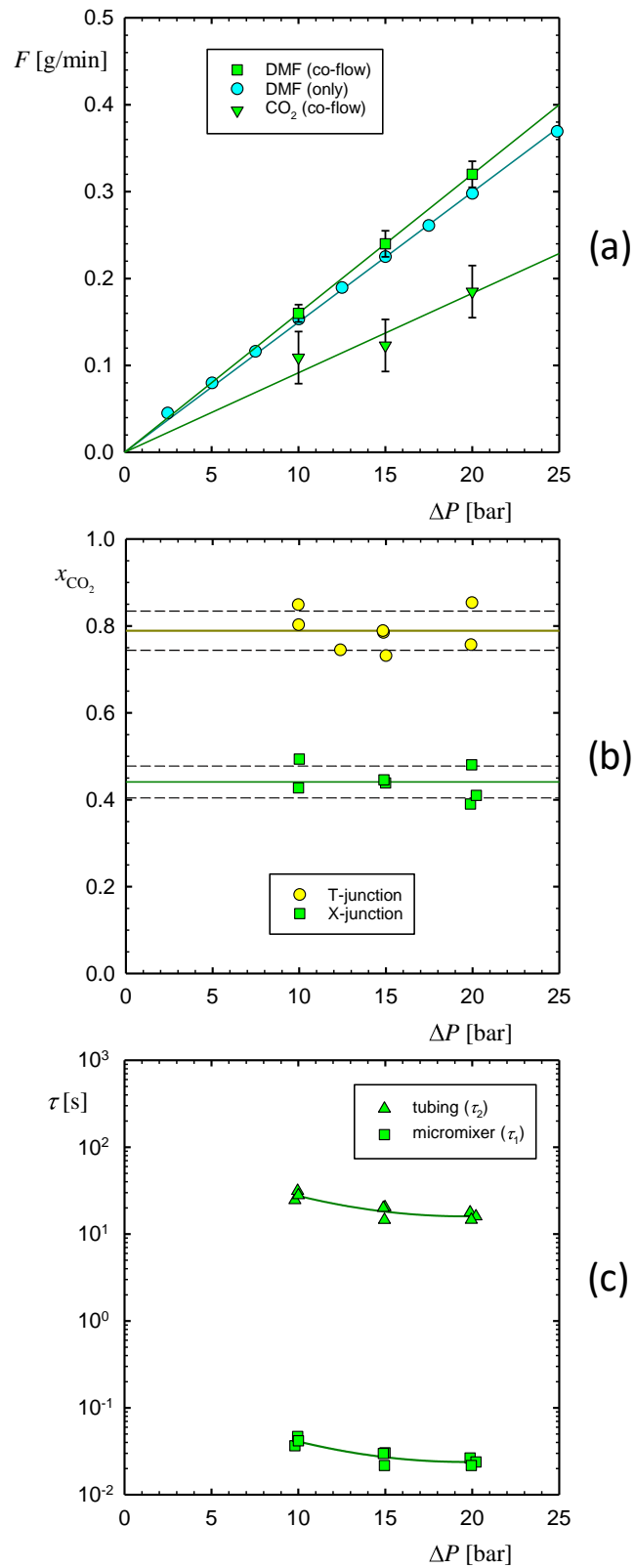


Figure 48. Flow characteristics in the micromixers: (a) mass flow rate, F , as a function of driving pressure, ΔP ; (b) equilibrium mole fraction (mean and standard deviation) of carbon dioxide, x_2 , as a function of driving pressure, ΔP ; (c) residence time within the X-micromixer, τ_1 , (\square), and within the outlet tubing, τ_2 , (\triangle), as a function of driving pressure, ΔP .

The fact that the total mass flow rate has increased in a channel of the same geometry implies that the fluid viscosity during co-flow is lower – Equation 27. In multi-component liquid systems, the resultant viscosities are known to be a function of composition, pressure, and temperature, and as a consequence, the density of the resulting liquid phase. For GXL systems where liquid phases are saturated with dissolved CO₂, the resultant viscosity is in between that of pure organic solvent and CO₂. Thus, the decrease in viscosity during co-flow is attributed to the formation of a gas-expanded liquid.(132) Thus, we confirm the formation of a gas-expanded liquid on-board the micromixer. The ratio of the viscosities of DMF and gas-expanded DMF (GXL) can be estimated as:

$$\frac{\mu_{GXL}}{\mu_{DMF}} = \frac{Q_{DMF}}{Q_{GXL}} = \frac{\rho_{GXL} F_{DMF}}{\rho_{DMF} F_{GXL}} \quad 27$$

When using the average flow rates, the above ratio is 0.33 for the T-mixer and 0.62 for the X-mixer. The relative viscosity of CO₂-expanded acetone (with a relative polarity similar to DMF) at these mole fractions is 0.40 and 0.67.(233) This closeness validates the estimated μ_{GXL} .

The mole fraction of the antisolvent, x_{CO_2} , was estimated using the experimentally measured volumetric flow rates of drug solution, Q_{DMF} , and carbon dioxide, Q_{CO_2} , and assuming complete mixing at the molecular level:(234)

$$x_{CO_2} = \frac{\left(\frac{F_{CO_2}}{M_{CO_2}}\right)}{\left(\frac{F_{DMF}}{M_{DMF}}\right) + \left(\frac{F_{CO_2}}{M_{CO_2}}\right)} \quad 28$$

In this equation, M_{DMF} and M_{CO_2} are the respective molecular weights. The solutions of GF in DMF were dilute (7.5% or less of the solubility of GF in DMF at 25 °C) and there was no significant difference between solutions and neat DMF.

For both micromixers, the mole fraction of CO₂ was independent of the driving pressure - Figure 48b. The average values were $x_{CO_2} = 0.79 \pm 0.05$ for the T-junction mixer and $x_{CO_2} = 0.44 \pm 0.04$ for the X-junction mixer. This difference reflects the geometric fact that, one wide channel feeds solution in the first case while two side channels of similar cross-section provide about twice as much solution in the second case - Figure 44.

The residence time, τ , was estimated as

$$\tau = \frac{LA}{Q} \quad 29$$

Where L and A are the length and cross-sectional area of the hydraulic section considered.

Because of the different cross-sectional area, the residence time in the micromixer, τ_1 , was much shorter than the residence time in the stainless-steel tubing connecting the micromixer to the discharge vessel, τ_2 . Both residence times decreased with driving pressure - Figure 48c. The residence times within the micromixers were 10-20 ms (T-mixer) and 20-40 ms (X-mixer). The residence times estimated for the tubing connecting the micromixer to the discharge vessel were about three orders of magnitude longer: 30-40 s (T-mixer) and 20-30 s (X-mixer).

The general procedure for the micronization experiments has been explained in section 2.8. The size of precipitated Griseofulvin (GF) particles using the T and X micromixers are shown in Figure 49. In the absence of carbon dioxide, the API solution reaches the discharge vessel (partially filled with water) and GF precipitates as its water solubility is low (9.6 mg/L at 25 °C(235)). The average particle size is (390 ± 20) nm and independent of driving pressure (horizontal lines in Figure 49). A benchtop experiment was performed by mixing 5 ml of 0.5% GF solution with 5 ml water under constant stirring followed by size analysis using DLS (open diamond symbol in Figure 49). This value indicates that this particle size is entirely due to water acting as antisolvent once the API solution reaches the discharge vessel (D in Figure 39).

The introduction of gaseous carbon dioxide in the system clearly affects precipitation and leads to larger particles. When the T-junction microfluidic mixer is used, particle size varies between 0.4 and 100 μm - Figure 49a. When the X-junction microfluidic mixer is used, particle size varies between 0.9 and 500 μm - Figure 49b. The overall conclusion is that particle size increases with API concentration, c_{GF} , and declines with increasing driving pressure, ΔP .

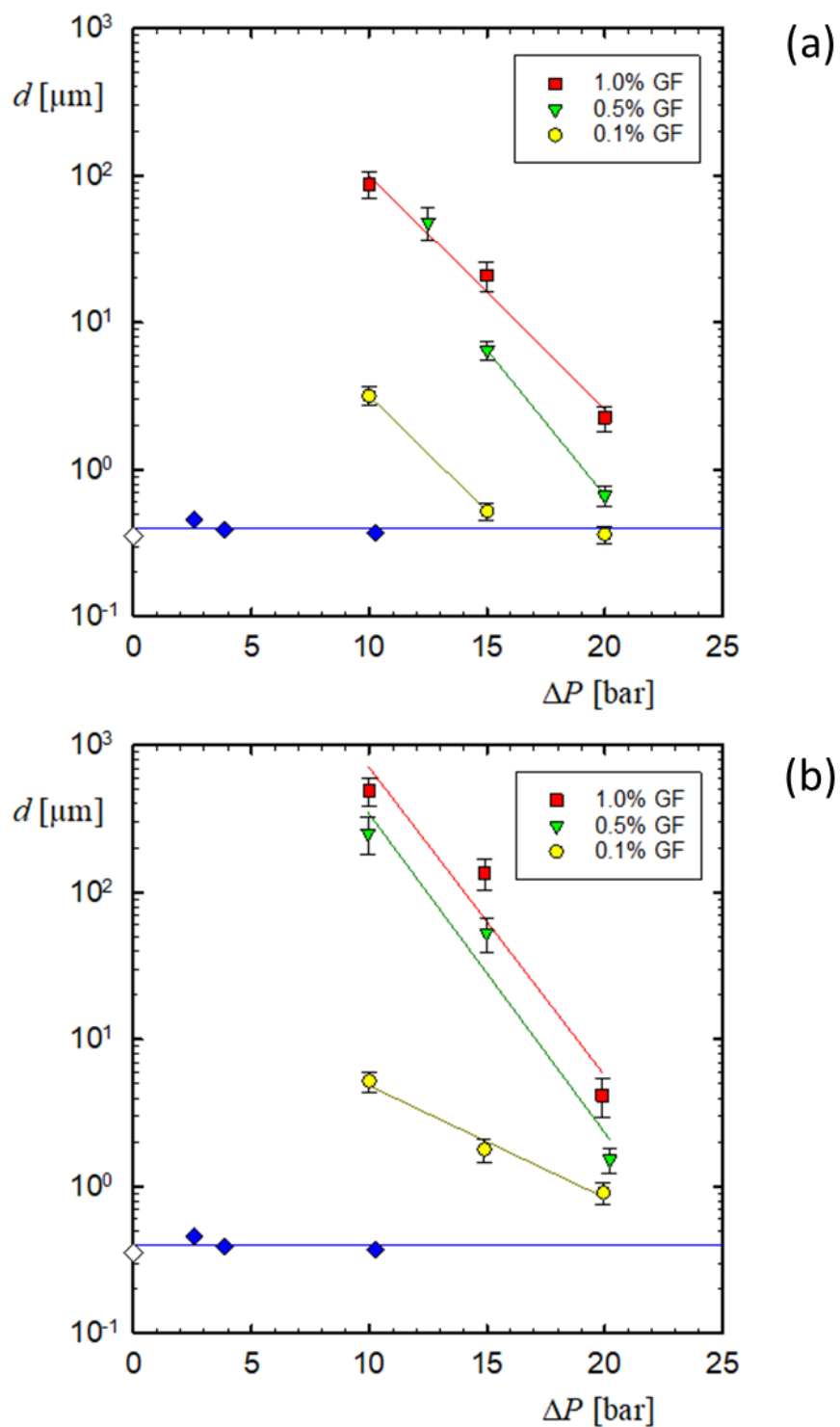


Figure 49. Particle size, d , as a function of driving pressure, ΔP , when using a: (a) T-junction microfluidic mixer, (b) X-junction micromixer. Concentration of Griseofulvin in DMF: (○) 0.1%, (▽) 0.5%, and (□) 1.0%. The horizontal baseline (◆) and the benchtop precipitation (◇) shows the particle size obtained under the same conditions without using any CO_2 .

The initial API concentration is a key parameter in the controlled precipitation of drug particles. The reports on the role of the initial concentration are contradictory. By using fractional factorial design to study the precipitation of ampicillin particles from N-methyl-2-pyrrolidone (NMP) using CO₂, the importance of concentration was ranked higher than that of temperature and nozzle diameter.(235) However, the direction in which particle size changes is unclear. Many studies report a decrease in particle size with increasing solute concentration. For instance, p-hydroxybenzoic acid precipitated from dichloromethane using CO₂,(236) salbutamol precipitated from dimethyl sulfoxide (DMSO) using scCO₂,(237) salicylamide from acetone using scCO₂,(238) theophylline precipitated from ethanol using scCO₂,(239) PVP-corticosteroids co-precipitated from ethanol using scCO₂,(240) and Griseofulvin particles precipitated from acetone using water.(241) A qualitative explanation is cast in terms of the classic crystallization theory. Upon antisolvent addition, a more concentrated solution reaches higher levels of supersaturation in comparison to a dilute solution. Because of that, under equal conditions, higher nucleation rates occur. This in turn implies that a larger number of smaller particles will precipitate from the more concentrated solution.(236) At the same time, an increase of particle size with the concentration of the initial solution has been reported in multiple instances of antisolvent precipitation. For example, the precipitation of amoxicillin particles from NMP(242) or DMSO(243) using scCO₂, Cefonicid particles from DMSO using scCO₂,(244) nicotinic acid from methanol(245) using scCO₂, and beclomethasone-17,21-dipropionate from acetone using subcritical CO₂.(246) The apparent contradiction between these two opposite trends demonstrates that the details of mixing cannot be ignored.

As soon as DMF and carbon dioxide meet at the junction they rapidly mix to form a gas-expanded liquid (GXL) – Figure 50. Because of the complete miscibility a real interface is not formed but due to the refractive index difference, the boundary between the phases can be traced along the mixing channel.(247)

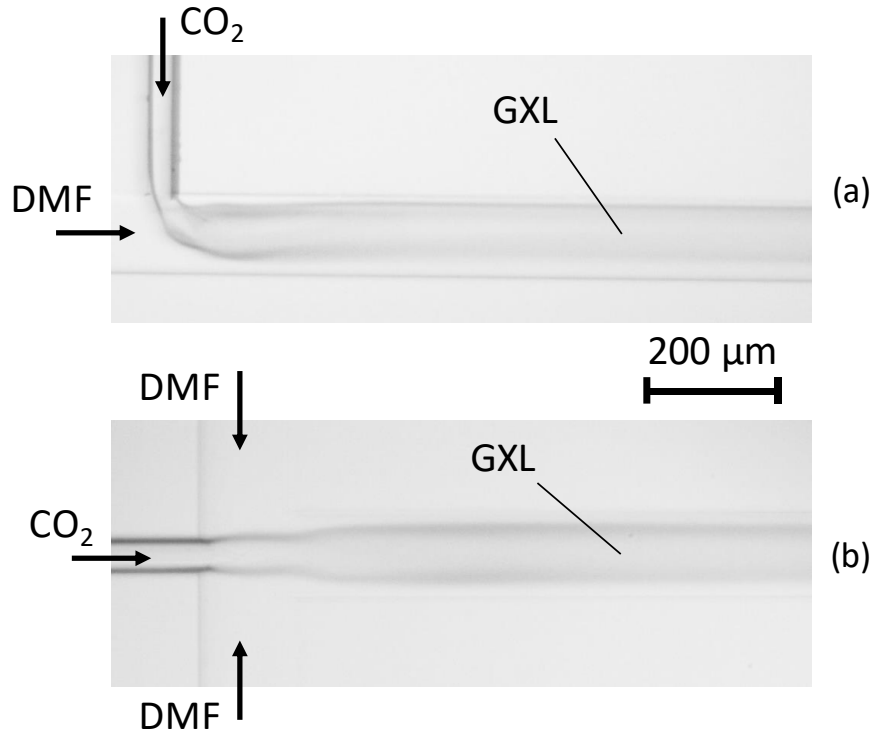


Figure 50. Mixing of DMF and CO₂ ($P_{\text{CO}_2} = 40$ bar, $P_{\text{DMF}} = 40$ bar, $\Delta P = 15$ bar, $c_{\text{GF}} = 0.1\%$) to form a gas-expanded DMF (GXL) when contacting in a (a) T-junction micromixer, and (b) X-junction micromixer.

A mixing length, L_{mix} , i.e. the distance from the junction to the point where the border between DMF solution and CO₂ fades away completely, was determined via optical observations. The results for a T-junction mixer are shown in Figure 51. The mixing length is (5.3 ± 0.5) mm and it is independent of driving pressure and also the pressure at which the gas and liquids are supplied (40, 50 and 60 bar). It is also very short compared to the post-junction length of the mixing channel (45 mm).

An order of magnitude estimate for the time needed to achieve mixing by diffusion only, τ_D , can be obtained by using a length $w_D = 40$ μm (width of the channel occupied by DMF) and a diffusion coefficient of CO₂ in DMF, $D = 3.6 \times 10^{-9}$ m²/s (25 °C)(248), as:

$$\tau_D = \frac{w_D^2}{4D} \approx 110 \text{ ms} \quad 30$$

This is 3-4 times longer than the estimated residence time within the microchannel, τ_1 , and therefore full mixing under laminar conditions would not be realised on board the

micromixer. The mixing we observed is much faster and we speculate that the enhancement is due to the CO₂ arriving at the junction of the micromixer at turbulent Reynolds numbers (6000-8000). We conclude that mixing is very efficient, happens within about 5 mm of the junction, and is not affected by driving pressure - Figure 51. Therefore, the differences in particle size are modulated by the crystal growth conditions.

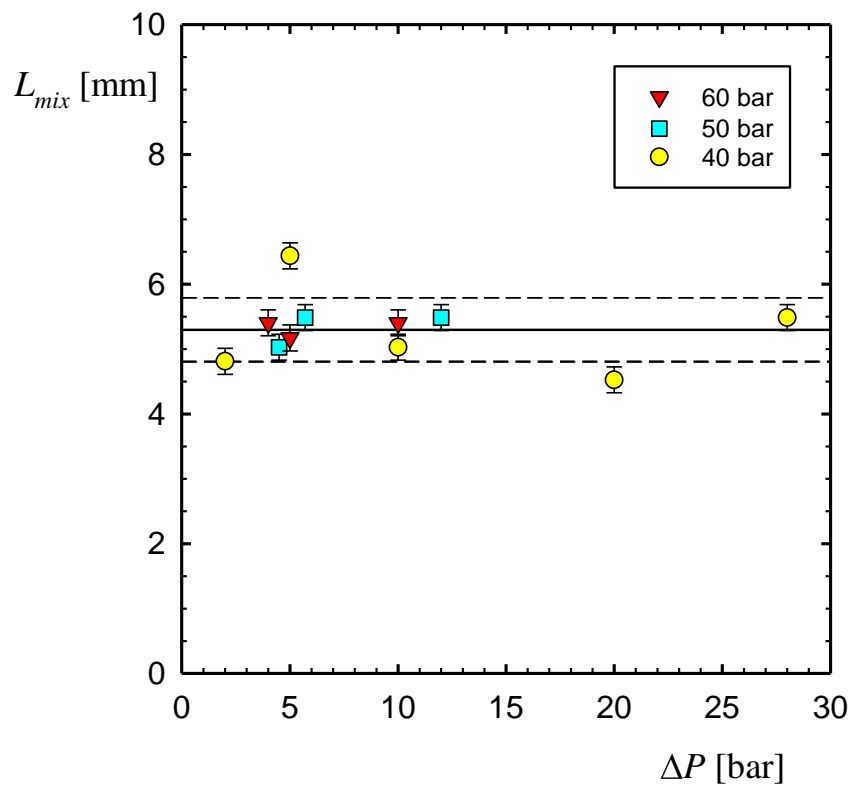


Figure 51. Mixing length, L_{mix} , inside a T-junction micromixer for DMF and CO₂ (supplied at 40, 50 and 60 bar) as a function of driving pressure, ΔP .

For any given GF concentration, increasing driving pressure decreases the time spent by the mixture in the system and smaller particles are produced. This is the experimental trend observed at all c_{GF} for both micromixers - Figure 49.

The decrease of particle size with driving pressure is presented in Figure 52a by the slope (rate of decrease), b ($= -\Delta \ln d / \Delta P$), as a function of c_{GF} . The values of b are practically the same for the two types of micromixers and the influence of c_{GF} is seen at lower concentrations only.

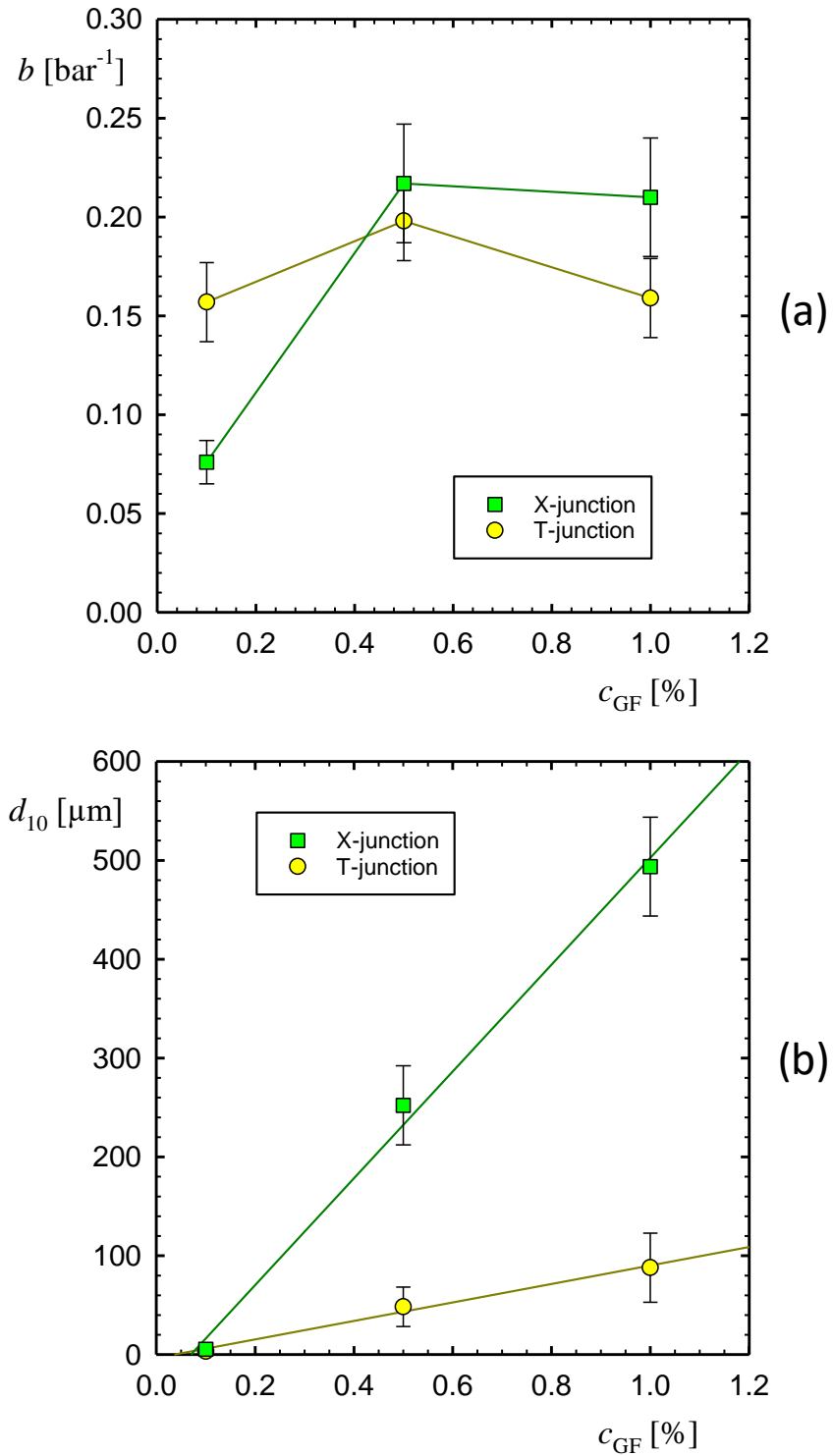


Figure 52. (a) Rate of decrease of particle size with respect to driving pressure, b ($= -d \ln d / d \Delta P$), as a function of the concentration of Griseofulvin in DMF, c_{GF} : (\square) X-junction micromixer, and (\circ) T-junction micromixer. (b) Size of particles produced at $\Delta P = 10$ bar, d_{10} , as a function of the concentration of Griseofulvin in DMF, c_{GF} : (\square) X-junction mixer, and (\circ) T-junction mixer.

On the other hand, particle size increases with GF concentration – Figure 49. Under fixed dynamic conditions, the particle size obtained at 10 bar driving pressure, d_{10} , increases linearly with the concentration, c_{GF} , and the dependence is steeper for the X-junction mixer - Figure 52b. We hypothesize that while mixing and nucleation occur within the micromixer, crystal growth occurs over the much longer time the particles take to reach the discharge vessel - Figure 48c. Given that at fixed driving pressure the GF particles spend the same time in the precipitation system, according to Equation 10 with all other parameters constant, their final size should be directly proportional to the bulk concentration of API as observed experimentally – Figure 52b. Because of the lower antisolvent-to-solution ratio (lower x_{CO_2}) realized in the X-junction mixer, crystal growth is faster and leads to significantly larger particles.

Griseofulvin particles precipitated using gas antisolvent techniques are often needle-shaped.(249, 250) Octahedral (bipyramidal) crystals were obtained by introducing a polymeric growth inhibitor.(251) Alternatively, Carr et al.(252) produced bipyramidal particles without using inhibitors by precipitation from superheated water (i.e. using cooling crystallization). Fully shaped crystals were obtained only when the concentration of the initial solution was sufficiently high otherwise some of the octahedra were hollow. A recent exploration of liquid antisolvent precipitation suggested that the octahedral crystal shape of Griseofulvin is formed by the fusion of smaller particles and it is the equilibrium one - Figure 53.(253)

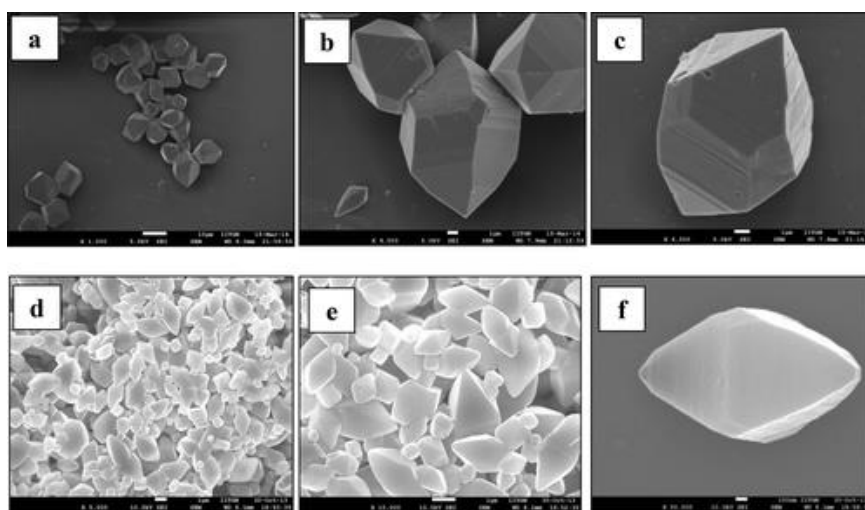


Figure 53. SEM micrographs of griseofulvin particles precipitated without any additive: (a–c) without ultrasound, (d–f) with ultrasound.(253)

This morphology could be achieved without any additive when using ultrasound-enhanced micromixing. Several examples of micronized Griseofulvin particles are shown in Figure 54.

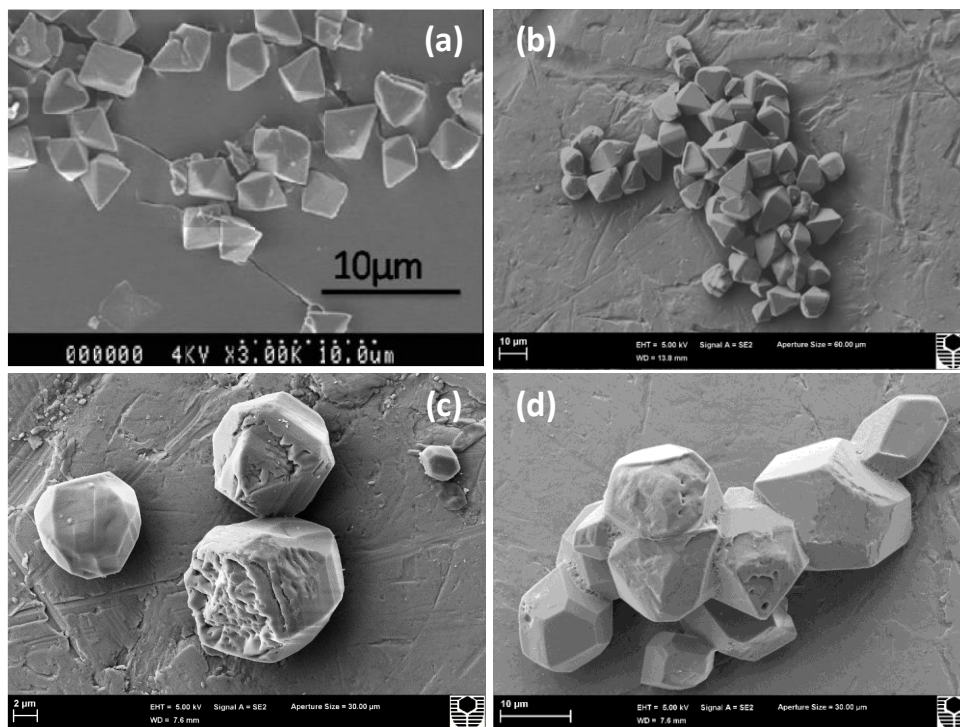


Figure 54. SEM images of Griseofulvin particles. (a) Obtained by precipitation from subcritical water (170 °C, 20 bar)(252). Obtained by precipitation from DMF using microfluidic gas antisolvent precipitation ($P_{CO_2} = 40$ bar, $P_{soln} = 40$ bar, $\Delta P = 20$ bar, $c_{GF} = 0.5\%$) using: (b) a T-junction micromixer and $\Delta P = 20$ bar, (c) a T-junction micromixer and $\Delta P = 10$ bar, and (d) an X-junction micromixer and $\Delta P = 20$ bar.

The characteristic bipyramidal crystals obtained by cooling crystallization from saturated subcritical water solutions(252) are shown in Figure 54a. Their formation was attributed to the uniform growth of different crystal faces made possible by fast mixing ensuring homogenous heat and mass transfer. Crystals of the same habit were produced in this work by precipitation from DMF ($c_{GF} = 0.5\%$) using the T-junction and a driving pressure of 20 bar - Figure 54b. The relatively high driving pressure ensured fast and homogeneous mixing within the microchannel. When using a lower driving pressure (10 bar), under the same conditions, the crystal shape of the particles appeared underdeveloped - Figure 54c. When the T-mixer was replaced with an X-

mixer (lower antisolvent-to-solvent ratio) the particles were larger (Figure 52 a), their morphology was less well defined and some crystal interpenetration was observed (Figure 54d).

3.4 Conclusions

A reliable high-pressure microfluidic system was assembled combining standard and bespoke components. Precipitation of Griseofulvin from DMF using gaseous CO₂ as antisolvent (25 °C, 40 bar) was performed with two different micromixers. Particle size was varied between 0.5 and 500 µm. Higher concentrations of Griseofulvin and lower driving pressures lead to the formation of larger particles. Gas-liquid mixing, i.e. the formation of a gas-expanded liquid, was completed within the micromixers, while crystal growth continued in the outlet tubing. The main difference between the two micromixers was the antisolvent-to-feed ratio. This high-pressure microfluidic platform is suitable for the micronization of APIs. More broadly, this work paves the way to transferring dense gas processes onto a flexible microfluidic platform and combining them with synthesis, purification, online characterization, and encapsulation of pharmaceutical compounds.

Chapter 4

Influence of API-Solvent Pair Interactions on the Micro-precipitation Process

4.1 Introduction

A key requirement for a therapeutic agent is to achieve a sufficiently high concentration in the physiological fluid. Thus, the dissolution of APIs is of crucial importance and particle engineering aims at improving it. After validating our high-pressure microfluidic platform for on-chip formation of a gas-expanded liquid and API precipitation (Chapter 3(254)), we now explore the chemical specificity of the microprecipitation process by varying the solvent and the API.

First, we crystallize the model API, Griseofulvin, from three different solvents namely DMF, acetone and ethyl acetate. This is done to investigate the role of solvent in the precipitation process, specifically its rate of expansion in contact with pressurized CO₂. Second, we crystallize three different APIs, Griseofulvin, Luteolin and Budesonide, from a common solvent (DMF). The chemical nature of the API which is defined by its molecular structure plays a significant role in determining the morphology and size of the precipitated crystals. By studying the microprecipitation of different API-solvent pairs we demonstrate that our approach allows for efficient crystal size and morphology manipulation. In this work the microprecipitation process is controlled through the driving pressure applied along an X-junction (X1) micromixer. We generate a wide range of crystal sizes ranging from 0.1 – 100 μm and various particle morphologies – from interconnected clumps of spherical particles to purely organic nanoflowers without using any additives.

4.2 Results and Discussion

The schematic for the glass micromixer design, X1, used in this work is shown in Figure 47b. The API solution is fed through the two side channels and dense-phase CO₂ is supplied through the channel at the centre. The input pressures for the gas and

liquid are kept the same (fixed $P = 40$ bar at 25 °C). The experimental rig described in section 2.7 is used for the micronization experiments.

For each micronization experiment, collection is performed for 15 minutes in a metal vessel filled partially with water. The HPLC pumps are rinsed with a suitable solvent for 3-5 times when switching between different API-solvent pairs. Figure 55 shows a depiction of the microprecipitation process.

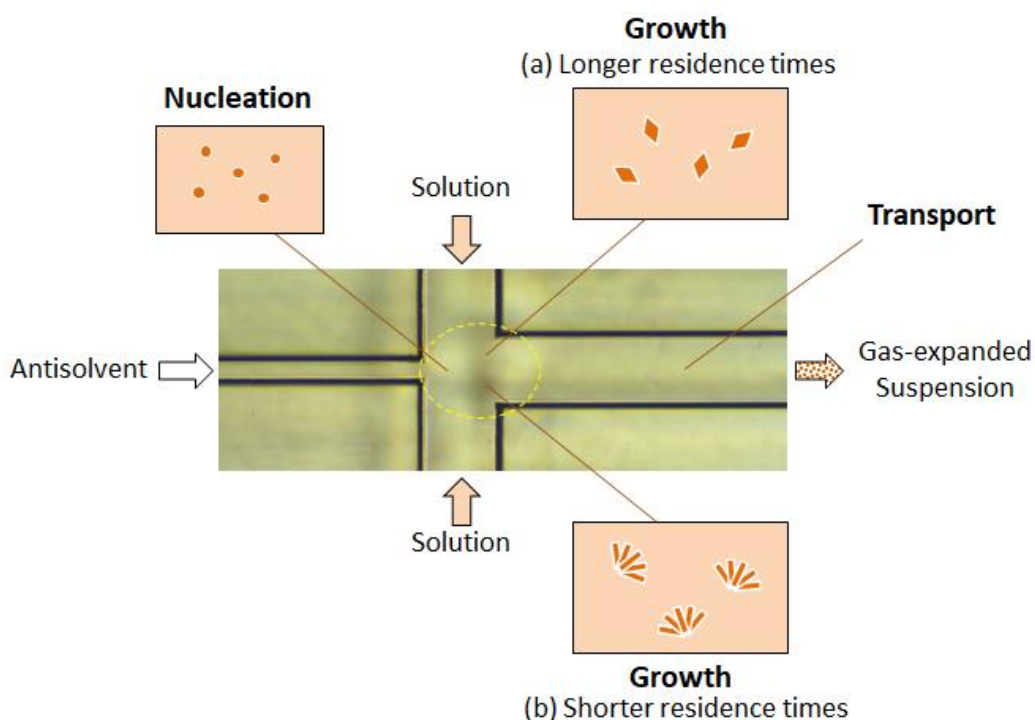


Figure 55. Schematic for the micro-GAS process.

The API solution and dense phase CO_2 meet at the junction and upon contact undergo mixing based on the CO_2 properties (density, viscosity). Beyond a certain expansion, the system reaches a state of supersaturation. This supersaturation triggers precipitation of the API particles from the solution. Depending on the process conditions, different particle sizes and shapes can be produced. The API suspension flows through the system and is collected in water for particle analysis. The precipitated crystals are characterized using DLS and SEM measurements to investigate the influence on crystal size and morphology.

Solvent Expansion

In the first instance, we precipitate the model API, Griseofulvin, from three different solvents. The input pressures for the fluids are kept the same (fixed at 40 bar and 25 °C) and the back pressure is varied to tune the driving pressure, ΔP . We map the corresponding volumetric flow rates, Q , for each of these solvents at different values of ΔP and compare them - Figure 56.

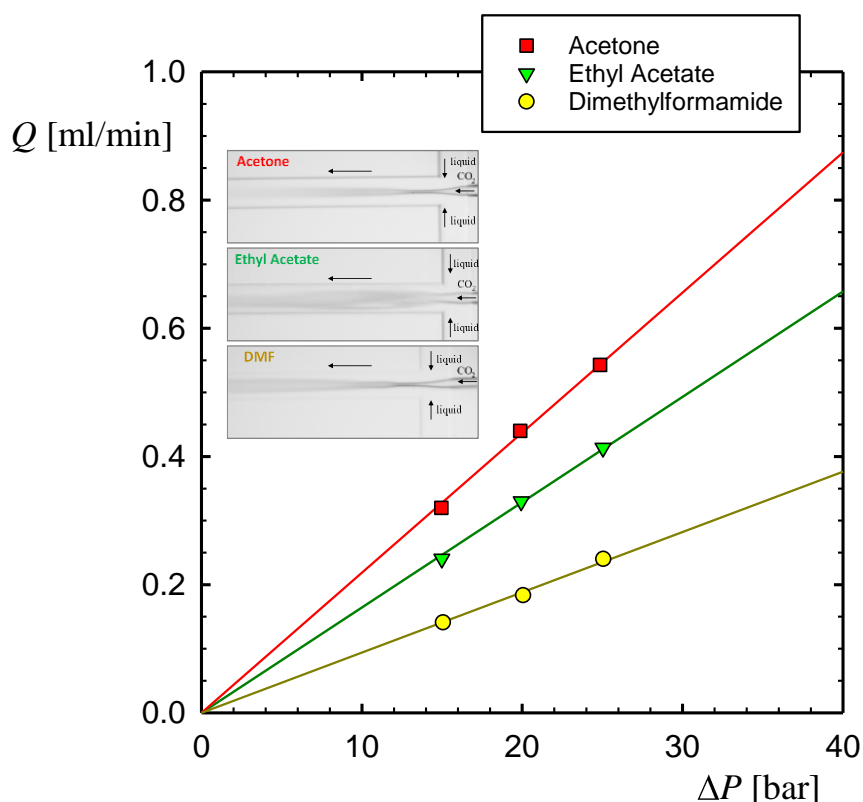


Figure 56. Volumetric flow rate, Q vs ΔP trends for acetone, ethyl acetate and DMF at 25 °C. The error bars are within the symbol size.

The magnitude of the volumetric flow rate for the three solvents decreases in the order: Acetone > Ethyl Acetate > DMF. The slope of the lines in this graph gives the inverse of the hydraulic resistance (Equation 24) experienced by the individual solvents when flowing through the same X1 mixer.

The slopes are different under the same experimental conditions and can be attributed to the different solvent viscosities - Figure 57. Since the same X1 mixer has been used

for all experiments, therefore the geometric factor ($\frac{8l}{\pi r^4}$) is fixed in each experiment. The inverse proportionality between the flow rates and viscosity should give higher values of Q for the least viscous solvent and lower values of Q for the most viscous solvent. This is why DMF, being the most viscous (0.928 cP)(216), has the smallest slope whereas acetone, being the least viscous (0.301 cP)(217), has the largest slope. The viscosity for ethyl acetate (0.426 cP)(218) is intermediate between that of acetone and DMF as is reflected in the corresponding volumetric flow rates.

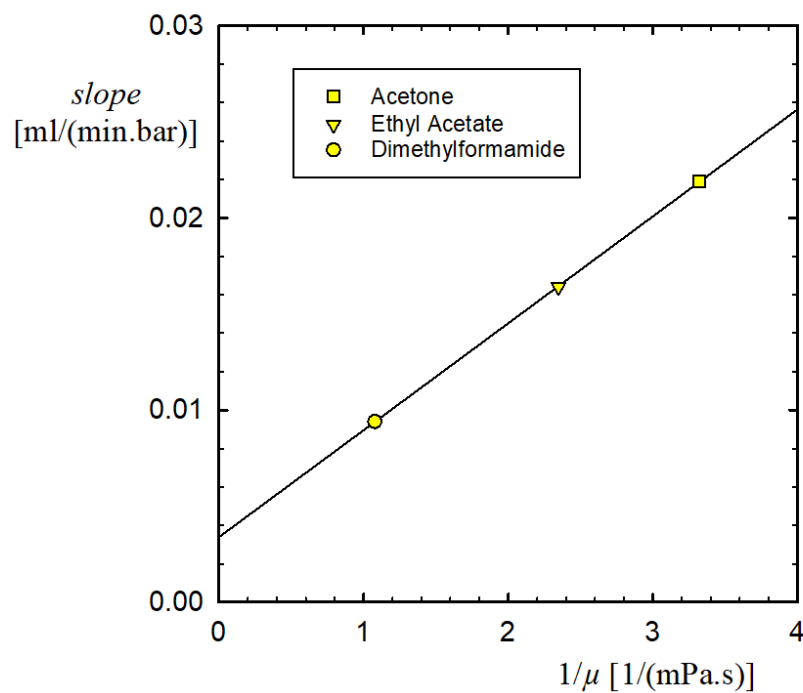


Figure 57. Slope as a function of inverse of solvent viscosity (μ). The slope error is within the symbol size.

The flow in the mixing channel of the micromixer is laminar but the CO₂ gas arriving at the junction is at much higher Re (2,500-12,000) (similar to chapter 3(254)) indicating turbulent behaviour. Thus, mixing is intense at the junction but turbulence is quickly suppressed and the complete mixing of the gas-rich and liquid-rich phases happens further along the mixing channel. This gradual mixing can be followed visually (Figure 58) and we measured the distances downstream from the junction at which optical homogeneity was attained.

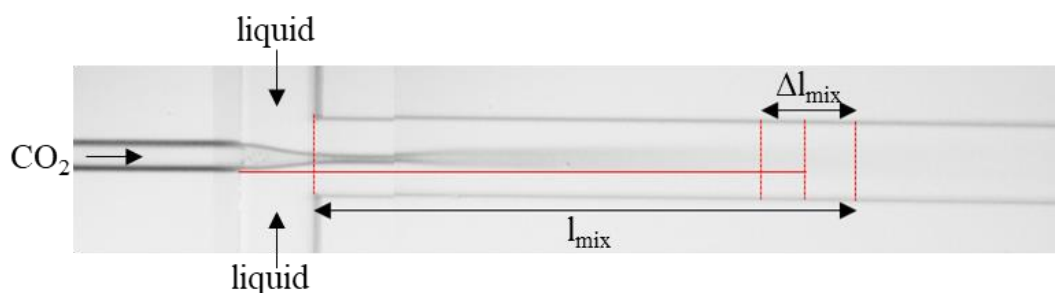


Figure 58. Mixing length for CO₂-acetone flow in the X-junction micromixer.

These mixing lengths, L_{mix} , are shown in Figure 59. They are about 10 times shorter than the overall length of the mixing channel (45 mm), confirming that under driving pressure of 15-25 bar the micromixer provides very efficient mixing.

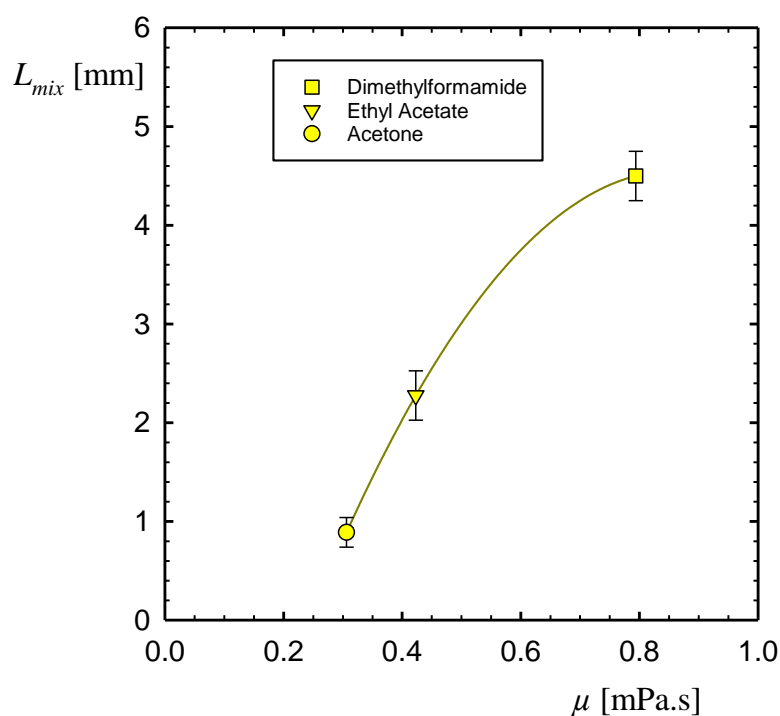


Figure 59. Mixing length (distance between the junction and the point of optical uniformity along the mixing channel), L_{mix} , as a function of solvent viscosity, μ (25 °C, fluid supply pressure is 40 bar). The total length of the mixing channel is 45 mm.

There is a marked increase in L_{mix} with solvent viscosity, μ . Since the flow observed in the mixing channel is laminar, the main mechanism of mixing there is by diffusion

and a higher solvent viscosity would imply a lower rate of diffusion (Equation 21). Under turbulent conditions (such as at the X-junction), mixing time is related to viscosity, μ , density, ρ , and energy dissipation rate per unit mass, ϵ :(255)

$$t_{mix} = 17 \left(\frac{\mu}{\rho \epsilon} \right)^{1/2} \quad 31$$

Therefore, for a more viscous solvent, mixing is less efficient under turbulent flow conditions (within the volume of the junction) and also further delayed by slower diffusion (along the mixing channel).

API Micronization

Taking advantage of this efficient micromixing, we micronize various APIs by varying the speed of mixing through flow conditions and more specifically, the driving pressure, ΔP . The results of microprecipitating Griseofulvin (GF) from three different solvents (DMF, acetone and ethyl acetate) are shown in Figure 60 as mean particle size, d , vs driving pressure applied along the mixing channel, ΔP .

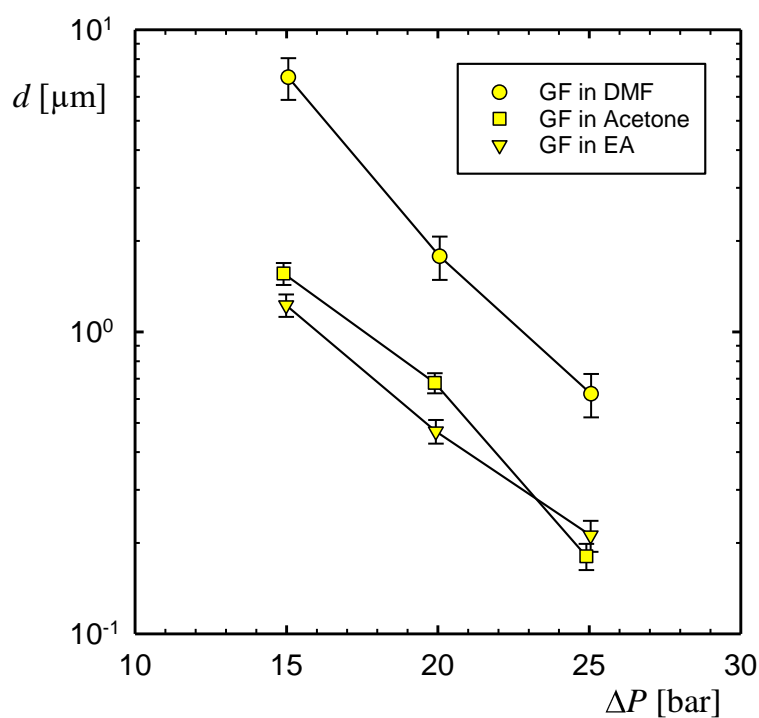


Figure 60. Mean particle size, d , of Griseofulvin particles precipitated from three different solvents at varying driving pressure, ΔP (25 °C, fluid supply pressure is 40 bar).

The mean particle size decreases with driving pressure (as already detailed in chapter 3(254)) and the rate of decrease with ΔP is approximately the same for all three solvents. The solvents are clearly ranked in terms of absolute particle size obtained under identical flow conditions as DMF > acetone > ethyl acetate. The size of the micronized particles can be understood in terms of the classical crystallization theory by considering the achieved supersaturation and the rate of reaching this supersaturation.

Supersaturation (the thermodynamic driving force for crystallization) is usually defined as the logarithm of the saturation ratio, S (Equation 4). We rewrite this ratio using the initial API concentration, c_1 , the initial volume of solvent/solution, V_1 , and the final volume of gas-expanded mixture, V_2 :

$$S = \frac{c}{c_E} = \frac{V_1 c_1}{V_2 c_E} \quad 32$$

Under fixed flow conditions, when allowing the solvent solution to expand from V_1 (dilute solution of API) to V_2 (gas-expanded liquid containing the API), a different S would be achieved unless the ratio c_1/c_E is kept fixed. For that reason, in the experiments shown in Figure 60 the initial API concentration was maintained at 4% of the Griseofulvin solubility (equilibrium saturated concentration) in the respective solvent. Thus, by keeping both V_1/V_2 and c_1/c_E ratios constant we achieved approximately the same supersaturation of Griseofulvin in the three different solvents. Therefore, particle size variation correlates with the solvent used (Figure 60) and must be related to its inherent properties.

The antisolvent action of CO_2 is due to its spontaneous mixing with the solvent and the sharp decrease in solvent power. The solvent is compatible with CO_2 and as its initial volume expands, its mole fraction decreases and so does the solvent power.(132) It is therefore meaningful to quantify the compatibility of the solvent- CO_2 pairs. All three solvents are fully miscible with CO_2 . The progress of their gas expansion is customarily characterized with the volumetric expansion, ε ($= (V_2 - V_1)/V_1$), versus equilibrium pressure, P , curves – Figure 61.

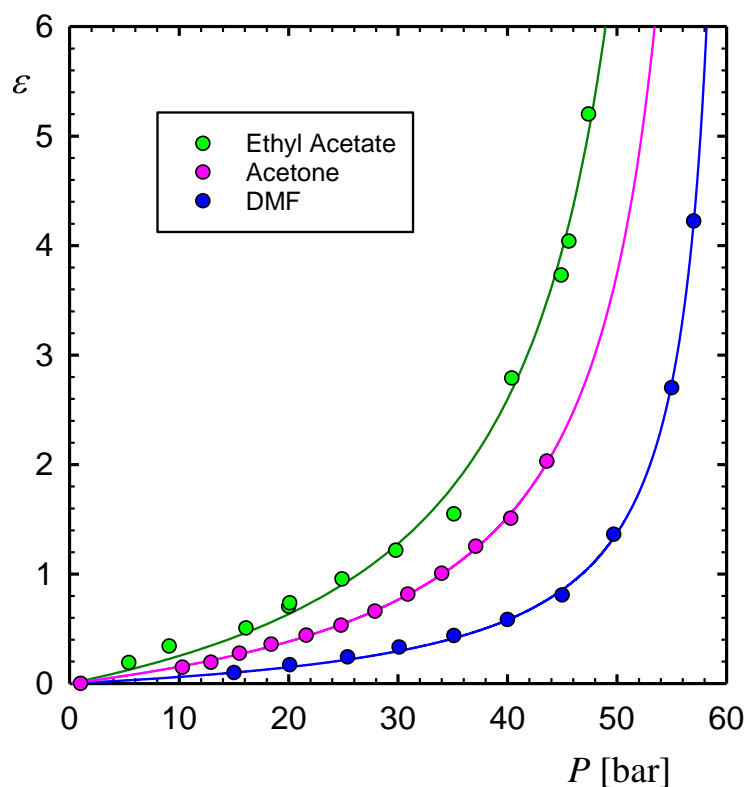


Figure 61. Volumetric expansion, ε , vs. equilibrium pressure, P (25 °C). EA and DMF data are from reference. (232) Acetone data are from reference.(233)

The data follow the same trend for all three solvents. The smooth curves were obtained by fitting the empirical equation $\varepsilon^{-1} = a + bP^{-1}$ (with a and b as free parameters), which can be seen as a truncated cubic equation of state. The differences are evident at any pressure and rank the solvents by their affinity to CO_2 as ethyl acetate > acetone > DMF. This solvent sequence corresponds to the solvent order defined by mean particle size - Figure 60.

We reason that because a solvent with a higher affinity to CO_2 expands further (i.e. to a larger equilibrium ε at any given pressure – Figure 61) it is also going to expand faster under dynamic conditions. With such a solvent, the critical supersaturation state is reached faster. Nucleation is triggered earlier and the distribution of the generated nuclei is more spatially uniform. The larger number of nuclei and the equal conditions for initial growth are likely to promote the formation of smaller particles. In other words, the equilibrium solvent expansion scale (Figure 61) correlates negatively with the average size of microprecipitated particles (Figure 60).

Expansion curves (ϵ vs. P) have been published for many solvent-gas combinations at various temperatures but it is worthwhile to link solvent expansion behaviour to an established quantitative scale. We rationalize the affinity of organic solvents towards CO_2 by considering their Hansen solubility parameters – Table 9.

Table 9. Hansen solubility parameters (256) and octanol-water partition coefficients (257) of the solvents used in this study. EA = ethyl acetate; DMF = dimethylformamide; δ = (total) solubility parameter (δ_D – dispersion component, δ_P – polar component, δ_H – hydrogen bonding component), $\log P$ = $\log(\text{octanol-water partition coefficient})$.

Solvent	δ_D [MPa ^{1/2}]	δ_P [MPa ^{1/2}]	δ_H [MPa ^{1/2}]	δ [MPa ^{1/2}]	$\log P$
EA	15.8	5.3	7.2	18.1	0.73
Acetone	15.5	10.4	7.0	20.0	-0.24
DMF	17.4	13.7	11.3	24.8	-1.01

The total solubility parameter, δ , is composed of three components reflecting various physical contributions to the cohesive energy of the liquid (D – dispersion forces, P – polar interactions, and H – hydrogen bonding) – Equation 12.(258) The compatibility of two solvents (1 and 2) is measured by the distance, R_a , between δ_1 and δ_2 taken as 3D vectors in the DPH space – Equation 13. Hence, a shorter Hansen distance between a solvent and CO_2 implies better compatibility and therefore larger expansion. This is exactly what we observe in Figure 62. Thus, the affinity for mixing with CO_2 and therefore rate of expansion can be predicted by using Hansen solubility parameters when considering solvents for use in the microprecipitation of APIs. Dielectric constant is often taken as a simple measure of the polarity of a solvent.(259) The three solvents used here are ranked identically by their Hansen distance from CO_2 , R_a , and their dielectric constant, ϵ_r . However, R_a and ϵ_r do not always correlate and, more broadly, the dielectric constant is not a good indicator of a solvent's polarity.(260) Hansen parameters, on the other hand, are established on thermodynamic grounds, reliably measured and useful compilations are available in the literature.(258, 261) Since CO_2 is essentially apolar, solvents which are more hydrophobic show higher

compatibility. The above ranking clearly follows the decrease in hydrophobicity (ethyl acetate > acetone > DMF) which can be represented by the octanol-water partition coefficient, logP (a popular measure of molecular hydrophobicity(262), Table 9).

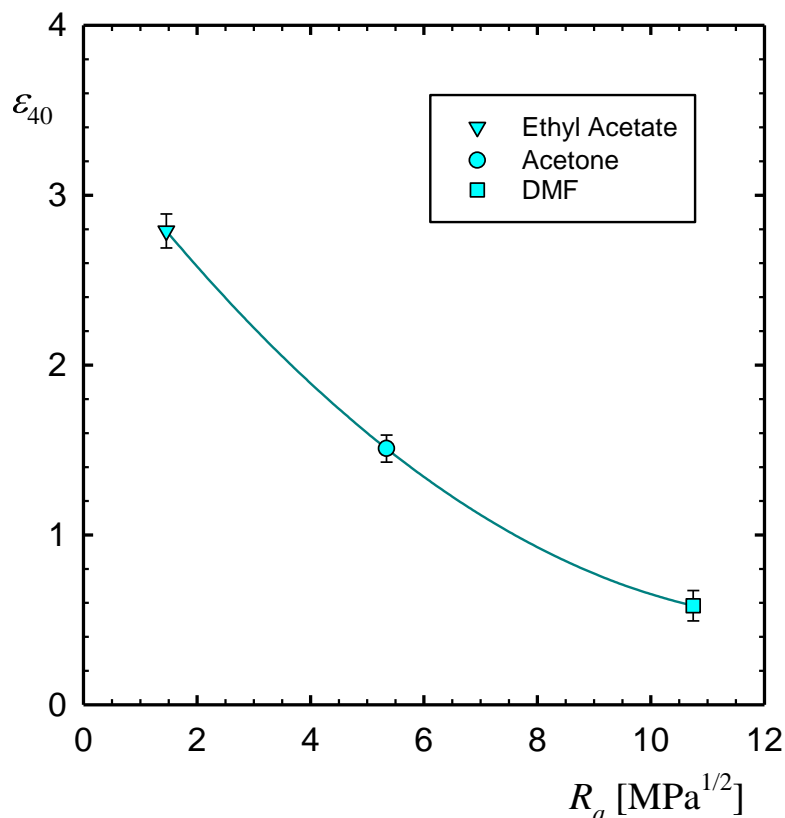


Figure 62. Relative volumetric expansion at 40 bar, ϵ_{40} (25 °C), as a function of the Hansen distance, R_a .

These values reflect the molecular distribution of a substance between water (polar) and octanol (apolar) phases and thus reflect the hydrophobicity of the molecule.(262) It is used as a guideline for predicting the compound's solubility characteristics in other aqueous and organic solvents. For instance, a compound that has a logP value of 1 indicates a 10:1 concentration ratio in an organic to aqueous phase. This implies that the compound is hydrophobic and will thus dissolve in an organic solvent. Whereas a logP value of -1 (such as in the case for DMF) indicates a 1:10 concentration ratio in an organic to aqueous phase thus implying that the compound will be soluble in an aqueous medium.

We now turn to the microprecipitation of different APIs from the same solvent. The mean particle size, d , of Luteolin (LT), Griseofulvin (GF) and Budesonide (BD) particles precipitated from DMF with CO₂ as antisolvent is shown in Figure 63. The size depends strongly on the API but its decline with driving pressure is about the same.

As the solvent is the same and flow conditions are identical, the above size variation must be due to molecular differences between the three APIs. Once again, we invoke crystallization theory. Accordingly, the rate of nucleation, J , is given by:(263)

$$\ln \frac{J}{J_0} = -\frac{16\pi\gamma_{SL}^3 V_M^2}{3(k_B T)^3 (\ln S)^2} = -\frac{A}{(\ln S)^2} \quad 33$$

In this expression γ_{SL} is the interfacial free energy of the solid-liquid (nucleus-solution) interface, V_M , is the molecular volume of the API, k_B is the Boltzmann constant, T is the absolute temperature, and S is the saturation ratio. The prefactor J_0 is a kinetic parameter related to the frequency of molecular collisions. The factor A is a thermodynamic factor related to the free energy barrier to nucleus formation.(263)

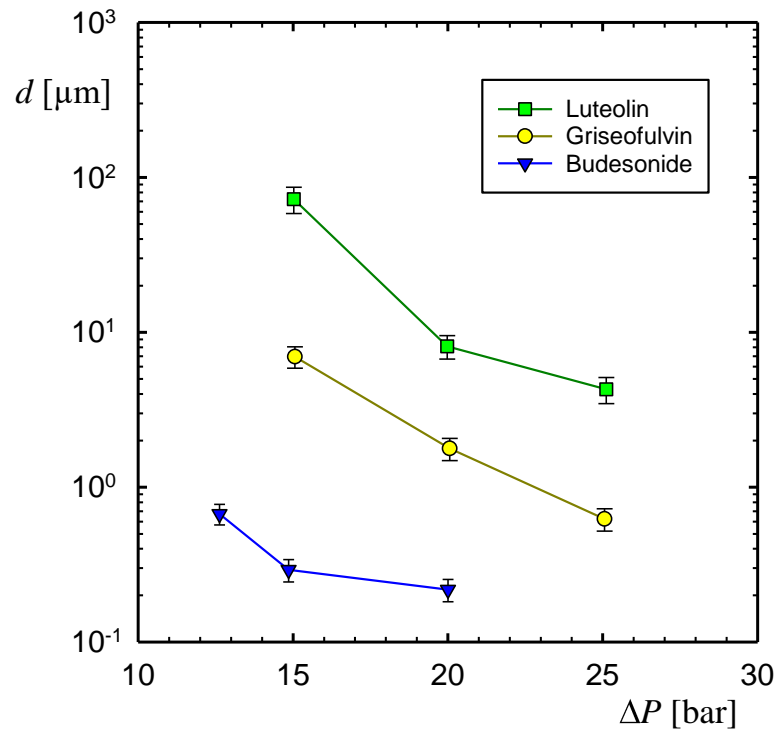


Figure 63. Mean particle size, d , of Luteolin, Griseofulvin and Budesonide particles precipitated from DMF at varying driving pressure, ΔP (25 °C).

It appears from Equation 33 that the significant differences between the three compounds seen in Figure 63 must be related to the interfacial free energy and molecular volume. The data for the APIs used in this study is listed in Table 10.

Table 10. Thermophysical parameters of the APIs used in this study. LT = Luteolin; GF = Griseofulvin; BD = Budesonide; M = molecular mass; ρ = density; V_M = molecular volume (calculated as M/ρ); γ_{SL} = interfacial free energy (obtained from contact angle measurements); δ = solubility parameter.(261, 264-266)

API	M [g/mol]	ρ [g/cm ³]	V_M [Å ³]	γ_{SL} [mJ/m ²]	logP
LT	286.2	1.3885	342	n/a	2.5
GF	352.8	1.3081	448	49.5	2.2
BD	430.5	1.1088	645	53.7	1.9

The molecular volume, V_M , is approximately proportional to the molecular mass, M. This makes sense given that these molecules are not particularly dissimilar, either structurally or compositionally. The interfacial free energy of the solid-liquid interface, γ_{SL} , increases with molecular mass. We compare only values obtained from contact angle measurements as other methodologies yield different numerical values and this discrepancy has not been resolved. Unfortunately, we could not source a literature value for Luteolin. In order to confirm the decrease in hydrophobicity (i.e. increase in interfacial free energy) with molecular mass we use the logP of the APIs. It is clear from these three parameters, plotted in Figure 64, that both V_M and γ_{SL} increase with molecular mass, while logP decreases, in the sequence: LT < GF < BD.

While the ranking of the APIs correlates with the ranking seen in Figure 63, the nucleation rate argument actually predicts the opposite trend in particle size. Therefore, we consider the importance of the intimately related process of crystal growth. Crystal growth occurs immediately after nucleation occurs, the environment around the nuclei is depleted of API molecules and the main mechanism of mass transport is diffusion. In this situation, the crystal growth rate, G ($=dL/dt$, where L is characteristic crystal size and t is time) is given by equation:(267)

$$G = \frac{2D}{\rho_c \lambda} (c - c_{int}) \quad 34$$

In this Equation, D is the diffusion coefficient of the API, ρ_c is the crystal density, λ is the diffusion layer thickness, c is the bulk API concentration, and c_{int} is the API concentration at the crystal-solution interface

Under similar conditions, the growth rate and therefore the final crystal size would be determined by the diffusion coefficient which decreases with molecular size (Stokes-Einstein equation, see Equation 21 in chapter 2). Therefore the results presented in Figure 63 suggest that, under the intense mixing conditions encountered in the micromixer's junction, crystal growth rather than nucleation rate determines the size of the micronized particles. In short, the size of the micronized drug particles decreases as the molecular volume of the API increases.

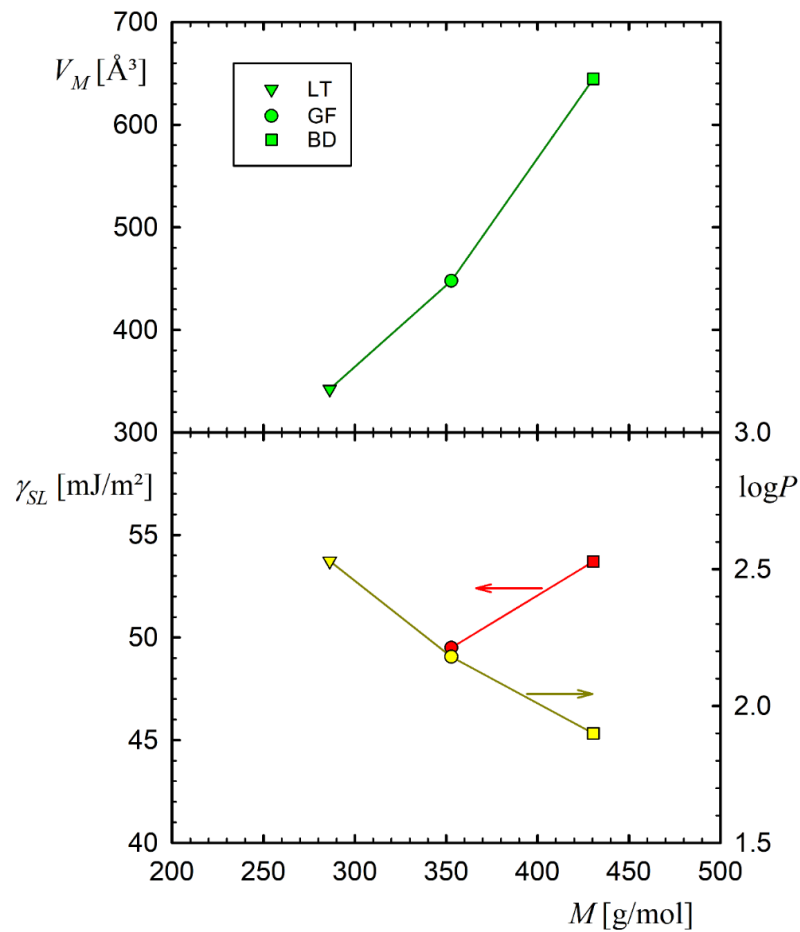


Figure 64. Molecular volume, V_M , solid-liquid free energy, γ_{SL} , and $\log P$ as functions of the API's molecular mass, M . The error bars are within the symbol size.

Particle Morphology

We have examined the variation in crystal morphology with driving pressure in Chapter 3.(254) A higher driving pressure promotes the formation of well-defined bipyramidal crystals when microprecipitating Griseofulvin from DMF (an example is shown in Figure 65a).

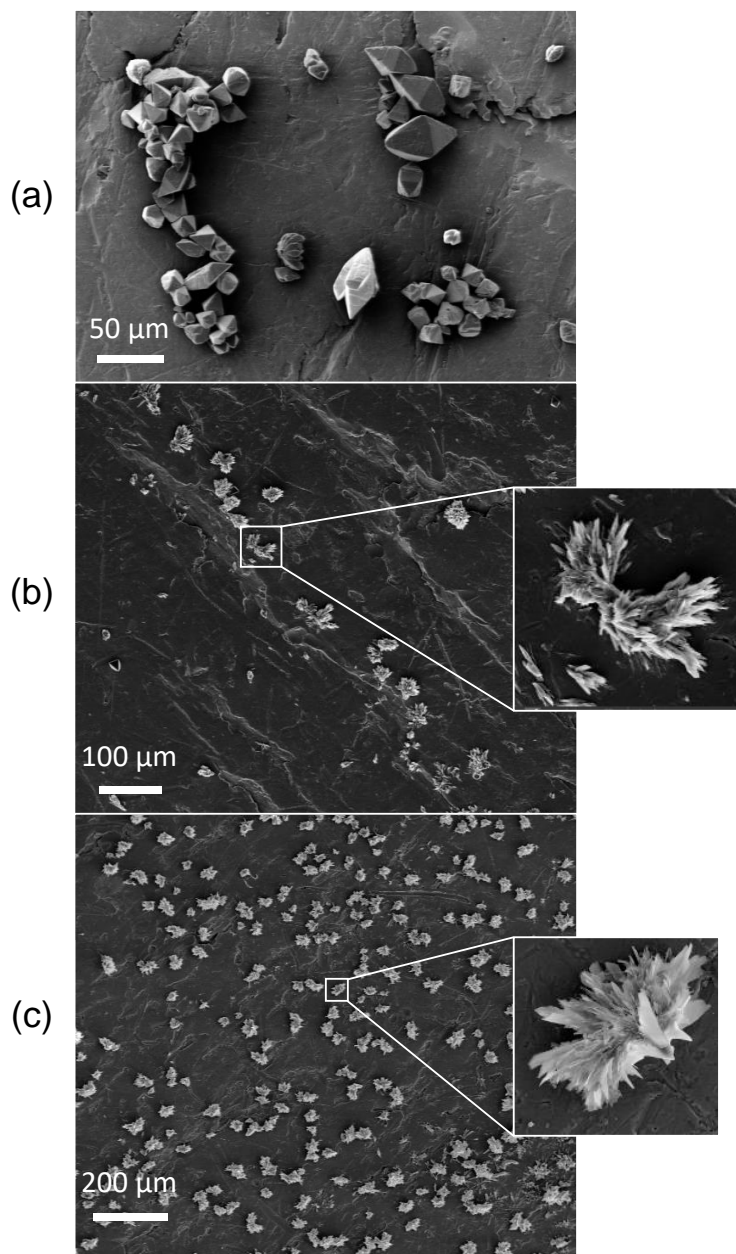


Figure 65. SEM images of Griseofulvin particles microprecipitated from (a) DMF, (b) Acetone and (c) Ethyl acetate (25 °C, $\Delta P = 25$ bar).

The bipyramidal shape is the most stable crystalline form of Griseofulvin(253) and its formation is attributed to a uniform growth of all crystal faces. The bipyramids obtained by microprecipitation are full (rather than partially hollow) which indicates that the API concentration was sufficiently high and mass transfer was quick enough. However, the morphology of the Griseofulvin particles microprecipitated from acetone and ethyl acetate (under the same flow conditions, 25 °C, $\Delta P = 25$ bar) is very different – Figure 65b, c. These particles exhibit flower-like structures composed of a multitude of thin petals (thinner than about 50 nm). At lower values of ΔP (15 or 20 bar), particle morphology was still bipyramidal when using any of the three solvents. Therefore flower-like particles were obtained only with the fastest mixing tested (highest ΔP) and rapidly expanding solvents (acetone and ethyl acetate).

The role of driving pressure is crucial and it is illustrated with Luteolin particles precipitated from DMF in Figure 66. At $\Delta P = 15$ bar, interconnected clumps of nanosized particles are produced - Figure 66a. At $\Delta P = 20$ bar, larger clumps are formed - Figure 66b. Their surface, formed by the fusion of smaller particles, is rough and irregular with protruding sharp edges. At $\Delta P = 25$ bar, the particles are fully developed nanoflowers - Figure 66c.

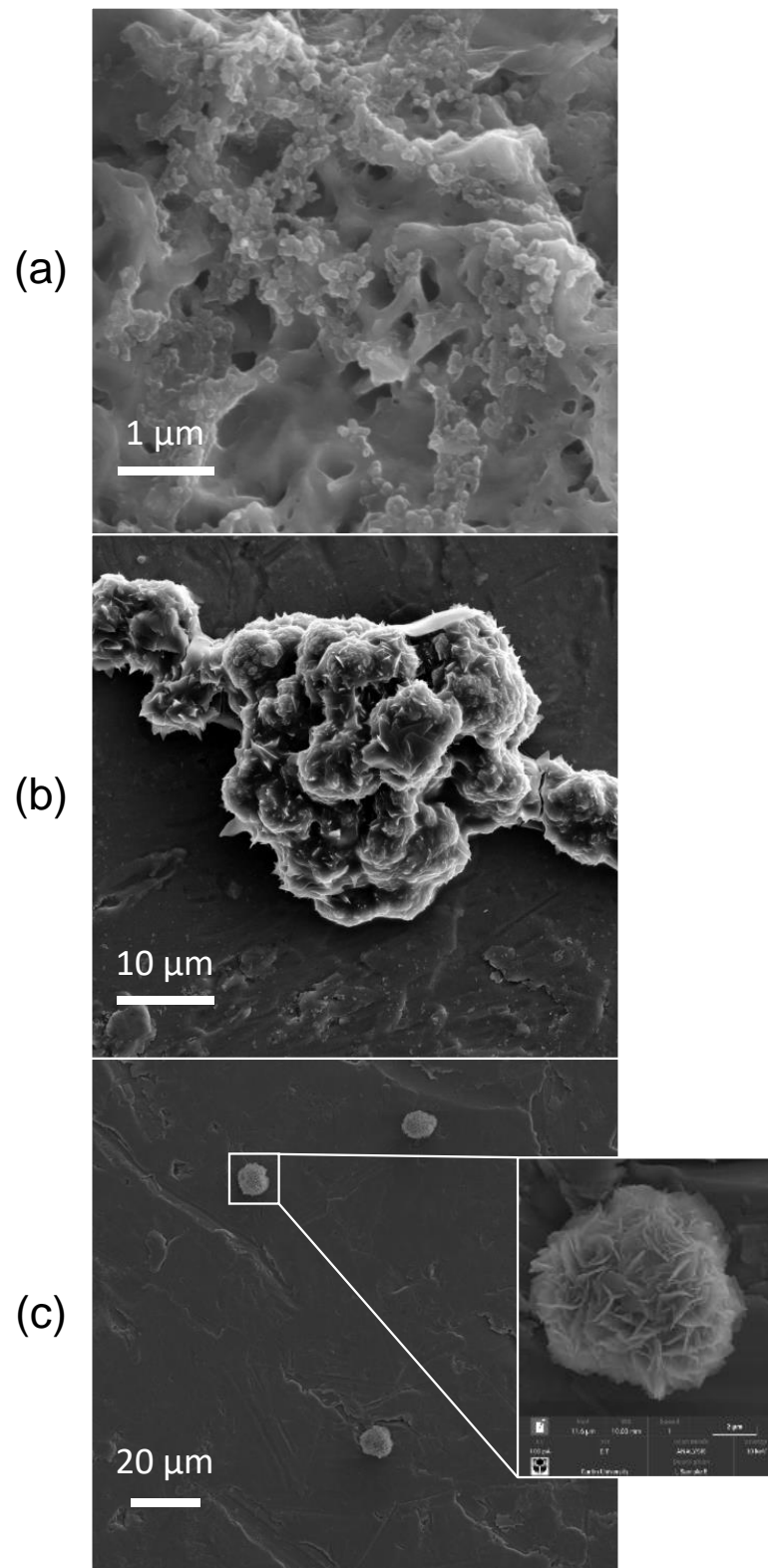


Figure 66. SEM images of Luteolin particles microprecipitated DMF (25 °C) at: (a) $\Delta P = 15$ bar, (b) $\Delta P = 20$ bar, and (c) $\Delta P = 25$ bar.

Assuming that the most intense nucleation and initial crystal growth happen within the junction of the micromixer (Figure 67), we estimate the characteristic time of nanoflower formation at about 30 μs .

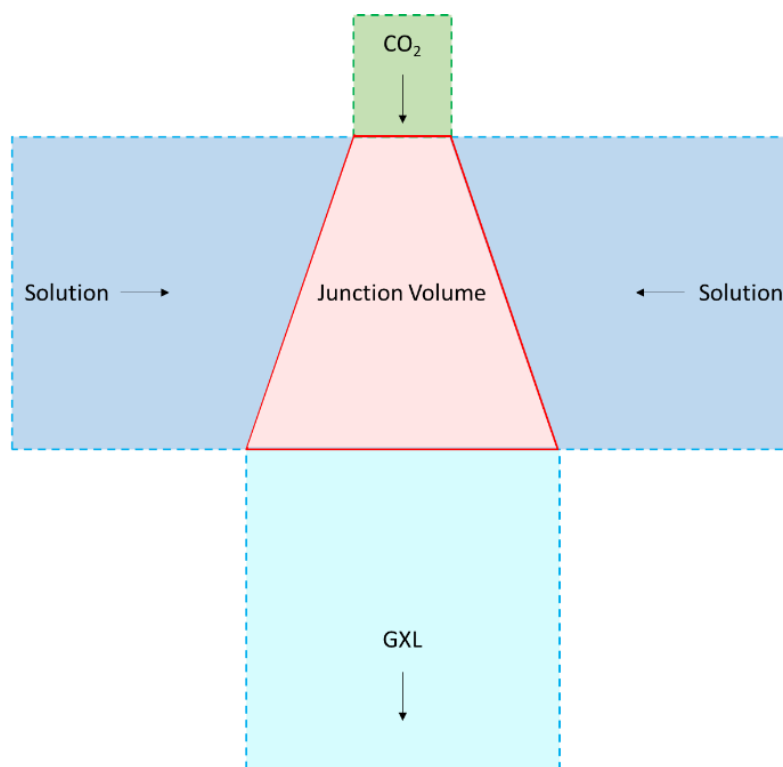


Figure 67. Schematic for trapezoidal window at the junction of the micromixer.

This is estimated by taking the ratio of the junction volume to the average flow rate at $\Delta P = 25$ bar. The average flow rate at this driving pressure is $6.9 \times 10^{-9} \text{ m}^3 \cdot \text{s}^{-1}$. We assume a trapezoidal window at the junction of the X-micromixer. The junction volume is estimated using the widths of the narrow ($32 \mu\text{m}$) and wide ($125 \mu\text{m}$) channels as the sides of the trapezoid and an etch depth of $20 \mu\text{m}$ ($\sim 200 \text{ pL}$).

Flower-like particles are geometrically interesting but it is their higher surface area, in comparison to compact shapes, that attracts increasing research interest. Typical nanoflowers are inorganic materials whose petal-like nanostructure offer benefits in various applications, e.g. tailoring surface hydrophobicity(268), catalysis(269), and gas sensing(270). A number of hybrid organic-inorganic flower-like structures have also been examined in relation to biotechnology, sensing and catalysis.(271) There is a definite interest in using nanoflowers to improve drug loading capacity. Nonsuwan

et al.(272) produced hybrid flower like structure of FA-CP/SeNPs (Figure 68 - right) and used these as drug templates for the anticancer drug, doxorubicin (DOX). An aqueous solution of DOX (1 mg/ml) was added to the nanoflower suspension and stirred at room temperature for 24 hours to achieve drug loading. The DOX-loaded hybrid flower structures showed a sustained drug release behaviour until reaching a plateau (Figure 68 - left).

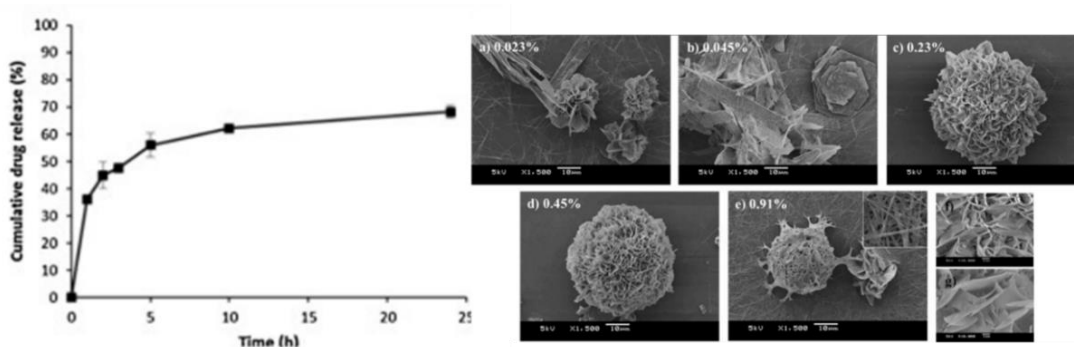


Figure 68. Left: Cumulative drug release (%) of DOX from DOX-loaded hybrid microflowers, and Right: SEM images of SeNPs shapes stabilized by FA-CP with variable FA-CP concentrations (a to e).(272)

The microflowers exhibited effective drug adsorption with a loading capacity of 142.2 mg.g^{-1} for doxorubicin which was three times higher than that for the doxorubicin-loaded spherical Se NPs.

The reports of purely organic flower-like structures are rare.(273-275) We present here a straightforward gas-antisolvent microprecipitation that produces flower-shaped particles. Luteolin (the smallest API molecule tested here) forms ideally shaped round nanoflowers when precipitated from DMF ($25 \text{ }^\circ\text{C}$, $\Delta P = 25 \text{ bar}$, Figure 66c). Under the same conditions, Griseofulvin forms nanoflowers but only when precipitated from acetone (Figure 65b) or ethyl acetate (Figure 65c). This API molecule is larger and the nanoflowers are less symmetric. Budesonide (the largest molecule tested here) did not form nanoflowers under the conditions tested here. This trend suggests that molecular volume and hence diffusivity are critical for the development of nanoflower structures within the short residence time in the junction space of the micromixer.

A growing body of work demonstrates that traditional modes of crystal growth via molecular addition (“classical crystallization”) should be considered along with the importance of the self-assembly of nanocrystalline subunits (“non-classical crystallization”).(276-279) Spherical morphology of aragonite was produced with silica gel at pH 10.5 through self-organized assembly of the platy subunits with preferential growth - Figure 69.

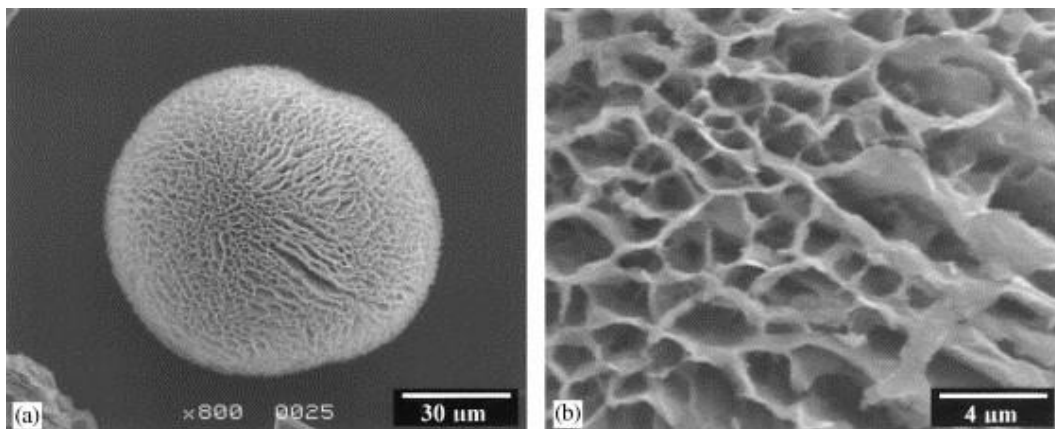


Figure 69. SEM images for the growing shapes of the porous structure of aragonite.(280)

This alternative mechanism of crystal growth can be manipulated, usually with additives, to achieve novel desired morphologies. Su et al.(275) suggested that such crystallization paths could lead to the formation of highly aligned arrays of nanoplatelets and provide the basis for nanoflower formation. We speculate that when mixing times become very short ($\sim 30 \mu\text{s}$) the formation of a stable 3D crystal is effectively outpaced by a fast growth in a preferred plane and this petal growth generates the nanoflowers obtained in our experiments - Figure 66.

Purely organic nanoflowers are held together by supramolecular forces as demonstrated in the case of 1,2-bis(tritylthio)ethane.(273) This molecule contains six phenyl rings and the sextuple phenyl embraces (a well-known π - π interaction(281)) and the π -stacking of aromatic rings stabilize the crystalline structure of the petals - Figure 70.

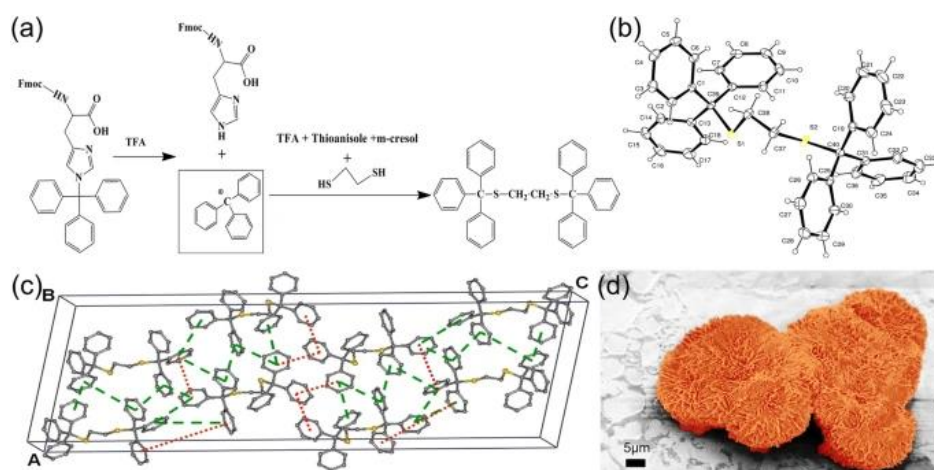


Figure 70. Synthesis, crystallization and nano-assembly of 1, 2-bis(tritylthio)ethane. (a) Scheme illustrating the reaction conditions for the synthesis and crystallization of 1, 2-bis(tritylthio)ethane. (b) ORTEP diagram of 1,2-bis(tritylthio)ethane. (c) The schematic unit cell of 1, 2-bis(tritylthio)ethane, showing the type of interactions in phenyl embraces (The green dashed line indicates T shaped edge to face interaction, and the red dotted line indicates parallel displaced orientation). (d) False-coloured FE-SEM image showing flower like assembly.(273)

The three APIs considered in this work have structures that support supramolecular arrangements. For instance, hydrogen bonding, $C-O\cdots H$ interactions and $C-O\cdots\pi$ contacts are present in Luteolin crystals.(282) Griseofulvin, under acidic conditions, undergoes dimerization through hydrogen bonding.(283) Hydrogen bonding and van der Waals contacts characterize the crystal packing of Budesonide.(284) In fact, the aromatic ring count (the number of aromatic and heteroaromatic rings(285)) ranks the APIs as $LT > GF > BD$, i.e. in exactly the same way as their size and energetic parameters.

Flower-like morphologies are desirable but, so far, experimental conditions favouring the growth of such structures were mostly discovered by chance. In an attempt to remedy the situation, Negrón et al.(274) developed hierarchically organized colloidal particles with a gel-like interior to encapsulate small or large molecules and consequently shape them into flower-like structures. Our approach does not involve the use of any additives and comes down to selecting an API-solvent combination and using flow conditions to ensure very fast mixing. Because of that our method could be used widely for screening purposes and production.

4.3 Conclusions

Carbon dioxide was used as an antisolvent to microprecipitate APIs from different solvents. In all cases an increase in driving pressure applied to the micromixer led to a logarithmic decay of the average particle size. Our microprecipitation approach is a chemically specific method for micronization. The absolute size of Griseofulvin particles decreased depending on the solvent used in the following order: DMF > acetone > ethyl acetate. We attribute this trend to the increasing affinity of the solvent to CO₂ and therefore its rate of expansion under intense mixing. The three APIs microprecipitated from DMF ranked as Luteolin > Griseofulvin > Budesonide with respect to average particle size. We correlate this order with the molecular and energetic parameters of the APIs: molecular mass and molecular volume, specific surface free energy and octanol-water partition coefficient, and also aromaticity (aromatic ring count). Precise particle size control is coupled with an opportunity to manipulate crystal habit. We synthesized rare flower-like particles (nanoflowers) by simply adjusting the flow conditions for specific API-solvent pairs. This appears to be the simplest and most promising method for organic nanoflower production. Our microfluidic platform allows an easy, green, and flexible micronization of various APIs.

Chapter 5

Influence of the Micromixer's Fluidic Resistance on the Microcrystallization of APIs

5.1 Introduction

The complexity of gas-liquid mixing stems from the poorly defined interface between the fluids under high pressure.(286) Under fast mixing conditions, higher gas and liquid flow rates result in flow disturbances such as waves or fluid entrainment (Chapter 3(254)). This results in uncertainty concerning the actual fluid geometries and available interfacial areas which often leads to inhomogeneity in the process conditions throughout the reactor volume.(287) This requires the development of reactors that allow for efficient mixing. The primary aim in gas-liquid reactors is to increase the interfacial area to allow fast and efficient fluid mixing which is related to the contact area between the two phases, fluid flow profile, properties of gas and liquid phases (density and viscosity), and mixing parameters such as mixer volume, average fluid speed, and residence times.(288-290) The main challenge, therefore, is to maximise the contact area between the two phases for efficient mixing.(291)

Most standard reactors are pressure vessels with sophisticated components used for fluid feed, outlets for fluids, and process homogenization. Thus, these represent substantial capital and operating costs.(292, 293) Microfluidic devices offer high interfacial areas and precise control over mixing conditions and can be used to facilitate and control gas-liquid mixing.(190) Moreover, the design flexibility(294, 295), well-established fabrication techniques(296, 297), and ease of scale-up(298, 299) offered by microfluidic reactors (volume on the scale of μl) can help overcome the limitations encountered with larger reactor vessels (>50 ml).

As described in Chapters 3(254) and 4, dense gas processes hold the potential to produce pharmaceutical compounds in an efficient way while eliminating issues related to solvent residue removal associated with traditional techniques (such as the use of a liquid antisolvent).(300, 301) However, the efficient use of such processes is limited by the lack of understanding of the kinetics of gas-liquid mixing.(302) The use

of a micromixer platform can help overcome this issue owing to well-defined contact areas and mixing/residence times in these devices.(190, 303) It can also help overcome the issue of inhomogeneity in process parameters associated with traditional reactors and lead to better control over particle size.(192, 304, 305)

We have shown the use of a high-pressure microfluidic platform for the micronization of APIs under dynamic flow conditions in Chapter 3.(254) In Chapter 4, we have shown how the selection of the API-solvent pair has a significant influence on the supersaturation rate and particle morphology. The influence of mixing conditions (fluid driving pressure, micromixer design) and crystallisation chemistry (solution concentration, role of API-solvent pairs) on the micronized particle size and morphology were investigated.(254) In this chapter we investigate the influence of the micromixer fluidic resistance on API microprecipitation.

5.2 Results and Discussion

API Micronization

We turn again to the microprecipitation of Griseofulvin from a solution in DMF using subcritical CO₂ as the antisolvent under different flow conditions. The micronization experiments were performed using the rig and method described in sections 2.7 and 2.8, respectively. The gas and liquid input pressures are maintained at the same value throughout the experiment. The back pressure is varied to regulate the driving pressure, ΔP , for the fluids in the system.

Two different micromixers are employed in this work - Figure 71. The X1 micromixer (Figure 71a), comprises three inlet channels, two of which are wider ($w = 124 \mu\text{m}$) and used to supply the pressurized solution from both sides of the junction. The central narrower channel ($w = 32 \mu\text{m}$) supplies the pressurised CO₂ gas. A mixing channel ($l = 52.5 \text{ mm}$, $w = 124 \mu\text{m}$) carries the gas-liquid mixture to the outlet. The X2 micromixer (Figure 71b) consists of the same junction geometry followed by a much longer mixing channel (a serpentine, $l = 161.5 \text{ mm}$). The depth of all channels was the same ($d = 19.5 \mu\text{m}$).

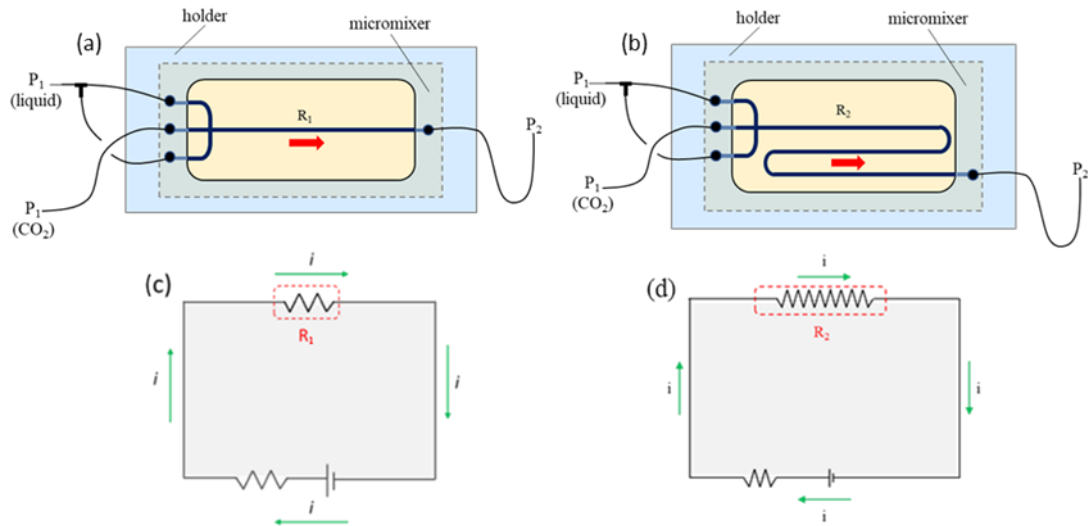


Figure 71. (a) X1 micromixer (post-junction length = 52.5 mm); (b) X2 micromixer (post-junction length = 161.5 mm); (c) & (d) show the electrical circuit modelling the micromixer resistance ($R_2 > R_1$).

The liquid volumetric flow rates (Q), under gas-liquid co-flow, are significantly different for the two micromixers under the same fluid driving pressures (ΔP) - Figure 72. The graph shows a linear dependence of Q on ΔP and the slope of this graph gives the inverse of the hydraulic resistance, R_H , experienced by the fluids in X1 and X2 micromixers – Equation 24.(254). The hydraulic resistance, R_H (Pa.s.m^{-3}), is related to the geometry of the channel and the viscosity of the fluid mixture:

$$R_H = \frac{8\mu l}{\pi r^4} \quad 35$$

Here μ is the viscosity of the fluid mixture (Pa.s) that forms post-junction, r is the hydraulic radius of the microchannel (m) and l its length (m).

An increase in R_H , thus, results in a drop in the magnitude of Q for the same driving pressure as seen in Figure 72. The cross-sections for the post-junction microchannels in X1 and X2 are similar, however, the channel length where the gas-liquid mixing/homogenization occurs is very different. The length of the mixing channel in X2 is about three times larger than in X1. For a fixed microchannel cross-section, the hydraulic resistance is determined by the viscosity, μ , of the resultant gas-liquid mixture (or GXL) and the length of the microchannel (l) – Equation 35. Since the mixer channel in X2 is 3 times longer than in X1, the value for Q (under the same

process conditions) obtained for X2 should be about one-third of the value in X1. However, the experimental difference in flow rates is much larger - about two orders of magnitude. Therefore, the average fluid speed in X2 is two orders of magnitude lower than that in X1. Consequently, the gas-liquid mixing at the identical junction is much less intense in X2. This delays the GXL formation and the related viscosity drop and leads to much lower volumetric flow rates - Figure 72.

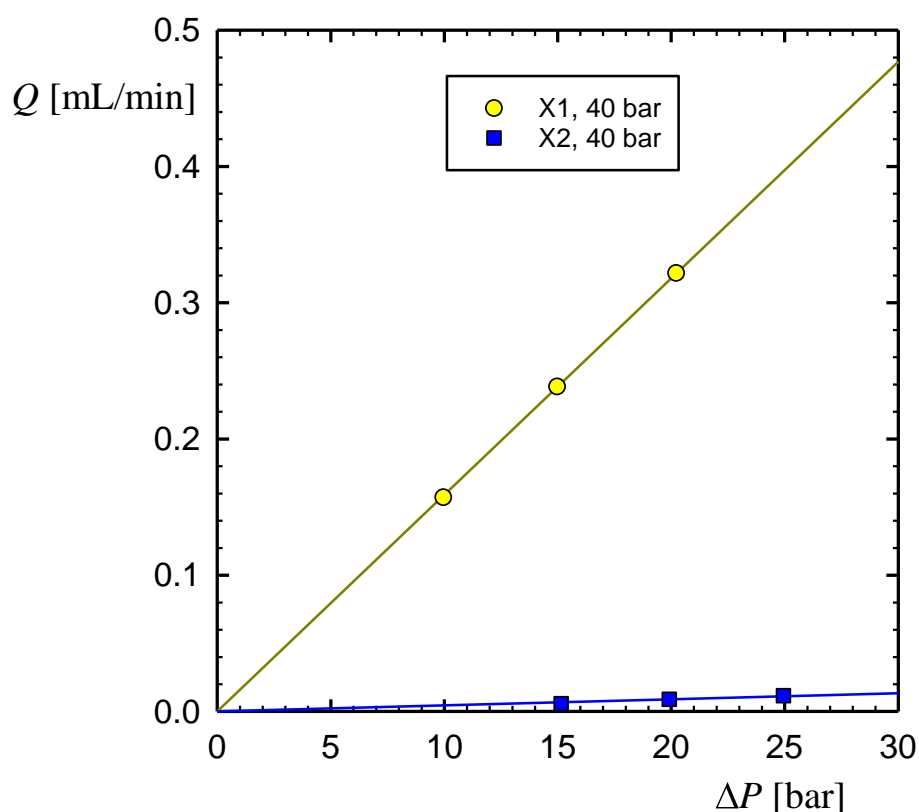


Figure 72. Liquid volumetric flow rates, under gas-liquid co-flow, obtained for X1 and X2 micromixers at fixed fluid input pressure (= 40 bar) and different driving pressure, ΔP . Error bars are within the symbol size.

We have discussed in Chapter 3(254) that the Poiseuille law for viscous flow in a channel is analogous to Ohm's law in electrical circuits. Thus, the longer mixing length in the X2 micromixer translates to a higher fluidic resistance which can be represented as an electrical circuit containing a larger resistor - Figure 71 c and d. The same ΔP when distributed over a much longer mixing channel (as in X2) generates a lower volumetric flow rate - Figure 72. Despite the identical cross-section geometry, the flow

and mixing patterns observed in the two microreactors are very different – Figure 73. The mixing in X2 micromixer is less intense than X1; the gas and liquid streams in X2 form distinct and sharp boundaries which slowly fade away over the length of the much longer mixing channel. Whereas in the X1 micromixer, the gas arrives at the junction at higher speeds and quickly mixes with the organic liquid. The homogenization of the gas-rich and liquid-rich phases occurs via diffusion along the mixer channel post-junction.

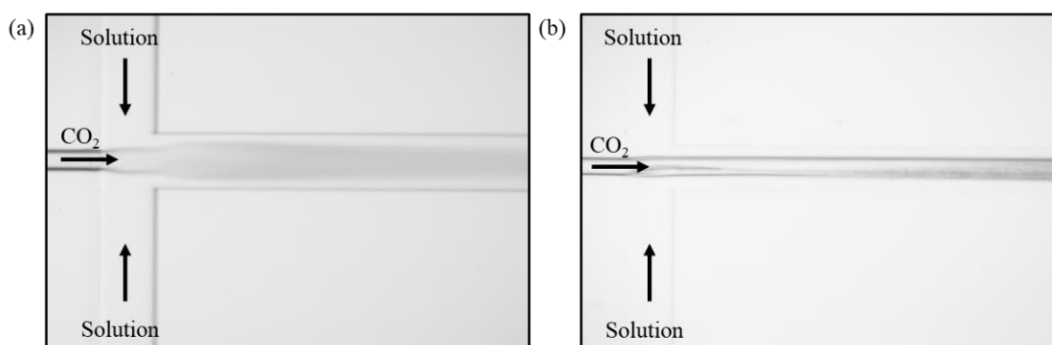


Figure 73. Gas-liquid flow profiles observed in micromixers (a) X1 and (b) X2.

The different mixing conditions generated in X1 and X2 produce different particle sizes and morphologies. The size of the microprecipitated API particles decreases with the fluid driving pressure for both the X1 and X2 micromixers - Figure 74. The intensity of gas-liquid mixing is influenced by the fluid speeds which leads to different flow profiles in the micromixers - Figure 73. This influences the gas-liquid mixing which further effects the supersaturation and consequently the properties for the precipitates. This illustrates the crucial role that gas-liquid mixing plays in the microprecipitation process. This fact could be used to control particle size by simply adjusting the length of the mixing channel in an X-junction micromixer. The API particle size decreases with the fluid driving pressure (Figure 74) as already discussed in Chapters 3(254) and 4. This can be explained in terms of the crystallisation kinetics. In brief, the decreasing trend in Figure 74 is attributed to the faster mixing achieved at higher driving pressure. Because of the faster mixing, critical supersaturation is achieved sooner and this promotes the formation of smaller particles. The trend for the X1 micromixer is identical to the one shown in Figure 49b in Chapter 3(254). The

trend for the X2 micromixer is similar but particle size is significantly smaller ($<1 \mu\text{m}$) as compared to the X1 micromixer (1-10 μm). We attribute this to the much slower mixing which is likely to be diffusion-controlled. The formation of the gas-expanded liquid is delayed and therefore critical supersaturation is reached later. Nucleation conditions are less favourable and crystal growth is also delayed. As a result, the particle size is significantly lower - Figure 74. The downward trend with driving pressure is present but less sensitive to changes in the driving pressure when compared to the X1 micromixer.

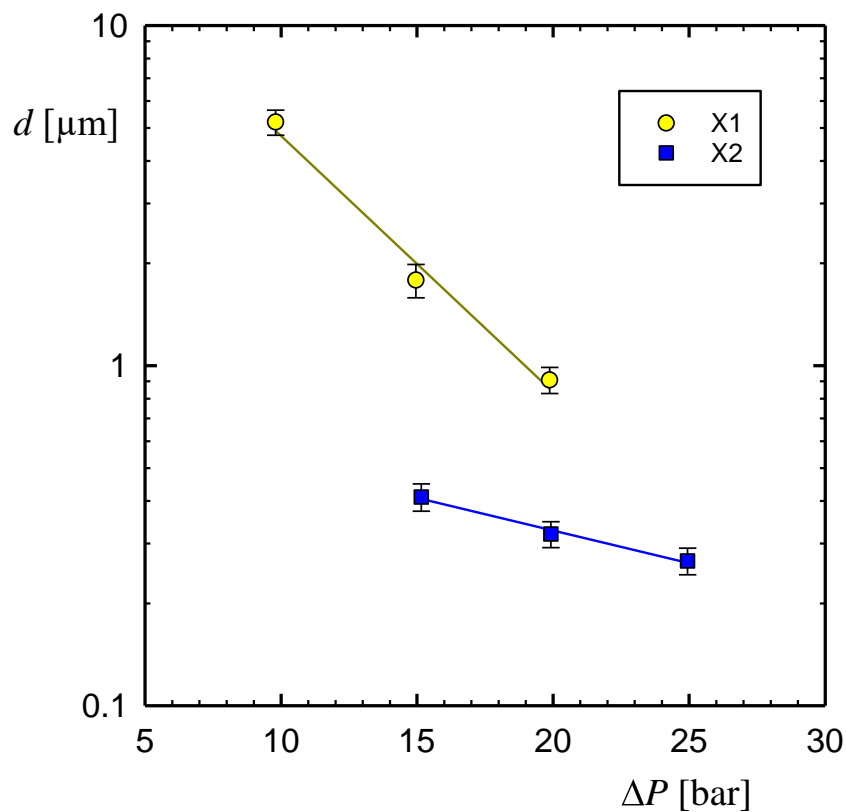


Figure 74. The particle size obtained from X1 and X2 micromixers at fixed fluid input pressure of 40 bar and variable fluid driving pressure ($C_{GF} = 0.1\%$).

We now examine the microprecipitation performance of the X2 micromixer under different supply pressures - Figure 75. The decreasing particle size with ΔP is consistent for the three input pressures employed for the fluids (40, 60, and 70 bar) when precipitating using the X2 micromixer.

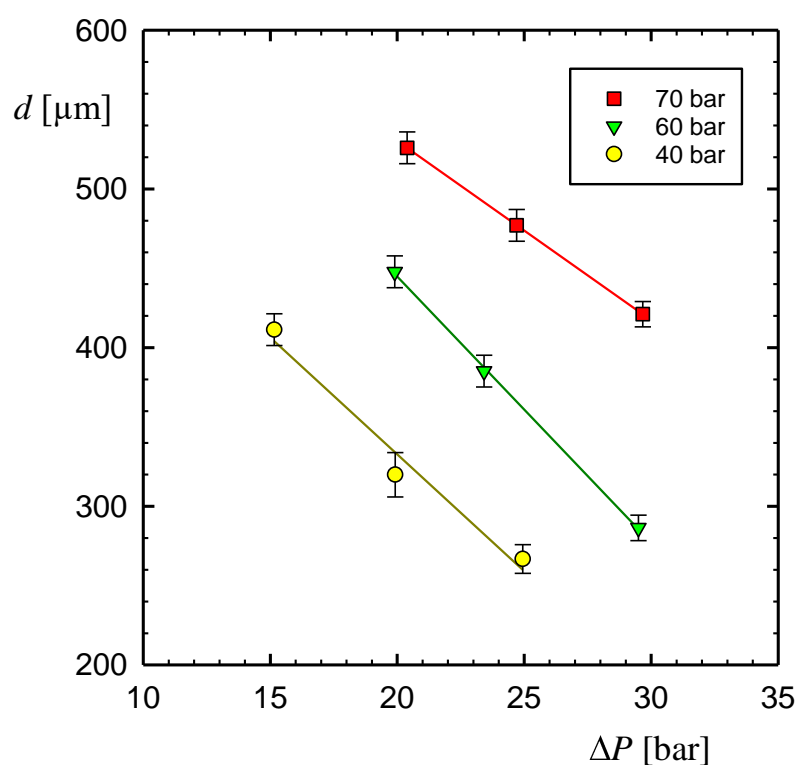


Figure 75. Particle size obtained from the X2 micromixer at different fluid input and driving pressures ($c_{GF} = 0.1\%$).

However, the particle size at a fixed ΔP goes up sharply with the fluid input pressure. This increase can be attributed to the change in the antisolvent properties with pressure which influences mixing. The main effect of input pressure is to increase the density and viscosity of CO_2 . Equilibrium values of these parameters are listed in Table 11.

Table 11. Density and viscosity values for CO_2 as a function of pressure (at $T = 25^\circ\text{C}$). The values for CO_2 density and viscosity at different conditions were obtained using Peace Software.(306)

Gas Pressure (bar)	ρ ($\text{kg}\cdot\text{m}^{-3}$)	μ (10^{-6} Pa.s)
40	93.6	15.9
50	132.3	16.7
60	258.4	21.8
70	700.9	59.1

The higher input pressure intensifies the microprecipitation process - Figure 75 and Figure 76. The higher density of CO₂, supplied under the same flow conditions, effectively means a higher concentration of antisolvent. In fact, the particle size increase with input pressure in Figure 75 and Figure 76, is reminiscent of the similar trend observed when increasing the API concentration (Figure 49, Chapter 3(254)). The linear increase with pressure in Figure 75 and Figure 76 (at fixed ΔP) mimics the linear increase with solute concentration in Figure 49. The reason in both cases is that the reaction rate, i.e. crystallization rate, is proportional to the concentration of reactants.

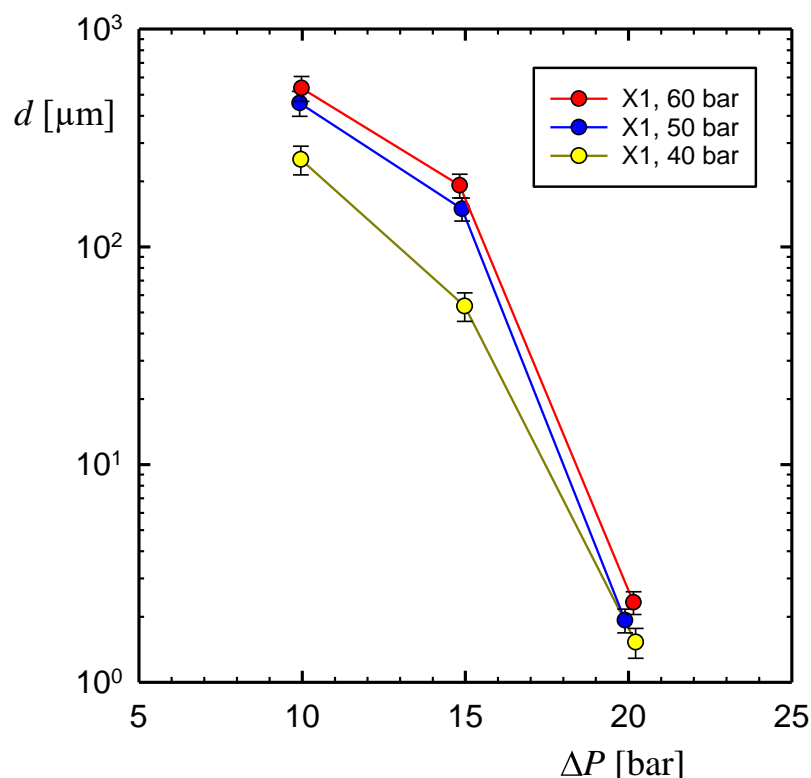


Figure 76. The particle size obtained from the X1 micromixer at different fluid input and driving pressures ($c_{GF} = 0.5\%$).

The above argument is qualitative as it uses as an approximation the equilibrium properties of pure CO₂. The relevant density and viscosity are the ones of the gas-expanded liquid formed in the micromixer. In the X2 micromixer, this formation is relatively slower and extends well into the mixing channel. However, a study of the time and space details of GXL formation was beyond the scope of this work.

Particle Morphology

Previously, we have investigated the variation in crystal morphology for GF particles with driving pressure when precipitated with an X1 micromixer (Chapters 3(254) and 4). At a lower driving pressure ($\Delta P = 20$ bar) the particles have a flower-like structure composed of a multitude of thin petals - Figure 77a. The bipyramidal shape is the most stable crystalline form of GF(253) and its formation is attributed to a uniform growth of all crystal faces. In this chapter, the bipyramidal shape is found when precipitating GF at an input pressure of 70 bar and a fluid driving pressure of 25 bar in the X2 micromixer - Figure 77b. This form of GF has been obtained under the same driving pressure ($\Delta P = 20$ bar) when precipitating from a solution in DMF ($P_{in} = 40$ bar, Chapter 3).(254) Whereas at $\Delta P = 30$ bar, we observe thin, long crystals that remain in an aggregated state - Figure 77c.

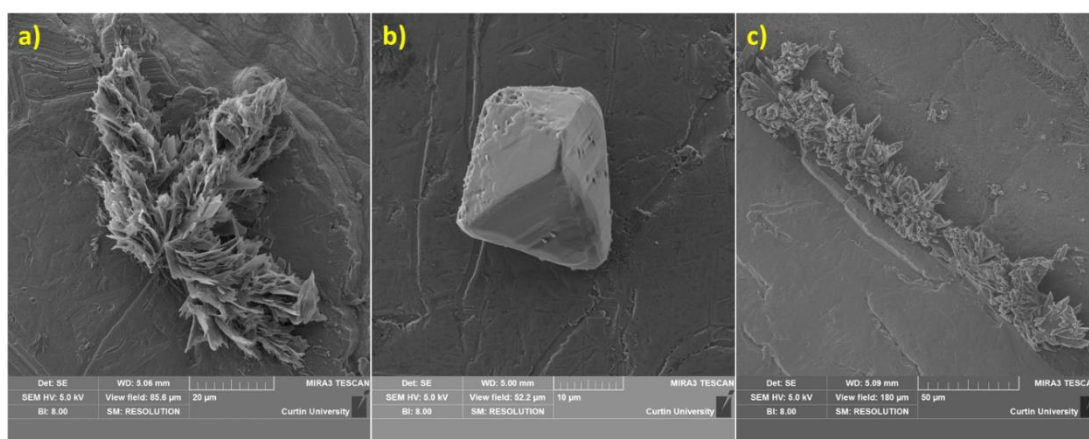


Figure 77. SEM images of GF particles precipitated from the X2 micromixer at fixed gas input pressure, $P_{in} = 70$ bar, with variable fluid driving pressure of: (a) 20 bar, (b) 25 bar, and (c) 30 bar.

Therefore flower-like particles were obtained only for the longest mixing time, i.e., the lowest ΔP , which implies that the higher supersaturation achieved under these conditions is crucial for the formation of these hierarchical structures.

Similar flower-like particles (or nanoflowers) were formed at the same driving pressure ($\Delta P = 20$ bar) for the gas input pressures of 40, 60, and 70 bar (Figure 78 a to c) when precipitating with the X2 micromixer.

Once again, the details of gas-liquid mixing play a major role in crystal formation and more specifically nanoflowers. We have first demonstrated the formation of organic nanoflowers using Luteolin when precipitating from a solution in DMF using our method ($P = 40$ bar, $\Delta P = 25$ bar, X1 micromixer). In this experiment, the intense gas-liquid mixing resulted in short mixing times ($\sim 30 \mu\text{s}$) at the junction and the formation of stable 3D crystals was outpaced by a fast growth in a preferred plane. This resulted in petal growth and the formation of nanoflowers.

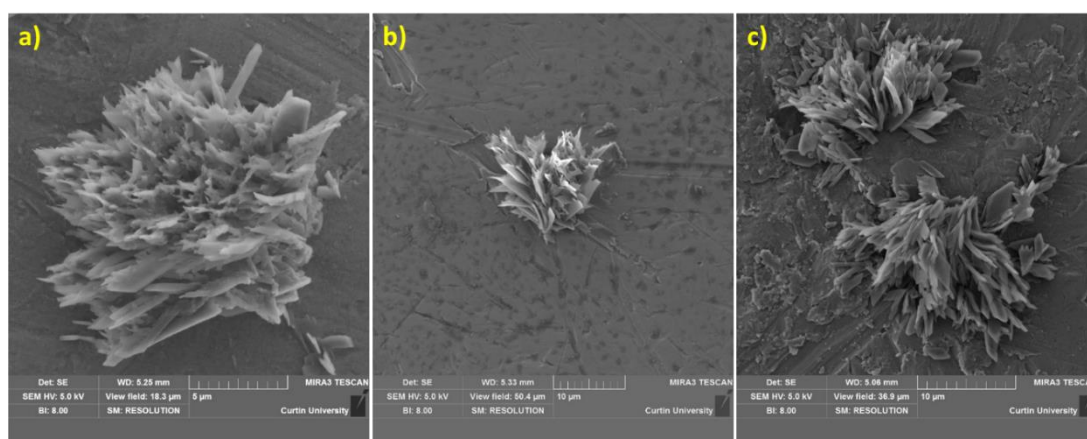


Figure 78. SEM images of the GF particles precipitated from the X2 micromixer at fixed fluid driving pressure, $\Delta P = 20$ bar, with variable input pressure of: (a) 40 bar, (b) 60 bar, and (c) 70 bar.

In X2 micromixer, the lower fluid speeds result in slower mixing. However, at $\Delta P = 20$ bar (lowest driving pressure tested), the longer residence times favour greater mixing and reaches supersaturation levels that promote the formation of nanoflowers - Figure 78. These flower-like morphologies are usually attained with additives which makes the process more complex. Our approach adjusts the mixing conditions to trigger precipitation and reproducibly create these hierarchical structures without the use of any additives. By simply changing the length of the mixing channel, we can tune the fluidic resistance of the micromixer and manipulate the intensity of the gas-liquid mixing. This significantly influences the microprecipitation process and allows us to control the crystallization outcomes (particle size and morphology). For instance, as proven here, changing the length of the mixer channel in an X-junction micromixer (3 times in X2) allows us to produce smaller, high-surface area GF particles.

5.3 Conclusions

We have demonstrated the influence of the micromixer's fluidic resistance on particle size with the example of GF particles microprecipitated from a solution in DMF. An identical X-junction performs very differently under the same driving pressure depending on the length of the mixing channel. The vastly different mixing conditions (more intense in X1 as compared with X2) are explained using the electric analogy of microfluidic circuits. The performance of X2 is similar to that of X1 in terms of fluid flow and trends for particle size with the fluid driving pressure. Fluids experience higher resistance in X2 and this leads to the following differences: the volumetric liquid flow rate is much lower for X2 under the same process conditions (P_{in} , ΔP , c_{GF}) and the size of the particles produced is below 1 μm for all process conditions tested.

It is possible to manipulate the size and morphology of the precipitated GF particles through different micromixer geometry and antisolvent properties. Flower-like morphologies are obtained for the lowest ΔP (= 20 bar) tested in X2 micromixer for all values of fluid input pressures. This chapter illustrates the use of micromixer design to adjust the type of flow conducive to different crystallization outcomes. It demonstrates the flexibility of the HPMF platform for API micronization.

Chapter 6

Formation of Pharmaceutical Cocrystals Using CO₂-Antisolvent Microprecipitation

6.1 Introduction

Size reduction is a mainstream approach to improving the solubility and therefore the bioavailability of poorly water-soluble (hydrophobic) APIs. An alternative approach consists of modifying the chemical form of the API using supramolecular chemistry. Researchers have identified two reliable ways of drastically improving the API solubility: forming a salt(307) or a cocrystal.(3, 308, 309) The salt form is composed of ions and thus is more soluble in water. The cocrystal combines neutral API and soluble cofomer.

In a salt, some or all the acid hydrogens have been replaced by a metal ion or a radical. Whereas cocrystals are single-phase crystalline materials composed of two or more molecules forming a common crystal lattice. The simplest pharmaceutical cocrystal is composed of an API and a cofomer (should be pharmaceutically acceptable).(105) Cofomer are different to excipients as excipients are chemically inert and show little or no interaction with the API. An excipient has no covalent or significant non-covalent interaction with the API structure and hence does not become a part of the API's crystal structure. Whereas a cofomer participates in intermolecular interactions with the API and thus becomes an integral part of the crystal structure. Such closer interaction makes the properties of the cocrystal different from those of the API.

Cocrystals between an API and a cofomer can have different stoichiometric ratios. For example, a cocrystal of carbamazepine (anti-epileptic drug(310)) and 4-aminobenzoic acid (cofomer) can have stoichiometric ratios of 1:1, 2:1, and 4:1.(311) Cocrystals are of significant interest to the pharmaceutical industry as these can be designed to have superior physical properties in comparison to the individual components. One key aspect of cocrystal formation is the enhancement of drug solubility. The large amount of data compiled in Figure 79 clearly shows that the use of more soluble cofomer produces a more soluble cocrystal. This in turn increases the

bioavailability of the API. Note that the increase in aqueous solubility is logarithmic, i.e. very sharp - Figure 79. The ability to form such cocrystals and improve or adjust their solubility is a powerful tool in the development of drug formulations.

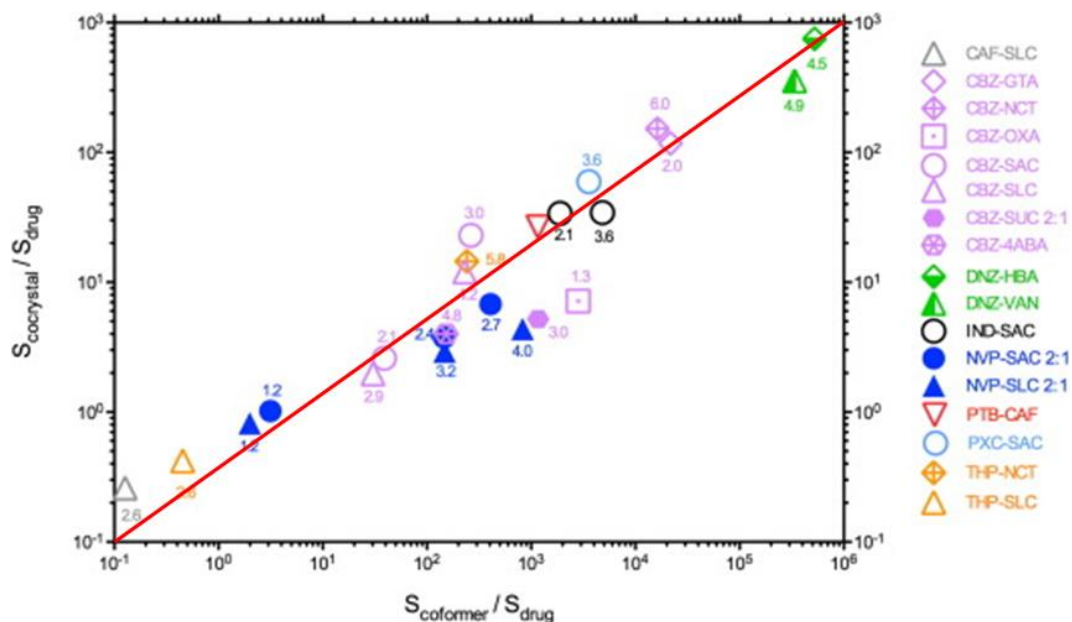


Figure 79. Cocrystal solubility advantage ($S_{\text{cocrystal}}/S_{\text{drug}}$) in aqueous media is related to the coformer and drug solubility ratio ($S_{\text{coformer}}/S_{\text{drug}}$). It is observed that $S_{\text{coformer}}/S_{\text{drug}} > 10$ leads to $S_{\text{cocrystal}}/S_{\text{drug}} > 1$. The solubility values refer to a specific pH value shown by the numbers above the data points, at 25 °C.(312)

Most APIs are molecules with hydrogen bonding ability. This allows for intermolecular interactions between different API moieties which facilitates the formation of cocrystals through supramolecular synthons - Figure 80.(3, 308, 309)

These supramolecular synthons consist of an assembly of organic crystals that is not just a result of geometrical interlinking between the API structures but is often the consequence of compromise or mutual interference between adjacent synthons. Besides intermolecular hydrogen bonding, cocrystals can also be produced by stacking or charge transfer interactions(313, 314) or through ionic interactions(315, 316) involving inorganic salts.

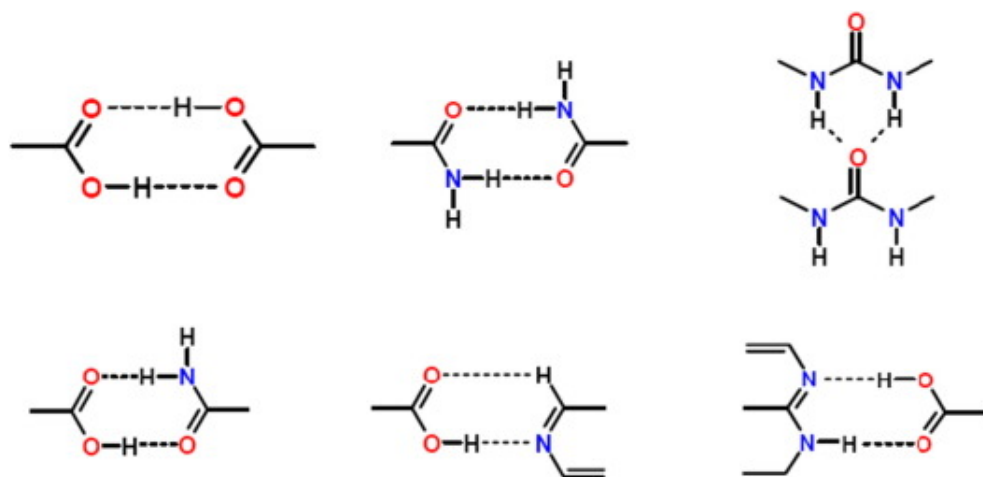


Figure 80. Common supramolecular synthons formed from carboxylic acids, amides, pyridines, and other aromatic nitrogens.(312)

Cocrystallization has been achieved through solid-based and solution-based methodologies. The solid-state cocrystal synthesis commonly consists of mechanical activation achieved by grinding the components together to form cocrystals. The solution-based methods involve generating supersaturation in a multicomponent solution. This is achieved by changing the solubility through alterations in pH, temperature, drug-to-coformer ratio or solvent evaporation. These methods often carry the inherent risk of crystallizing individual components instead of cocrystals.

In the quest to develop suitable cocrystals a range of solvents and experimental conditions (rate of evaporation or cooling, initial concentrations) must be screened for obtaining optimal results. Given that the typical formation of cocrystals can take up to several days(317) such task becomes highly time consuming. The hypothesis guiding the work presented in this chapter is that this process could be intensified with the use of the gas-antisolvent microprecipitation methodology developed in previous chapters.

We have already demonstrated the use of CO₂ as an antisolvent to be an attractive method for the generation of API crystals (Chapters 3(254) - 5). The technique can be directly applied to mixed solution of an API and a suitable coformer without any alterations. Compressed CO₂ is used here to gas-expand a multicomponent solution which decreases the solvent power and thus results in the coprecipitation of the two solutes. We work under the assumption that under given conditions these coprecipitates would be pharmaceutical cocrystals.

As explained in Chapters 1 and 3(254), the moderate process conditions employed in the GAS process eliminate many of the drawbacks associated with other techniques such as mechanical/thermal degradation of the API or costly removal of residual solvent. In fact, cocrystals have been produced using GAS crystallization. Carbamazepine (API, anti-epileptic drug) - nicotinamide (coformer, vitamin B3 analogue) cocrystals were formed by using a GAS process using ethanol as the solvent. Interestingly, cocrystal formation in this case was an unintended outcome.(318) Another example is the formation of itraconazole (API, antifungal drug) - L-malic acid (coformer, β -hydroxy acid) cocrystals from tetrahydrofuran using GAS cocrystallization. The morphology of these cocrystals obtained using liquid antisolvent method and GAS cocrystallization is presented in Figure 81.

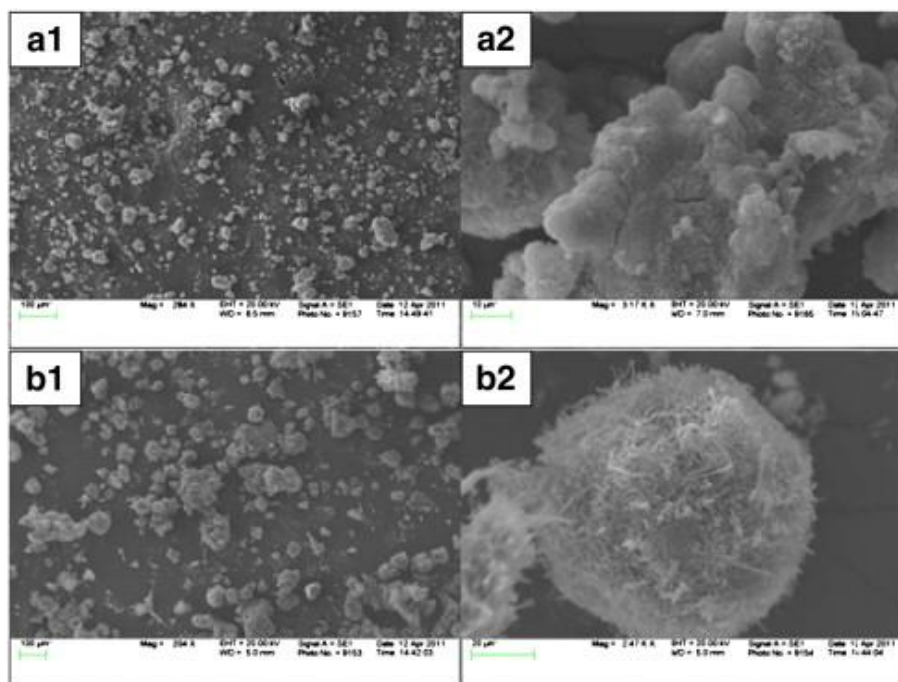


Figure 81. SEM images of itraconazole/L-malic acid cocrystals: (a1 and a2) obtained from n-heptane, and (b1 and b2) produced by GAS.(319)

The particle shape for both the techniques is homogenous and distinctly different from either of the pure components. However, the particles obtained using the liquid antisolvent technique are irregularly shaped whereas the particles produced using the GAS method are spherical and fibrous.

In this chapter, we attempt the cocrystallization of two model active pharmaceutical ingredients: Luteolin (LT), which is an anticancer drug, and Dapsone (DAP), which is an antileprotic drug (section 2.1.1). The formation of the DAP-LT cocrystals has been demonstrated by Jiang et al.(317) using slow-evaporative crystallization experiments. They prepare an equimolar solution of DAP and LT in a binary mixture of ethanol and acetone in a 1:1 volumetric ratio. DAP-LT cocrystals were harvested after slow evaporation of the solvent in a desiccator and were obtained after *one month* - Figure 82.

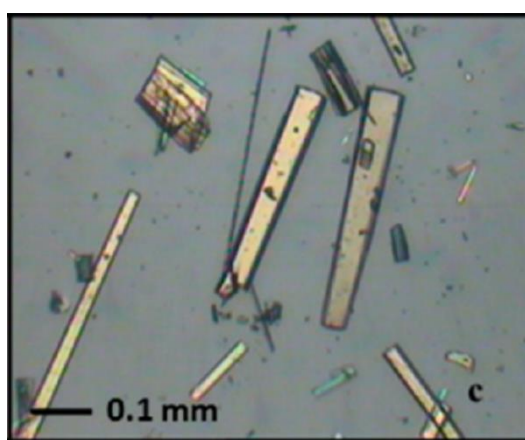


Figure 82. Polarized light microscopy photographs of DAP-LT co-crystals.(317)

They observed that the inclusion of ethanol molecules is important in facilitating the formation and stabilization of the DAP-LT cocrystals. This was confirmed upon heating the cocrystal sample at 170 °C under reduced pressure where the cocrystal sample changed back to a physical mixture of DAP and LT.

We follow their work by using the optimal conditions for cocrystal formation. Accordingly, the two drugs are dissolved in a mixture of ethanol and acetone (1:1 ratio by volume). The double API solution is crystallised using the high-pressure rig described in section 2.7. An X-junction (X1) micromixer is used for performing the on-chip GAS process using subcritical CO₂ ($P_{in} = 40$ bar, $T = 25$ °C). The micronization experiments are performed in a similar fashion as the previous work (Chapter 3(254), 4 & 5). Collection of the precipitated particles in the discharge vessel was performed for a longer duration (90 min). This was needed to collect sufficient material for reliable particle characterization. The experimental conditions are listed

in Table 12. Characterization was done through SEM and powder-XRD analysis (see Chapter 2).

Table 12. Experimental scheme for the cocrystallization of DAP & LT.

API	Molar Ratio	c% (w/w)	ΔP (bar)
DAP	-	0.22	25
LT	-	0.25	25
DAP-LT	1:1	0.11/0.12	25
DAP-LT	1:1	0.11/0.12	10
DAP-LT	5:1	0.28/0.06	10

6.2 Results and Discussion

The XRD pattern for untreated Luteolin, i.e. the material as received from the company, was analysed and compared for two separate stocks - Figure 83.

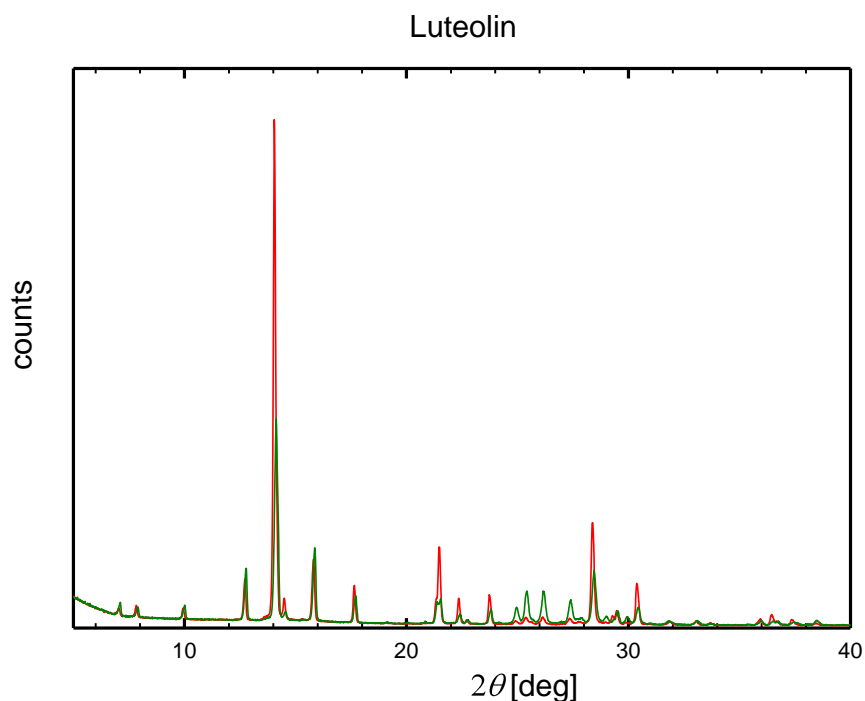


Figure 83. PXRD patterns for untreated LT as received from the company: the green lines represent pattern obtained for the old stock whereas the red lines represent pattern obtained for the fresh stock.

The peak intensities differ for the two data sets however the peak positions are the same. This confirms that the stocks are the same material and the old stock suffered no material degradation. The difference in peak intensities can be attributed to the limited API material available in the old stock which resulted in lower peak intensities. We compare untreated Luteolin with previously published results - Figure 84. There is a definite disagreement in the XRD patterns for Luteolin, which raises the concern that the starting material for these works was different, complicating our purpose of producing cocrystals using the proposed technique and comparing it to the literature.

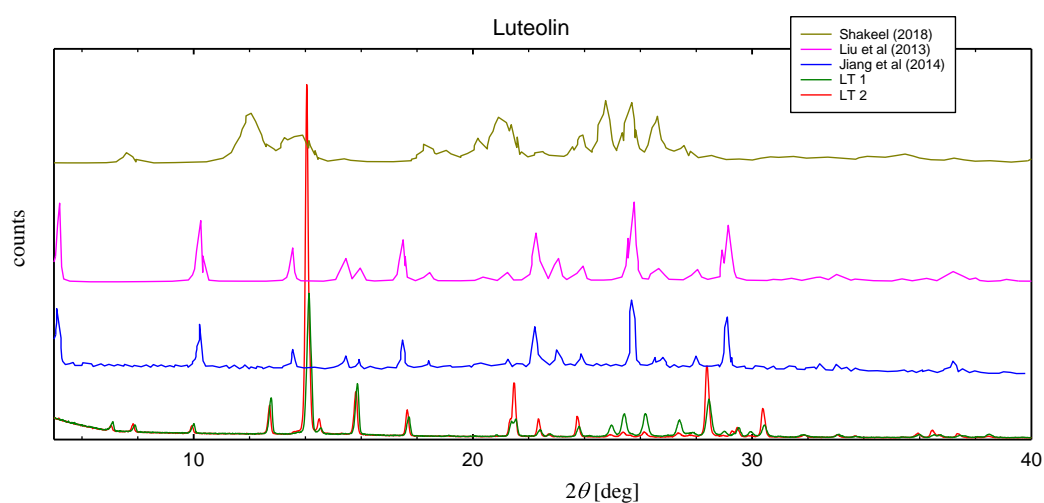


Figure 84. PXRD patterns for untreated luteolin as reported in literature.(317, 320, 321) (Note: patterns have been vertically offset for clarity).

However we have shown in Figure 83 that the XRD for our material is reproducible and hence serves as a reliable tool for crystal structure analysis. Moreover, XRD is not the focus of this work but serves as a tool to validate changes in material structure when treated using our platform. Hence, we focus on mapping any changes in the XRD patterns for the untreated and treated material to validate the formation of cocrystals.

The individual APIs were first crystallised using our microprecipitation technique under fixed process conditions. A solution of Luteolin (molarity 6.8 mmol/l) was prepared in the binary solvent. Luteolin was microprecipitated as presented in Chapter 4. The gas and solution input pressures were fixed at 40 bar, while the fluid driving

pressure was fixed at 25 bar. The recovered material was dried and the sample crystallinity was assessed using powder X-ray diffraction - Figure 85.

The XRD patterns for the two samples are significantly different. The peaks at 2θ values for the material processed using our technique (2θ values of 15.3, 23, 30.8 and 38.8°) are different to those of the untreated material (2θ values of 12.8, 14.1, 15.9, 17.7, 21.6 and 28.5°). It is evident from Figure 85 that the proposed microGAS process produces crystalline material.

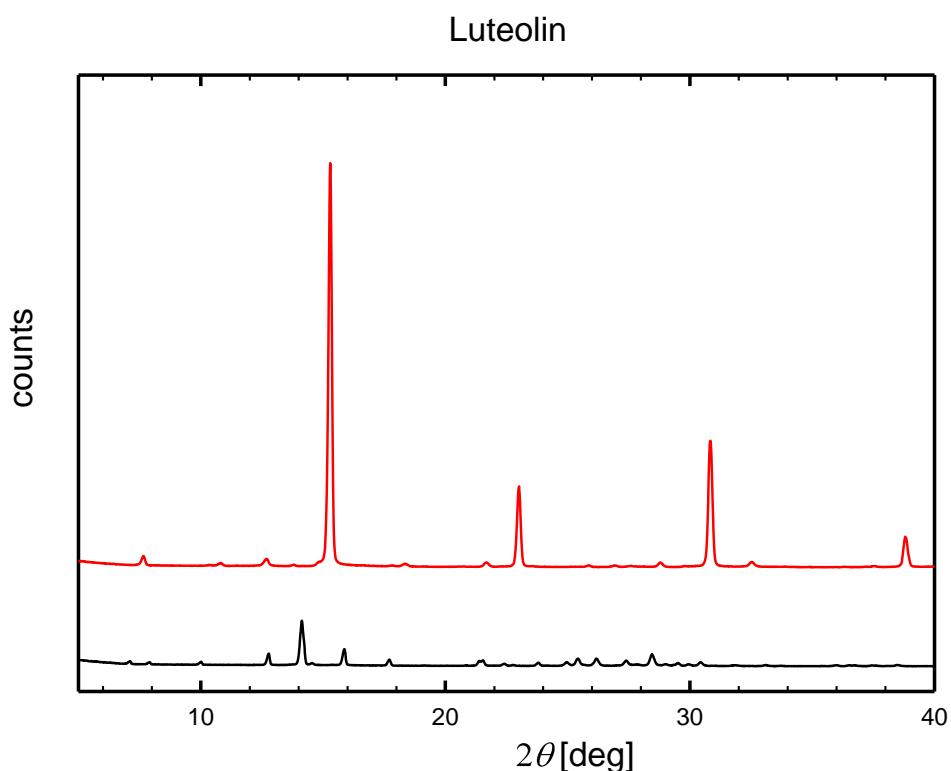


Figure 85. PXRD pattern for LT: untreated (as received) and treated (at $P_{in} = 40$ bar and $\Delta P = 25$ bar). Red lines represent treated LT and black lines represent untreated LT. (Note: patterns have been vertically offset for clarity).

The SEM images for the two samples are shown in Figure 86. The untreated sample contains crystals that are about $50 \mu\text{m}$ long with thin edges - Figure 86a. The treated sample shows a large portion of unaltered material but also nanoflowers of varying sizes - Figure 86b.

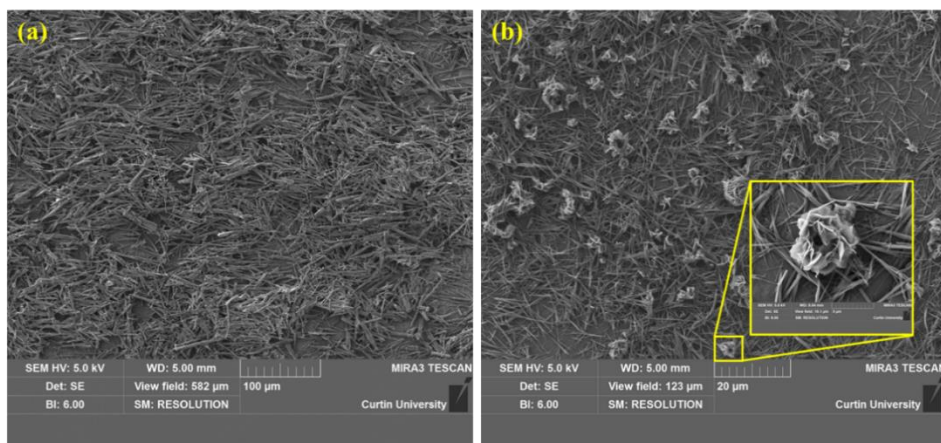


Figure 86. SEM images for Luteolin: (a) untreated and (b) treated material at $P_{in} = 40$ bar and $\Delta P = 25$ bar.

DAP was microprecipitated from a solution of the same molarity as LT (6.8 mmol/l) from the binary solvent, under the same conditions: $P_{in} = 40$ bar and $\Delta P = 25$ bar. The XRD patterns for untreated and treated DAP appear substantially similar - Figure 87.

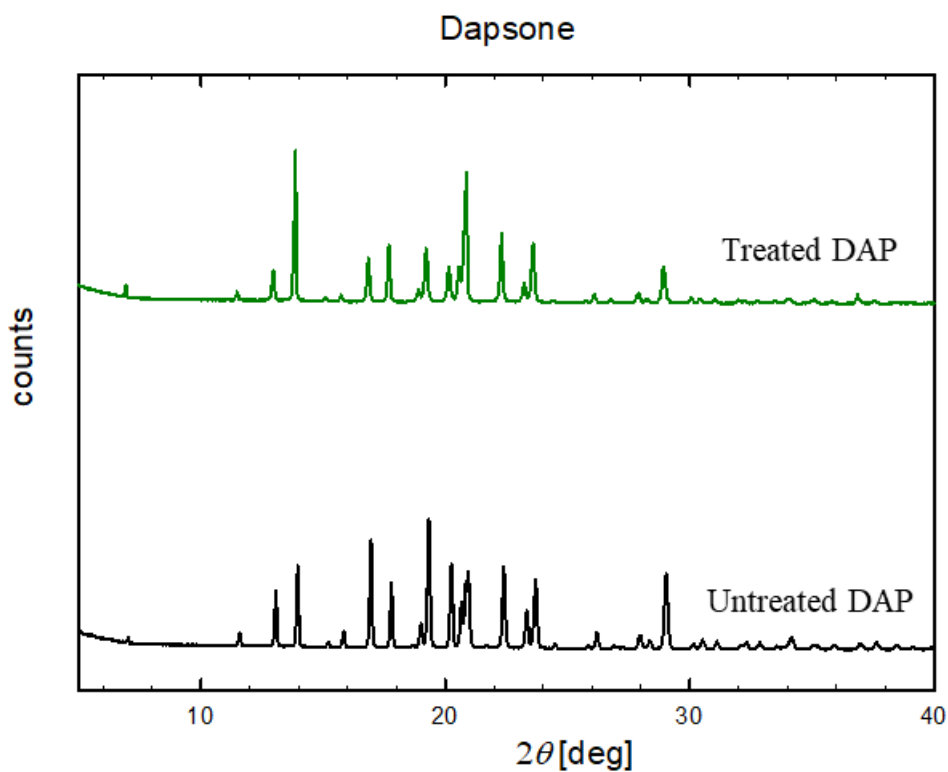


Figure 87. PXRD pattern for DAP: untreated (as received) and treated (at $P_{in} = 40$ bar and $\Delta P = 25$ bar). (Note: patterns have been vertically offset for clarity).

It was observed that 2θ values for the two samples were the same with some differences in the peak intensities (2θ values of 13.8, 17.7, 19.2, 22.3, 23.6 and 28.9°). This implies that the crystal structure for DAP remained effectively unaltered when microcrystallized under the given processing conditions.

The SEM images for the untreated and treated DAP samples are shown in Figure 88. We see poorly defined shapes for the untreated sample (Figure 88a) whereas the material crystallized through the micromixer has long, well-defined crystals (Figure 88b). This implies that the morphology for the DAP crystals was modified when using the GAS process however the crystal structure remained unchanged.

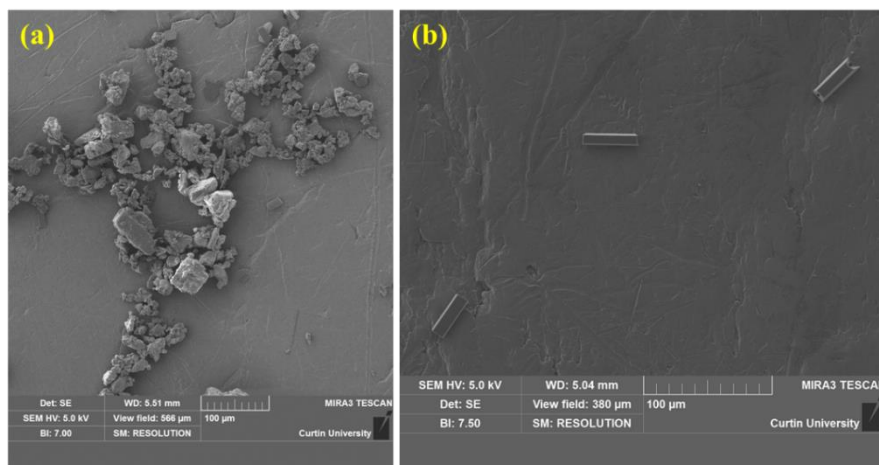


Figure 88. SEM images for DAP: (a) untreated and (b) treated material at $P_{in} = 40$ bar and $\Delta P = 25$ bar.

We have successfully microprecipitated the individual APIs using the proposed microGAS process. However, it was observed that even though LT showed a significant difference in crystal structure after processing, DAP remained essentially unchanged under the same process conditions when microprecipitating from the binary solvent.

An equimolar solution of DAP and LT (3.4 mmol/l each) in the binary solvent was then microcrystallized under the same process conditions ($P_{in} = 40$ bar, $\Delta P = 25$ bar). The XRD pattern for the mixed sample is shown in Figure 89. The 2θ values for the peaks of individual APIs and mixed samples are listed in Table 13.

Table 13. Peak positions for DAP, LT, and DAP-LT samples microprecipitated at $P_{in} = 40$ bar and $\Delta P = 25$ bar.

API	Molar Ratio	$^{\circ} 2\theta$
DAP	-	13.8, 17.7, 19.2, 22.3, 23.6 and 28.9
LT	-	15.3, 23, 30.8 and 38.8
DAP-LT	1:1	15.3, 23.0, 30.8 and 38.8
DAP-LT	5:1	13.9, 15.3, 17.7, 19.2, 20.9, and 23.6

The comparison of the peak positions of the DAP-LT samples with the individual APIs shows that the significant peak positions of the mixed sample resemble those for the individual APIs - Figure 89. Majority of the DAP-LT peaks coincide with the peak positions for treated LT (Figure 85) with very few peaks of DAP. This shows that the XRD peaks for DAP from the cocrystal sample are missing. This indicates that we have successfully produced crystalline particles of LT from the binary solution whereas the DAP remained unaltered.

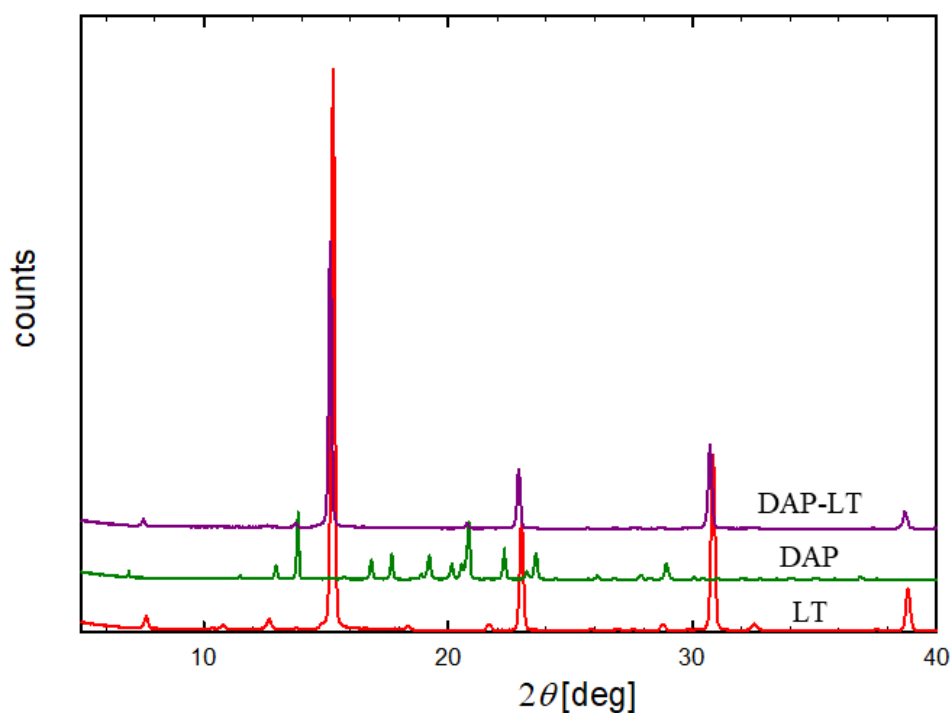


Figure 89. PXRD pattern for LT, DAP and DAP-LT (equimolar) samples processed at $P_{in} = 40$ bar and $\Delta P = 25$ bar. (Note: patterns have been vertically offset for clarity).

We further compare the XRD patterns for cocrystal samples (equimolar solution) crystallized at two different values of the fluid driving pressure (10 bar and 25 bar) - Figure 90. The sample patterns are almost identical. Since driving pressure mostly affects the residence time in the micromixer (Chapter 3(254)) this implies that shorter fluid residence times in the micromixer do not promote the formation of a cocrystal. In other words, faster mixing was not the reason for the absence of cocrystals in experiments carried out at $\Delta P = 25$ bar.

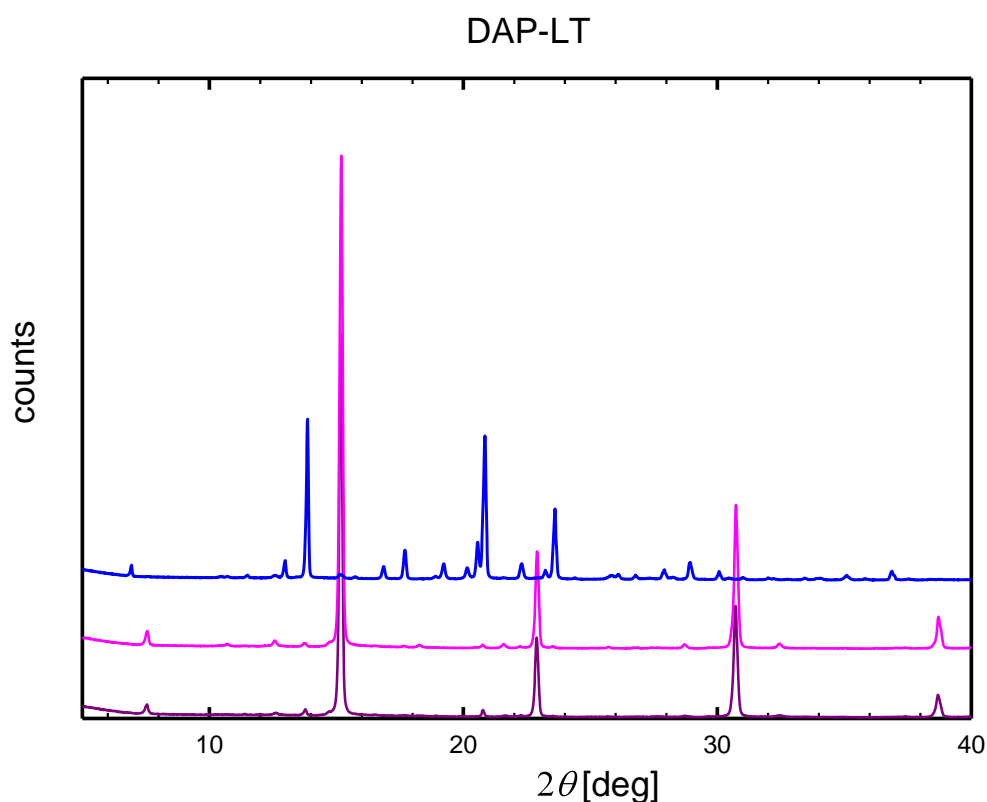


Figure 90. PXRD pattern for DAP-LT samples processed at $P_{in} = 40$ bar: blue lines ($\Delta P = 10$ bar, 5:1), pink lines ($\Delta P = 10$ bar, 1:1) and purple lines ($\Delta P = 25$ bar, 1:1). (Note: patterns have been vertically offset for clarity).

The ratio of DAP to LT in the binary solution was increased from 1:1 to 5:1 to probe the influence of drug-drug ratio on the cocrystallization process ($P_{in} = 40$ bar, $\Delta P = 10$ bar). The XRD patterns for the two samples are very different – Figure 90. In the sample with 5:1 ratio we observe new peaks at 2θ values corresponding to DAP along with very few peaks of LT -Table 13. This shows that when precipitating DAP-LT

from a 5:1 solution the presence of DAP is significant when analysing the mixed sample.

Since no new peaks are observed for DAP-LT samples other than the characteristic peaks for the APIs, we speculate that the data represents the crystals for DAP and LT as a physical mixture - Figure 91. However, the density of characteristic peaks for an individual API can be varied by manipulating its concentration ratio in the multicomponent solution.

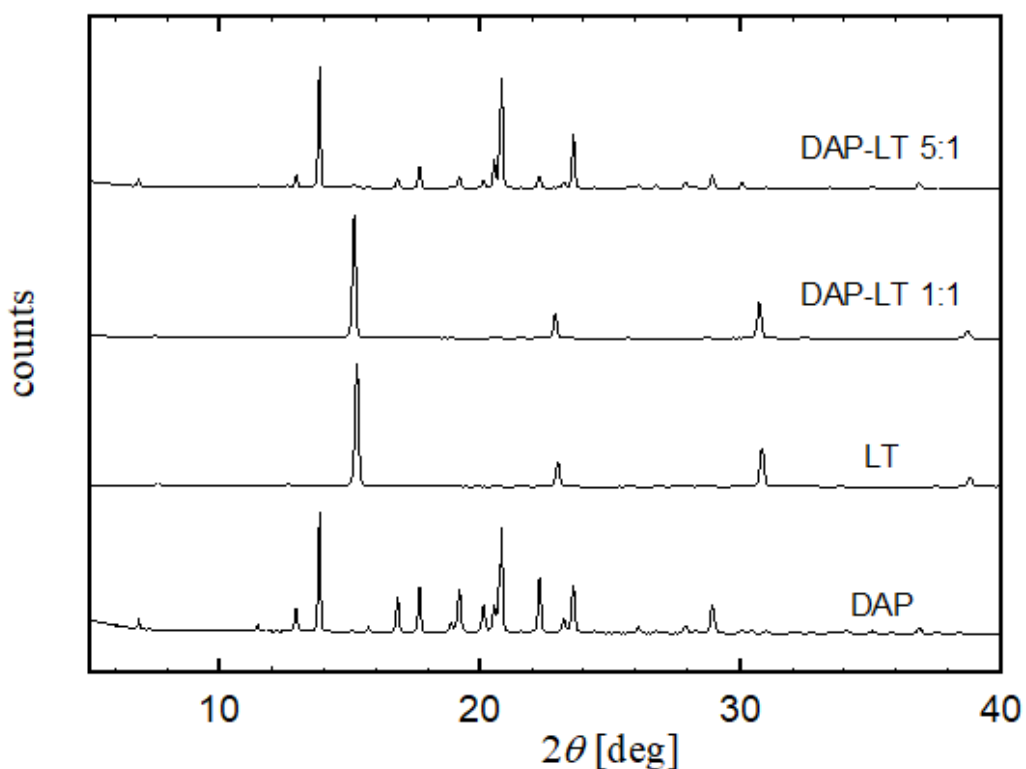


Figure 91. Comparison of the XRD peaks for the individual APIs and their mixtures. (Note: patterns have been vertically offset for clarity).

The formation of caffeine/dapsone (CAF/DAP) cocrystals by slow evaporation method from different solvents and solvent combinations was investigated by Amaral et al.(322) The simulated PXRD pattern for the CAF/DAP cocrystal (1:1) analysis shows peaks at 5.3°, 11.0°, 13.0°, 14.0°, 15.1°, and 24.2 ° (2θ), related to the CAF/DAP (1:1) cocrystal; peaks at 26.6° and 28.2° (2θ) possibly due the shift of peaks at 26.4°

and 28.4° from CAF; and peaks at 20.0° and 28.2° (2θ) possibly due the shift of peaks at 20.2° and 29.0° present in DAP, respectively - Figure 92.

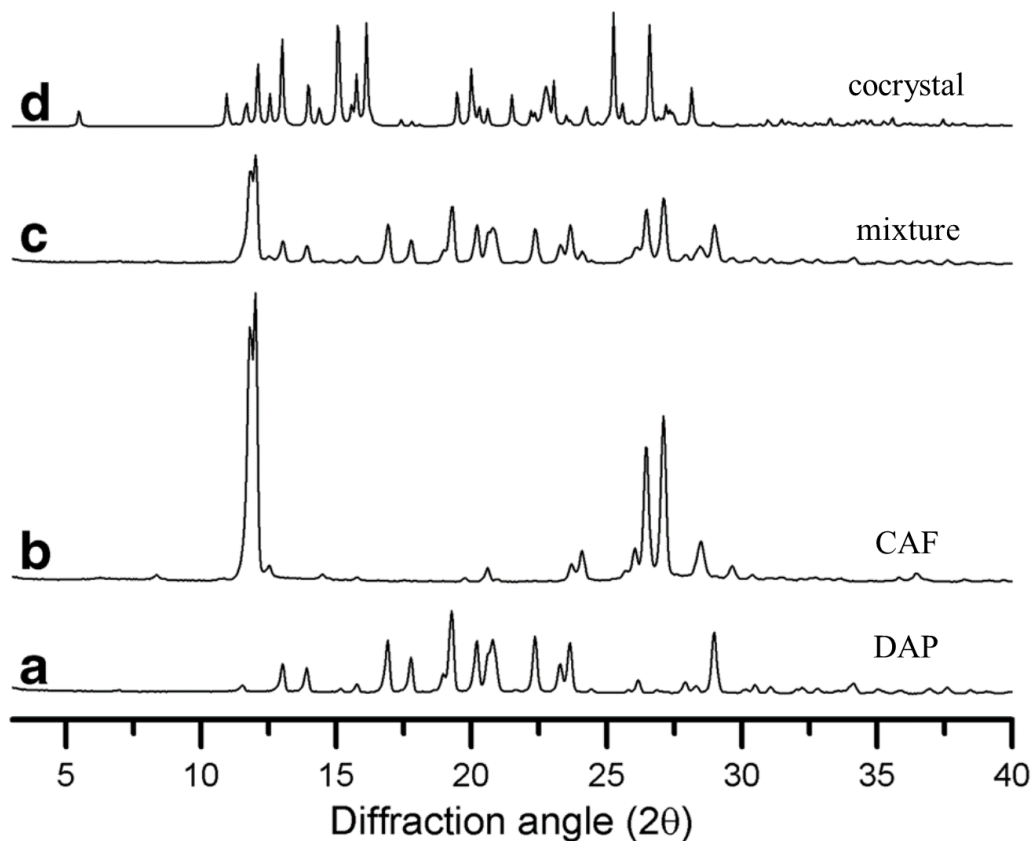


Figure 92. PXRD pattern of dapsone (a), caffeine (b), physical mixture CAF/DAP (1:1) PM (c), cocrystal CAF/DAP (1:1) and simulated (d). (322)

The SEM images of the precipitates obtained from the three mixed samples (compared in Figure 90) are shown in Figure 93. There was a homogeneity in the morphology for the particles obtained for the binary samples processed under different conditions. Some unaltered material can be seen along with these new crystal shapes resembling an octahedra. However, for lower fluid driving pressures, the octahedral shapes are rather poorly defined.

Further experimentation on the possible cocrystallization of DAP and LT could not be conducted due to time restrictions. Nevertheless, we can examine the results and define an improved strategy for cocrystallization.

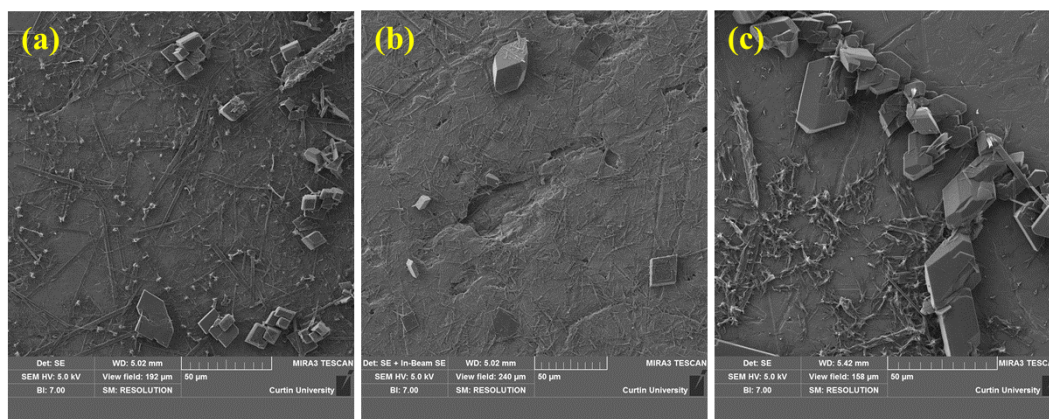


Figure 93. SEM images for DAP-LT particles at $P_{in} = 40$ bar: (a) API ratio of 1:1 produced at $\Delta P = 25$ bar, (b) API ratio of 1:1 produced at $\Delta P = 10$ bar, and (c) API ratio of 5:1 produced at $\Delta P = 10$ bar.

Table 14 shows the API solubilities in the individual solvents (we could not source for a solubility value of the APIs in the binary solvent but estimate it to be the average of the API solubility in the individual solvents). The difference between LT and DAP solubilities is significant with the DAP solubility being ~ 10 times more. This vast difference in the API solubilities shows that when an equimolar solution of the two APIs is microprecipitated using our rig, significantly different supersaturation states were obtained for the two drugs.

Table 14. Solubility values for DAP and LT in individual solvents at 25 °C.

API	Solvent	S (mg/ml)
DAP(323)	Ethanol	20.3
	Acetone	327.1
LT(324)	Ethanol	9.0
	Acetone	6.1

The supersaturation achieved for DAP, for the concentrations used in the experiments, is roughly 10 times smaller than that for LT (Equation 32). Increasing the relative

concentration of DAP leads to a clearly selected presence of DAP in the DAP-LT mixture - Figure 90. It makes sense that further increase of DAP concentration should be pursued. Ideally, the supersaturation of both API should be the same because it may correspond better to the equimolar conditions used by Jiang et al.(317) in the slow formation of cocrystals. With DAP and LT it seems possible to achieve the same supersaturation state for DAP-LT ratio of 10:1. Thus, while we did not achieve a fast microprecipitation of an API cocrystal we believe our technique has real potential to achieve that goal.

6.3 Conclusions

We have demonstrated the microprecipitation of a combination of two model APIs, Dapsone and Luteolin, from a binary solvent of ethanol and acetone (1:1 v/v). From particle characterization we observed that LT formed highly crystalline particles under the given process conditions with some unaltered material in the background. The XRD pattern for the LT precipitates was significantly different from that of the untreated material. However, DAP showed no noticeable variant in its crystallinity. Upon microprecipitation of the multicomponent solution, we noticed that the particles for different DAP-LT ratios (1:1 and 5:1) show the significant peaks for the individual APIs. Thus, successful coprecipitation of the model APIs was achieved, however, XRD analysis showed no new peaks that would indicate the formation of cocrystals. We propose to vary the API concentrations and drug-drug ratios in the future work, especially significantly increasing DAP concentrations in the multicomponent solution (~10x for DAP-LT) for successful formation of cocrystals. The current platform holds the potential for manufacturing cocrystals for a range of API combinations under optimized conditions. Moreover, it could be used for the coprecipitation of API-polymer formulations where the API can be suspended in a polymer matrix for drug delivery purposes.

7 Conclusions

In pharmaceutical manufacturing, particle size and morphology must be controlled reliably as they determine the physicochemical properties of APIs produced. Dense gas processing is a viable alternative to traditional pharmaceutical crystallization, e.g. cooling, evaporative or liquid antisolvent. The use of compressed CO₂ as an antisolvent allows for greener processing of pharmaceutical compounds by reducing the amount of solvent needed and facilitating the removal of organic residues. Current dense gas processes are batch-based and hence there is significant scope for process intensification by converting them to continuous flow processes. The motivation behind the present work was to incorporate a gas antisolvent process on a microfluidic platform in order to combine the benefits of the two techniques.

In this thesis, we developed a novel microfluidic platform that allows carrying continuous crystallization of pharmaceutical products. Using dense CO₂ as an antisolvent, we successfully controlled the particle size and crystal morphology obtained during microcrystallization.

The first task was to assemble a reliable high-pressure microfluidic system that can sustain pressures required in classical dense gas processing, i.e. about an order of magnitude higher than what is standard in microfluidics (below 5 bar). This required careful consideration of the design of the micromixers and all connections, especially when interfacing the micromixers. We constructed and validated a rig that can sustain pressures up to 100 bar (at 25 °C). A key element was the fabrication of a bespoke metal holder which allowed reliable delivery of pressurized fluids to and from the micromixers. A gas antisolvent (GAS) process was carried out using this microfluidic platform. Subcritical CO₂ was used as its density provided the required antisolvent effect in all cases studied. A gas-expanded liquid was formed under dynamic conditions in micromixers of various design.

The second task was to validate the use of the platform for the microcrystallization of various APIs. Solutions of APIs in organic solvents were crystallized using the GAS process. Anticancer, antifungal, antileprotic, and corticosteroid drugs were successfully processed and characterized. The role of key process parameters (CO₂ density and viscosity, fluid driving pressure, micromixer geometry, solution concentration) on crystallization kinetics was investigated. Experiments showed that

gas-liquid mixing has a strong influence on the microprecipitation process. In general, faster mixing led to the generation of smaller particles whereas increased initial API concentration resulted in an increase in particle size.

The third task was to investigate the crystallization behaviour of various API-solvent combinations. By selecting different compounds, we obtained a range of particle sizes with different morphologies. The size of griseofulvin particles decreased depending on the solvent used in the order: DMF > acetone > ethyl acetate. The role of the solvent was mainly related to its ability to mix with CO₂. Higher solvent affinity to CO₂ resulted in faster expansion which led to the formation of smaller particles.

Various APIs produced different outcomes when crystallized from the same solvent. When precipitating from DMF, particle size decreased in the order: Luteolin > Griseofulvin > Budesonide. This behaviour was correlated with the molecular size of the API suggesting that diffusion-based crystal growth dominates the process of crystallization. Under conditions of fast gas-liquid mixing (higher fluid driving pressure or solvent expansion rate), we produced organic particles with the unique nanoflower morphology. This was done without the use of any additives and demonstrates the potential of our platform in producing purely organic, hierarchical nanostructures. Current methods for synthesizing nanoflower particles require the use of additives or rather complex procedures.

The fourth task was to examine the role that micromixer geometry plays in the process of microcrystallization. We used the same junction where gas and solution meet but varied the length of the mixing channel that follows. The different fluidic resistance led to a comparison between the intensity of gas-liquid mixing which in turn influenced the microprecipitation process. Smaller particles (<1 μm) were obtained under slow mixing conditions as compared to the particles (1-10 μm) produced from more intense gas-liquid mixing.

The fifth task was to produce cocrystals of an API and a suitable coformer. Cocrystals provide the opportunity to improve the properties of the API (e.g. solubility and hence bioavailability) without modifying them chemically. It is also possible to create cocrystals with enhanced therapeutic effects. Traditional cocrystal formation is based on slow evaporation from concentrated mixed solutions and is time consuming. Our microfluidic platform allows the collection of sufficient product for physical

characterization in minutes. We produced a solid mixture of dapsone and luteolin but did not obtain strong evidence of cocrystal formation. We estimate that the vast difference in API solubilities led to very different supersaturation levels and prevented cocrystallization from happening. This problem could be resolved by adjusting the properties of the solvent used and/or the concentrations in the feed solution. Thus, the formation of cocrystals could be a meaningful extension of this work.

In summary, the work included in this thesis demonstrated the building of a high-pressure microfluidic platform and exploring its potential for crystallizing APIs in a reliable, continuous fashion. The micromixers were fabricated using standard lithography which allows for design flexibility and the bespoke metal holder enables the use of off-the-shelf components and connectors to standard pumps for high-pressure fluid delivery. Hence the proposed platform provides the opportunity to implement a variety of processes using the same rig. Control over particle size and morphology was achieved by manipulation of the basic process parameters for various API-solvent pairs. This platform offers great control over particle size and morphology and can solve some of the deficits of current crystallization methods. The microcrystallization described here is fast and could be extended to the formation of cocrystals or API encapsulation in suitable biopolymers. The technique should be of considerable interest to researchers involved in pharmaceutical production and innovation.

8 Appendices

8.1 Holders for High-Pressure Experiments

The two holders used for the initial high-pressure tests to check the durability of commonly used components are shown in Figure 94. The PMMA holder has a window deeper than the width for the bonded micromixer substrate - Figure 94a (left). Hence spacers need to be used to fill into that space. A stack of BF33 substrates (unbonded) of the same dimensions as the micromixers (70 x 30 mm) is used for this purpose. Figure 94b shows the widening on the port cavity where the flangeless fittings are screwed in. This damages the threads in the polymer substrate due to overtightening of the fittings to avoid leaks. The metal holder is made in stainless-steel, of equivalent design, and does not require any spacer - Figure 94a (right). The crack in the micromixer (Figure 94a) is due to the pressure generated from the metal holder on the micromixer's edge.

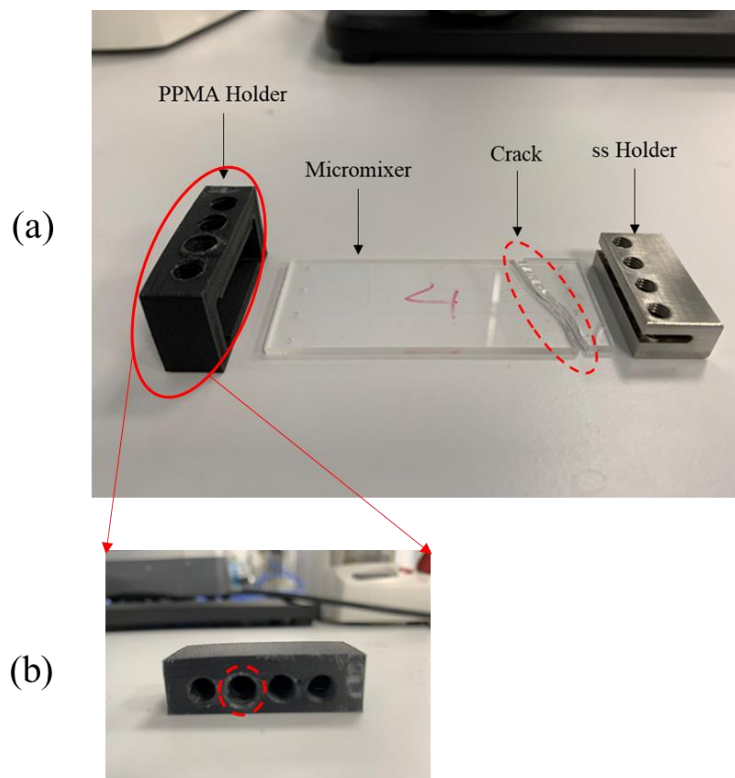


Figure 94. (a) Two different holders (on left – polymer & on right – metal) used for testing the durability for commonly used components under high-pressures. (b) Widening of the port cavities in the polymer holder due to overtightening of flangeless fittings.

8.2 Connectors for the Interface

During the high-pressure experiments, the polymer tubing tends to pop out of the flangeless fittings. To hold the polymer tubing in place, we tried gluing the tubing to the ferrule using a superglue purchased from the supermarket (LOCTITE® EPOXY PLASTIC) - Figure 95. However, this assembly fails after a short period.

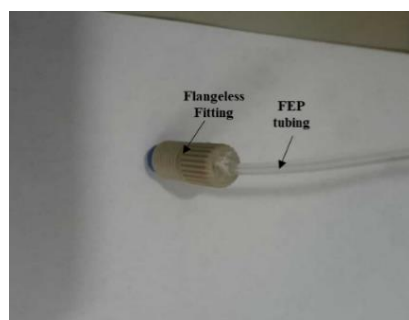


Figure 95. FEP tubing glued at the end that goes into the flangeless fitting.

To address this issue, we use HPLC connectors (Valco ZBU1XC) for interfacing the micromixer where the tubing is swaged into the connector. This assembly can sustain high pressures (up to 100 bar at 25 °C) without failure.

8.3 Metal Holder

The schematic (Figure 96) representing the principle behind the holder depicts the micromixer encapsulation between the two holder plates and interfacing for fluid delivery.

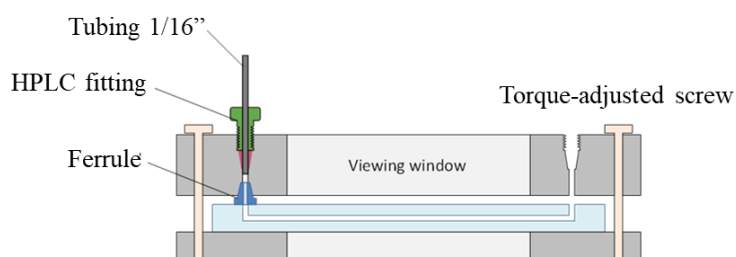


Figure 96. Schematic showing the holder-micromixer assembly used for the high-pressure experiments.

This is designed to allow the use of HPLC fittings (Valco ZBU1XC) for interfacing the ISCO pumps, commonly used with traditional engineering rigs, to a glass micromixer which is commonly employed in microfluidics. The idea behind this holder is to have increased durability from the metal substrate that maintains thread integrity and avoid leaks at the interface for extended periods under the high pressures employed (up to 100 bar). The other key requirement for the holder is to maintain homogenous pressure across the micromixer. To achieve that the holder is made of two parts, the micromixer is sandwiched between these parts, that can be held together using metal bolts.

8.4 Attribution Statement

This is to confirm that despite repeated reminders, Deepali was unable to get a response from Prof Neil Foster (one of the authors on a manuscript) regarding signing of the Authors Attribution Form. Subsequently, the matter was discussed with the Dean (R&D) Prof Kate Trinajstic, who advised to get a written confirmation from the all remaining authors – Prof Craig Priest, Dr Rossen Sedev and Dr Jane Beh. I wish to confirm that we now have consents from them regarding the attribution to Prof Neil Foster.

With regards

Vishnu

Vishnu Pareek
John Curtin Distinguished Professor
Dean of Engineering, Faculty of Science and Engineering
GPO Box U1987 Perth WA 6845 Australia

Curtin University
Tel | +61 8 9266 4687


Email | v.pareek@curtin.edu.au
Web | <http://curtin.edu.au>



Curtin University is a trademark of Curtin University of Technology
CRICOS Provider Code 003022 (2016)

8.5 Copyright Permissions

For Figure 1

This page is available in the following languages: 



Creative Commons License Deed

Attribution 4.0 International (CC BY 4.0)



This is a human-readable summary of (and not a substitute for) the [license](#).

You are free to:

Share — copy and redistribute the material in any medium or format

Adapt — remix, transform, and build upon the material

for any purpose, even commercially.

The licensor cannot revoke these freedoms as long as you follow the license terms.

Under the following terms:

Attribution — You must give appropriate credit, provide a link to the license, and indicate if changes were made. You may do so in any reasonable manner, but not in any way that suggests the licensor endorses you or your use.

No additional restrictions — You may not apply legal terms or technological measures that legally restrict others from doing anything the license permits.

For Figure 2

Case CSCSI0021301 comments added

Comments:

09-03-2021 06:12:53 AM EDT - Vojin Vucic

Additional comments

Dear Dr. Arora,

Thank you for contacting ACS Publications Support.

Your permission request is granted and there is no fee for this reuse.

In your planned reuse, you must cite the ACS article as the source, add this direct link:

<https://pubs.acs.org/doi/10.1021/acs.cgd.8b01200>, and include a notice to readers that further permissions related to the material excerpted should be directed to the ACS.

Please do not hesitate to contact us if you need any further assistance.

Sincerely,

Vojin Vucic
ACS Publications Support
Customer Services & Information
Website: <https://acs.service-now.com/acs>
Email: support@services.acs.org
Phone: 800-227-9919 | 202-872-(HELP) 4357

Ref.MSG0155750_NDDqegXICBfZgCkOTDih

For Figure 3

ELSEVIER LICENSE TERMS AND CONDITIONS

Sep 03, 2021

This Agreement between Curtin University -- Deepali Arora ("You") and Elsevier ("Elsevier") consists of your license details and the terms and conditions provided by Elsevier and Copyright Clearance Center.

License Number	5141210157066
License date	Sep 03, 2021
Licensed Content Publisher	Elsevier
Licensed Content Publication	International Journal of Pharmaceutics
Licensed Content Title	Nanosuspension for improving the bioavailability of a poorly soluble drug and screening of stabilizing agents to inhibit crystal growth
Licensed Content Author	Indrajit Ghosh,Sonali Bose,Radha Vippagunta,Ferris Harmon
Licensed Content Date	May 16, 2011
Licensed Content Volume	409
Licensed Content Issue	1-2
Licensed Content Pages	9
Start Page	260
End Page	268
Type of Use	reuse in a thesis/dissertation
Portion	figures/tables/illustrations
Number of figures/tables/illustrations	1
Format	electronic
Are you the author of this Elsevier article?	No
Will you be translating?	No
Title	Miss
Institution name	Curtin University
Expected presentation date	Sep 2021
Portions	Figure 8
Requestor Location	Curtin University Kent Street Bentley Perth, WA 6102 Australia Attn: Curtin University
Publisher Tax ID	GB 494 6272 12
Total	0.00 AUD

For Figure 4

SPRINGER NATURE LICENSE TERMS AND CONDITIONS

Sep 03, 2021

This Agreement between Curtin University -- Deepali Arora ("You") and Springer Nature ("Springer Nature") consists of your license details and the terms and conditions provided by Springer Nature and Copyright Clearance Center.

License Number	5141210660975
License date	Sep 03, 2021
Licensed Content Publisher	Springer Nature
Licensed Content Publication	Springer eBook
Licensed Content Title	Metastability of Supersaturated Solution and Nucleation
Licensed Content Author	Noriaki Kubota, Masanori Kobari, Izumi Hirasawa
Licensed Content Date	Jan 1, 2015
Type of Use	Thesis/Dissertation
Requestor type	academic/university or research institute
Format	electronic
Portion	figures/tables/illustrations
Number of figures/tables/illustrations 1	
Will you be translating?	no
Circulation/distribution	50000 or greater
Author of this Springer Nature content	no
Title	Miss
Institution name	Curtin University
Expected presentation date	Sep 2021
Portions	Figure 7.4
Requestor Location	Curtin University Kent Street Bentley Perth, WA 6102 Australia Attn: Curtin University
Total	0.00 AUD

For Figure 5



This is a License Agreement between Deepali Arora (Curtin University) ("User") and Copyright Clearance Center, Inc. ("CCC") on behalf of the Rightsholder identified in the order details below. The license consists of the order details, the CCC Terms and Conditions below, and any Rightsholder Terms and Conditions which are included below. All payments must be made in full to CCC in accordance with the CCC Terms and Conditions below.

Order Date	03-Sep-2021	Type of Use	Republish in a thesis/dissertation
Order License ID	1145328-1	Publisher	ROYAL SOCIETY OF CHEMISTRY
ISSN	1466-8033	Portion	Chart/graph/table/figure

LICENSED CONTENT

Publication Title	CrystEngComm	Publication Type	e-Journal
Article Title	Supersaturation and solvent dependent nucleation of carbamazepine polymorphs during rapid cooling crystallization	Start Page	813
		End Page	823
		Issue	4
Author/Editor	Royal Society of Chemistry (Great Britain)	Volume	23
Date	01/01/1999	URL	http://www.rsc.org/Publishing/journals/ce/index.asp
Language	English		
Country	United Kingdom of Great Britain and Northern Ireland		
Rightsholder	Royal Society of Chemistry		

REQUEST DETAILS

Portion Type	Chart/graph/table/figure	Distribution	Worldwide
Number of charts / graphs / tables / figures requested	1	Translation	Original language of publication
Format (select all that apply)	Electronic	Copies for the disabled?	No
Who will republish the content?	Academic institution	Minor editing privileges?	No
Duration of Use	Life of current edition	Incidental promotional use?	No
Lifetime Unit Quantity	Up to 4,999	Currency	AUD
Rights Requested	Main product		

NEW WORK DETAILS

Title	Miss	Institution name	Curtin University
Instructor name	Prof Vishnu Pareek	Expected presentation date	2021-09-03


ADDITIONAL DETAILS

Order reference number	N/A	The requesting person / organization to appear on the license	Deepali Arora (Curtin University)
------------------------	-----	---	-----------------------------------

REUSE CONTENT DETAILS


Title, description or numeric reference of the portion(s)	Figure 11	Title of the article/chapter the portion is from	Supersaturation and solvent dependent nucleation of carbamazepine polymorphs during rapid cooling crystallization
Editor of portion(s)	Ouyang, Jinbo; Chen, Jian; Rosbottom, Ian; Chen, Wenqian; Guo, Mingxia; Heng, Jerry Y. Y.	Author of portion(s)	Ouyang, Jinbo; Chen, Jian; Rosbottom, Ian; Chen, Wenqian; Guo, Mingxia; Heng, Jerry Y. Y.
Volume of serial or monograph	23	Issue, if republishing an article from a serial	4
Page or page range of portion	813-823	Publication date of portion	2021-01-01

For Figure 6

HomeHelp ▾Live ChatDeepali Arora ▾

A Review of Classical and Nonclassical Nucleation Theories

Author: S. Karthika, T. K. Radhakrishnan, P. Kalaichelvi

 ACS Publications
Most Trusted. Most Cited. Most Read.

Publication: Crystal Growth and Design

Publisher: American Chemical Society

Date: Nov 1, 2016

Copyright © 2016, American Chemical Society

PERMISSION/LICENSE IS GRANTED FOR YOUR ORDER AT NO CHARGE

This type of permission/license, instead of the standard Terms and Conditions, is sent to you because no fee is being charged for your order. Please note the following:

- Permission is granted for your request in both print and electronic formats, and translations.
- If figures and/or tables were requested, they may be adapted or used in part.
- Please print this page for your records and send a copy of it to your publisher/graduate school.
- Appropriate credit for the requested material should be given as follows: "Reprinted (adapted) with permission from {COMPLETE REFERENCE CITATION}. Copyright {YEAR} American Chemical Society." Insert appropriate information in place of the capitalized words.
- One-time permission is granted only for the use specified in your RightsLink request. No additional uses are granted (such as derivative works or other editions). For any uses, please submit a new request.

If credit is given to another source for the material you requested from RightsLink, permission must be obtained from that source.

BACK

CLOSE WINDOW

© 2021 Copyright - All Rights Reserved | Copyright Clearance Center, Inc. | Privacy statement | Terms and Conditions
Comments? We would like to hear from you. E-mail us at customer@copyright.com

For Figure 7

© 2012 The Author(s). Licensee IntechOpen. This chapter is distributed under the terms of the [Creative Commons Attribution 3.0 License](#), which permits unrestricted use, distribution, and reproduction in any medium, provided the original work is properly cited.


How to cite and reference
Link to this chapter [copy to clipboard](#)

<https://www.intechopen.com/chapters/36355>


Cite this chapter [copy to clipboard](#)

Miray Çelikbilek, Ali Erçin Ersundu and Süheyla Aydın (April 27th 2012). Crystallization Kinetics of Amorphous Materials, *Advances in Crystallization Processes*, Yitzhak Mastai, IntechOpen, DOI: 10.5772/35347. Available from: <https://www.intechopen.com/chapters/36355>

For Figure 8

Home Help ▾ Live Chat Deepali Arora ▾

Cooling Crystallization of Indomethacin: Effect of Supersaturation, Temperature, and Seeding on Polymorphism and Crystal Size Distribution

 **ACS Publications**
Most Trusted. Most Cited. Most Read.

Author: Chandrakant R. Malwade, Haiyan Qu

Publication: Organic Process Research & Development

Publisher: American Chemical Society

Date: Jun 1, 2018

Copyright © 2018, American Chemical Society

PERMISSION/LICENSE IS GRANTED FOR YOUR ORDER AT NO CHARGE

This type of permission/license, instead of the standard Terms and Conditions, is sent to you because no fee is being charged for your order. Please note the following:

- Permission is granted for your request in both print and electronic formats, and translations.
- If figures and/or tables were requested, they may be adapted or used in part.
- Please print this page for your records and send a copy of it to your publisher/graduate school.
- Appropriate credit for the requested material should be given as follows: "Reprinted (adapted) with permission from {COMPLETE REFERENCE CITATION}. Copyright {YEAR} American Chemical Society." Insert appropriate information in place of the capitalized words.
- One-time permission is granted only for the use specified in your RightsLink request. No additional uses are granted (such as derivative works or other editions). For any uses, please submit a new request.

If credit is given to another source for the material you requested from RightsLink, permission must be obtained from that source.

[BACK](#)

[CLOSE WINDOW](#)

© 2021 Copyright - All Rights Reserved | [Copyright Clearance Center, Inc.](#) | [Privacy statement](#) | [Terms and Conditions](#)
Comments? We would like to hear from you. E-mail us at customercare@copyright.com

For Figure 9

JOHN WILEY AND SONS LICENSE TERMS AND CONDITIONS

Sep 03, 2021

This Agreement between Curtin University -- Deepali Arora ("You") and John Wiley and Sons ("John Wiley and Sons") consists of your license details and the terms and conditions provided by John Wiley and Sons and Copyright Clearance Center.

License Number	5141261133511
License date	Sep 03, 2021
Licensed Content Publisher	John Wiley and Sons
Licensed Content Publication	Wiley Books
Licensed Content Title	Sodium Chloride
Licensed Content Author	Franz Götzfried, Georg Steinhauser, Christian Bonal, et al
Licensed Content Date	Jan 15, 2010
Licensed Content Pages	48
Type of use	Dissertation/Thesis
Requestor type	University/Academic
Format	Electronic
Portion	Figure/table
Number of figures/tables	1
Will you be translating?	No
Title	Miss
Institution name	Curtin University
Expected presentation date	Sep 2021
Portions	Figure 1
Requestor Location	Curtin University Kent Street Bentley Perth, WA 6102 Australia Attn: Curtin University
Publisher Tax ID	EU826007151
Total	0.00 AUD

For Figure 10

ELSEVIER LICENSE TERMS AND CONDITIONS

Sep 08, 2021

This Agreement between Curtin University -- Deepali Arora ("You") and Elsevier ("Elsevier") consists of your license details and the terms and conditions provided by Elsevier and Copyright Clearance Center.

License Number	5144071504302
License date	Sep 08, 2021
Licensed Content Publisher	Elsevier
Licensed Content Publication	Journal of Crystal Growth
Licensed Content Title	Effects of operating conditions on agglomeration and habit of paracetamol crystals in anti-solvent crystallization
Licensed Content Author	Z.Q. Yu,R.B.H. Tan,P.S. Chow
Licensed Content Date	Jun 1, 2005
Licensed Content Volume	279
Licensed Content Issue	3-4
Licensed Content Pages	12
Start Page	477
End Page	488

Type of Use	reuse in a thesis/dissertation
Portion	figures/tables/illustrations
Number of figures/tables/illustrations	1
Format	electronic
Are you the author of this Elsevier article?	No
Will you be translating?	No
Title	Miss
Institution name	Curtin University
Expected presentation date	Sep 2021
Portions	Figure 6
Requestor Location	Curtin University Kent Street Bentley Perth, WA 6102 Australia Attn: Curtin University
Publisher Tax ID	GB 494 6272 12
Total	0.00 AUD

For Figure 11

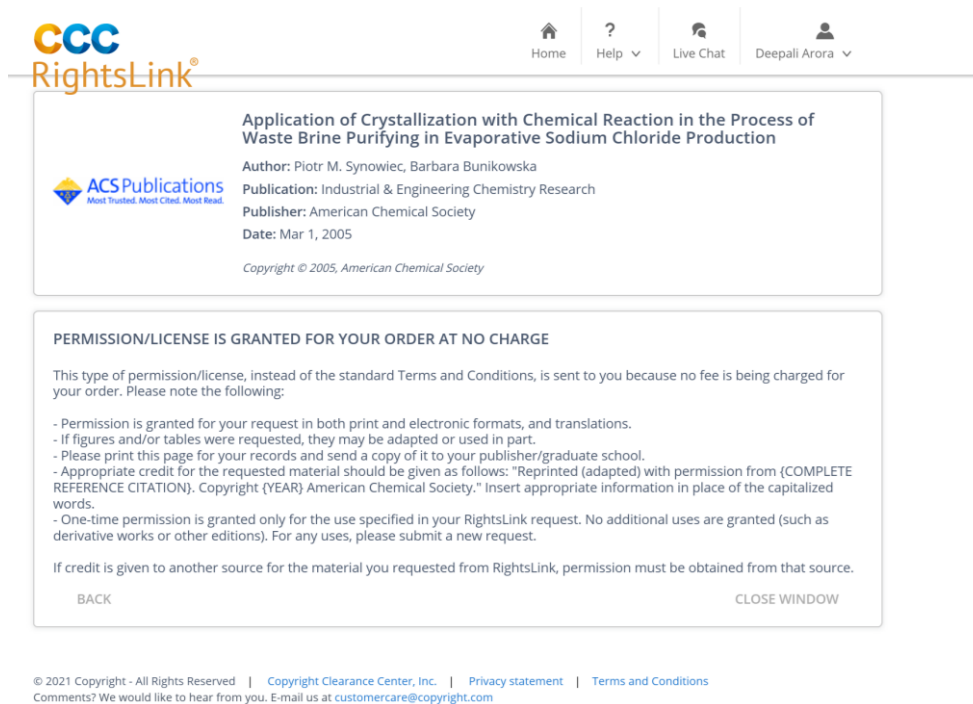
ELSEVIER LICENSE TERMS AND CONDITIONS

Sep 03, 2021

This Agreement between Curtin University -- Deepali Arora ("You") and Elsevier ("Elsevier") consists of your license details and the terms and conditions provided by Elsevier and Copyright Clearance Center.

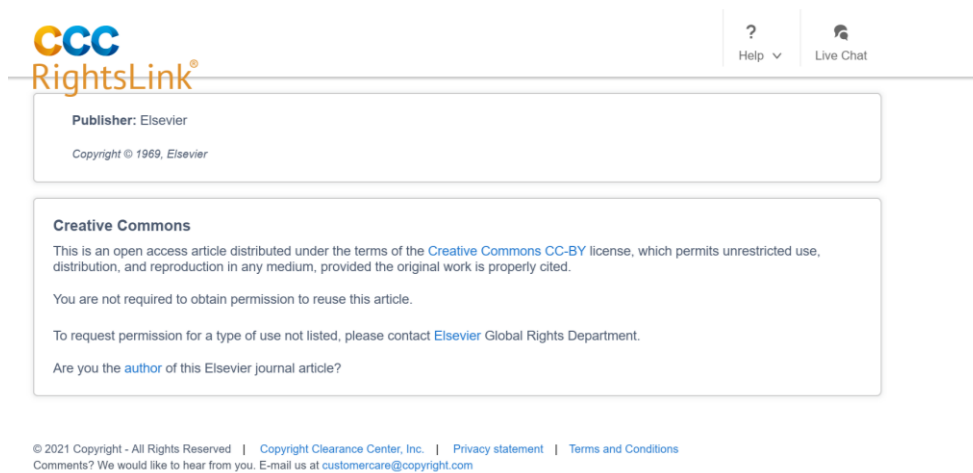
License Number	5141330604723
License date	Sep 03, 2021
Licensed Content Publisher	Elsevier
Licensed Content Publication	Biophysical Journal
Licensed Content Title	The Effect of Temperature and Solution pH on the Nucleation of Tetragonal Lysozyme Crystals
Licensed Content Author	Russell A. Judge,Randolph S. Jacobs,Tyralynn Frazier,Edward H. Snell,Marc L. Pusey
Licensed Content Date	Sep 1, 1999
Licensed Content Volume	77
Licensed Content Issue	3
Licensed Content Pages	9
Start Page	1585
End Page	1593
Type of Use	reuse in a thesis/dissertation
Portion	figures/tables/illustrations
Number of figures/tables/illustrations	1
Format	electronic
Are you the author of this Elsevier article?	No
Will you be translating?	No
Title	Miss
Institution name	Curtin University
Expected presentation date	Sep 2021
Portions	Figure 4
Requestor Location	Curtin University Kent Street Bentley Perth, WA 6102 Australia Attn: Curtin University
Publisher Tax ID	GB 494 6272 12
Total	0.00 AUD

For Figure 12




The screenshot shows the CCC RightsLink interface. At the top left is the logo for CCC RightsLink. On the top right, there are navigation links: Home, Help (with a dropdown arrow), Live Chat, and a user profile for Deepali Arora (with a dropdown arrow). The main content area is divided into two sections. The first section is titled "Application of Crystallization with Chemical Reaction in the Process of Waste Brine Purifying in Evaporative Sodium Chloride Production". It lists the author as Piotr M. Synowiec, Barbara Bunikowska, the publication as Industrial & Engineering Chemistry Research, the publisher as American Chemical Society, and the date as Mar 1, 2005. It also includes the copyright notice: Copyright © 2005, American Chemical Society. The second section is titled "PERMISSION/LICENSE IS GRANTED FOR YOUR ORDER AT NO CHARGE". It explains that this type of permission/license is granted instead of standard Terms and Conditions because no fee is being charged. It lists several conditions: permission is granted in both print and electronic formats; figures and tables may be adapted; users should print the page and send a copy to their publisher/graduate school; appropriate credit should be given as follows: "Reprinted (adapted) with permission from {COMPLETE REFERENCE CITATION}. Copyright {YEAR} American Chemical Society."; and one-time permission is granted only for the use specified in the request. It also states that if credit is given to another source, permission must be obtained from that source. At the bottom of this section are two buttons: "BACK" and "CLOSE WINDOW". At the very bottom of the page, there is a footer with copyright information: © 2021 Copyright - All Rights Reserved | Copyright Clearance Center, Inc. | Privacy statement | Terms and Conditions. It also includes a comment: "Comments? We would like to hear from you. E-mail us at customer-care@copyright.com".

For Figure 13



The screenshot shows the CCC RightsLink interface. At the top left is the logo for CCC RightsLink. On the top right, there are navigation links: Help (with a dropdown arrow) and Live Chat. The main content area is divided into two sections. The first section is titled "Publisher: Elsevier" and includes the copyright notice: Copyright © 1969, Elsevier. The second section is titled "Creative Commons". It states that this is an open access article distributed under the terms of the Creative Commons CC-BY license, which permits unrestricted use, distribution, and reproduction in any medium, provided the original work is properly cited. It also states that users are not required to obtain permission to reuse this article. To request permission for a type of use not listed, users should contact Elsevier Global Rights Department. At the bottom of this section is a question: "Are you the author of this Elsevier journal article?". At the very bottom of the page, there is a footer with copyright information: © 2021 Copyright - All Rights Reserved | Copyright Clearance Center, Inc. | Privacy statement | Terms and Conditions. It also includes a comment: "Comments? We would like to hear from you. E-mail us at customer-care@copyright.com".

For Figure 14

Home | Help | Live Chat | Deepali Arora

Economic Analysis of Integrated Continuous and Batch Pharmaceutical Manufacturing: A Case Study

Author: Spencer D. Schaber, Dimitrios I. Gerogiorgis, Rohit Ramachandran, et al
Publication: Industrial & Engineering Chemistry Research
Publisher: American Chemical Society
Date: Sep 1, 2011

Copyright © 2011, American Chemical Society

PERMISSION/LICENSE IS GRANTED FOR YOUR ORDER AT NO CHARGE

This type of permission/license, instead of the standard Terms and Conditions, is sent to you because no fee is being charged for your order. Please note the following:

- Permission is granted for your request in both print and electronic formats, and translations.
- If figures and/or tables were requested, they may be adapted or used in part.
- Please print this page for your records and send a copy of it to your publisher/graduate school.
- Appropriate credit for the requested material should be given as follows: "Reprinted (adapted) with permission from {COMPLETE REFERENCE CITATION}. Copyright (YEAR) American Chemical Society." Insert appropriate information in place of the capitalized words.
- One-time permission is granted only for the use specified in your RightsLink request. No additional uses are granted (such as derivative works or other editions). For any uses, please submit a new request.

If credit is given to another source for the material you requested from RightsLink, permission must be obtained from that source.

[BACK](#) [CLOSE WINDOW](#)

© 2021 Copyright - All Rights Reserved | [Copyright Clearance Center, Inc.](#) | [Privacy statement](#) | [Terms and Conditions](#)
Comments? We would like to hear from you. E-mail us at customer@copyright.com

For Figure 15







ELSEVIER LICENSE TERMS AND CONDITIONS

Sep 04, 2021


This Agreement between Curtin University -- Deepali Arora ("You") and Elsevier ("Elsevier") consists of your license details and the terms and conditions provided by Elsevier and Copyright Clearance Center.

License Number	5141940261038
License date	Sep 04, 2021
Licensed Content Publisher	Elsevier
Licensed Content Publication	Chemical Engineering Research and Design
Licensed Content Title	Process modelling and simulation for continuous pharmaceutical manufacturing of ibuprofen
Licensed Content Author	Hikaru G. Jolliffe, Dimitrios I. Gerogiorgis
Licensed Content Date	May 1, 2015
Licensed Content Volume	97
Licensed Content Issue	n/a
Licensed Content Pages	17
Start Page	175
End Page	191
Type of Use	reuse in a thesis/dissertation
Portion	figures/tables/illustrations
Number of figures/tables/illustrations	1
Format	electronic
Are you the author of this Elsevier article?	No
Will you be translating?	No
Title	Miss
Institution name	Curtin University
Expected presentation date	Sep 2021
Portions	Figure 4
Requestor Location	Curtin University Kent Street Bentley Perth, WA 6102 Australia Attn: Curtin University
Publisher Tax ID	GB 494 6272 12
Total	0.00 AUD

For Figure 17

  Home  Help  Email Support  Sign in  Create Account

Gas-Expanded Liquids

 **Author:** Philip G. Jessop, Bala Subramaniam
Publication: Chemical Reviews
Publisher: American Chemical Society
Date: Jun 1, 2007

Copyright © 2007, American Chemical Society

PERMISSION/LICENSE IS GRANTED FOR YOUR ORDER AT NO CHARGE

This type of permission/license, instead of the standard Terms and Conditions, is sent to you because no fee is being charged for your order. Please note the following:

- Permission is granted for your request in both print and electronic formats, and translations.
- If figures and/or tables were requested, they may be adapted or used in part.
- Please print this page for your records and send a copy of it to your publisher/graduate school.
- Appropriate credit for the requested material should be given as follows: "Reprinted (adapted) with permission from {COMPLETE REFERENCE CITATION}. Copyright (YEAR) American Chemical Society." Insert appropriate information in place of the capitalized words.
- One-time permission is granted only for the use specified in your RightsLink request. No additional uses are granted (such as derivative works or other editions). For any uses, please submit a new request.

If credit is given to another source for the material you requested from RightsLink, permission must be obtained from that source.

[BACK](#) [CLOSE WINDOW](#)

© 2021 Copyright - All Rights Reserved | [Copyright Clearance Center, Inc.](#) | [Privacy statement](#) | [Terms and Conditions](#)
Comments? We would like to hear from you. E-mail us at customer@copyright.com

For Figure 19

ELSEVIER LICENSE TERMS AND CONDITIONS

Sep 03, 2021

This Agreement between Curtin University -- Deepali Arora ("You") and Elsevier ("Elsevier") consists of your license details and the terms and conditions provided by Elsevier and Copyright Clearance Center.

License Number	5141640041770
License date	Sep 03, 2021
Licensed Content Publisher	Elsevier
Licensed Content Publication	The Journal of Supercritical Fluids
Licensed Content Title	Volume expansion in relation to the gas-antisolvent process
Licensed Content Author	J.C. de la Fuente Badilla,C.J. Peters,J. de Swaan Arons
Licensed Content Date	Feb 29, 2000
Licensed Content Volume	17
Licensed Content Issue	1
Licensed Content Pages	11
Start Page	13
End Page	23
Type of Use	reuse in a thesis/dissertation
Portion	figures/tables/illustrations
Number of figures/tables/illustrations	1
Format	electronic
Are you the author of this Elsevier article?	No
Will you be translating?	No
Title	Miss
Institution name	Curtin University
Expected presentation date	Sep 2021
Portions	Figure 3
Requestor Location	Curtin University Kent Street Bentley Perth, WA 6102 Australia Attn: Curtin University
Publisher Tax ID	GB 494 6272 12
Total	0.00 AUD

For Figures 20 and 21, and Table 4

CCC
RightsLink®

Home Help Email Support Sign in Create Account

Synthesis, Purification, and Micronization of Pharmaceuticals Using the Gas Antisolvent Technique

ACS Publications
Most Trusted. Most Cited. Most Read.

Author: B. Warwick, F. Dehghani, N. R. Foster, et al
Publication: Industrial & Engineering Chemistry Research
Publisher: American Chemical Society
Date: Dec 1, 2000
Copyright © 2000, American Chemical Society

PERMISSION/LICENSE IS GRANTED FOR YOUR ORDER AT NO CHARGE

This type of permission/license, instead of the standard Terms and Conditions, is sent to you because no fee is being charged for your order. Please note the following:

- Permission is granted for your request in both print and electronic formats, and translations.
- If figures and/or tables were requested, they may be adapted or used in part.
- Please print this page for your records and send a copy of it to your publisher/graduate school.
- Appropriate credit for the requested material should be given as follows: "Reprinted (adapted) with permission from {COMPLETE REFERENCE CITATION}. Copyright {YEAR} American Chemical Society." Insert appropriate information in place of the capitalized words.
- One-time permission is granted only for the use specified in your RightsLink request. No additional uses are granted (such as derivative works or other editions). For any uses, please submit a new request.

If credit is given to another source for the material you requested from RightsLink, permission must be obtained from that source.

BACK CLOSE WINDOW

© 2021 Copyright - All Rights Reserved | Copyright Clearance Center, Inc. | Privacy statement | Terms and Conditions
Comments? We would like to hear from you. E-mail us at customer-care@copyright.com

For Figure 22

CCC
RightsLink®

Help Email Support

Microfluidics for studying metastatic patterns of lung cancer

SPRINGER NATURE

Author: Monika Ruzicka et al
Publication: Journal of Nanobiotechnology
Publisher: Springer Nature
Date: May 27, 2019
Copyright © 2019, The Author(s)

Creative Commons

This is an open access article distributed under the terms of the [Creative Commons CC BY](#) license, which permits unrestricted use, distribution, and reproduction in any medium, provided the original work is properly cited.

You are not required to obtain permission to reuse this article.
CC0 applies for supplementary material related to this article and attribution is not required.

© 2021 Copyright - All Rights Reserved | Copyright Clearance Center, Inc. | Privacy statement | Terms and Conditions
Comments? We would like to hear from you. E-mail us at customer-care@copyright.com

For Figure 23

ELSEVIER LICENSE TERMS AND CONDITIONS

Sep 03, 2021

This Agreement between Curtin University -- Deepali Arora ("You") and Elsevier ("Elsevier") consists of your license details and the terms and conditions provided by Elsevier and Copyright Clearance Center.

License Number	5141640736581
License date	Sep 03, 2021
Licensed Content Publisher	Elsevier
Licensed Content Publication	Sensors and Actuators A: Physical
Licensed Content Title	A microfluidic relative permittivity sensor for feedback control of carbon dioxide expanded liquid flows
Licensed Content Author	Martin Andersson,Anton Wilson,Klas Hjort,Lena Klinberg
Licensed Content Date	Jan 1, 2019
Licensed Content Volume	285
Licensed Content Issue	n/a
Licensed Content Pages	8
Start Page	165
End Page	172
Type of Use	reuse in a thesis/dissertation
Portion	figures/tables/illustrations
Number of figures/tables/illustrations	1
Format	electronic
Are you the author of this Elsevier article?	No
Will you be translating?	No
Title	Miss
Institution name	Curtin University
Expected presentation date	Sep 2021
Portions	Figure 6
Requestor Location	Curtin University Kent Street Bentley Perth, WA 6102 Australia Attn: Curtin University
Publisher Tax ID	GB 494 6272 12
Total	0.00 AUD

For Figure 24

ELSEVIER LICENSE TERMS AND CONDITIONS

Sep 03, 2021

This Agreement between Curtin University -- Deepali Arora ("You") and Elsevier ("Elsevier") consists of your license details and the terms and conditions provided by Elsevier and Copyright Clearance Center.

License Number	5141640966752
License date	Sep 03, 2021
Licensed Content Publisher	Elsevier
Licensed Content Publication	Chemical Engineering Journal
Licensed Content Title	Mixing intensification under turbulent conditions in a high pressure microreactor
Licensed Content Author	Fan Zhang,Samuel Marre,Arnaud Erriguible
Licensed Content Date	Feb 15, 2020
Licensed Content Volume	382
Licensed Content Issue	n/a
Licensed Content Pages	1
Start Page	122859
End Page	0
Type of Use	reuse in a thesis/dissertation
Portion	figures/tables/illustrations
Number of figures/tables/illustrations	1
Format	electronic
Are you the author of this Elsevier article?	No
Will you be translating?	No
Title	Miss
Institution name	Curtin University
Expected presentation date	Sep 2021
Portions	Figure from Graphical Abstract
Requestor Location	Curtin University Kent Street Bentley Perth, WA 6102 Australia Attn: Curtin University
Publisher Tax ID	GB 494 6272 12
Total	0.00 AUD

For Figure 25

ELSEVIER LICENSE TERMS AND CONDITIONS

Sep 03, 2021

This Agreement between Curtin University -- Deepali Arora ("You") and Elsevier ("Elsevier") consists of your license details and the terms and conditions provided by Elsevier and Copyright Clearance Center.

License Number	5141641139633
License date	Sep 03, 2021
Licensed Content Publisher	Elsevier
Licensed Content Publication	Chemical Engineering Journal
Licensed Content Title	Process intensification for the synthesis of ultra-small organic nanoparticles with supercritical CO ₂ in a microfluidic system
Licensed Content Author	T. Jaouhari, F. Zhang, T. Tassaing, S. Fery-Forgues, C. Aymonier, S. Marre, A. Erriguible
Licensed Content Date	Oct 1, 2020
Licensed Content Volume	397
Licensed Content Issue	n/a
Licensed Content Pages	1
Start Page	125333
End Page	0
Type of Use	reuse in a thesis/dissertation
Portion	figures/tables/illustrations
Number of figures/tables/illustrations	1
Format	electronic
Are you the author of this Elsevier article?	No
Will you be translating?	No
Title	Miss
Institution name	Curtin University
Expected presentation date	Sep 2021
Portions	Figure 8
Requestor Location	Curtin University Kent Street Bentley Perth, WA 6102 Australia Attn: Curtin University
Publisher Tax ID	GB 494 6272 12
Total	0.00 AUD

For Figure 26

ELSEVIER LICENSE TERMS AND CONDITIONS

Sep 03, 2021

This Agreement between Curtin University -- Deepali Arora ("You") and Elsevier ("Elsevier") consists of your license details and the terms and conditions provided by Elsevier and Copyright Clearance Center.

License Number	5141650132556
License date	Sep 03, 2021
Licensed Content Publisher	Elsevier
Licensed Content Publication	Elsevier Books
Licensed Content Title	xPharm: The Comprehensive Pharmacology Reference
Licensed Content Author	Christine D. Waugh
Licensed Content Date	Jan 1, 2007
Licensed Content Pages	4
Start Page	1
End Page	4
Type of Use	reuse in a thesis/dissertation
Portion	figures/tables/illustrations
Number of figures/tables/illustrations	1
Format	electronic
Are you the author of this Elsevier chapter?	No
Will you be translating?	No
Title	Miss
Institution name	Curtin University
Expected presentation date	Sep 2021
Portions	Chemical Structure of Griseofulvin
Requestor Location	Curtin University Kent Street Bentley Perth, WA 6102 Australia Attn: Curtin University
Publisher Tax ID	GB 494 6272 12
Total	0.00 AUD

For Figure 27

Copyright

As a member of Publisher International Linking Association, PILA, Longdom Publishing follows the Creative Commons Attribution License and Scholars Open Access publishing policies. All the works published by Longdom Publishing are under the terms of the Creative Commons Attribution License. Most of the journals follows CC-BY and few journals follows the derivatives of CC-BY.

Content Links

[Tools](#)
[Feedback](#)
[Careers](#)
[Privacy Policy](#)
[Terms & Conditions](#)
[Authors, Reviewers & Editors](#)

Contact Longdom

Longdom Group SA
Avenue Roger Vandendriessche,
18, 1150 Brussels, Belgium
Phone: +34 911 877 608
Email: info@longdom.org

Connect

 [Facebook](#)
 [LinkedIn](#)
 [Twitter](#)

[GET THE APP](#)



Copyright © 2021 Longdom Publishing.

For Figure 28

SPRINGER NATURE LICENSE TERMS AND CONDITIONS

Sep 03, 2021

This Agreement between Curtin University -- Deepali Arora ("You") and Springer Nature ("Springer Nature") consists of your license details and the terms and conditions provided by Springer Nature and Copyright Clearance Center.

License Number	5141651082122
License date	Sep 03, 2021
Licensed Content Publisher	Springer Nature
Licensed Content Publication	AAPS PharmSciTech
Licensed Content Title	Optimization and Evaluation of the Thermosensitive In Situ and Adhesive Gel for Rectal Delivery of Budesonide
Licensed Content Author	Lin Chen et al
Licensed Content Date	Mar 3, 2020
Type of Use	Thesis/Dissertation
Requestor type	academic/university or research institute
Format	electronic
Portion	figures/tables/illustrations
Number of figures/tables/illustrations	1
Will you be translating?	no
Circulation/distribution	10000 - 19999
Author of this Springer Nature content	no
Title	Miss
Institution name	Curtin University
Expected presentation date	Sep 2021
Portions	Figure 1
Requestor Location	Curtin University Kent Street Bentley Perth, WA 6102 Australia Attn: Curtin University
Total	0.00 AUD

For Figure 29

SPRINGER NATURE LICENSE TERMS AND CONDITIONS

Sep 03, 2021

This Agreement between Curtin University -- Deepali Arora ("You") and Springer Nature ("Springer Nature") consists of your license details and the terms and conditions provided by Springer Nature and Copyright Clearance Center.

License Number	5141651330956
License date	Sep 03, 2021
Licensed Content Publisher	Springer Nature
Licensed Content Publication	Pharmaceutical Research
Licensed Content Title	Emerging Technologies to Target Drug Delivery to the Skin – the Role of Crystals and Carrier-Based Systems in the Case Study of Dapsone
Licensed Content Author	Gabriela Schneider-Rauber et al
Licensed Content Date	Nov 9, 2020
Type of Use	Thesis/Dissertation
Requestor type	academic/university or research institute
Format	electronic
Portion	figures/tables/illustrations
Number of figures/tables/illustrations	1
Will you be translating?	no
Circulation/distribution	10000 - 19999
Author of this Springer Nature content	no
Title	Miss
Institution name	Curtin University
Expected presentation date	Sep 2021
Portions	Figure 1
Requestor Location	Curtin University Kent Street Bentley Perth, WA 6102 Australia Attn: Curtin University
Total	0.00 AUD

For Table 5

ELSEVIER LICENSE TERMS AND CONDITIONS

Sep 03, 2021

This Agreement between Curtin University -- Deepali Arora ("You") and Elsevier ("Elsevier") consists of your license details and the terms and conditions provided by Elsevier and Copyright Clearance Center.

License Number 5141660000177

License date Sep 03, 2021

Licensed Content Publisher Elsevier

Licensed Content Publication Nutrition Research

Licensed Content Title Ethanol in medicines and other products intended for children: Commentary on a medical paradox

Licensed Content Author A Flocchi,E Riva,M Giovannini

Licensed Content Date Mar 1, 1999

Licensed Content Volume 19

Licensed Content Issue 3

Licensed Content Pages 7

Start Page 373

End Page 379

Type of Use reuse in a thesis/dissertation

Portion figures/tables/illustrations

Number of figures/tables/illustrations 1

Format electronic

Are you the author of this Elsevier article? No

Will you be translating? No

Title Miss

Institution name Curtin University

Expected presentation date Sep 2021

Portions Table 1

Requestor Location Curtin University
Kent Street
Bentley
Perth, WA 6102
Australia
Attn: Curtin University

Publisher Tax ID GB 494 6272 12

Total 0.00 AUD

For Figures 31, 32 and 33c

PERMISSION TO USE COPYRIGHT MATERIAL AS SPECIFIED BELOW:

Images of Fabrication Equipment used at ANFF-SA

I hereby give permission for Deepali Arora to include the abovementioned material(s) in her higher degree thesis for Curtin University, and to communicate this material via the espace institutional repository. This permission is granted on a non-exclusive basis and for an indefinite period.

I confirm that I am the copyright owner of the specified material.

Signed:

Name: Simon Doe

Position: ANFF-SA Facility Manager

Date: 6 September 2021

Please return signed form to Deepali Arora at deepali.arora@postgrad.curtin.edu.au.

For Figure 40

Try out [PMC Labs](#) and tell us what you think. [Learn More](#).

Nature Public Health Emergency Collection

Public Health Emergency COVID-19 Initiative

[Radiation in Bioanalysis](#), 2019; 8: 173–193.

Published online 2019 Jul 29. doi: [10.1007/978-3-030-28247-9_6](https://doi.org/10.1007/978-3-030-28247-9_6)

PMCID: PMC7120185

Dynamic Light Scattering (DLS)

Principles, Perspectives, Applications to Biological Samples

Guest Editor (s): Alice S. Pereira,² Pedro Tavares,³ and Paulo Limão-Vieira⁴

²Molecular Biophysics Lab., UCIBIO/Requimte, Department of Chemistry, Faculdade de Ciências e Tecnologia, Universidade NOVA de Lisboa, Caparica, Portugal

³Molecular Biophysics Lab., UCIBIO/Requimte, Department of Chemistry, Faculdade de Ciências e Tecnologia, Universidade NOVA de Lisboa, Caparica, Portugal

⁴Atomic and Molecular Collisions Laboratory, CEFITEC, Department of Physics, Faculdade de Ciências e Tecnologia, Universidade NOVA de Lisboa, Caparica, Portugal

Alice S. Pereira, Phone: +351351212948300, Fax: +351351212948550, Email: masp@fct.unl.pt.

[Contributor Information](#).

Sven Falke and Christian Betze[✉]

Laboratory for Structural Biology of Infection and Inflammation, Department of Chemistry, University of Hamburg, c/o DESY, 22607 Hamburg, Germany

Sven Falke, Email: Falke@chemie.uni-hamburg.de.

[Contributor Information](#).

[✉]Corresponding author.

Copyright © Springer Nature Switzerland AG 2019

This article is made available via the PMC Open Access Subset for unrestricted research re-use and secondary analysis in any form or by any means with acknowledgement of the original source. These permissions are granted for the duration of the World Health Organization (WHO) declaration of COVID-19 as a global pandemic.

For Figure 42

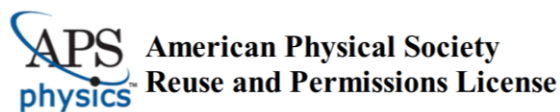
ELSEVIER LICENSE TERMS AND CONDITIONS

Sep 03, 2021

This Agreement between Curtin University -- Deepali Arora ("You") and Elsevier ("Elsevier") consists of your license details and the terms and conditions provided by Elsevier and Copyright Clearance Center.

License Number	5141670349788
License date	Sep 03, 2021
Licensed Content Publisher	Elsevier
Licensed Content Publication	Elsevier Books
Licensed Content Title	Materials for Ultra-Supercritical and Advanced Ultra-Supercritical Power Plants
Licensed Content Author	A. Di Gianfrancesco
Licensed Content Date	Jan 1, 2017
Licensed Content Pages	49
Start Page	197
End Page	245
Type of Use	reuse in a thesis/dissertation
Portion	figures/tables/illustrations
Number of figures/tables/illustrations	1
Format	electronic
Are you the author of this Elsevier chapter?	No
Will you be translating?	No
Title	Miss
Institution name	Curtin University
Expected presentation date	Sep 2021
Portions	Figure 8.24
Requestor Location	Curtin University Kent Street Bentley Perth, WA 6102 Australia Attn: Curtin University
Publisher Tax ID	GB 494 6272 12
Total	0.00 AUD

For Figure 45



03-Sep-2021

This license agreement between the American Physical Society ("APS") and Deepali Arora ("You") consists of your license details and the terms and conditions provided by the American Physical Society and SciPris.

Licensed Content Information

License Number: RNP/21/SEP/044094
License date: 03-Sep-2021
DOI: 10.1103/PhysRevLett.80.3863
Title: Hydrodynamic Focusing on a Silicon Chip: Mixing Nanoliters in Microseconds
Author: James B. Knight et al.
Publication: Physical Review Letters
Publisher: American Physical Society
Cost: USD \$ 0.00

Request Details

Does your reuse require significant modifications: No
Specify intended distribution locations: Worldwide
Reuse Category: Reuse in a thesis/dissertation
Requestor Type: Student
Items for Reuse: Figures/Tables
Number of Figure/Tables: 1
Figure/Tables Details: Figure 1
Format for Reuse: Electronic

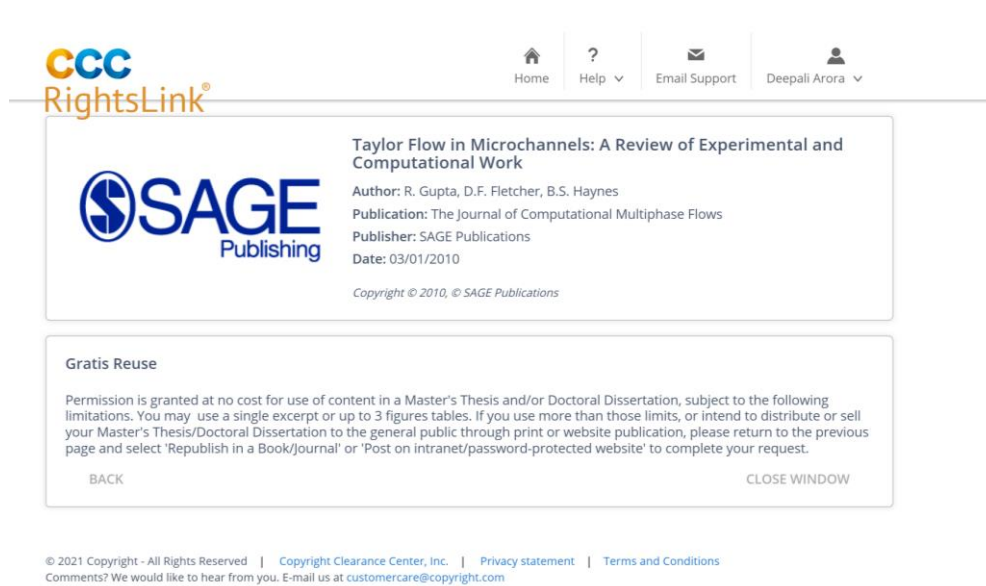
Information about New Publication:

University/Publisher: Curtin University
Title of dissertation/thesis: High-Pressure Microfluidic Crystallization of Active Pharmaceutical Ingredients Using a Gas Antisolvent Process
Author(s): Deepali Arora
Expected completion date: Sep. 2021

License Requestor Information

Name: Deepali Arora
Affiliation: Individual
Email Id: deepali.arora@postgrad.curtin.edu.au
Country: Australia

For Figure 46



The screenshot shows the CCC RightsLink interface. At the top left is the CCC RightsLink logo. On the top right, there are navigation links: Home, Help, Email Support, and a user profile for Deepali Arora. The main content area features the SAGE Publishing logo and the title "Taylor Flow in Microchannels: A Review of Experimental and Computational Work". Below the title, it lists the author (R. Gupta, D.F. Fletcher, B.S. Haynes), the publication (The Journal of Computational Multiphase Flows), the publisher (SAGE Publications), and the date (03/01/2010). A copyright notice for 2010 is also present. Below this is a "Gratis Reuse" section with a detailed permission statement and "BACK" and "CLOSE WINDOW" buttons. At the bottom, there is a footer with copyright information and contact details.

CCC RightsLink®

Home Help Email Support Deepali Arora

SAGE Publishing

Taylor Flow in Microchannels: A Review of Experimental and Computational Work

Author: R. Gupta, D.F. Fletcher, B.S. Haynes
Publication: The Journal of Computational Multiphase Flows
Publisher: SAGE Publications
Date: 03/01/2010

Copyright © 2010, © SAGE Publications

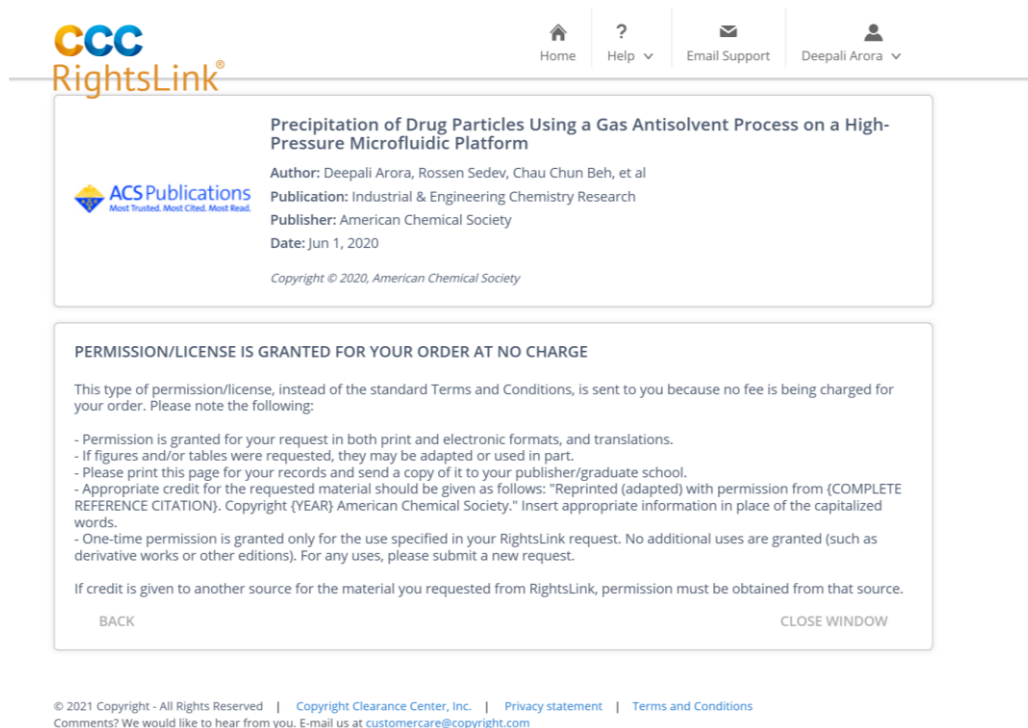
Gratis Reuse

Permission is granted at no cost for use of content in a Master's Thesis and/or Doctoral Dissertation, subject to the following limitations. You may use a single excerpt or up to 3 figures tables. If you use more than those limits, or intend to distribute or sell your Master's Thesis/Doctoral Dissertation to the general public through print or website publication, please return to the previous page and select 'Republish in a Book/Journal' or 'Post on intranet/password-protected website' to complete your request.

BACK CLOSE WINDOW

© 2021 Copyright - All Rights Reserved | Copyright Clearance Center, Inc. | Privacy statement | Terms and Conditions
Comments? We would like to hear from you. E-mail us at customercare@copyright.com

For Chapter 3(254)



The screenshot shows the CCC RightsLink interface. At the top left is the CCC RightsLink logo. On the top right, there are navigation links: Home, Help, Email Support, and a user profile for Deepali Arora. The main content area features the ACS Publications logo and the title "Precipitation of Drug Particles Using a Gas Antisolvent Process on a High-Pressure Microfluidic Platform". Below the title, it lists the author (Deepali Arora, Rossen Sedev, Chau Chun Beh, et al), the publication (Industrial & Engineering Chemistry Research), the publisher (American Chemical Society), and the date (Jun 1, 2020). A copyright notice for 2020 is also present. Below this is a "PERMISSION/LICENSE IS GRANTED FOR YOUR ORDER AT NO CHARGE" section with a detailed permission statement and "BACK" and "CLOSE WINDOW" buttons. At the bottom, there is a footer with copyright information and contact details.

CCC RightsLink®

Home Help Email Support Deepali Arora

ACS Publications
Most Trusted. Most Cited. Most Read.

Precipitation of Drug Particles Using a Gas Antisolvent Process on a High-Pressure Microfluidic Platform

Author: Deepali Arora, Rossen Sedev, Chau Chun Beh, et al
Publication: Industrial & Engineering Chemistry Research
Publisher: American Chemical Society
Date: Jun 1, 2020

Copyright © 2020, American Chemical Society

PERMISSION/LICENSE IS GRANTED FOR YOUR ORDER AT NO CHARGE

This type of permission/license, instead of the standard Terms and Conditions, is sent to you because no fee is being charged for your order. Please note the following:

- Permission is granted for your request in both print and electronic formats, and translations.
- If figures and/or tables were requested, they may be adapted or used in part.
- Please print this page for your records and send a copy of it to your publisher/graduate school.
- Appropriate credit for the requested material should be given as follows: "Reprinted (adapted) with permission from {COMPLETE REFERENCE CITATION}. Copyright (YEAR) American Chemical Society." Insert appropriate information in place of the capitalized words.
- One-time permission is granted only for the use specified in your RightsLink request. No additional uses are granted (such as derivative works or other editions). For any uses, please submit a new request.

If credit is given to another source for the material you requested from RightsLink, permission must be obtained from that source.

BACK CLOSE WINDOW

© 2021 Copyright - All Rights Reserved | Copyright Clearance Center, Inc. | Privacy statement | Terms and Conditions
Comments? We would like to hear from you. E-mail us at customercare@copyright.com

For Figure 53

CCC RightsLink Home Help Email Support Deepali Arora

Understanding Morphological Evolution of Griseofulvin Particles into Hierarchical Microstructures during Liquid Antisolvent Precipitation

Author: Rupanjali Prasad, Sameer V. Dalvi
Publication: Crystal Growth and Design
Publisher: American Chemical Society
Date: Oct 1, 2019
Copyright © 2019, American Chemical Society

PERMISSION/LICENSE IS GRANTED FOR YOUR ORDER AT NO CHARGE

This type of permission/license, instead of the standard Terms and Conditions, is sent to you because no fee is being charged for your order. Please note the following:

- Permission is granted for your request in both print and electronic formats, and translations.
- If figures and/or tables were requested, they may be adapted or used in part.
- Please print this page for your records and send a copy of it to your publisher/graduate school.
- Appropriate credit for the requested material should be given as follows: "Reprinted (adapted) with permission from (COMPLETE REFERENCE CITATION). Copyright (YEAR) American Chemical Society." Insert appropriate information in place of the capitalized words.
- One-time permission is granted only for the use specified in your RightsLink request. No additional uses are granted (such as derivative works or other editions). For any uses, please submit a new request.

If credit is given to another source for the material you requested from RightsLink, permission must be obtained from that source.

BACK CLOSE WINDOW

© 2021 Copyright - All Rights Reserved | Copyright Clearance Center, Inc. | Privacy statement | Terms and Conditions
Comments? We would like to hear from you. E-mail us at customercare@copyright.com

For Figure 54a

CCC RightsLink Home Help Email Support Sign in Create Account

Solubility and Micronization of Griseofulvin in Subcritical Water

Author: Adam G. Carr, Raffaella Mammucari, Neil R. Foster
Publication: Industrial & Engineering Chemistry Research
Publisher: American Chemical Society
Date: Apr 1, 2010
Copyright © 2010, American Chemical Society

PERMISSION/LICENSE IS GRANTED FOR YOUR ORDER AT NO CHARGE

This type of permission/license, instead of the standard Terms and Conditions, is sent to you because no fee is being charged for your order. Please note the following:

- Permission is granted for your request in both print and electronic formats, and translations.
- If figures and/or tables were requested, they may be adapted or used in part.
- Please print this page for your records and send a copy of it to your publisher/graduate school.
- Appropriate credit for the requested material should be given as follows: "Reprinted (adapted) with permission from (COMPLETE REFERENCE CITATION). Copyright (YEAR) American Chemical Society." Insert appropriate information in place of the capitalized words.
- One-time permission is granted only for the use specified in your RightsLink request. No additional uses are granted (such as derivative works or other editions). For any uses, please submit a new request.

If credit is given to another source for the material you requested from RightsLink, permission must be obtained from that source.

BACK CLOSE WINDOW

© 2021 Copyright - All Rights Reserved | Copyright Clearance Center, Inc. | Privacy statement | Terms and Conditions
Comments? We would like to hear from you. E-mail us at customercare@copyright.com

For Figure 68

ELSEVIER LICENSE TERMS AND CONDITIONS

Sep 04, 2021

This Agreement between Curtin University -- Deepali Arora ("You") and Elsevier ("Elsevier") consists of your license details and the terms and conditions provided by Elsevier and Copyright Clearance Center.

License Number	5141720770571
License date	Sep 04, 2021
Licensed Content Publisher	Elsevier
Licensed Content Publication	Carbohydrate Polymers
Licensed Content Title	Novel organic/inorganic hybrid flower-like structure of selenium nanoparticles stabilized by pullulan derivatives
Licensed Content Author	Punnida Nonsuwan, Songchan Puthong, Tanapat Palaga, Nongnui Muangsin
Licensed Content Date	Mar 15, 2018
Licensed Content Volume	184
Licensed Content Issue	n/a
Licensed Content Pages	11
Start Page	9
End Page	19
Type of Use	reuse in a thesis/dissertation
Portion	figures/tables/illustrations
Number of figures/tables/illustrations	2
Format	electronic
Are you the author of this Elsevier article?	No
Will you be translating?	No
Title	Miss
Institution name	Curtin University
Expected presentation date	Sep 2021
Portions	Figures 4 and 7a
Requestor Location	Curtin University Kent Street Bentley Perth, WA 6102 Australia Attn: Curtin University
Publisher Tax ID	GB 494 6272 12
Total	0.00 AUD

For Figure 69

ELSEVIER LICENSE TERMS AND CONDITIONS

Sep 04, 2021

This Agreement between Curtin University -- Deepali Arora ("You") and Elsevier ("Elsevier") consists of your license details and the terms and conditions provided by Elsevier and Copyright Clearance Center.

License Number	5141721002874
License date	Sep 04, 2021
Licensed Content Publisher	Elsevier
Licensed Content Publication	Journal of Crystal Growth
Licensed Content Title	Self-organized formation of porous aragonite with silicate
Licensed Content Author	Hiroaki Imai, Tomohiro Terada, Takashi Miura, Satoshi Yamabi
Licensed Content Date	Oct 1, 2002
Licensed Content Volume	244
Licensed Content Issue	2
Licensed Content Pages	6
Start Page	200
End Page	205
Type of Use	reuse in a thesis/dissertation
Portion	figures/tables/illustrations
Number of figures/tables/illustrations	1
Format	electronic
Are you the author of this Elsevier article?	No
Will you be translating?	No
Title	Miss
Institution name	Curtin University
Expected presentation date	Sep 2021
Portions	Figure 4
Requestor Location	Curtin University Kent Street Bentley Perth, WA 6102 Australia Attn: Curtin University
Publisher Tax ID	GB 494 6272 12
Total	0.00 AUD

For Figure 70



?
Help ▾

✉
Email Support

SPRINGER NATURE

Single Crystal Organic Nanoflowers

Author: Sajitha Sasidharan et al

Publication: Scientific Reports

Publisher: Springer Nature

Date: Dec 11, 2017

Copyright © 2017, The Author(s)

Creative Commons

This is an open access article distributed under the terms of the [Creative Commons CC BY](#) license, which permits unrestricted use, distribution, and reproduction in any medium, provided the original work is properly cited.

You are not required to obtain permission to reuse this article.

To request permission for a type of use not listed, please contact [Springer Nature](#)

© 2021 Copyright - All Rights Reserved | [Copyright Clearance Center, Inc.](#) | [Privacy statement](#) | [Terms and Conditions](#)
Comments? We would like to hear from you. E-mail us at customercare@copyright.com

For Figures 79 and 80

ELSEVIER LICENSE TERMS AND CONDITIONS

Sep 04, 2021

This Agreement between Curtin University -- Deepali Arora ("You") and Elsevier ("Elsevier") consists of your license details and the terms and conditions provided by Elsevier and Copyright Clearance Center.

License Number	5141721477050
License date	Sep 04, 2021
Licensed Content Publisher	Elsevier
Licensed Content Publication	Advanced Drug Delivery Reviews
Licensed Content Title	Cocrystals to facilitate delivery of poorly soluble compounds beyond-rule-of-5
Licensed Content Author	Gislaine Kuminek, Fengjuan Cao, Alanny Bahia de Oliveira da Rocha, Simone Gonçalves Cardoso, Nair Rodriguez-Hornedo
Licensed Content Date	Jun 1, 2016
Licensed Content Volume	101
Licensed Content Issue	n/a
Licensed Content Pages	24
Start Page	143
End Page	166
Type of Use	reuse in a thesis/dissertation
Portion	figures/tables/illustrations
Number of figures/tables/illustrations	2
Format	electronic
Are you the author of this Elsevier article?	No
Will you be translating?	No
Title	Miss
Institution name	Curtin University
Expected presentation date	Sep 2021
Portions	Figures 3 and 11
Requestor Location	Curtin University Kent Street Bentley Perth, WA 6102 Australia Attn: Curtin University
Publisher Tax ID	GB 494 6272 12
Total	0.00 AUD

For Figure 81

ELSEVIER LICENSE TERMS AND CONDITIONS

Sep 04, 2021

This Agreement between Curtin University -- Deepali Arora ("You") and Elsevier ("Elsevier") consists of your license details and the terms and conditions provided by Elsevier and Copyright Clearance Center.

License Number	5141730171397
License date	Sep 04, 2021
Licensed Content Publisher	Elsevier
Licensed Content Publication	Powder Technology
Licensed Content Title	Formation of itraconazole L-malic acid cocrystals by gas antisolvent cocrystallization
Licensed Content Author	Courtney A. Ober, Stephen E. Montgomery, Ram B. Gupta
Licensed Content Date	Feb 1, 2013
Licensed Content Volume	236
Licensed Content Issue	n/a
Licensed Content Pages	10
Start Page	122
End Page	131
Type of Use	reuse in a thesis/dissertation
Portion	figures/tables/illustrations
Number of figures/tables/illustrations	1
Format	electronic
Are you the author of this Elsevier article?	No
Will you be translating?	No
Title	Miss
Institution name	Curtin University
Expected presentation date	Sep 2021
Portions	Figure 11
Requestor Location	Curtin University Kent Street Bentley Perth, WA 6102 Australia Attn: Curtin University
Publisher Tax ID	GB 494 6272 12
Total	0.00 AUD

For Figure 82

The screenshot shows the CCC RightsLink interface. At the top left is the logo for CCC RightsLink. To the right are navigation links: Home, Help, Email Support, and a user profile for Deepali Arora. The main content area is divided into two sections. The first section contains the title "Preparation and Solid-State Characterization of Dapsone Drug-Drug Co-Crystals", the ACS Publications logo, and the following information: Author: Linglei Jiang, Ying Huang, Qi Zhang, et al; Publication: Crystal Growth and Design; Publisher: American Chemical Society; Date: Sep 1, 2014; Copyright © 2014, American Chemical Society. The second section is titled "PERMISSION/LICENSE IS GRANTED FOR YOUR ORDER AT NO CHARGE" and contains a paragraph explaining that this type of permission is granted instead of standard terms and conditions. It lists several conditions: permission is granted in both print and electronic formats; figures and tables may be adapted; users should print the page and send a copy to their publisher; appropriate credit should be given; and one-time permission is granted only for the specified use. At the bottom of this section are "BACK" and "CLOSE WINDOW" buttons. A footer at the very bottom contains copyright information for 2021 and contact details for the Copyright Clearance Center.

CCC RightsLink®

Home Help Email Support Deepali Arora

Preparation and Solid-State Characterization of Dapsone Drug-Drug Co-Crystals

Author: Linglei Jiang, Ying Huang, Qi Zhang, et al
Publication: Crystal Growth and Design
Publisher: American Chemical Society
Date: Sep 1, 2014
Copyright © 2014, American Chemical Society

PERMISSION/LICENSE IS GRANTED FOR YOUR ORDER AT NO CHARGE

This type of permission/license, instead of the standard Terms and Conditions, is sent to you because no fee is being charged for your order. Please note the following:

- Permission is granted for your request in both print and electronic formats, and translations.
- If figures and/or tables were requested, they may be adapted or used in part.
- Please print this page for your records and send a copy of it to your publisher/graduate school.
- Appropriate credit for the requested material should be given as follows: "Reprinted (adapted) with permission from {COMPLETE REFERENCE CITATION}. Copyright {YEAR} American Chemical Society." Insert appropriate information in place of the capitalized words.
- One-time permission is granted only for the use specified in your RightsLink request. No additional uses are granted (such as derivative works or other editions). For any uses, please submit a new request.

If credit is given to another source for the material you requested from RightsLink, permission must be obtained from that source.

BACK CLOSE WINDOW

© 2021 Copyright - All Rights Reserved | Copyright Clearance Center, Inc. | Privacy statement | Terms and Conditions
Comments? We would like to hear from you. E-mail us at customercare@copyright.com

For Figure 84

This screenshot is identical to the one for Figure 82, showing the same CCC RightsLink interface and content. It displays the title "Preparation and Solid-State Characterization of Dapsone Drug-Drug Co-Crystals", the ACS Publications logo, and the author and publication information. The second section, titled "PERMISSION/LICENSE IS GRANTED FOR YOUR ORDER AT NO CHARGE", contains the same explanatory text and list of conditions as in Figure 82. The interface includes navigation links at the top and a footer with copyright information.

CCC RightsLink®

Home Help Email Support Deepali Arora

Preparation and Solid-State Characterization of Dapsone Drug-Drug Co-Crystals

Author: Linglei Jiang, Ying Huang, Qi Zhang, et al
Publication: Crystal Growth and Design
Publisher: American Chemical Society
Date: Sep 1, 2014
Copyright © 2014, American Chemical Society

PERMISSION/LICENSE IS GRANTED FOR YOUR ORDER AT NO CHARGE

This type of permission/license, instead of the standard Terms and Conditions, is sent to you because no fee is being charged for your order. Please note the following:

- Permission is granted for your request in both print and electronic formats, and translations.
- If figures and/or tables were requested, they may be adapted or used in part.
- Please print this page for your records and send a copy of it to your publisher/graduate school.
- Appropriate credit for the requested material should be given as follows: "Reprinted (adapted) with permission from {COMPLETE REFERENCE CITATION}. Copyright {YEAR} American Chemical Society." Insert appropriate information in place of the capitalized words.
- One-time permission is granted only for the use specified in your RightsLink request. No additional uses are granted (such as derivative works or other editions). For any uses, please submit a new request.

If credit is given to another source for the material you requested from RightsLink, permission must be obtained from that source.

BACK CLOSE WINDOW

© 2021 Copyright - All Rights Reserved | Copyright Clearance Center, Inc. | Privacy statement | Terms and Conditions
Comments? We would like to hear from you. E-mail us at customercare@copyright.com

ELSEVIER LICENSE
TERMS AND CONDITIONS

Sep 04, 2021

This Agreement between Curtin University -- Deepali Arora ("You") and Elsevier ("Elsevier") consists of your license details and the terms and conditions provided by Elsevier and Copyright Clearance Center.

License Number	5141730565650
License date	Sep 04, 2021
Licensed Content Publisher	Elsevier
Licensed Content Publication	Food Chemistry
Licensed Content Title	Physicochemical characterisation of the supramolecular structure of luteolin/cyclodextrin inclusion complex
Licensed Content Author	Benguo Liu,Wei Li,Jian Zhao,Yang Liu,Xiaoai Zhu,Guizhao Liang
Licensed Content Date	Nov 15, 2013
Licensed Content Volume	141
Licensed Content Issue	2
Licensed Content Pages	7
Start Page	900
End Page	906
Type of Use	reuse in a thesis/dissertation
Portion	figures/tables/illustrations
Number of figures/tables/illustrations	1
Format	electronic
Are you the author of this Elsevier article?	No
Will you be translating?	No
Title	Miss
Institution name	Curtin University
Expected presentation date	Sep 2021
Portions	Figure 7 (2)
Requestor Location	Curtin University Kent Street Bentley Perth, WA 6102 Australia Attn: Curtin University
Publisher Tax ID	GB 494 6272 12
Total	0.00 AUD

ELSEVIER LICENSE
TERMS AND CONDITIONS

Sep 04, 2021

This Agreement between Curtin University -- Deepali Arora ("You") and Elsevier ("Elsevier") consists of your license details and the terms and conditions provided by Elsevier and Copyright Clearance Center.

License Number	5141730728771
License date	Sep 04, 2021
Licensed Content Publisher	Elsevier
Licensed Content Publication	Journal of Molecular Liquids
Licensed Content Title	Solubility, thermodynamic properties and solute-solvent molecular interactions of luteolin in various pure solvents
Licensed Content Author	Faiyaz Shakeel,Nazrul Haq,Sultan Alshehri,Mohamed A. Ibrahim,Ehab M. Elzayat,Mohammad A. Altamimi,Kazi Mobsin,Faris K. Alanazi,Ibrahim A. Alsarra
Licensed Content Date	Apr 1, 2018
Licensed Content Volume	255
Licensed Content Issue	n/a
Licensed Content Pages	8
Start Page	43
End Page	50
Type of Use	reuse in a thesis/dissertation
Portion	figures/tables/illustrations
Number of figures/tables/illustrations	1
Format	electronic
Are you the author of this Elsevier article?	No
Will you be translating?	No
Title	Miss
Institution name	Curtin University
Expected presentation date	Sep 2021
Portions	Figure 3(A)
Requestor Location	Curtin University Kent Street Bentley Perth, WA 6102 Australia Attn: Curtin University
Publisher Tax ID	GB 494 6272 12
Total	0.00 AUD

For Figure 92

SPRINGER NATURE LICENSE TERMS AND CONDITIONS

Sep 04, 2021

This Agreement between Curtin University -- Deepali Arora ("You") and Springer Nature ("Springer Nature") consists of your license details and the terms and conditions provided by Springer Nature and Copyright Clearance Center.

License Number	5141731074013
License date	Sep 04, 2021
Licensed Content Publisher	Springer Nature
Licensed Content Publication	AAPS PharmSciTech
Licensed Content Title	Development and Characterization of Dapsone Cocrystal Prepared by Scalable Production Methods
Licensed Content Author	Lilian Henriques do Amaral et al
Licensed Content Date	Jul 2, 2018
Type of Use	Thesis/Dissertation
Requestor type	academic/university or research institute
Format	electronic
Portion	figures/tables/illustrations
Number of figures/tables/illustrations	1
Will you be translating?	no
Circulation/distribution	10000 - 19999
Author of this Springer Nature content	no
Title	Miss
Institution name	Curtin University
Expected presentation date	Sep 2021
Portions	Figure 1
Requestor Location	Curtin University Kent Street Bentley Perth, WA 6102 Australia Attn: Curtin University
Total	0.00 AUD

References

1. Variankaval N, Cote AS, Doherty MF. From form to function: Crystallization of active pharmaceutical ingredients. *AIChE Journal*. 2008;54(7):1682-8.
2. Chen J, Sarma B, Evans JMB, Myerson AS. Pharmaceutical Crystallization. *Crystal Growth & Design*. 2011;11(4):887-95.
3. Almarsson Ö, Zaworotko MJ. Crystal engineering of the composition of pharmaceutical phases. Do pharmaceutical co-crystals represent a new path to improved medicines? *Chemical communications*. 2004(17):1889-96.
4. Arida AI, Al-Tabakha MM, Hamoury HAJ. Improving the High Variable Bioavailability of Griseofulvin by SEDDS. *Chemical and Pharmaceutical Bulletin*. 2007;55(12):1713-9.
5. Berglund KA. 4 - Analysis and measurement of crystallization utilizing the population balance. In: Myerson AS, editor. *Handbook of Industrial Crystallization (Second Edition)*. Woburn: Butterworth-Heinemann; 2002. p. 101-13.
6. Ghosh I, Bose S, Vippagunta R, Harmon F. Nanosuspension for improving the bioavailability of a poorly soluble drug and screening of stabilizing agents to inhibit crystal growth. *International Journal of Pharmaceutics*. 2011;409(1):260-8.
7. Jinno J-i, Kamada N, Miyake M, Yamada K, Mukai T, Odomi M, et al. Effect of particle size reduction on dissolution and oral absorption of a poorly water-soluble drug, cilostazol, in beagle dogs. *Journal of Controlled Release*. 2006;111(1):56-64.
8. Gerogiorgis DI, Jolliffe HG, editors. *Continuous pharmaceutical process engineering and economics: Investigating technical efficiency, environmental impact and economic viability* 2015.
9. Grön H, Mougín P, Thomas A, White G, Wilkinson D, Hammond RB, et al. Dynamic In-Process Examination of Particle Size and Crystallographic Form under Defined Conditions of Reactant Supersaturation as Associated with the Batch Crystallization of Monosodium Glutamate from Aqueous Solution. *Industrial & Engineering Chemistry Research*. 2003;42(20):4888-98.
10. Shekunov BY, York P. Crystallization processes in pharmaceutical technology and drug delivery design. *Journal of Crystal Growth*. 2000;211(1):122-36.
11. MacCalman ML, Roberts KJ, Kerr C, Hendriksen B. On-line processing of pharmaceutical materials using in situ X-ray diffraction. *Journal of Applied Crystallography*. 1995;28(5):620-2.

12. Lee SL, O'Connor TF, Yang X, Cruz CN, Chatterjee S, Madurawe RD, et al. Modernizing Pharmaceutical Manufacturing: from Batch to Continuous Production. *Journal of Pharmaceutical Innovation*. 2015;10(3):191-9.
13. York M, Edenharter A. A Two-Stage Continuous-Flow Synthesis of Spirooxazine Photochromic Dyes. *Australian Journal of Chemistry*. 2013;66(2):172-7.
14. Frederick MO, Pietz MA, Kjell DP, Richey RN, Tharp GA, Touge T, et al. Development of a Leuckart–Wallach Reaction in Flow for the Synthesis of Abemaciclib. *Organic Process Research & Development*. 2017;21(9):1447-51.
15. Johnson MD, May SA, Haeberle B, Lambertus GR, Pulley SR, Stout JR. Design and Comparison of Tubular and Pipes-in-Series Continuous Reactors for Direct Asymmetric Reductive Amination. *Organic Process Research & Development*. 2016;20(7):1305-20.
16. Turk M. Particle Formation with Supercritical Fluids. Elsevier. 2017;6(1st Edition):152.
17. Senčar-Božič P, Srčić S, Knez Z, Kerč J. Improvement of nifedipine dissolution characteristics using supercritical CO₂. *International Journal of Pharmaceutics*. 1997;148(2):123-30.
18. Subramaniam B, Saim S, Rajewski R, Stella VJ. Green Process Concepts for the Pharmaceutical Industry. *Green Engineering*. ACS Symposium Series. 766: American Chemical Society; 2000. p. 96-110.
19. Snavelly WK, Subramaniam B, Rajewski RA, Defelippis MR. Micronization of insulin from halogenated alcohol solution using supercritical carbon dioxide as an antisolvent. *Journal of Pharmaceutical Sciences*. 2002;91(9):2026-39.
20. *Microreactors - New Technology for Modern Chemistry* Wolfgang Ehrfeld Volker Hessel Holger Löwe Wiley-VCH: Weinheim. 2000. 288 pp. Price £80. ISBN3-527-29590-9. *Organic Process Research & Development*. 2001;5(1):89-.
21. Jensen K. Microchemical systems: Status, challenges, and opportunities. *Aiche Journal*. 1999;45:2051-4.
22. Jensen KF. Microreaction engineering — is small better? *Chemical Engineering Science*. 2001;56(2):293-303.
23. Anastas P, Eghbali N. *Green Chemistry: Principles and Practice*. *Chemical Society Reviews*. 2010;39(1):301-12.

24. Song Y, Zhao X, Tian Q, Liang H. Fundamental Concepts and Physics in Microfluidics. *Microfluidics: Fundamental, Devices and Applications* 2018. p. 19-111.
25. Dekker T. Definition of Active Pharmaceutical Ingredient. World Health Organization. 2011;11:426.
26. Cha J, Gilmor T, Lane P, Ranweiler JS. 12 - Stability Studies. In: Ahuja S, Scypinski S, editors. *Separation Science and Technology*. 10: Academic Press; 2011. p. 459-505.
27. Karpinski PH. Polymorphism of Active Pharmaceutical Ingredients. *Chemical Engineering & Technology*. 2006;29(2):233-7.
28. Bansal GCaAK. Challenges in Polymorphism of Pharmaceuticals. *CRIPS*. 2004;5:9-12.
29. Bonfilio R, Leal JS, Santos OMM, Pereira GR, Doriguetto AC, de Araújo MB. Analysis of chlorthalidone polymorphs in raw materials and tablets and the effect of forms I and II on the dissolution properties of drug products. *J Pharm Biomed Anal*. 2014;88:562-70.
30. Brincat A, Azzopardi LM, Zarb Adami M, Serracino-Inglott A. Development and evaluation of a Drug Information Bulletin. *Journal of Pharmaceutical Health Services Research*. 2014;5(2):81-8.
31. Fang Z, Zhang L, Mao S, Rohani S, Ulrich J, Lu J. Solubility measurement and prediction of clopidogrel hydrogen sulfate polymorphs in isopropanol and ethyl acetate. *The Journal of Chemical Thermodynamics*. 2015;90:71-8.
32. Foresti E, Sabatino P, Riva di Sanseverino L, Fusco R, Tosi C, Tonani R. Structure and molecular orbital study of ergoline derivatives. 1-(6-Methyl-8 β -ergolinylmethyl)imidazolidine-2,4-dione (I) and 2-(10-methoxy-1,6-dimethyl-8 β -ergolinyl)ethyl 3,5-dimethyl-1H-2-pyrrololecarboxylate toluene hemisolvate (II) and comparison with nicergoline (III). *Acta Crystallographica Section B*. 1988;44(3):307-15.
33. Khankari RK, Grant DJW. Pharmaceutical hydrates. *Thermochimica Acta*. 1995;248:61-79.
34. Rajamma AJ, Sateesha SB, Narode MK, Prashanth VRSS, Karthik AM. Preparation and crystallographic analysis of gliclazide polymorphs. *Indian J Pharm Sci*. 2015;77(1):34-40.

35. Zhai J, Chen Z, Liu X, Zhang L, Lu J. Solubility measurement, model evaluation and thermodynamic analysis of rivaroxaban polymorphs in organic solvents. *The Journal of Chemical Thermodynamics*. 2017;104:218-29.
36. Bauer J, Spanton S, Henry R, Quick J, Dziki W, Porter W, et al. Ritonavir: An Extraordinary Example of Conformational Polymorphism. *Pharmaceutical Research*. 2001;18(6):859-66.
37. Raza K, Kumar P, Ratan S, Malik R, Arora S, editors. *Polymorphism : The Phenomenon Affecting the Performance of Drugs* 2014.
38. He G, Wong ABH, Chow PS, Tan RBH. Effects of the rate of supersaturation generation on polymorphic crystallization of m-hydroxybenzoic acid and o-aminobenzoic acid. *Journal of Crystal Growth*. 2011;314(1):220-6.
39. Karpinski PH. Polymorphism of Active Pharmaceutical Ingredients. *Chemical Engineering Technology*. 2006;29(2):233-7.
40. An J-H, Jin F, Kim HS, Ryu HC, Kim JS, Kim HM, et al. Investigation of the Polymorphic Transformation of the Active Pharmaceutical Ingredient Clopidogrel Bisulfate Using the Ionic Liquid AEImBF₄. *Crystal Growth & Design*. 2016;16(4):1829-36.
41. Malaj L, Censi R, Capsoni D, Pellegrino L, Bini M, Ferrari S, et al. Characterization of Nicergoline Polymorphs Crystallized in Several Organic Solvents. *Journal of Pharmaceutical Sciences*. 2011;100(7):2610-22.
42. Muramatsu M, Iwahashi M, Masumoto K. Polymorphic effects of chloramphenicol palmitate on thermodynamic stability in crystals and solubilities in water and in aqueous urea solution. *Journal of Chemical & Engineering Data*. 1975;20(1):6-9.
43. Nicoud L, Licordari F, Myerson AS. Estimation of the Solubility of Metastable Polymorphs: A Critical Review. *Crystal Growth & Design*. 2018;18(11):7228-37.
44. Pandey KU, Dalvi SV. Understanding stability relationships among three curcumin polymorphs. *Advanced Powder Technology*. 2019;30(2):266-76.
45. He F, Wang Y, Yin Q, Tao L, Lv J, Xu Z, et al. Effect of polymorphism on thermodynamic properties of cefamandole nafate. *Fluid Phase Equilibria*. 2016;422:56-65.
46. Censi R, Di Martino P. Polymorph Impact on the Bioavailability and Stability of Poorly Soluble Drugs. *Molecules*. 2015;20(10):18759-76.

47. Dokoumetzidis A, Macheras P. A century of dissolution research: From Noyes and Whitney to the Biopharmaceutics Classification System. *International Journal of Pharmaceutics*. 2006;321(1):1-11.
48. Sinko PJ. *Martin's Physical Pharmacy and Pharmaceutical Sciences*. 6th ed. Baltimore: Wolters Kluwer; 2011.
49. Wu W, Nancollas GH. A New Understanding of the Relationship Between Solubility and Particle Size. *Journal of Solution Chemistry*. 1998;27(6):521-31.
50. Kipp JE. The role of solid nanoparticle technology in the parenteral delivery of poorly water-soluble drugs. *International Journal of Pharmaceutics*. 2004;284(1):109-22.
51. Babu V, S.H.Areefulla, Mallikarjun V. Solubility and Dissolution Enhancement: An overview. *Journal of Pharmacy Research*. 2015:141-5.
52. Dong Y, Ng WK, Shen S, Kim S, Tan RBH. Preparation and characterization of spironolactone nanoparticles by antisolvent precipitation. *International Journal of Pharmaceutics*. 2009;375(1):84-8.
53. Kocbek P, Baumgartner S, Kristl J. Preparation and evaluation of nanosuspensions for enhancing the dissolution of poorly soluble drugs. *International Journal of Pharmaceutics*. 2006;312(1):179-86.
54. Rao G, Kumar MS, Mathivanan N, Rao MEB. Nanosuspensions as the most promising approach in nanoparticulate drug delivery systems. *Die Pharmazie*. 2004;59 1:5-9.
55. Date AA, Patravale VB. Current strategies for engineering drug nanoparticles. *Current Opinion in Colloid & Interface Science*. 2004;9(3):222-35.
56. Rabinow BE. Nanosuspensions in drug delivery. *Nature Reviews Drug Discovery*. 2004;3(9):785-96.
57. Hüttenrauch R, Fricke S, Zielke P. Mechanical Activation of Pharmaceutical Systems. *Pharmaceutical Research*. 1985;2(6):302-6.
58. Heng JYY, Thielmann F, Williams DR. The Effects of Milling on the Surface Properties of Form I Paracetamol Crystals. *Pharmaceutical Research*. 2006;23(8):1918-27.
59. Joshi V, Dwivedi S, Ward GH. Increase in the Specific Surface Area of Budesonide During Storage Postmicronization. *Pharmaceutical Research*. 2002;19(1):7-12.

60. D. Ticehurst M, A. Basford P, I. Dallman C, M. Lukas T, V. Marshall P, Nichols G, et al. Characterisation of the influence of micronisation on the crystallinity and physical stability of revatropate hydrobromide. *International Journal of Pharmaceutics*. 2000;193(2):247-59.
61. Kramer HJM, van Rosmalen GM. CRYSTALLIZATION. In: Wilson ID, editor. *Encyclopedia of Separation Science*. Oxford: Academic Press; 2000. p. 64-84.
62. Mullin JW. 3 - Solutions and solubility. In: Mullin JW, editor. *Crystallization (Fourth Edition)*. Oxford: Butterworth-Heinemann; 2001. p. 86-134.
63. Kubota N, Kobari M, Hirasawa I. Metastability of Supersaturated Solution and Nucleation. In: Tamura R, Miyata M, editors. *Advances in Organic Crystal Chemistry: Comprehensive Reviews 2015*. Tokyo: Springer Japan; 2015. p. 115-38.
64. Kashchiev D. *Nucleation : basic theory with applications*. Oxford; Boston: Butterworth Heinemann; 2000.
65. Davey RJ. *Polymorphism in Molecular Crystals* Joel Bernstein. Oxford University Press, New York, 2002. ISBN 0198506058. *Crystal Growth & Design*. 2002;2(6):675-6.
66. Kee NCS, Tan RBH, Braatz RD. Selective Crystallization of the Metastable α -Form of l-Glutamic Acid using Concentration Feedback Control. *Crystal Growth & Design*. 2009;9(7):3044-51.
67. Kitamura M. Controlling Factors and Mechanism of Polymorphic Crystallization. *Crystal Growth & Design*. 2004;4(6):1153-9.
68. Ouyang J, Chen J, Rosbottom I, Chen W, Guo M, Heng JYY. Supersaturation and solvent dependent nucleation of carbamazepine polymorphs during rapid cooling crystallization. *CrystEngComm*. 2021.
69. Karthika S, Radhakrishnan TK, Kalaichelvi P. A Review of Classical and Nonclassical Nucleation Theories. *Crystal Growth & Design*. 2016;16(11):6663-81.
70. Guillory JK. *Handbook of Aqueous Solubility Data* By Samuel H. Yalkowsky and Yan He. CRC Press, Boca Raton, FL. 2003. xii + 1496 pp. 18 × 26 cm. ISBN 0-89493-1532-8. \$299.95. *Journal of Medicinal Chemistry*. 2003;46(19):4213-.
71. Kadi KE, Janajreh I, editors. *Desalination by Freeze Crystallization : An Overview*2017.
72. Jones AG, Mullin JW. Programmed cooling crystallization of potassium sulphate solutions. *Chemical Engineering Science*. 1974;29(1):105-18.

73. Mullin JW, Nývlt J. Programmed cooling of batch crystallizers. *Chemical Engineering Science*. 1971;26(3):369-77.
74. Malwade CR, Qu H. Cooling Crystallization of Indomethacin: Effect of Supersaturation, Temperature, and Seeding on Polymorphism and Crystal Size Distribution. *Organic Process Research & Development*. 2018;22(6):697-706.
75. Westphal G, Kristen G, Wegener W, Ambatiello P, Geyer H, Epron B, et al. Sodium Chloride. *Ullmann's Encyclopedia of Industrial Chemistry*.
76. Yu ZQ, Tan RBH, Chow PS. Effects of operating conditions on agglomeration and habit of paracetamol crystals in anti-solvent crystallization. *Journal of Crystal Growth*. 2005;279(3):477-88.
77. Judge RA, Jacobs RS, Frazier T, Snell EH, Pusey ML. The Effect of Temperature and Solution pH on the Nucleation of Tetragonal Lysozyme Crystals. *Biophysical Journal*. 1999;77(3):1585-93.
78. Synowiec PM, Bunikowska B. Application of Crystallization with Chemical Reaction in the Process of Waste Brine Purifying in Evaporative Sodium Chloride Production. *Industrial & Engineering Chemistry Research*. 2005;44(7):2273-80.
79. Miller JM, Collman BM, Greene LR, Grant DJW, Blackburn AC. Identifying the Stable Polymorph Early in the Drug Discovery–Development Process. *Pharmaceutical Development and Technology*. 2005;10(2):291-7.
80. Gu C-H, Young V, Grant DJW. Polymorph screening: Influence of solvents on the rate of solvent-mediated polymorphic transformation. *Journal of Pharmaceutical Sciences*. 2001;90(11):1878-90.
81. Hilfiker R, Berghausen J, Blatter F, Burkhard A, De Paul SM, Freiermuth B, et al. Polymorphism - integrated approach from high-throughput screening to crystallization optimization. *Journal of Thermal Analysis and Calorimetry*. 2003;73(2):429-40.
82. Kelly RC, Rodríguez-Hornedo N. Solvent Effects on the Crystallization and Preferential Nucleation of Carbamazepine Anhydrous Polymorphs: A Molecular Recognition Perspective. *Organic Process Research & Development*. 2009;13(6):1291-300.
83. Miller JM, Rodríguez-Hornedo N, Blackburn AC, Macikenas D, Collman BM. Solvent Systems for Crystallization and Polymorph Selection. In: Augustijns P, Brewster ME, editors. *Solvent Systems and Their Selection in Pharmaceuticals and Biopharmaceutics*. New York, NY: Springer New York; 2007. p. 53-109.

84. Khoshkhoo S, Anwar J. Crystallization of polymorphs: the effect of solvent. *Journal of Physics D: Applied Physics*. 1993;26(8B):B90-B3.
85. Blagden N, J. Davey R, F. Lieberman H, Williams L, Payne R, Roberts R, et al. Crystal chemistry and solvent effects in polymorphic systems Sulfathiazole. *Journal of the Chemical Society, Faraday Transactions*. 1998;94(8):1035-44.
86. Davey RJ, Blagden N, Righini S, Alison H, Ferrari ES. Nucleation Control in Solution Mediated Polymorphic Phase Transformations: The Case of 2,6-Dihydroxybenzoic Acid. *The Journal of Physical Chemistry B*. 2002;106(8):1954-9.
87. Bond AD. Polymorphism in molecular crystals. *Current Opinion in Solid State and Materials Science*. 2009;13(3):91-7.
88. Cheuk D, Svärd M, Rasmuson ÅC. Thermodynamics of the Enantiotropic Pharmaceutical Compound Benzocaine and Solubility in Pure Organic Solvents. *Journal of Pharmaceutical Sciences*. 2020;109(11):3370-7.
89. Hansen CM. *Hansen Solubility Parameters: A User's Handbook, Second Edition*. Baton Rouge: Baton Rouge: CRC Press; 2007.
90. Burke J, editor *Solubility Parameters: Theory and Application* 1984.
91. Hansen CM. *Hansen solubility parameters: a user's handbook*: CRC Press; 2007.
92. Schaber SD, Gerogiorgis DI, Ramachandran R, Evans JMB, Barton PI, Trout BL. Economic Analysis of Integrated Continuous and Batch Pharmaceutical Manufacturing: A Case Study. *Industrial & Engineering Chemistry Research*. 2011;50(17):10083-92.
93. Tavare NS. Batch Crystallizer. *Industrial Crystallization: Process Simulation Analysis and Design*. Boston, MA: Springer US; 1995. p. 93-139.
94. Zhang D, Xu S, Du S, Wang J, Gong J. Progress of Pharmaceutical Continuous Crystallization. *Engineering*. 2017;3(3):354-64.
95. Jiang M, Braatz RD. Designs of continuous-flow pharmaceutical crystallizers: developments and practice. *CrystEngComm*. 2019;21(23):3534-51.
96. Orehek J, Teslić D, Likozar B. Continuous Crystallization Processes in Pharmaceutical Manufacturing: A Review. *Organic Process Research & Development*. 2021;25(1):16-42.
97. Plutschack MB, Pieber B, Gilmore K, Seeberger PH. The Hitchhiker's Guide to Flow Chemistry. *Chemical Reviews*. 2017;117(18):11796-893.

98. Kundra M, Grall T, Ng D, Xie Z, Hornung CH. Continuous Flow Hydrogenation of Flavorings and Fragrances Using 3D-Printed Catalytic Static Mixers. *Industrial & Engineering Chemistry Research*. 2021;60(5):1989-2002.
99. Lebl R, Zhu Y, Ng D, Hornung CH, Cantillo D, Kappe CO. Scalable continuous flow hydrogenations using Pd/Al₂O₃-coated rectangular cross-section 3D-printed static mixers. *Catalysis Today*. 2020.
100. Jolliffe HG, Gerogiorgis DI. Process modelling and simulation for continuous pharmaceutical manufacturing of ibuprofen. *Chemical Engineering Research and Design*. 2015;97:175-91.
101. What is Flow Chemistry? : CSIRO; [Available from: <https://research.csiro.au/flowworks/our-labs/flowworks-technology/?web=1&wdLOR=c86016FDB-80E6-4702-97BB-3A616910BE6E>].
102. Inada Y. CONTINUOUS MANUFACTURING DEVELOPMENT IN PHARMACEUTICAL AND FINE CHEMICALS INDUSTRIES Mitsui & Co. Global Strategic Studies Institute; 2019.
103. Lohr L. Abemaciclib (Verzenio™). *Oncology Times*. 2018;40(6):12.
104. Döhner H, Estey E, Grimwade D, Amadori S, Appelbaum FR, Büchner T, et al. Diagnosis and management of AML in adults: 2017 ELN recommendations from an international expert panel. *Blood*. 2017;129(4):424-47.
105. Duggirala NK, Perry ML, Almarsson Ö, Zaworotko MJ. Pharmaceutical cocrystals: along the path to improved medicines. *Chemical communications*. 2016;52(4):640-55.
106. Billich A. S-1360 Shionogi-GlaxoSmithKline. *Curr Opin Investig Drugs*. 2003;4(2):206-9.
107. Magnus NA, Astleford BA, Laird DLT, Maloney TD, McFarland AD, Rizzo JR, et al. Additives Promote Noyori-type Reductions of a β -Keto- γ -lactam: Asymmetric Syntheses of Serotonin Norepinephrine Reuptake Inhibitors. *The Journal of Organic Chemistry*. 2013;78(11):5768-74.
108. Allison G, Cain YT, Cooney C, Garcia T, Bizjak TG, Holte O, et al. Regulatory and Quality Considerations for Continuous Manufacturing May 20–21, 2014 Continuous Manufacturing Symposium. *Journal of Pharmaceutical Sciences*. 2015;104(3):803-12.

109. Badman C, Trout BL. Achieving Continuous Manufacturing May 20–21 2014 Continuous Manufacturing Symposium. *Journal of Pharmaceutical Sciences*. 2015;104(3):779-80.
110. Badman C, Cooney CL, Florence A, Konstantinov K, Krumme M, Mascia S, et al. Why We Need Continuous Pharmaceutical Manufacturing and How to Make It Happen. *Journal of Pharmaceutical Sciences*. 2019;108(11):3521-3.
111. Byrn S, Futran M, Thomas H, Jayjock E, Maron N, Meyer RF, et al. Achieving continuous manufacturing for final dosage formation: challenges and how to meet them. May 20-21, 2014 Continuous Manufacturing Symposium. *J Pharm Sci*. 2015;104(3):792-802.
112. Poehlauer P, Manley J, Broxterman R, Gregertsen B, Ridemark M. Continuous Processing in the Manufacture of Active Pharmaceutical Ingredients and Finished Dosage Forms: An Industry Perspective. *Organic Process Research & Development*. 2012;16(10):1586-90.
113. Warwick B. SYNTHESIS, PURIFICATION AND MICRONISATION OF COPPER INDOMETHACIN USING DENSE GAS TECHNOLOGY: THE UNIVERSITY OF NEW SOUTH WALES; 2001.
114. Warwick B, Dehghani F, Foster NR, Biffin JR, Regtop HL. Synthesis, Purification, and Micronization of Pharmaceuticals Using the Gas Antisolvent Technique. *Industrial & Engineering Chemistry Research*. 2000;39(12):4571-9.
115. Foster N, Mammucari R, Dehghani F, Barrett A, Bezanehtak K, Coen E, et al. Processing Pharmaceutical Compounds Using Dense Gas Technology. *Industrial & Engineering Chemistry Research*. 2003;42(25):6476-93.
116. Lichtenthaler RN. Gerd Brunner: Gas Extraction - An Introduction to Fundamentals of Supercritical Fluids and the Application to Separation Processes. *Topics in Physical Chemistry, Vol. 4*, eds. H. Baumgärtel, E. U. Franck, W. Grünbein. Steinkopff, Darmstadt/Springer, New York, 1994, 387 S., DM 64,—. *Berichte der Bunsengesellschaft für physikalische Chemie*. 1996;100(6):1090-1.
117. Morrell JJ. 14 - Protection of Wood-Based Materials. In: Kutz M, editor. *Handbook of Environmental Degradation of Materials (Second Edition)*. Oxford: William Andrew Publishing; 2012. p. 407-39.
118. Braeuer A. Chapter 1 - High Pressure: Fellow and Opponent of Spectroscopic Techniques. In: Braeuer A, editor. *Supercritical Fluid Science and Technology*. 7: Elsevier; 2015. p. 1-40.

119. Schermann J-P. 3 - Experimental Methods. In: Schermann J-P, editor. Spectroscopy and Modeling of Biomolecular Building Blocks. Amsterdam: Elsevier; 2008. p. 129-207.
120. Guo G, Wang F, Liu G-Q, Luo S-J, Guo R-B. Calculation on the phase equilibrium and critical temperature of CH₄/CO₂. Process Safety and Environmental Protection. 2018;113:369-77.
121. "Guidance for industry: content and format of chemistry, manufacturing and controls information and establishment description information for a biological in vitro diagnostic product;" availability. Food and Drug Administration, HHS. Notice. Federal register. 1999;64(44):11023-4.
122. Foster NR, Mammucari R, Danh LT, Teoh WH. Particle Engineering by Dense Gas Technologies Applied to Pharmaceuticals. Dense Phase Carbon Dioxide. p. 199-226.
123. Nunes AVM, Duarte CMM. Dense CO₂ as a Solute, Co-Solute or Co-Solvent in Particle Formation Processes: A Review. Materials. 2011;4(11):2017-41.
124. Matos RL, Vieira de Melo SAB, Cabral Albuquerque ECM, Foster NR. Dense CO₂ technology: Overview of recent applications for drug processing/formulation/delivery. Chemical Engineering and Processing - Process Intensification. 2019;140:64-77.
125. Subramaniam B, Rajewski RA, Snavely K. Pharmaceutical processing with supercritical carbon dioxide. J Pharm Sci. 1997;86(8):885-90.
126. Fages J, Sauceau M, Letourneau JJ, Rodier É, editors. Supercritical carbon dioxide : an efficient tool for the production of ultra-fine particles for the food and pharmaceutical industries. NEPTIS-13 -13th Nisshin Engineering Particle Technology International Seminar; 2004 2004-11-14; Awaji, Japan: INSTITUTE OF MULTIDISCIPLINARY RESEARCH FOR ADVANCED MATERIALS, TOHOKU UNIVERSITY; <https://hal.archives-ouvertes.fr/hal-01781676/document>
<https://hal.archives-ouvertes.fr/hal-01781676/file/Fages-Neptis13-Awaji-2004.pdf>.
127. Martín Á, Pham HM, Kilzer A, Kareth S, Weidner E. Micronization of polyethylene glycol by PGSS (Particles from Gas Saturated Solutions)-drying of aqueous solutions. Chemical Engineering and Processing: Process Intensification. 2010;49(12):1259-66.

128. Jung J, Perrut M. Particle design using supercritical fluids: Literature and patent survey. *The Journal of Supercritical Fluids*. 2001;20(3):179-219.
129. Chen Z, Zhang J, Guo Y, Zhang H, Cao J, Xu Q, et al. Effects of various factors on the modification of carbon nanotubes with polyvinyl alcohol in supercritical CO₂ and their application in electrospun fibers. *Chemical Research in Chinese Universities*. 2014;30(4):690-7.
130. O'Neil A, Wilson C, Webster JM, Allison FJ, Howard JAK, Poliakoff M. The Supercritical Fluid Antisolvent Synthesis of C₆₀(C₂H_x) (x=4 or 6); The Crystal Structures of Two Materials Which Were Thought Unlikely to Exist. *Angewandte Chemie International Edition*. 2002;41(20):3796-9.
131. Ghaderi R, Artursson P, Carlfors J. Preparation of Biodegradable Microparticles Using Solution-Enhanced Dispersion by Supercritical Fluids (SEDS). *Pharmaceutical Research*. 1999;16(5):676-81.
132. Jessop PG, Subramaniam B. Gas-Expanded Liquids. *Chemical Reviews*. 2007;107(6):2666-94.
133. Niu F, Roby KF, Rajewski RA, Decedue C, Subramaniam B. Paclitaxel Nanoparticles: Production Using Compressed CO₂ as Antisolvent: Characterization and Animal Model Studies. *Polymeric Drug Delivery II. ACS Symposium Series*. 924: American Chemical Society; 2006. p. 262-77.
134. Ventosa N, Sala S, Veciana J, Torres J, Llibre J. Depressurization of an Expanded Liquid Organic Solution (DELOS): A New Procedure for Obtaining Submicron- or Micron-Sized Crystalline Particles. *Crystal Growth & Design*. 2001;1(4):299-303.
135. Cano M, Gimeno M, Sala S, Veciana J, Muntó M, Ventosa N. New technologies for the preparation of micro- and nanostructured materials with potential applications in drug delivery and clinical diagnostics. *Contributions to science*. 2005;3:11-8.
136. Wu T, Han B. Supercritical Carbon Dioxide (CO₂) as Green Solvent. In: Meyers RA, editor. *Encyclopedia of Sustainability Science and Technology*. New York, NY: Springer New York; 2019. p. 1-25.
137. Zhang H, Lu J, Han B. Precipitation of lysozyme solubilized in reverse micelles by dissolved CO₂. *The Journal of Supercritical Fluids*. 2001;20(1):65-71.

138. Chen J, Zhang J, Liu D, Liu Z, Han B, Yang G. Investigation on the precipitation, microenvironment and recovery of protein in CO₂-expanded reverse micellar solution. *Colloids and Surfaces B: Biointerfaces*. 2004;33(1):33-7.
139. Zhang J, Han B, Liu J, Zhang X, Liu Z, He J. A new method to recover the nanoparticles from reverse micelles: recovery of ZnS nanoparticles synthesized in reverse micelles by compressed CO₂. *Chemical Communications*. 2001(24):2724-5.
140. Zhang J, Han B, Liu J, Zhang X, He J, Liu Z, et al. Recovery of Silver Nanoparticles Synthesized in AOT/C12E4 Mixed Reverse Micelles by Antisolvent CO₂. *Chemistry – A European Journal*. 2002;8(17):3879-83.
141. Gallagher PM, Coffey MP, Krukonis VJ, Klasutis N. Gas Antisolvent Recrystallization: New Process To Recrystallize Compounds Insoluble in Supercritical Fluids. *Supercritical Fluid Science and Technology*. ACS Symposium Series. 406: American Chemical Society; 1989. p. 334-54.
142. Jovanović N, Bouchard A, Hofland GW, Witkamp G-J, Crommelin DJA, Jiskoot W. Stabilization of Proteins in Dry Powder Formulations Using Supercritical Fluid Technology. *Pharmaceutical Research*. 2004;21(11):1955-69.
143. de la Fuente Badilla JC, Peters CJ, de Swaan Arons J. Volume expansion in relation to the gas–antisolvent process. *The Journal of Supercritical Fluids*. 2000;17(1):13-23.
144. Garg S, Heuck G, Ip S, Ramsay E. Microfluidics: a transformational tool for nanomedicine development and production. *Journal of Drug Targeting*. 2016;24(9):821-35.
145. Fanchi JR. Chapter 9 - Fluid Flow Equations. In: Fanchi JR, editor. *Shared Earth Modeling*. Woburn: Butterworth-Heinemann; 2002. p. 150-69.
146. Ruzycka M, Cimpan MR, Rios-Mondragon I, Grudzinski IP. Microfluidics for studying metastatic patterns of lung cancer. *Journal of Nanobiotechnology*. 2019;17(1):71.
147. Costa Junior JM, Naveira-Cotta CP, de Moraes DB, Inforçatti Neto P, Maia IA, da Silva JVL, et al. Innovative Metallic Microfluidic Device for Intensified Biodiesel Production. *Industrial & Engineering Chemistry Research*. 2020;59(1):389-98.
148. Fornell A, Söderbäck P, Liu Z, De Albuquerque Moreira M, Tenje M. Fabrication of Silicon Microfluidic Chips for Acoustic Particle Focusing Using Direct Laser Writing. *Micromachines*. 2020;11(2):113.

149. Smetana W, Balluch B, Atassi I, Kügler P, Gaubitzer E, Edetsberger M, et al., editors. A Ceramic Microfluidic Device for Monitoring Complex Biochemical Reactive Systems. *Biomedical Engineering Systems and Technologies*; 2010 2010//; Berlin, Heidelberg: Springer Berlin Heidelberg.
150. Wang T, Chen J, Zhou T, Song L. Fabricating Microstructures on Glass for Microfluidic Chips by Glass Molding Process. *Micromachines (Basel)*. 2018;9(6).
151. Ciprian I, Bangtao C, Jianmin M, editors. Deep wet etching-through 1mm pyrex glass wafer for microfluidic applications. 2007 IEEE 20th International Conference on Micro Electro Mechanical Systems (MEMS); 2007 21-25 Jan. 2007.
152. Lin Y-C, Lee C-C, Lin H-S, Hong Z-H, Hsu F-C, Hung T-P, et al. Fabrication of microfluidic structures in quartz via micro machining technologies. *Microsystem Technologies*. 2017;23(6):1661-9.
153. Fujii T. PDMS-based microfluidic devices for biomedical applications. *Microelectronic Engineering*. 2002;61-62:907-14.
154. Matellan C, del Río Hernández AE. Cost-effective rapid prototyping and assembly of poly(methyl methacrylate) microfluidic devices. *Scientific Reports*. 2018;8(1):6971.
155. Strong EB, Schultz SA, Martinez AW, Martinez NW. Fabrication of Miniaturized Paper-Based Microfluidic Devices (MicroPADs). *Scientific Reports*. 2019;9(1):7.
156. Ding R, Hung K-C, Mitra A, Ung LW, Lightwood D, Tu R, et al. Rapid isolation of antigen-specific B-cells using droplet microfluidics. *RSC Advances*. 2020;10(45):27006-13.
157. Prodanović R, Ung WL, Ilić Đurđić K, Fischer R, Weitz DA, Ostafe R. A High-Throughput Screening System Based on Droplet Microfluidics for Glucose Oxidase Gene Libraries. *Molecules*. 2020;25(10):2418.
158. Wheeler AR, Thronset WR, Whelan RJ, Leach AM, Zare RN, Liao YH, et al. Microfluidic Device for Single-Cell Analysis. *Analytical Chemistry*. 2003;75(14):3581-6.
159. Livak-Dahl E, Sinn I, Burns M. Microfluidic chemical analysis systems. *Annual review of chemical and biomolecular engineering*. 2011;2:325-53.
160. Nosrati R, Graham PJ, Zhang B, Riordon J, Lagunov A, Hannam TG, et al. Microfluidics for sperm analysis and selection. *Nature Reviews Urology*. 2017;14(12):707-30.

161. Shallan AI, Priest C. Microfluidic process intensification for synthesis and formulation in the pharmaceutical industry. *Chemical Engineering and Processing - Process Intensification*. 2019;142:107559.
162. Liu Z, Fontana F, Python A, Hirvonen JT, Santos HA. Microfluidics for Production of Particles: Mechanism, Methodology, and Applications. *Small*. 2020;16(9):1904673.
163. Geczy R, Agnoletti M, Hansen MF, Kutter JP, Saatchi K, Häfeli UO. Microfluidic approaches for the production of monodisperse, superparamagnetic microspheres in the low micrometer size range. *Journal of Magnetism and Magnetic Materials*. 2019;471:286-93.
164. Kim JH, Jeon TY, Choi TM, Shim TS, Kim S-H, Yang S-M. Droplet Microfluidics for Producing Functional Microparticles. *Langmuir*. 2014;30(6):1473-88.
165. Wang J, Li Y, Wang X, Wang J, Tian H, Zhao P, et al. Droplet Microfluidics for the Production of Microparticles and Nanoparticles. *Micromachines*. 2017;8(1):22.
166. Deshpande S, Dekker C. On-chip microfluidic production of cell-sized liposomes. *Nature Protocols*. 2018;13(5):856-74.
167. Wang J, Shao C, Wang Y, Sun L, Zhao Y. Microfluidics for Medical Additive Manufacturing. *Engineering*. 2020;6(11):1244-57.
168. Sarah S, Linda H, Ben JB, Arlene M. Microfluidics for the Production of Nanomedicines: Considerations for Polymer and Lipid-based Systems. *Pharmaceutical Nanotechnology*. 2019;7(6):423-43.
169. Liu Y, Yang G, Baby T, Tengjisi, Chen D, Weitz D, et al. Stable Polymer Nanoparticles with Exceptionally High Drug Loading by Sequential Nanoprecipitation. *Angewandte Chemie*. 2020;59(12):4720-8.
170. Shashi Menon E. Chapter Five - Fluid Flow in Pipes. In: Shashi Menon E, editor. *Transmission Pipeline Calculations and Simulations Manual*. Boston: Gulf Professional Publishing; 2015. p. 149-234.
171. Tabeling P, Chen S. *Introduction to Microfluidics*: OUP Oxford; 2005.
172. deMello AJ. Control and detection of chemical reactions in microfluidic systems. *Nature*. 2006;442(7101):394-402.
173. Song Y, Zhao X, Tian Q, Liang H. *Fundamental Concepts and Physics in Microfluidics*. Weinheim, Germany: Weinheim, Germany: Wiley-VCH Verlag GmbH & Co. KGaA; 2018. p. 19-111.

174. Quintanar-Guerrero D, Allémann E, Fessi H, Doelker E. Preparation Techniques and Mechanisms of Formation of Biodegradable Nanoparticles from Preformed Polymers. *Drug Development and Industrial Pharmacy*. 1998;24(12):1113-28.
175. Bilati U, Allémann E, Doelker E. Development of a nanoprecipitation method intended for the entrapment of hydrophilic drugs into nanoparticles. *European Journal of Pharmaceutical Sciences*. 2005;24(1):67-75.
176. Phapal SM, Sunthar P. Influence of micro-mixing on the size of liposomes self-assembled from miscible liquid phases. *Chem Phys Lipids*. 2013;172-173:20-30.
177. Kriel F, Binder C, Priest C. A Multi-Stream Microchip for Process Intensification of Liquid-Liquid Extraction. *Chemical Engineering & Technology*. 2017;40.
178. Jähnisch K, Hessel V, Löwe H, Baerns M. Chemistry in Microstructured Reactors. *Angewandte Chemie International Edition*. 2004;43(4):406-46.
179. Chambers RD, Fox MA, Sandford G, Trmcic J, Goeta A. Elemental fluorine: Part 20. Direct fluorination of deactivated aromatic systems using microreactor techniques. *Journal of Fluorine Chemistry*. 2007;128(1):29-33.
180. Chambers RD, Fox MA, Sandford G. Elemental fluorine Part 18. Selective direct fluorination of 1,3-ketoesters and 1,3-diketones using gas/liquid microreactor technology. *Lab on a Chip*. 2005;5(10):1132-9.
181. de la Iglesia O, Sebastián V, Mallada R, Nikolaidis G, Coronas J, Kolb G, et al. Preparation of Pt/ZSM-5 films on stainless-steel microreactors. *Catalysis Today*. 2007;125(1):2-10.
182. Goodwin AK, Rorrer GL. Conversion of Glucose to Hydrogen-Rich Gas by Supercritical Water in a Microchannel Reactor. *Industrial & Engineering Chemistry Research*. 2008;47(12):4106-14.
183. Goodwin AK, Rorrer GL. Conversion of Xylose and Xylose-Phenol Mixtures to Hydrogen-Rich Gas by Supercritical Water in an Isothermal Microtube Flow Reactor. *Energy & Fuels*. 2009;23(7):3818-25.
184. Knitter R, Göhring D, Risthaus P, Haußelt J. Microfabrication of ceramic microreactors. *Microsystem Technologies*. 2001;7(3):85-90.
185. Christian, Mitchell M, Kenis PJA. Ceramic microreactors for on-site hydrogen production from high temperature steam reforming of propane. *Lab on a Chip*. 2006;6(10):1328-37.

186. Iliescu C, Chen B, Miao J. On the wet etching of Pyrex glass. *Sensors and Actuators A: Physical*. 2008;143(1):154-61.
187. Andersson M, Wilson A, Hjort K, Klintberg L. A microfluidic relative permittivity sensor for feedback control of carbon dioxide expanded liquid flows. *Sensors and Actuators A-Physical*. 2019;285:165-72.
188. Marre S, Adamo A, Basak S, Aymonier C, Jensen KF. Design and Packaging of Microreactors for High Pressure and High Temperature Applications. *Industrial & Engineering Chemistry Research*. 2010;49(22):11310-20.
189. Zhang F, Marre S, Erriguible A. Mixing intensification under turbulent conditions in a high pressure microreactor. *Chemical Engineering Journal*. 2020;382.
190. Zhang F, Erriguible A, Marre S. Investigating laminar mixing in high pressure microfluidic systems. *Chemical Engineering Science*. 2019;205:25-35.
191. Zhang F, Marre S, Erriguible A. Mixing intensification under turbulent conditions in a high pressure microreactor. *Chemical Engineering Journal*. 2020;382:122859.
192. Jaouhari T, Zhang F, Tassaing T, Fery-Forgues S, Aymonier C, Marre S, et al. Process intensification for the synthesis of ultra-small organic nanoparticles with supercritical CO₂ in a microfluidic system. *Chemical Engineering Journal*. 2020;397:125333.
193. Gothsch T, Schilcher C, Richter C, Beinert S, Dietzel A, Büttgenbach S, et al. High-pressure microfluidic systems (HPMS): flow and cavitation measurements in supported silicon microsystems. *Microfluidics and Nanofluidics*. 2015;18(1):121-30.
194. Kaushik S, editor ENHANCEMENT OF SOLUBILITY AND DISSOLUTION PROPERTY OF GRISEOFULVIN BY NANOCRYSTALLIZATION 2011.
195. Waugh CD. Griseofulvin. In: Enna SJ, Bylund DB, editors. *xPharm: The Comprehensive Pharmacology Reference*. New York: Elsevier; 2007. p. 1-4.
196. Shukla R, Pandey V, Vadnere GP, Lodhi S. Chapter 18 - Role of Flavonoids in Management of Inflammatory Disorders. In: Watson RR, Preedy VR, editors. *Bioactive Food as Dietary Interventions for Arthritis and Related Inflammatory Diseases (Second Edition)*: Academic Press; 2019. p. 293-322.
197. Pervin M, Unno K, Nakamura Y, Imai S. Luteolin Suppresses Ultraviolet A- and B-induced Matrix Metalloproteinase 1- and 9 Expression in Human Dermal Fibroblast Cells. *Journal of Nutrition and Food Sciences*. 2016;6:1-6.

198. Lin Y, Shi R, Wang X, Shen H-M. Luteolin, a flavonoid with potential for cancer prevention and therapy. *Curr Cancer Drug Targets*. 2008;8(7):634-46.
199. Szeffler SJ. Pharmacodynamics and pharmacokinetics of budesonide: A new nebulized corticosteroid. *Journal of Allergy and Clinical Immunology*. 1999;104(4, Supplement):S175-S83.
200. Gavins F, Flower RJ. Budesonide. In: Enna SJ, Bylund DB, editors. *xPharm: The Comprehensive Pharmacology Reference*. New York: Elsevier; 2008. p. 1-5.
201. Belloni Fortina A, Romano I, Peserico A, Eichenfield LF. Contact sensitization in very young children. *Journal of the American Academy of Dermatology*. 2011;65(4):772-9.
202. Chen L, Han X, Xu X, Zhang Q, Zeng Y, Su Q, et al. Optimization and Evaluation of the Thermosensitive In Situ and Adhesive Gel for Rectal Delivery of Budesonide. *AAPS PharmSciTech*. 2020;21(3):97.
203. Sheehy TW, Reba RC, Neff TA, Gaintner JR, Tigertt WD. Supplemental Sulfone (Dapsone) Therapy: Use in Treatment of Chloroquine-Resistant Falciparum Malaria. *Archives of Internal Medicine*. 1967;119(6):561-6.
204. Coleman MD. Dapsone-mediated agranulocytosis: risks, possible mechanisms and prevention. *Toxicology*. 2001;162(1):53-60.
205. Wozel G, Blasum C. Dapsone in dermatology and beyond. *Arch Dermatol Res*. 2014;306(2):103-24.
206. Schneider-Rauber G, Argenta DF, Caon T. Emerging Technologies to Target Drug Delivery to the Skin – the Role of Crystals and Carrier-Based Systems in the Case Study of Dapsone. *Pharmaceutical Research*. 2020;37(12):240.
207. Vardanyan RS, Hruby VJ. 34 - Antimycobacterial Drugs. In: Vardanyan RS, Hruby VJ, editors. *Synthesis of Essential Drugs*. Amsterdam: Elsevier; 2006. p. 525-34.
208. Corradini F, Marcheselli L, Tassi L, Tosi G. Static dielectric constants of the N,N-dimethylformamide/2-methoxyethanol solvent system at various temperatures. *Canadian Journal of Chemistry*. 1992;70(12):2895-9.
209. Heravi Majid M, Ghavidel M, Mohammadkhani L. Beyond a solvent: triple roles of dimethylformamide in organic chemistry. *RSC Advances*. 2018;8(49):27832-62.
210. Strohm B. Ethanol. In: Wexler P, editor. *Encyclopedia of Toxicology (Third Edition)*. Oxford: Academic Press; 2014. p. 488-91.

211. Parker WA. Alcohol-Containing Pharmaceuticals. *The American Journal of Drug and Alcohol Abuse*. 1982;9(2):195-209.
212. Fiocchi A, Riva E, Giovannini M. Ethanol in medicines and other products intended for children: Commentary on a medical paradox. *Nutrition Research*. 1999;19(3):373-9.
213. Marino DJ. Ethyl Acetate*. In: Wexler P, editor. *Encyclopedia of Toxicology (Second Edition)*. New York: Elsevier; 2005. p. 277-9.
214. Grodowska K, Parczewski A. Organic solvents in the pharmaceutical industry. *Acta poloniae pharmaceutica*. 2010;67(1):3-12.
215. Reichardt C. *Directory of Solvents*. Herausgegeben von B. P. Whim und P. G. Johnson. Blackie Academic & Professional — An Imprint of Chapman & Hall, London, 1996. 612 S., geb. 149.00 £.—ISBN 0-7514-0245-1. *Angewandte Chemie*. 1997;109(12):1419-20.
216. Alam MS, Ashokkumar B, Siddiq AM. The density, dynamic viscosity and kinematic viscosity of protic and aprotic polar solvent (pure and mixed) systems: An experimental and theoretical insight of thermophysical properties. *Journal of Molecular Liquids*. 2019;281:584-97.
217. Noda K, Ohashi M, Ishida K. Viscosities and densities at 298.15 K for mixtures of methanol, acetone, and water. *Journal of Chemical & Engineering Data*. 1982;27(3):326-8.
218. González B, Domínguez A, Tojo J. Dynamic Viscosities, Densities, and Speed of Sound and Derived Properties of the Binary Systems Acetic Acid with Water, Methanol, Ethanol, Ethyl Acetate and Methyl Acetate at T = (293.15, 298.15, and 303.15) K at Atmospheric Pressure. *Journal of Chemical & Engineering Data*. 2004;49(6):1590-6.
219. Song H, Ismagilov RF. Millisecond Kinetics on a Microfluidic Chip Using Nanoliters of Reagents. *Journal of the American Chemical Society*. 2003;125(47):14613-9.
220. Kashid MN, Kiwi-Minsker L. Microstructured Reactors for Multiphase Reactions: State of the Art. *Industrial & Engineering Chemistry Research*. 2009;48(14):6465-85.
221. Falke S, Betzel C. Dynamic Light Scattering (DLS): Principles, Perspectives, Applications to Biological Samples. *Radiation in Bioanalysis*. 2019;8:173-93.

222. Stetefeld J, McKenna SA, Patel TR. Dynamic light scattering: a practical guide and applications in biomedical sciences. *Biophys Rev.* 2016;8(4):409-27.
223. Di Gianfrancesco A. 8 - Technologies for chemical analyses, microstructural and inspection investigations. In: Di Gianfrancesco A, editor. *Materials for Ultra-Supercritical and Advanced Ultra-Supercritical Power Plants*: Woodhead Publishing; 2017. p. 197-245.
224. Bragg WH, Bragg WL, James RW, Lipson H. *The crystalline state*. New York: Macmillan; 1934.
225. Knight JB, Vishwanath A, Brody JP, Austin RH. Hydrodynamic Focusing on a Silicon Chip: Mixing Nanoliters in Microseconds. *Physical Review Letters.* 1998;80(17):3863-6.
226. Hessel V, Angeli P, Gavriilidis A, Löwe H. Gas-Liquid and Gas-Liquid-Solid Microstructured Reactors: Contacting Principles and Applications. *Industrial & Engineering Chemistry Research.* 2005;44(25):9750-69.
227. Yoshida J-i, Nagaki A, Yamada T. Flash Chemistry: Fast Chemical Synthesis by Using Microreactors. *Chemistry – A European Journal.* 2008;14(25):7450-9.
228. Gupta R, Fletcher DF, Haynes BS. Taylor Flow in Microchannels: A Review of Experimental and Computational Work. *The Journal of Computational Multiphase Flows.* 2010;2(1):1-31.
229. Bruus H. *Theoretical Microfluidics*. Oxford UK: Oxford University Press; 2007.
230. Haynes WM, editor. *CRC Handbook of Chemistry and Physics*. 97th ed. Boca Raton: CRC Press; 2016-2017.
231. Lemmon EW, Huber ML, McLinden MO. *NIST Standard Reference Database 23: Reference Fluid Thermodynamic and Transport Properties-REFPROP*. 9.1 ed. Gaithersburg: National Institute of Standards and Technology; 2013. p. Standard Reference Data Program.
232. Kordikowski A, Schenk AP, Van Nielen RM, Peters CJ. Volume expansions and vapor-liquid equilibria of binary mixtures of a variety of polar solvents and certain near-critical solvents. *The Journal of Supercritical Fluids.* 1995;8(3):205-16.
233. Sih R, Foster NR. Viscosity measurements on saturated gas expanded liquid systems—Acetone and carbon dioxide. *The Journal of Supercritical Fluids.* 2008;47(2):233-9.

234. Bristow S, Shekunov T, Shekunov BY, York P. Analysis of the supersaturation and precipitation process with supercritical CO₂. *J Supercrit Fluids*. 2001;21(3):257-71.
235. Tenorio A, Gordillo MD, Pereyra CM, Martínez de la Ossa EJ. Relative Importance of the Operating Conditions Involved in the Formation of Nanoparticles of Ampicillin by Supercritical Antisolvent Precipitation. *Ind Eng Chem Res*. 2007;46(1):114-23.
236. Tu LS, Dehghani F, Foster NR. Micronisation and microencapsulation of pharmaceuticals using a carbon dioxide antisolvent. *Powder Technology*. 2002;126(2):134-49.
237. Reverchon E, Della Porta G, Pallado P. Supercritical antisolvent precipitation of salbutamol microparticles. *Powder Technology*. 2001;114(1):17-22.
238. Su C-S, Chen Y-P. Recrystallization of Salicylamide using a Batch Supercritical Antisolvent Process. *Chemical Engineering & Technology*. 2005;28(10):1177-81.
239. Subra P, Laudani C-G, Vega-González A, Reverchon E. Precipitation and phase behavior of theophylline in solvent–supercritical CO₂ mixtures. *The Journal of Supercritical Fluids*. 2005;35(2):95-105.
240. Prosapio V, De Marco I, Reverchon E. PVP/corticosteroid microspheres produced by supercritical antisolvent coprecipitation. *Chem Eng J*. 2016;292:264-75.
241. Dalvi SV, Dave RN. Controlling Particle Size of a Poorly Water-Soluble Drug Using Ultrasound and Stabilizers in Antisolvent Precipitation. *Ind Eng Chem Res*. 2009;48(16):7581-93.
242. Reverchon E, Della Porta G, Falivene MG. Process parameters and morphology in amoxicillin micro and submicro particles generation by supercritical antisolvent precipitation. *The Journal of Supercritical Fluids*. 2000;17(3):239-48.
243. Kalogiannis CG, Pavlidou E, Panayiotou CG. Production of Amoxicillin Microparticles by Supercritical Antisolvent Precipitation. *Industrial & Engineering Chemistry Research*. 2005;44(24):9339-46.
244. Reverchon E, De Marco I. Supercritical antisolvent micronization of Cefonicid: thermodynamic interpretation of results. *J Supercrit Fluids*. 2004;31(2):207-15.

245. Rehman M, Shekunov BY, York P, Colthorpe P. Solubility and Precipitation of Nicotinic Acid in Supercritical Carbon Dioxide. *Journal of Pharmaceutical Sciences*. 2001;90(10):1570-82.
246. Bakhbakhi Y, Charpentier PA, Rohani S. Experimental study of the GAS process for producing microparticles of beclomethasone-17,21-dipropionate suitable for pulmonary delivery. *International Journal of Pharmaceutics*. 2006;309(1):71-80.
247. Arora D, Sedev R, Priest C, Beh CC, Foster NR, editors. *Drug Micronization Using High-Pressure Microfluidics*. MicroTAS; 2019; Basel.
248. Wadhawan JD, Welford PJ, McPeak HB, Hahn CEW, Compton RG. The simultaneous voltammetric determination and detection of oxygen and carbon dioxide: A study of the kinetics of the reaction between superoxide and carbon dioxide in non-aqueous media using membrane-free gold disc microelectrodes. *Sensors and Actuators B: Chemical*. 2003;88(1):40-52.
249. Reverchon E. Supercritical antisolvent precipitation of micro- and nanoparticles. *The Journal of Supercritical Fluids*. 1999;15(1):1-21.
250. Chattopadhyay P, Gupta RB. Production of griseofulvin nanoparticles using supercritical CO₂ antisolvent with enhanced mass transfer. *International Journal of Pharmaceutics*. 2001;228(1):19-31.
251. Jarmer DJ, Lengsfeld CS, Anseth KS, Randolph TW. Supercritical fluid crystallization of griseofulvin: crystal habit modification with a selective growth inhibitor. *Journal of Pharmaceutical Sciences*. 2005;94(12):2688-702.
252. Carr AG, Mammucari R, Foster NR. Solubility and Micronization of Griseofulvin in Subcritical Water. *Industrial & Engineering Chemistry Research*. 2010;49(7):3403-10.
253. Prasad R, Dalvi SV. Understanding Morphological Evolution of Griseofulvin Particles into Hierarchical Microstructures during Liquid Antisolvent Precipitation. *Crystal Growth & Design*. 2019;19(10):5836-49.
254. Arora D, Sedev R, Beh CC, Priest C, Foster NR. Precipitation of Drug Particles Using a Gas Antisolvent Process on a High-Pressure Microfluidic Platform. *Industrial & Engineering Chemistry Research*. 2020;59(25):11905-13.
255. Paul EL, Atiemo-Obeng VA, Kresta SM. *Handbook of Industrial Mixing*: Wiley-Interscience; 2004.
256. Whim BP, Johnson PG. *Directory of Solvents*. London: Chapman & Hall; 1996.

257. Haynes WM. Handbook of Chemistry and Physics. 97th ed. Boca Raton: CRC Press; 2016-2017.
258. Hansen CM. Hansen Solubility Parameters. 2nd ed. Boca Raton: CRC Press; 2007. 519 p.
259. Brunner G. Gas Extraction. 1st ed. Heidelberg: Steinkopff-Verlag; 1994. XII, 387 p.
260. Reichardt C, Welton T. Solvents and Solvent Effects in Organic Chemistry. 4th ed. Weinheim: Wiley-VCH; 2011.
261. Yaws CL. Thermophysical Properties of Chemicals and Hydrocarbons. Amsterdam: Elsevier; 2009.
262. Lindsley CW. Lipophilicity. Encyclopedia of Psychopharmacology 2014. p. 1-6.
263. Mullin JW. Crystallization. 4th ed. Oxford: Butterworth-Heinemann; 2001. xv+594 p.
264. Kim S, Chen J, Cheng T, Gindulyte A, He J, He S, et al. PubChem 2019 update: improved access to chemical data. Nucleic Acids Research. 2018;47(D1):D1102-D9.
265. Claeys B. Determination of Surface Energy Using Different Approaches [MSc]: Gent University; 2008-2009.
266. Traini D, Rogueda P, Young P, Price R. Surface Energy and Interparticle Force Correlation in Model pMDI Formulations. Pharmaceutical Research. 2005;22(5):816-25.
267. Karpinski PH, Wey JS. Precipitation Processes. In: Myerson AS, editor. Handbook of Industrial Crystallization. 2nd ed. Amsterdam: Elsevier; 2002. p. 141-60.
268. Li H, Yu S, Han X. Fabrication of CuO hierarchical flower-like structures with biomimetic superamphiphobic, self-cleaning and corrosion resistance properties. Chemical Engineering Journal. 2016;283:1443-54.
269. Shen G, Liu M, Wang Z, Wang Q. Hierarchical Structure and Catalytic Activity of Flower-Like CeO(2) Spheres Prepared Via a Hydrothermal Method. Nanomaterials (Basel). 2018;8(10).
270. Wei Z, Zhou Q, Zeng W. Hierarchical WO₃-NiO microflower for high sensitivity detection of SF₆ decomposition byproduct H₂S. Nanotechnology. 2020;31(21):215701.

271. Lee SW, Cheon SA, Kim MI, Park TJ. Organic–inorganic hybrid nanoflowers: types, characteristics, and future prospects. *Journal of Nanobiotechnology*. 2015;13(1):54.
272. Nonsuwan P, Puthong S, Palaga T, Muangsin N. Novel organic/inorganic hybrid flower-like structure of selenium nanoparticles stabilized by pullulan derivatives. *Carbohydr Polym*. 2018;184:9-19.
273. Sasidharan S, P CS, Chaudhary N, Ramakrishnan V. Single Crystal Organic Nanoflowers. *Sci Rep*. 2017;7(1):17335.
274. Negron LM, Diaz TL, Ortiz-Quiles EO, Dieppa-Matos D, Madera-Soto B, Rivera JM. Organic Nanoflowers from a Wide Variety of Molecules Templated by a Hierarchical Supramolecular Scaffold. *Langmuir*. 2016;32(10):2283-90.
275. Su Y, Yan X, Wang A, Fei J, Cui Y, He Q, et al. A peony-flower-like hierarchical mesocrystal formed by diphenylalanine. *Journal of Materials Chemistry*. 2010;20(32):6734-40.
276. Cölfen H, Antonietti M. Mesocrystals: Inorganic Superstructures Made by Highly Parallel Crystallization and Controlled Alignment. *Angewandte Chemie International Edition*. 2005;44(35):5576-91.
277. Ma Y, Cölfen H, Antonietti M. Morphosynthesis of Alanine Mesocrystals by pH Control. *The Journal of Physical Chemistry B*. 2006;110(22):10822-8.
278. Meldrum FC, Cölfen H. Controlling Mineral Morphologies and Structures in Biological and Synthetic Systems. *Chemical Reviews*. 2008;108(11):4332-432.
279. Jongen N, Bowen P, Lemaître J, Valmalette J-C, Hofmann H. Precipitation of Self-Organized Copper Oxalate Polycrystalline Particles in the Presence of Hydroxypropylmethylcellulose (HPMC): Control of Morphology. *Journal of Colloid and Interface Science*. 2000;226(2):189-98.
280. Imai H, Terada T, Miura T, Yamabi S. Self-organized formation of porous aragonite with silicate. *Journal of Crystal Growth*. 2002;244(2):200-5.
281. Steed JW, Atwood JL. *Supramolecular Chemistry*. 2nd ed. Chichester,; Wiley; 2009.
282. Cox PJ, Kumarasamy Y, Nahar L, Sarker SD, Shoeb M. Luteolin. *Acta Crystallographica Section E*. 2003;59(7):o975-o7.
283. Leśniewska B, Jebors S, Coleman AW, Suwińska K. Transformations of Griseofulvin in Strong Acidic Conditions – Crystal Structures of 2'-

- Demethylgriseofulvin and Dimerized Griseofulvin. *Nat Prod Commun.* 2012;7(3):327-32.
284. Albertsson J, Oskarsson Å, Svensson C. X-ray Study of Budesonide: Molecular Structures and Solid Solutions of the (22S) and (22R) Epimers of 11 β ,21-Dihydroxy-16 α ,17 α -propylmethylenedioxy-1,4-pregnadiene-3,20-dione. *Acta Cryst.* 1978;B34:3027-36.
285. Ritchie TJ, Macdonald SJ. The impact of aromatic ring count on compound developability - are too many aromatic rings a liability in drug design? *Drug Discov Today.* 2009;14(21-22):1011-20.
286. Zhang J, Teixeira AR, Zhang H, Jensen KF. Determination of fast gas-liquid reaction kinetics in flow. *Reaction Chemistry & Engineering.* 2020;5(1):51-7.
287. Feng D-y. Analysis on Influencing Factors of the Gas-liquid Mixing Effect of Compressed Air Foam Systems. *Procedia Engineering.* 2013;52:105-11.
288. Sajjadi B, Raman AAA, Ibrahim S, Shah RSSRE. Review on gas-liquid mixing analysis in multiscale stirred vessel using CFD. *Reviews in Chemical Engineering.* 2012;28(2-3):171-89.
289. Gloerfelt X, Robinet JC, Sciacovelli L, Cinnella P, Grasso F. Dense-gas effects on compressible boundary-layer stability. *Journal of Fluid Mechanics.* 2020;893:A19.
290. Chapter Seven - Fluid Mixing in Reactors. In: Coker AK, Kayode CA, editors. *Modeling of Chemical Kinetics and Reactor Design.* Woburn: Gulf Professional Publishing; 2001. p. 552-662.
291. Himmelsbach W, Keller W, Lovallo M, Grebe T, Ekato DH. Increase productivity through better gas-liquid mixing. *Chemical Engineering.* 2007;114.
292. Alvarado U, Bistué G, Adín I. Mixer Design. In: Alvarado U, Bistué G, Adín I, editors. *Low Power RF Circuit Design in Standard CMOS Technology.* Berlin, Heidelberg: Springer Berlin Heidelberg; 2012. p. 129-77.
293. Dickey DS, Fasano JB. Mechanical Design of Mixing Equipment. *Handbook of Industrial Mixing* 2003. p. 1247-332.
294. Lee JW, Daly SR, Huang-Saad AY, Seifert CM, Lutz J. Using design strategies from microfluidic device patents to support idea generation. *Microfluidics and Nanofluidics.* 2018;22(7):70.
295. Zhou T, Liu T, Deng Y, Chen L, Qian S, Liu Z. Design of microfluidic channel networks with specified output flow rates using the CFD-based optimization method. *Microfluidics and Nanofluidics.* 2017;21(1):11.

296. Fiorini GS, Chiu DT. Disposable microfluidic devices: fabrication, function, and application. *BioTechniques*. 2005;38(3):429-46.
297. Gale BK, Jafek AR, Lambert CJ, Goenner BL, Moghimifam H, Nze UC, et al. A Review of Current Methods in Microfluidic Device Fabrication and Future Commercialization Prospects. *Inventions*. 2018;3(3):60.
298. Jeong H-H, Issadore D, Lee D. Recent developments in scale-up of microfluidic emulsion generation via parallelization. *Korean Journal of Chemical Engineering*. 2016;33(6):1757-66.
299. Gdowski A, Johnson K, Shah S, Gryczynski I, Vishwanatha J, Ranjan A. Optimization and scale up of microfluidic nanolipomer production method for preclinical and potential clinical trials. *Journal of Nanobiotechnology*. 2018;16(1):12.
300. Foster NR, Dehghani F, Charoenchaitrakoo KM, Warwick B. Application of dense gas techniques for the production of fine particles. *AAPS PharmSci*. 2003;5(2):E11-E.
301. Meure LA, Foster NR, Dehghani F. Conventional and Dense Gas Techniques for the Production of Liposomes: A Review. *AAPS PharmSciTech*. 2008;9(3):798.
302. Wang H, Viswanathan NN, Ballal NB, Seetharaman S. Modelling of Physico-Chemical Phenomena between Gas inside a Bubble and Liquid Metal during Injection of Oxidant Gas. *International Journal of Chemical Reactor Engineering*. 2010;8(1).
303. Arif M, Abu-Khamsin SA, Zhang Y, Iglauer S. Experimental investigation of carbonate wettability as a function of mineralogical and thermo-physical conditions. *Fuel*. 2020;264:116846.
304. Marre S, Park J, Rempel J, Guan J, Bawendi MG, Jensen KF. Supercritical Continuous-Microflow Synthesis of Narrow Size Distribution Quantum Dots. *Advanced Materials*. 2008;20(24):4830-4.
305. Marre S, Baek J, Park J, Bawendi MG, Jensen KF. High-Pressure/High-Temperature Microreactors for Nanostructure Synthesis. *Journal of the Association for Laboratory Automation*. 2009;14(6):367-73.
306. Richard-Wagner-Str BWa. Peace Software 10585 Berlin2007 [Available from: http://www.peacesoftware.de/einigewerte/co2_e.html].
307. Berge SM, Bighley LD, Monkhouse DC. Pharmaceutical salts. *Journal of pharmaceutical sciences*. 1977;66(1):1-19.
308. Vishweshwar P, McMahon JA, Bis JA, Zaworotko MJ. Pharmaceutical co-crystals. *Journal of pharmaceutical sciences*. 2006;95(3):499-516.

309. Shan N, Zaworotko MJ. The role of cocrystals in pharmaceutical science. *Drug discovery today*. 2008;13(9-10):440-6.
310. Vogna D, Marotta R, Andreozzi R, Napolitano A, d'Ischia M. Kinetic and chemical assessment of the UV/H₂O₂ treatment of antiepileptic drug carbamazepine. *Chemosphere*. 2004;54(4):497-505.
311. Li Z, Matzger AJ. Influence of coformer stoichiometric ratio on pharmaceutical cocrystal dissolution: three cocrystals of carbamazepine/4-aminobenzoic acid. *Molecular pharmaceutics*. 2016;13(3):990-5.
312. Kuminek G, Cao F, Bahia de Oliveira da Rocha A, Gonçalves Cardoso S, Rodríguez-Hornedo N. Cocrystals to facilitate delivery of poorly soluble compounds beyond-rule-of-5. *Advanced Drug Delivery Reviews*. 2016;101:143-66.
313. Wuest JD. Co-crystals give light a tune-up. *Nature chemistry*. 2012;4(2):74-5.
314. Sharma C. VK; Panneerselvam, K.; Pilati, T.; Desiraju. *GR J Chem Soc, Perkin Trans*. 1993;2:2209.
315. Braga D, Grepioni F, Maini L, Prosperi S, Gobetto R, Chierotti MR. From unexpected reactions to a new family of ionic co-crystals: the case of barbituric acid with alkali bromides and caesium iodide. *Chemical communications*. 2010;46(41):7715-7.
316. Ong TT, Kavuru P, Nguyen T, Cantwell R, Wojtas Ł, Zaworotko MJ. 2: 1 Cocrystals of homochiral and achiral amino acid zwitterions with Li⁺ salts: water-stable zeolitic and diamondoid metal–organic materials. *Journal of the American Chemical Society*. 2011;133(24):9224-7.
317. Jiang L, Huang Y, Zhang Q, He H, Xu Y, Mei X. Preparation and Solid-State Characterization of Dapsone Drug–Drug Co-Crystals. *Crystal Growth & Design*. 2014;14(9):4562-73.
318. Shikhar A, Bommana MM, Gupta SS, Squillante E. Formulation development of Carbamazepine–Nicotinamide co-crystals complexed with γ -cyclodextrin using supercritical fluid process. *The Journal of Supercritical Fluids*. 2011;55(3):1070-8.
319. Ober CA, Montgomery SE, Gupta RB. Formation of itraconazole/L-malic acid cocrystals by gas antisolvent cocrystallization. *Powder Technology*. 2013;236:122-31.
320. Liu B, Li W, Zhao J, Liu Y, Zhu X, Liang G. Physicochemical characterisation of the supramolecular structure of luteolin/cyclodextrin inclusion complex. *Food Chemistry*. 2013;141(2):900-6.

321. Shakeel F, Haq N, Alshehri S, Ibrahim MA, Elzayat EM, Altamimi MA, et al. Solubility, thermodynamic properties and solute-solvent molecular interactions of luteolin in various pure solvents. *Journal of Molecular Liquids*. 2018;255:43-50.
322. do Amaral LH, do Carmo FA, Amaro MI, de Sousa VP, da Silva L, de Almeida GS, et al. Development and Characterization of Dapsone Cocrystal Prepared by Scalable Production Methods. *AAPS PharmSciTech*. 2018;19(6):2687-99.
323. Li W, Ma Y, Yang Y, Xu S, Shi P, Wu S. Solubility measurement, correlation and mixing thermodynamics properties of dapsone in twelve mono solvents. *Journal of Molecular Liquids*. 2019;280:175-81.
324. Peng B, Zi J, Yan W. Measurement and Correlation of Solubilities of Luteolin in Organic Solvents at Different Temperatures. *Journal of Chemical & Engineering Data*. 2006;51(6):2038-40.

Every reasonable effort has been made to acknowledge the owners of copyright material. I would be pleased to hear from any copyright owner who has been omitted or incorrectly acknowledged.